Search for extremely short transient gamma-ray sources with the VERITAS observatory

D I S S E R T A T I O N

zur Erlangung des akademischen Grades

doctor rerum naturalium
(Dr. rer. nat.)
im Fach Physik

eingereicht an der
Mathematisch-Naturwissenschaftlichen Fakultät
der Humboldt-Universität zu Berlin

von

Dipl.-Phys. Christian Skole

Präsidentin der Humboldt-Universität zu Berlin:
Frau Prof. Dr.-Ing. Dr. Sabine Kunst

Dekan der Mathematisch-Naturwissenschaftlichen Fakultät:
Herr Prof. Dr. Elmar Kulke

Gutachter/innen:
1. Dr. Gernot Maier
2. Prof. Dr. Elisa Bernardini
3. Prof. Dr. A. Nepomuk Otte

Tag der mündlichen Prüfung: 5. September 2016

Abstract

In astronomy, many of the observed sources show a transient behavior. Examples are gamma-ray bursts (GRBs) and active galactic nuclei (AGN). For those source types the variability can be very short, in the order of seconds to minutes. Measuring the flux variations is necessary to understand the underlying physical processes responsible for the emission. However, the detection of very short flares can be difficult in the very high-energy range, in which imaging atmospheric Cherenkov telescopes like VERITAS are operating. This is due to the large background and the comparable low signal rates.
This thesis discusses the implementation of advanced statistical methods (*exp-test* and *Bayesian-Blocks*) into the VERITAS analysis framework, that are optimized for the detection of significant variations in the event rate. The performance of these methods is evaluated and compared by using Monte Carlo simulations of minute-scale flares for two different VERITAS states, pre- and post-hardware-upgrade. It is shown that the advanced methods can improve the detection sensitivity for short flares with high fluxes of more than the Crab flux (Crab unit = C.U.). For example, flares at 2 C.U. with short durations down to 100 sec are now detectable, which is not possible with the standard method.
In the next step of this thesis, 6 GRB afterglows and 450 runs of AGN data, observed by VERITAS, are analyzed with the advanced methods. In none of the AGN runs a significant detection of short time variability is made, which is in consistence with the canonical AGN models. The investigation of the 6 GRB afterglows also did not reveal any short flares in the GeV-TeV range. However, for two of them it was possible to estimate an upper flux limit of 1.25 C.U. ($\approx 3,7 \cdot 10^{-10}$ erg cm^{-1}s^{-1} [0,1;10 TeV]).

Kurzfassung

In der Astronomie zeigen viele Quellen ein veränderliches Verhalten. Beispiele dafür sind Gammablitze (GB) und aktive Galaxienkerne (AGK). Der zeitliche Rahmen, in dem bei diesen Quellen beobachtbare Veränderungen stattfinden, kann sehr kurz sein und im Bereich von Sekunden bis Minuten liegen. Um die zugrundeliegenden und für die Photonenemission verantwortlichen, physikalischen Prozesse besser zu verstehen, ist eine Messung der Flussänderungen notwendig. Allerdings kann die Entdeckung sehr kurzzeitiger Ausbrüche im sehr hochenergetischen Bereich des Spektrums, für welche abbildende atmosphärische Cherenkov Teleskope, wie z.B. VERITAS, zum Einsatz kommen, schwierig sein. Die Ursache dafür ist der hohe Untergrund und die vergleichsweise niedrige Signalrate.
Diese Dissertation behandelt die Implementierung fortschrittlicher und für die Entdeckung signifikanter Ratenänderung optimierter, statistischer Methoden (*exp-test* and *Bayesian-Blocks*) innerhalb des VERITAS-Analyse-Programms. Das Verhalten dieser Methoden wird anhand von Daten minutenlanger Ausbrüche, die mittels Monte-Carlo-Technik für zwei unterschiedliche VERITAS Stadien simuliert wurden (vor und nach der Hardware-Aufrüstung), bewertet und miteinander verglichen. Es zeigt sich, dass die fortschrittlichen Methoden die Empfindlichkeit bei der Entdeckung von kurzzeitigen Ausbrüchen verbessern, wenn deren Fluss den des Krebsnebels übersteigt (Krebsnebel-Einheit = K.E.). Beispielsweise sind nun Ausbrüche von 2 K.E. selbst dann nachweisbar, wenn deren Dauer nur 100 Sek. beträgt. Dies ist mit der Standardmethode nicht möglich.
Im darauffolgenden Schritt dieser Doktorarbeit werden das Nachglühen von 6 GB sowie die 450, ebenfalls mit VERITAS erzeugten, Aufnahmen von AGK-Quellen mittels der fortschrittlichen Methoden analysiert. In keiner der AGK-Aufnahmen wird eine signifikante Entdeckung kurzzeitiger Variabilität gemacht, was mit den anerkannten AGK-Modellen übereinstimmt. Auch die Untersuchung des Nachglühens der 6 GB offenbart keine kurzen Ausbrüche im GeV-TeV Bereich. Jedoch ist es für 2 von ihnen möglich, ein oberes Flusslimit von 1.25 K.E. ($\approx 3,7 \cdot 10^{-10}$ erg cm^{-1}s^{-1} [0,1;10 TeV]) abzuschätzen.

Contents

List of Figures

Chapter 1

Introduction

Gamma-rays are the most energetic known forms of electromagnetic radiation, spanning at least 8 decades of energy from 10^6 eV to greater than 10^{14} eV. They are produced by non-thermal processes in the most extreme conditions and environments of the universe. Similar to optical photons, but hundred thousand times more energetic, the gamma-ray photons propagate through space without changing their direction and without loosing much of their energy. This is because they are not affected by the interstellar and intergalactic magnetic fields like the cosmic ray particles (protons and electrons). Therefore, gamma rays are perfect candidates to gain insights into particle acceleration processes and to provide the exact origin of those.

In general the emission spectrum of this non-thermal processes is decreasing in the energy range of gamma-rays. While the flux from X-ray up to MeV/GeV energies is still large enough to provide a sufficient amount of direct detections in a space-based experiment, it was necessary to develop other experiments with much larger collection areas to measure the low rates of photons with energies above 50 GeV. As the deployment of such a large construction in space is too expensive, only ground-based experiments come into question. These kind of experiments make use of the fact that energetic gamma-ray photons decay into electron-positron pairs and induce showers of relativistic particles when they propagate through the earth atmosphere. The direction and energy of the primary gamma-ray photon can only be measured indirectly.
There are two types of ground-based experiments: one is based on the detection of the shower particles itself, while the other detects the Cherenkov light emitted within the air shower. The advantage of the particle detectors is the large field of view ($\sim$ 1 sr) and a duty cycle of nearly 100%. The challenge is the distinction between gamma-rays and the much more frequent comic-rays, that initiate air showers as well. There is a difference in the development of both kind of showers, which is difficult to discover just by measuring the shower particles that hit the detector on the ground. This is why a new type of observation technique had been developed, that uses the Cherenkov light emitted by each particle of the shower.
With one or more telescopes, the Cherenkov light of a shower is focussed onto fast recording, pixelized cameras which results in digitized images of the shower. These images are used to reconstruct the energy and direction of the primary particle and

to distinguish between a gamma ray and cosmic ray. Instruments that use this technique are called Imaging Atmospheric Cherenkov Telescopes (IACTs). Currently there exist four IACT instruments on the globe: H.E.S.S, MAGIC, FACT and VERITAS. These instruments have a typical field of view of 3 - 5° and a duty cycle of about 10% (∼ 1000 hours/year).

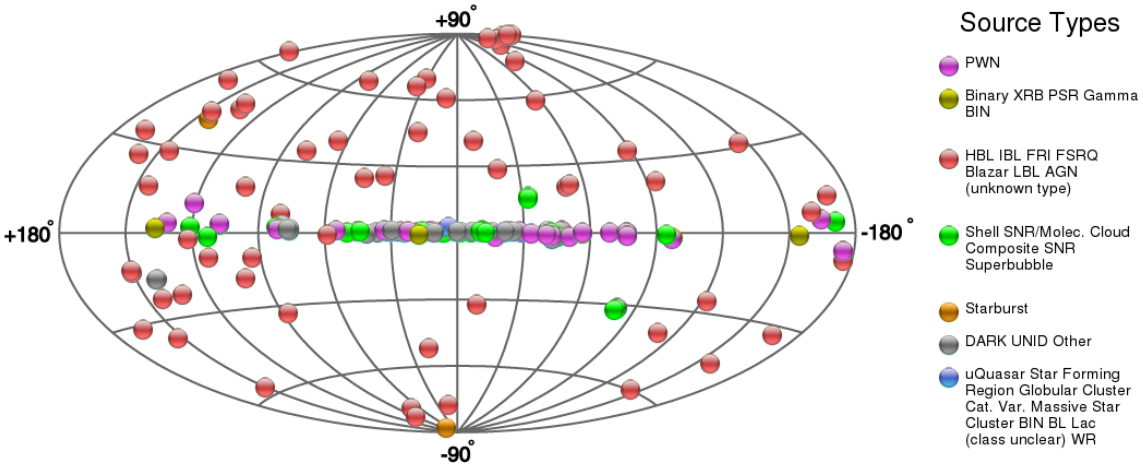

Fig. 1.1: *Locations of all the detected TeV emitters, given in galactic coordinates. The color of each point represents the different source class as explained in the legend. Image credit: [Wakely et al. (2016)].*

With those instruments, altogether more than 170 VHE gamma-ray emitters [Wakely *et al.* (2016)] had been discovered (see Fig. 1.1). The VHE sources found within our galaxy are supernova remnants, pulsar wind nebulae (PWN), X-ray binaries and other unidentified objects. Outside of our galaxy, the known TeV gamma-ray emitters are starburst galaxies and various types of active galactic nuclei (AGN). In addition to those objects, other source classes are thought to be possible VHE emitters, including galaxy clusters, microquasars, gamma-ray bursts (GRBs) and possible signatures from dark matter.

A very important part during the study of these sources is the determination of their temporal behavior. Knowing the duration of an enhanced emission in a specific energy range helps to adjust the parameters of existing theoretical models that describe the source or rule out particular models if there are more than one. Especially if the occurrence of a flux change in one energy band correlates with the occurrence in an other band. However, measuring the temporal flux variations in the VHE range with an IACT can be challenging if the duration of the enhanced flux is very short ($10^0 - 10^2$ sec). This is because an observation usually has to take at least several thousands of seconds to get enough signal data that significantly exceed the background. Therefore, the detection of very short VHE emission periods can only be improved either by increasing the instruments sensitivity or by applying different statistical methods during the data analysis.
Typical source types with very short emission durations are GRBs. Those objects are the most extreme explosive events in the Universe with a total isotropic equivalent energy output of $10^{52} - 10^{54}$ ergs. They emit short, bright flashes of photonic

radiation with peak energies in the gamma-ray band between $\sim$ 100 keV and $\sim$ 1 MeV. This prompt emission can last from milliseconds to several hours and is usually followed by a longer-lived "afterglow" emitted at longer wavelengths (X-ray to radio). Unfortunately, GRBs have yet to be detected in energy range greater than 100GeV and only flux upper limits have been reported.
Also microquasars are supposed to show some fast variability from the radio to the X-ray band. A microquasar is a X-ray binary formed by a normal star and a compact object which can be a stellar black hole or a neutron star with few solar masses. It accretes mass from the normal star under the formation of an x-ray emitting accretion disk and relativistic radio jets. It is also expected that VHE photons are produced inside these jets. This radiation should be temporally connected to the emission at lower energies. If VHE emission exists and varies on very short time scales has to be verified.
In general, the physical processes happening at a microquasar are the same ones that occur inside quasars (or AGN) but on much smaller spatial scales. Because the mass of a blackhole at the center of the AGN is supermassive (millions of solar masses) also the measured duration of any physical change inside an AGN is much longer compared to the one in a microquasar. However, AGN are much more energetic than microquasars and many of them have already been detected in the VHE range. These sources mainly belong to the AGN subgroup of Blazars. There exist also some AGN with VHE flux variations down to several minutes. Detecting and studying this short time variability is necessary for fine tuning the parameters of existing canonical AGN models or it leads to the verification or the rejection of specific model extensions.

The focus of this thesis is the test of different statistical methods, inside the VERITAS analysis procedure, with the goal to improve the detection of very short ($\sim$ few minutes) VHE flux variations. The standard procedure is the accumulation of all gamma-like events measured during an observation and use this number together with an expected number of background events to calculate the significance of a detection. An enhanced emission only during a small period of the observation will then be averaged over the whole data taking duration and probably won't get detected. However, there exist some advanced statistical methods, developed by J. Prahl [Prahl (1999)] and J. D. Scargle [Scargle (1998), Scargle *et al.* (2013)], which take into account the additional temporal information of each event to determine if the measured rate changes significantly during an observation.
This thesis here describes the implementation of these methods into the VERITAS analysis framework and compares their detection sensitivity with the one of the standard method on basis of Monte Carlo (MC) generated simulations of minute-scale flares. In a further step, these methods are applied to VERITAS data of potential VHE sources with short-time variability. This gives a hint about the general detection rate of such variability in the VHE regime and constrains the duration and amplitude of such flux variations.

The thesis is structured as follows. Chapter 2 starts with a brief introduction into the physics of air showers and discusses the imaging atmospheric Cherenkov technique, along with hardware and software information of the VERITAS array. It is followed

by Chapter 3, which describes the very-high-energetic astrophysics and gives an overview of the different types of transient gamma-ray sources. In Chapter 4 the different statistical methods, used throughout this thesis to calculate the significance of a data measurement, are derived in detail. The implementation of the advanced methods into the VERITAS analysis framework is described in Chapter 5. In the same chapter the performances of the advanced methods and the standard method are compared by applying them to MC generated simulations of minute-scale flares. The next step, presented in Chapter 6, was the usage of these methods to search for short flux variations in VERITAS data of known transient gamma-ray sources. The list of analyzed sources comprises 13 AGN, 6 GRBs and the Crab Pulsar. Further the data, taken during a flaring period of the Blazar Markarian 421, was studied in more detail within the same chapter. Finally, in Chapter 7 a brief summary of the results is provided, followed by an overview of the improvements expected from a future IACT like CTA (Cherenkov Telescope Array).

Chapter 2

Measurement of very high-energetic gamma-rays

In this chapter we explain the detection of very high-energetic (VHE) gamma-rays with *Imaging Atmospheric Cherenkov Telescopes (IACT)*. Therefore it is necessary to describe the characteristic effects induced by such VHE photons entering the atmosphere before we explain the detection technique of an IACT. As we use data measured by the *Very Energetic Radiation Imaging Telescope Array System (VERITAS)* we will provide a detailed look into its hardware components and into the standard analysis with this instrument.

2.1 Air showers

When a high-energy cosmic-ray particle interacts with the molecules of the atmosphere it is able to initiate a cascade of particles. Some of these energetic secondary particles of the cascade lose a part of their energy by emitting *Cherenkov radiation*. By measuring this light with a dedicated telescope system, one is able to gain information about the primary particle hitting the atmosphere. Depending on the primary particle, there are two different types of air showers, electromagnetic and hadronic, which have distinctive features.

2.1.1 Electromagnetic air showers

A high-energy photon, electron or positron that enters the atmosphere initiates an electromagnetic shower. In case of a photon, the primary process will be a $e^{\pm}$-pair-production within the Coulomb field of an atmospheric nucleus. Other processes like the photoelectric effect, Compton scattering and $\mu^{\pm}$-pair-production are suppressed for initial photon energies E_0 above a few MeV. The primary energy loss of an incoming electron or positron is the emission of bremsstrahlung (see Fig. 2.1,a).

If the remaining energy of the secondary particles is still very high, then subsequent bremsstrahlung and pair-production processes occur which in turn produce additional photons and $e^{\pm}$-pairs. In the simplified model of Heitler [Matthews (2005)], one assumes the alternating continuation of these two processes while the energy at each iteration is equally distributed across the particles: photons and leptons. Hence, the energy of each particle decreases by the factor of two after each step

while the number of particles obviously doubles each time. In this model, the distance between subsequent interactions is $d = X_0 \ln 2$ where X_0 is the characteristic amount of matter traversed by a particle, the so-called the *radiation length*, which is usually measured in g/cm^2 ($X_0 \simeq 37$g/cm^2 in air). It corresponds to 7/9 of the mean free path for pair production by a high-energy photon and to the mean distance over which a high-energy electron loses all but 1/e of its energy by bremsstrahlung [Rieke (2012), Weekes (2003)].
As the shower evolves with atmospheric depth, the energy of each individual particle reaches the critical energy E_c (≈ 83 MeV in air), where energy losses through ionization become the dominant process for electrons which rapidly cool and thermalize. At this point in the atmosphere the number of particles in the shower reaches its maximum $N_{max} = E_0/E_c$ and starts to decrease below this height. As also the energy of the bremsstrahlung photons falls below the pair production threshold no new leptons will be produced and this is why the cascade dies out. In the simplified Heitler model the ratio between photons and electrons at the shower maximum is 1 to 2. In real showers, however, it is shifted more towards photons as more than one bremsstrahlung photon is created during one radiation length transversed and because many electrons are absorbed in the air.
Besides the longitudinal expansion of a shower there is also a lateral spread due to multiple scatterings of low-energy electrons within the air shower and the deflection of charged particles within the Earth's magnetic field. A cylinder around the shower axis with the Molière radius $R_{mol} = 9.6$ g·cm$^{-2}/\rho \approx 80$m (at sea level) contains on average 90% of the shower energy.
The whole shower evolution takes about 10^{-4} s while traversing the atmosphere. The maximum number of particles in the shower is proportional to E_0 and the depth of the shower maximum scales with the logarithm: $\ln E_0$. The atmospheric height of about 7 to 12 km above sea level corresponds to the shower maximum of gamma-rays of 20 GeV to 20 TeV and the first interaction usually happens after the gamma ray traversed one radiation length of atmosphere, which is at an typical altitude of 20km. [Grieder (2010)]

2.1.2 Hadronic air showers

Besides the electromagnetic air showers a much more frequent scenario occurring in the atmosphere is the generation of *hadronic air showers*. They are induced by a series of successive inelastic collisions of high-energy cosmic-ray particles like a proton (or a heavier nucleus) with the nuclei of air molecules and are far more numerous than the VHE gamma rays.
During each strong interaction, an energy dependent number of secondaries (e.g. pions, kaons, nucleons, light baryons) is produced. Most of these secondaries (e.g. charged pions) will also collide with other nuclei of the atmosphere, while others rather decay into photons or leptons. This particle multiplication gives rise to a cascade of secondary particles (see Fig. 2.1,a).

One can divide the hadronic air showers into three components: the electromagnetic, the muonic, and the hadronic component. The electromagnetic component contains the electrons, positrons and photons produced in sub-cascades that have

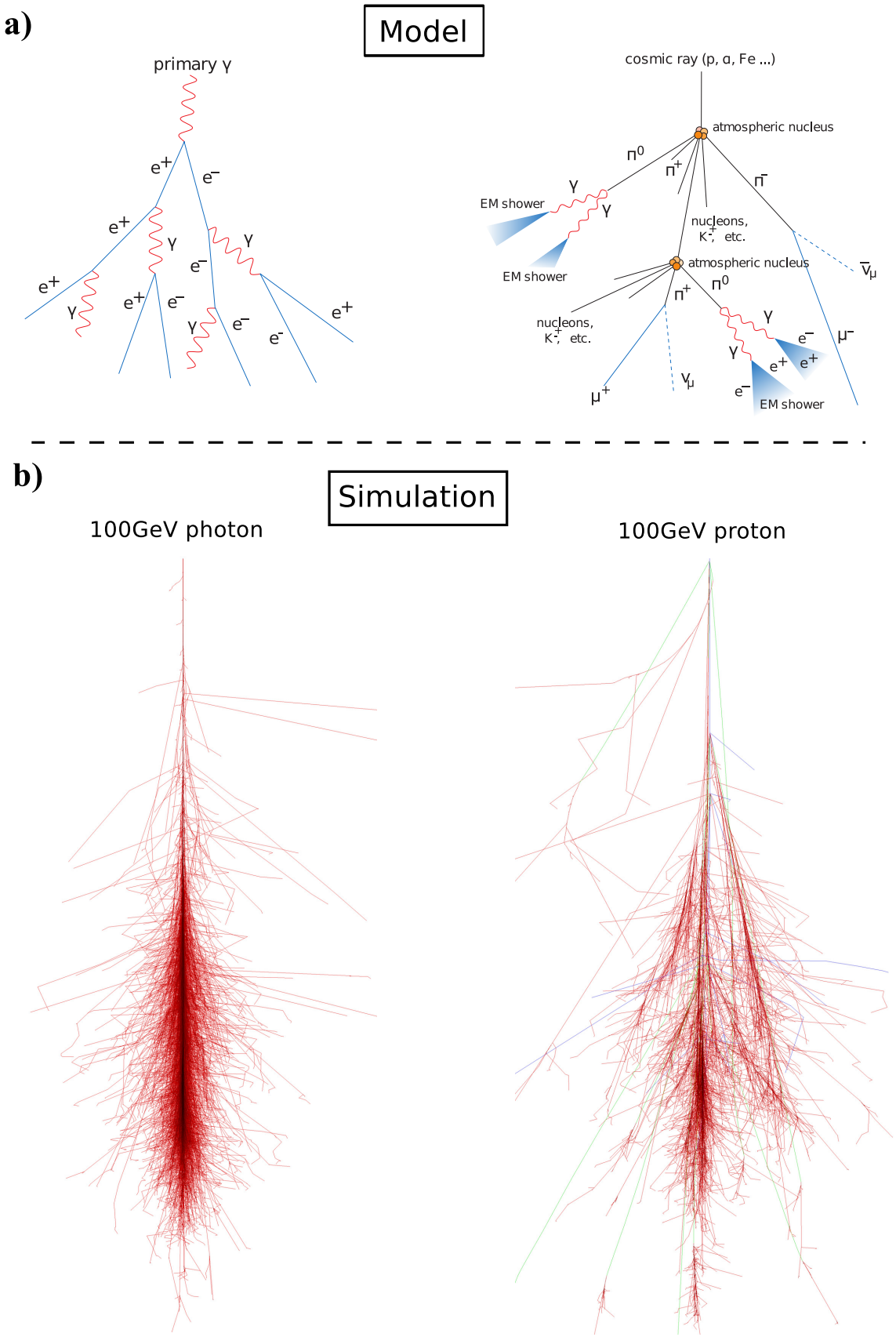

Fig. 2.1: a) *Schematic view of the development of the two different types of air showers: electromagnetic (left) and hadronic (right) [Otte (2007)].*
b) *Monte-Carlo simulations of extensive air showers show the longitudinal developments of a cascade initiated by a single 100 GeV photon and a single 100 GeV proton. Red tracks are used to indicate electrons, positrons and gamma rays. [Schmidt (2005)]*

been initiated by the almost immediate decays ($\approx 10^{-16}$ s) of neutral pions into two gamma rays.
The charged pions and kaons, however, have much larger decay times ($\approx 10^{-8}$ s). This is why they rather collide with nuclei of the atmosphere before they decay and produce new generations of less energetic hadronic secondaries. The multiplication will continue until the energy of each secondary drops below the pion-production threshold. Those remaining nucleons and other high-energy hadrons belong to the hadronic component of the shower.
The smaller energy of secondaries makes the decay of the charged pions and kaons into muons more likely. The muons (and neutrinos), generated during such decays, represent the muonic component of the shower.
Because most of the produced hadronic secondaries are pions, with about equal partition into π^+, π^- and π^0, is assumed that at each interaction about one third of the energy is dissipated by the electromagnetic component. Taking into account all possible interactions, the overall fraction of the initial energy E_0 that is transferred to electrons, positrons and photons depends on the magnitude of E_0.

As one can see in Fig. 2.1, there exist significant differences between both types of air showers. The lateral spread, for example, is much wider in case of hadronic showers than in electromagnetic ones due to the high transverse momentum gained by the secondary particles in inelastic scattering and decay processes. Further the irregular structure of the cascade, due to complex multiparticle processes, is a clear sign for a hadronic shower as well. A third distinctive characteristic of hadronic showers is the larger interaction length which made them penetrate more deeply into the atmosphere than it is the case for electromagnetic showers. More detailed descriptions can be found in [Gaisser (1990), Grieder (2010)].

2.1.3 Cherenkov emission of air showers

The energetic secondary particles generated during the evolution of an air shower move with ultrarelativistic speed v through the atmosphere whose refractive index $n(> 1)$ decreases with height h. If $v > c/n$ the charged secondaries emit the so-called *Cherenkov radiation*. A simplified explanation of this type of photon emission makes use of Huygens' construction.
A charged particle, moving through a dielectric medium, polarizes the molecules of the medium which relax back to mechanical equilibrium and emit electromagnetic waves as the particle passes by. According to the Huygens principle, the emitted waves move out spherically at the phase velocity of the medium. If the particle moves faster than the phase velocity $c' = c/n$ of the medium, the emitted waves add up constructively to a wavefront propagating away in a cone around the particle direction with an opening angle of θ (see Fig. 2.2):

$$\cos(\theta) = \frac{c'}{v} = \frac{1}{\beta \cdot n(h)} \tag{2.1}$$

$$\text{with:} \quad n(h) = 1 + \eta_0 \cdot \mathrm{e}^{-h/h_0} \tag{2.2}$$

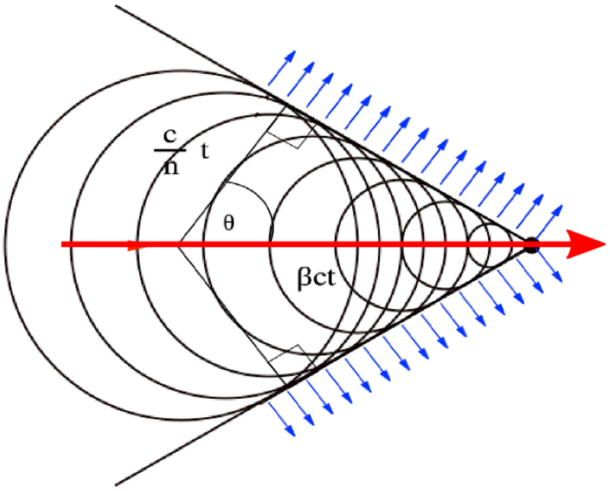

Fig. 2.2: *Huygens' construction of the wavefront which leads to the coherent Cherenkov radiation (blue) if the charged particle (red) moves with a constant velocity $v > c/n$ through the medium with refractive index n. The emission angle is $\theta = \arccos(1/n\beta)$.*

To estimate the dependance of the refractive index $n(h)$ on the altitude, we assume an isothermal atmosphere and use the barometric formula with $\eta_0 = 2.9 \cdot 10^{-4}$ and $h_0 = 7.1\text{km}$.
In a more detailed explanation of the Cherenkov emission, found in [Longair (2011)], the approach is the calculation of the radiation energy E_{rad} emitted by a single charged particle moving at constant speed v through a dielectric medium. In the final term it is shown that

$$E_{\text{rad}} \propto \left| \int \exp\left[i \left(\boldsymbol{k} \cdot \boldsymbol{x} + \frac{\omega x}{v} \right) \right] \mathrm{d}x \right|^2 = \left| \int \exp\left[ikx \left(\cos(\theta) + \frac{\omega}{kv} \right) \right] \mathrm{d}x \right|^2 . \quad (2.3)$$

If the exponent in the last equation is not zero, then the integral over all x is always zero and there will be no radiative energy loss which means there is no Cherenkov radiation. Hence, only if $\cos(\theta) = -\omega/kv$, there will be Cherenkov emission. This condition leads to Equ. (2.1) if one takes into account that $\omega/k = c/n$.
The full equation for E_{rad} (see [Longair (2011)]) is used to derive the amount of photons emitted per unit of the path length, the particle with charge Ze has travelled. This formula is named *Frank-Tamm-Formula* and can be written in the following form [Beringer *et al.* (2012)]:

$$\frac{\mathrm{d}N}{\mathrm{d}x} = \frac{\mathrm{d}E_{\text{rad}}}{\mathrm{d}x} \frac{1}{\hbar\omega} = \int \frac{2\pi\alpha Z^2}{\lambda^2} \left(1 - \frac{c^2}{v^2 n^2} \right) \mathrm{d}\lambda \quad (2.4)$$

In this equation $\alpha = e^2/4\pi\epsilon_0\hbar c$ ($\simeq 1/137$) represents the fine structure constant and the refractive index depends not only on the height but also on the wavelength: $n \to n(h, \lambda)$.

During the evolution of an air shower, charged hadrons and electrons travel only short distances in a specific direction before the next interaction happens that induces the emission of new particles, moving in different directions (see Fig. 2.1,b). The distribution of Cherenkov photons on the ground is a superposition of the emission cones around each single path of a charged particle taking into account the increasing refraction index, the decreasing particle energy and the absorption

of Cherenkov photons by the atmosphere. This is also the reason why the observed spectrum deviates from the λ^{-2}-dependancy given in Equ. (2.4) and peaks at UV/blue-wavelengths (see Fig. 2.3,b).
The best estimates of the Cherenkov spectrum and the spatial photon distribution are achieved by numerical Monte Carlo simulations of air showers. In case of an vertical electromagnetic shower induced by a 300 GeV gamma ray, the distribution of the Cherenkov photons on the ground and their spectrum is similar to the one in Fig. 2.3. One can see an almost constant photon density around the core position up to a radius of $\sim$ 120m. Beyond that distance, the density decreases exponentially. The region of constant photon density is usually denoted as the *Cherenkov light pool* of the shower and its diameter is independent of the initial energy of the

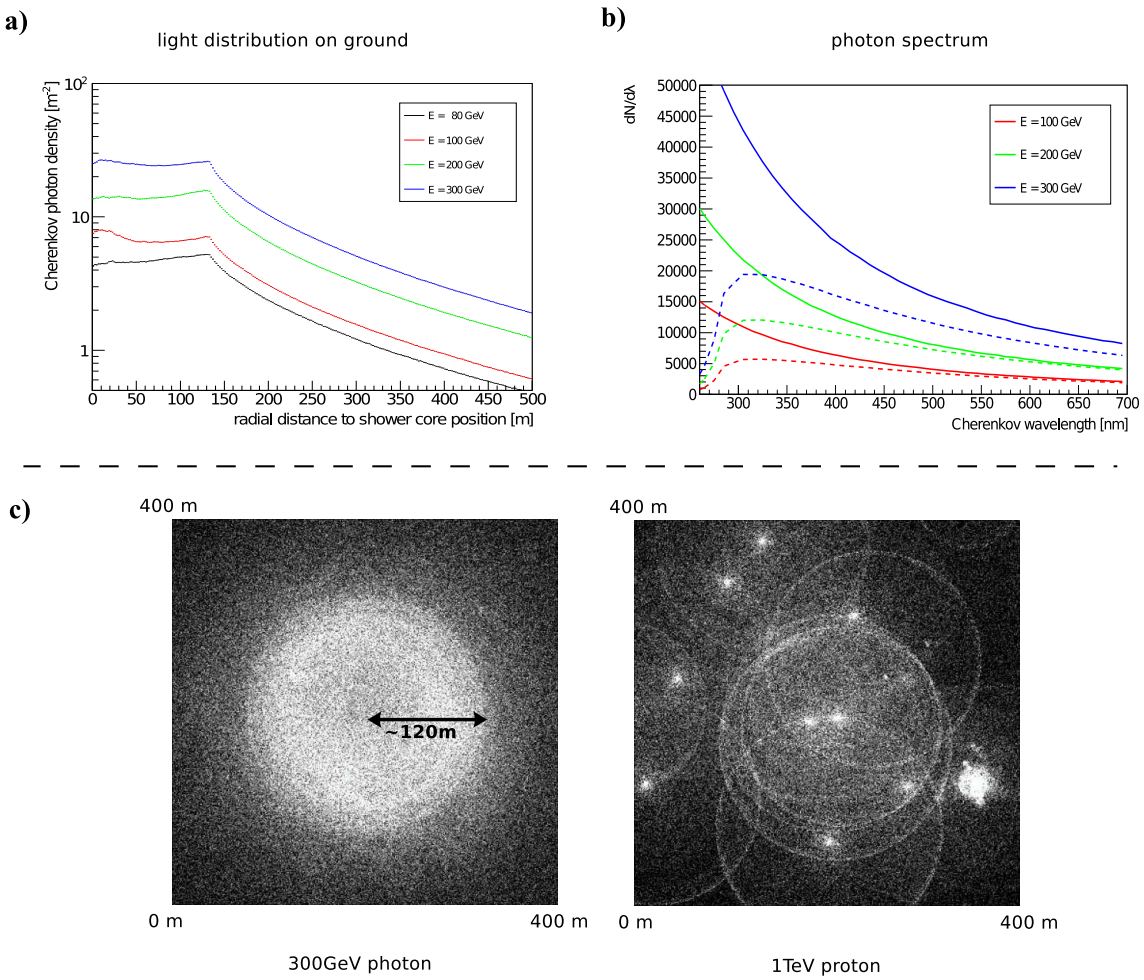

Fig. 2.3: a) *Average radial Cherenkov photon distribution around the core position of a simulated vertical gamma-ray shower (averaged over 100 showers). For comparison four different initial energies are simulated [Prokoph (2013)].*
b) *The spectrum of the Cherenkov photons emitted by the same gamma-ray showers simulated in a). With the absorption of the atmosphere taken into account (dashed lines) and without (solid lines) [Prokoph (2013)].*
c) *Comparison of the Cherenkov light distribution on the ground between Monte Carlo simulations of a 300 GeV gamma ray (left) and a 1TeV proton (right) for a detector 1.8km above sea level [Bernlöhr (2000)].*

primary particle. The number of Cherenkov photons, however, depends strongly on the energy of the primary particle and its zenith angle. This is because the amount of atmosphere that has to be traversed by the cascade particles is much larger at higher zenith angles which affects the shower evolution, the Cherenkov emission and the photon absorption.
In contrast to an electromagnetic shower the distribution of Cherenkov photons is much more diffuse in case of hadronic showers which is due to their erratic structure. This can be seen in the right picture of Fig. 2.3,c. Remarkable structures in this distribution are the several circles of high photon density. The rings are caused by muons that hit the ground before they decay. As the refractive index increases at lower altitude also the Cherenkov angle increases. Hence, Cherenkov photons emitted at large altitudes intersect with photons emitted by the same muon at lower heights which leads to distribution of photons that peaks at a specific radius around the impact point of the muon.

As a shower develops nearly with the speed of light, Cherenkov photons emitted at different locations (heights) inside the shower reach the ground almost at the same time. Hence, the time interval of Cherenkov photons produced in a typical electromagnetic shower is in a range of 2 - 5 ns, while for hadronic showers the interval is much wider (10 - 15 ns) due to its electromagnetic subshowers and the larger transverse momentum of hadronic interactions.

2.2 Imaging Atmospheric Cherenkov Telescopes - IACTs

Due to the opacity of the earth's atmosphere to gamma rays, there is no chance of observing them directly with ground-based telescopes. While satellite observatories are able to measure high energy (HE) photons up to several hundreds of GeV, their detector size is to small for efficient VHE detections as those fluxes are much lower. However, we know from the explanations above that such VHE gamma-rays generate air showers, which in turn produce Cherenkov light pools on the ground. Hence, a detector, located somewhere inside this region and able to measure the Cherenkov light, could be used to detect VHE gamma-rays indirectly with a much larger effective area compared to space-based observatories. Basically the Earth's atmosphere is used as a calorimeter to sample the Cherenkov light from air showers [Jelley *et al.* (1963)].
As the Cherenkov spectrum is close to the optical spectrum a specific detector setup is necessary to reduce the background during the observations at night. Daytime observations are not possible at all. Furthermore good weather conditions are also required to reduce the absorption of Cherenkov photons in the atmosphere. Therefore the duty cycle of ground-based detector systems is only at $\sim 11\%$.

2.2.1 Detection principle

Night sky background

A major difficulty in detecting air showers by the emission of their Cherenkov light is the high flux of *night sky background (NSB)* photons ($\sim 10^{12}$ photons m^{-2} s^{-1} sr^{-1}). The NSB is a combination of several different light sources which contribute to the overall NSB light with different intensities depending on the pointing of the telescopes, the location, the current date and the time of day. The different contributions are:

zodiacal light: caused by the scattering of sunlight at the interplanetary dust near the ecliptic; most intense shortly after sunset or before sunrise

air-glow: light emitted by atoms and molecules in the upper atmosphere; intensity increases with larger zenith angle

man-made light: light from nearby cities or roads; depends on the detector location

starlight: optical light from the stars; higher contribution at galactic sources

moon light: direct light from the moon or its scattering at clouds

The density of photons on the ground produced during the development of a gamma-ray air shower depends on the initial energy (given in TeV). It is 100 photons m^{-2} TeV^{-1}. All these photons reach the ground within a short period of $\sim 10^{-9}$s - 10^{-8}s which leads to an average rate of $\sim 10^{10}$ - 10^{11} m^{-2} s^{-1} for a 1TeV shower. This is still smaller than the overall NSB rate but the direction of Cherenkov photons is concentrated on a much smaller ellipsoidal area in the sky [Preuss *et al.* (2002)].

By imaging the light onto a camera which consists of many pixels, one is able to determine the direction of the incoming photons which helps to distinguish Cherenkov light from the NSB and other background sources (see 2.2.2). The rate of NSB photons per pixel is more or less constant over all pixels (not at the edge) and doesn't change drastically within minutes. The number of Cherenkov photons of an air shower entering a specific pixel during a small time interval of several nano seconds will exceed the number of NSB photons entering the same pixel during the same periode. To measure this effect a high sampling rate of the data acquisition system is necessary. In order to make it simple, one can say that we take an image of the sky with a temporal resolution high enough to resolve single photons.

A telescope, able to map the light with spherical or parabolic mirrors onto a fast camera in the focal plane of the mirrors [Weekes *et al.* (1989)], is therefore the most suitable detector system. The camera of current systems usually consists of hundreds of photomultiplier tubes (PMTs) sensitive in the wavelength range of Cherenkov photons. Each of those PMTs represents one pixel of the camera. The PMTs and the subsequent data acquisition system operate in the nano second regime. The dish is large enough ($\geqslant$ 10m diameter) to collect sufficient amount of photons to improve the signal-background ratio. Its shape is optimized to light sources far away from the telescope which is true for air showers whose maxima is typically in heights of 8 km to 12 km.

Reconstruction of gamma-ray direction

The detection principle is illustrated in Fig. 2.4. If the telescopes are inside the Cherenkov light pool, the emission angle of each single region in the ellipsoidal gamma-ray air showers will comprise the whole area of the dish. The nearly parallel Cherenkov light beams of a single region in the shower is focused onto the camera as can be seen in the enlarged side view of the telescope in Fig. 2.4.

The angular deviation from the optical axis of each emission point inside the shower is measured by the distance of the image of this point from the center of the camera. The image of the whole shower inside the camera is a slightly asymmetric ellipse with an axis that is pointing towards the negative angular coordinates of the original gamma-photon (ϕ_γ and θ_γ). This point in the angular coordinate system of the camera represents a direction parallel to the gamma-photon direction. It would be shone on only if the Cherenkov emission started already at the source of the gamma-photon at nearly infinity.

As this is not the case, one has to estimate its position in the camera by extrapolating the axis of the shower image. The asymmetry and the roundness of the elliptical shower image gives a hint on the distance of the point from the center of the image. This method has to be used in systems with only one telescope [Otte (2007)] while systems with more than one telescope, like VERITAS, use a different reconstruction method [Hofmann *et al.* (1999)]. The advantage of several telescopes pointing all at the same direction is the fact that due to their different locations on the ground the

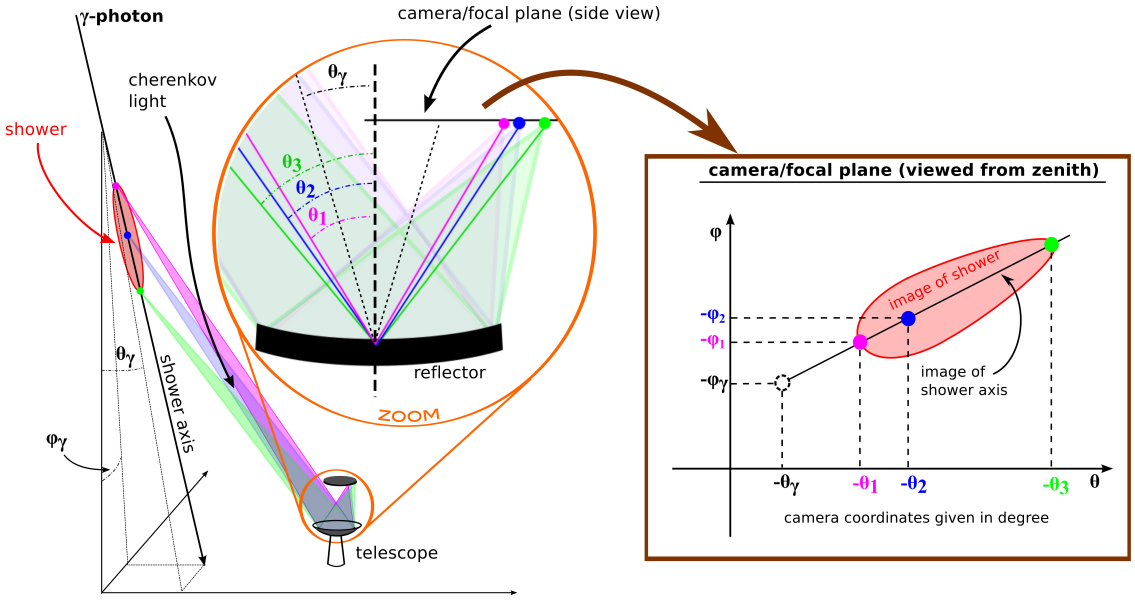

Fig. 2.4: *Sketched is the mapping of the shower image into the focal plane of a telescope. As can be seen from the inset, the orientation of the image depends on the inclination of the shower with respect to the telescope optical axis. The dashed point in the inset at (-ϕ_γ, -θ_γ) marks the image position a Cherenkov photon would produce if it would have been emitted directly at the gamma-ray source. Therefore it corresponds to the reflected direction of the primary gamma-ray. It is not visible but can be reconstructed with the help of different shower images from different telescopes in the array (see text).*

shower images in the cameras have different orientations. As all shower axes of the different camera images of the same shower point towards the same coordinates -ϕ_γ and -θ_γ one can draw them together in one camera coordinate system and determine the intersection point of the different shower axes to measure the direction of the initial gamma-photon: ϕ_γ and θ_γ.

Besides the direction of the gamma-ray one is also able to reconstruct the core position where the gamma-ray would hit the ground if there would be no atmosphere and no shower development. In a first step a common coordinate system has to be introduced, which is called the *shower plane*. The shower plane is a plane perpendicular to the reconstructed shower direction.
Taking into account the position of each telescope with respect to the shower plane on can project all different camera images of the same shower on the common shower plane. By extrapolating the axes of each projected shower image one should theoretically find a single intersection point. In reality one has to average over several intersection points as each pair of axes intersect at a slightly different position due to the inaccurate axis determination. At the center of gravity between all these intersection points the shower axis is supposed to crosses the shower plane. The coordinates of this point together with the information of the plane orientation in the ground coordinate system are sufficient to calculate the core position of the shower.

2.2.2 Background

Besides the NSB there exist other sources of background light that make it harder for IACTs to detect gamma rays. Especially cosmic hadrons (basically protons and helium nuclei), cosmic electrons and muons can mimic gamma-ray showers in the camera [Maier *et al.* (2007)].

Because hadrons are about one thousand times more numerous than gamma rays their contribution to the background is the most prominent. But due to the much wider, longer and more irregular shape of most of the hadron showers, their images in the camera differ from the elliptical-shaped ones of gamma-ray showers. In section 2.4 it will be described how the images are parameterized and which are the most distinctive parameters to separate gamma-ray showers from hadron showers. Unfortunately, this method only works for high-energetic hadron showers as it is more difficult for an IACT-system to distinguish between a low-energetic hadron and a gamma-ray just by the shape of its image.
As the charged hadrons get reflected by the interstellar magnetic fields they arrive isotropically on Earth. Only a small fraction of all the hadron showers detected by the IACT has the same direction as the gamma-rays from a point source. Therefore restricting the accepted arrival direction to a small area around the expected source position will additionally help to suppress the hadron background.

Nearly impossible to suppress, are the electromagnetic showers induced by electrons because they have the same elliptical shape. Although the number of cosmic electrons is much smaller than the amount of hadrons entering the atmosphere [Chaisson *et al.* (2013)], their contribution to the background becomes quite important after

the shape cuts had been applied. The only way to reject most of them, is by restricting the accepted shower direction to a small area around the expected position of the gamma-ray source. This works because the arrival direction of the charged electrons is isotropic.

Another important contribution to the background is the Cherenkov emission of muons produced in hadronic air showers. Their lifetime is long enough to hit the ground.
Depending on their impact parameter and their angular deviation from the optical axis, different images are produced in the camera, as can bee seen in Fig. 2.5. Especially the image of an muon hitting the ground some meters next to the mirror can imitate a gamma-ray shower. (see Fig. 2.5,b).
To suppress this kind of background, the stereoscopic approach of several telescopes has been established. If the distance between the telescopes is large enough a muon will produce an gamma-like image only in one of those telescopes. Requiring at least

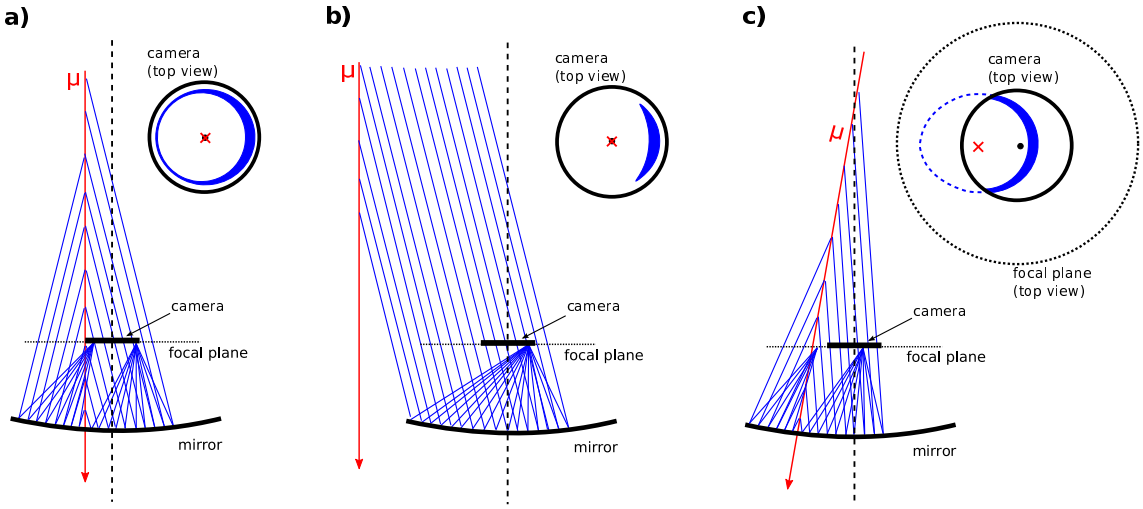

Fig. 2.5: *Sketched is the mapping of the different images a muon can produce in the camera of a telescope. It is assumed that the Cherenkov angle is constant for all the photons entering the telescopes:*
a) *A muon hitting the mirror parallel to the optical axis will produce a circle (blue) in the camera. The red cross marks the center of the circle while the black dot is the camera center. There is more light on the right side of the circle because the muon crosses the mirror left of the center.*
b) *A muon with the same direction as in a) but not hitting the mirror. The resulting image is an incomplete circle as only a small part of the rotational symmetric Cherenkov emission enters the mirror. The center of the incomplete circle is still in the middle of the camera.*
c) *A muon not parallel to the optical axis hitting the mirror. It produces a distorted circle in the focal plane with a center that deviates form the camera center. As the camera covers only a small area in the focal plane, only the right part of the circle is recorded.*
If the camera coordinates are given in degrees, then the red cross represents the angular deviation of the muon direction from the optical axis and the radius of the circular image corresponds to the Cherenkov angle of the atmosphere ∼ 10 - 100 meters above the telescopes.

two images in two different telescopes will significantly reduce the amount of false detections induced by muons.

2.3 The Very Energetic Radiation Imaging Telescope Array System (VERITAS)

The *Very Energetic Radiation Imaging Telescope Array System (VERITAS)* is a ground-based gamma-ray observatory consisting of four imaging Cherenkov telescopes, sensitive to gamma-ray photons at energies between $\sim$ 85 GeV and $\sim$ 30 TeV, with an energy resolution of $\sim$ 15% at 1 TeV. The angular resolution of the reconstructed gamma-ray direction is $\sim 0.1^\circ$ at 1 TeV (68% containment). VERITAS is located at the *Fred Lawrence Whipple Observatory (FLWO)* in southern Arizona, USA (+31° 40' 30.21", -110° 57' 7.7"), at an altitude of about 1270 m above sea level [Holder *et al.* (2011)]. As operations are only possible in dark nights during good weather conditions, VERITAS currently obtains about 1000 h of observations in a typical calendar year. During the monsoon season in July and August no observations are possible and the whole system is shut down.
In 2005 the first telescope started observations and it took two additional years until the full, four telescope configuration was completed. The full array began operation in April, 2007 but was improved in Summer, 2009, by the relocation of one of the four telescopes. This modification made the overall array layout more symmetric, as can be seen in Fig. 2.6, which in turn led to a better sensitivity primarily through an improved angular resolution. In this configuration less than 30 hours are necessary to detect a 1% Crab Nebula-like source with 5 standard deviations (5σ) [Perkins *et al.* (2009)]. A further improvement was made in Summer, 2012, as all PMTs in all four cameras were replaced by high-quantum-efficiency devices [Kieda (2011)]. The

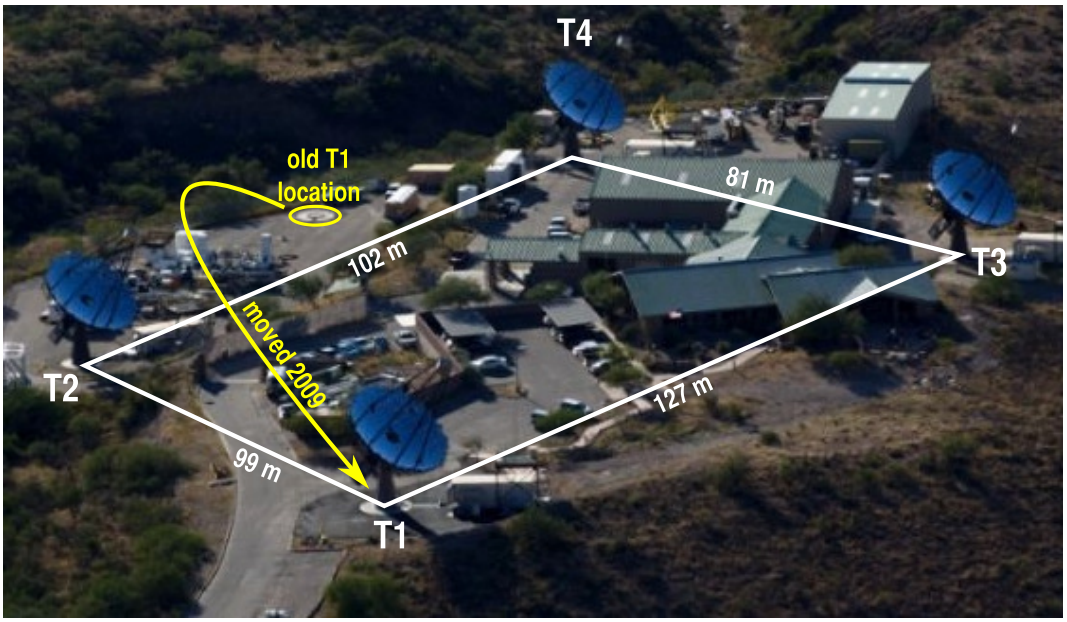

Fig. 2.6: *Aerial view of the VERITAS array around the FLWO Visitors Center at the base of Mount Hopkins, Arizona. Image credit: VERITAS collaboration*

data that is used in this study was taken before and after that upgrade. Therefore both VERITAS states will be described in the following sections.

2.3.1 Telescopes

Mechanical structure and optics

For the VERITAS telescopes a Davies-Cotton design [Davies *et al.* (1957)] was favored over a parabolic design. In a Davis-Cotton design, several small, spherical mirrors, that are equally distributed all over the dish, are arranged in a specific way to create a common focus at the focal length f (see Fig. 2.7,a). This is not possible with a single, spherical mirror that has the same size as the dish. The Davis-Cotton design requires a spherical shaped dish with a curvature radius of f. The camera is located at the focal length f. The single, spherical mirror tiles, with curvature radii of $2f$ and focal lengths of f, are mounted on the dish and are aligned towards a point on the optical axis of the telescope that is $2f$ apart from the center of the dish. This way, a distant (at infinity) point-like object, located along the optical axis, will be focused exactly onto the center of the camera.

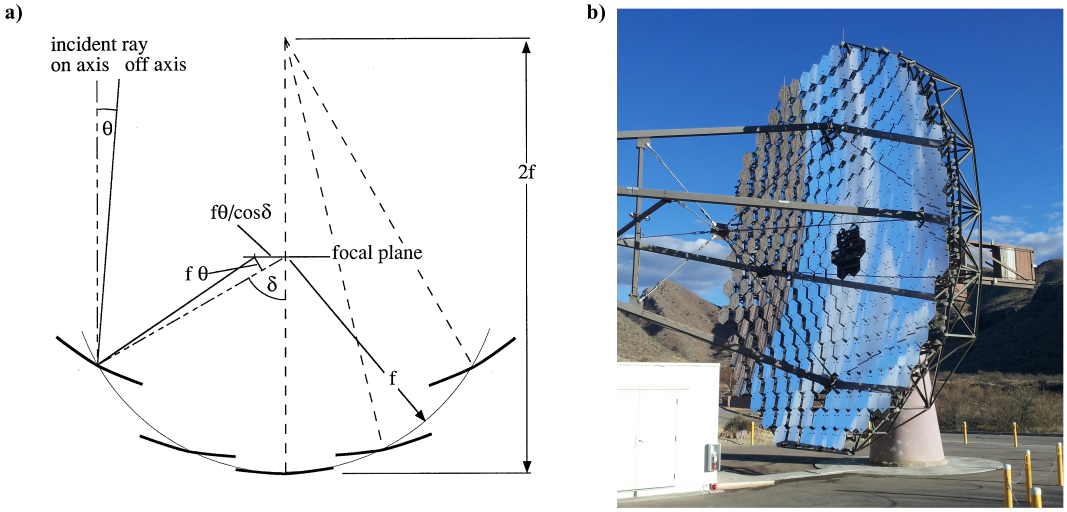

Fig. 2.7: a) *Illustrated is the mapping of on-axis and off-axis rays onto the focal plane of a Davies-Cotton mirror geometry. The angle between the on-axis ray (parallel to the optical axis) and the off-axis ray is θ. Taken from [Actis et al. (2011)]*
b) *Picture of a VERITAS telescope: mirror tiles, OSS, counterweight and quadrupod*

As the reflector consists of several small, identical mirror facets, the production is much cheaper than that of a reflector with a parabolic design, where each mirror facet has to have a different shape, depending on its position on the dish, in order to form a single, big parabolic mirror together with the other facets. It is also much easier to maintain and replace parts of the reflector. This design also has smaller off-axis aberrations than a parabolic reflector so that it has good image quality out to a few degrees from the optical axis. The only disadvantage is the time spread in the point-like image of a planar wavefront impinging perpendicularly on the telescope. This spread is caused by the different lengths of reflected rays depending on

the position where they hit the reflector. Such a problem could only be avoided by a parabolic reflector. However, analytic and simulated studies by [White (2005)] show that 90% of the light received by a VERITAS reflector reaches the camera within 2 ns. So it is still small enough to study the time dispersion of the Cherenkov emission from an air shower.

In case of a VERITAS telescope, the single mirror facets are mounted on a tubular steel optical support structure (OSS) with a diameter of 12 m and a curvature radius of 12 m as well (see Fig. 2.7,b). The total reflector area is about 110 m^2 and consists of 350 identical hexagonal, spherical mirror facets with a side-to-side dimension of 61 cm and a curvature radius of 24 m. The mirror reflectivity is better than 80% over the wavelength range relevant to Cherenkov light (280 nm - 450 nm) and is better than 90% at the peak Cherenkov radiation wavelength of 320 nm [Holder *et al.* (2006)]. As the reflectivity decreases over the time, the single facets have to be re-coated from time to time. Each of those mirror tiles has to be aligned manually to achieve a common focal plane 12 m apart from the dish. After a perfect alignment the point spread function (PSF) of the whole dish is less than 0.05° [McCann *et al.* (2010)] at the center of the camera which is smaller than the size of a single PMT (0.15°).
The camera of each telescope is mounted on a quadrupod that is attached to the OSS. To balance out the torque on the system from the camera, counterweights are located behind the OSS. This whole construction is attached to an altitude-over-azimuth positioner at the top of a $\sim$ 6m tall pedestal. The slewing speed in both axes, altitude and azimuth, is one degree per second during normal operations. To monitor the current pointing direction, a database logs the information send from the positioner encoder every 250 ms. The mechanical pointing accuracy of a VERITAS telescope is typically better than $\pm$0.01° [Holder *et al.* (2006)].

Camera and electronics

The camera of each telescope is installed inside a focus box which is a tough light-tight, water-tight structure attached to the quadrupod. It can closed during daytime with a remote control operated garage-style shutter to protect the PMTs from UV exposure. The camera consists of 499 cylindrical PMTs arranged in a hexagonal grid forming a circle (see Fig. 2.8,a) with a diameter large enough to provide a FOV of 3.5°. Because there is still dead space between the PMTs due to their cylinder shape, additional light concentrators are attached to the front of each PMT which focus the light on the center of the PMT photocathode. These so-called *Winston cones* have a hexagonal entrance aperture to fit perfectly next to the neighboring Winston cones in the camera (see Fig. 2.8,b). The diameter of each entrance aperture corresponds to a FOV of 0.15°. All the light captured by a single PMT and its Winston cone represents the signal of one single camera pixel. An additional feature of the Winston cones is the fact that the PMTs are protected from ambient background light as the angle of entry is so small that only light coming from the opposing dish is able to reach the PMT photocathode [Nagai *et al.* (2007)].

The main characteristic of the PMTs is that they provide fast reaction times ($\lesssim$ 2 ns) and high gains to capture the quick Cherenkov light pulses from the air showers. In

the beginning all VERITAS telescopes had been equipped with Photonis XP2970 PMTs whose quantum efficiency (QE) inside the range of the Cherenkov spectrum was 18%-22%. These PMTs got replaced by new super-bialkali Hamamatsu R10560-100-20 PMTs in summer, 2012. The new PMTs are characterized by a higher QE of 32%-34%, which results in a 35-50% increase in photon sensitivity compared to the previous ones. This effect leads to a lower energy threshold for the whole VERITAS array [Kieda (2011)].

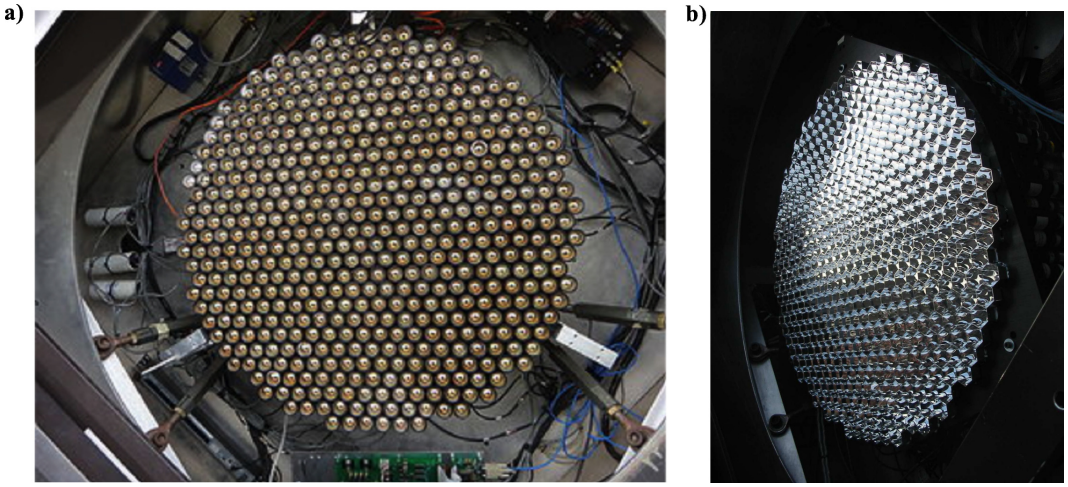

Fig. 2.8: a) *The 499 pixel camera in the focus box. The PMTs are mounted on specially designed bases that fit into an aluminum frame. The preamplifiers are located immediately behind the PMTs. Taken from [Varlotta (2013)]*
b) *Winston cones mounted on the 499 pixel camera. The front face of the light cones is the focal plane of the camera. Taken from [Cogan (2006)]*

The current amplification factor between the photocathode and the last anode inside the PMT is called *gain*. It depends on many factors which are slightly different for each PMT. Fortunately it can be adjusted by changing the high voltage (HV). In case of VERITAS the nominal gain for all PMTs is set to $2 \cdot 10^5$. Therefore the voltage of each PMT has to be controlled by a multi-channel power supply. A typical value of the applied HV is $\sim$ 850 V. The best HV value for each PMT, to ensure an equal response across the entire camera, is stored in a database. These values can change during the lifetime of the instrument, therefore they have to be validated from time to time by dedicated calibration tests. As it is necessary to protect the PMTs against too high anode currents a HV control program suppresses the high voltage in the PMT in case the current exceeds 40 μA or is above 30 μA for several seconds. Before the anode signal is sent out to the data acquisition (DAQ) and trigger system, a preamplifier, located at the base of each PMT, boosts the anode current signal by an additional gain of 6.6 and converts it to a voltage signal. Bias currents from the night sky background are removed in the preamplifier through an AC coupling with the PMT signals.

2.3.2 Trigger- and Data Acquisition System

Trigger

Due to the night sky background and the large amount of relativistic muons in the atmosphere, a sophisticated trigger system is necessary to accept only the Cherenkov photons coming from air showers as the readout rate is limited in the data acquisition system. Therefore the trigger consists of three hierarchical conditions and is explained in detail in [Weinstein (2007)].

The first-level trigger (L1), which works on the single-pixel level, consists of *constant fraction discriminators (CFD)* processing the analogue photomultiplier-tube signals. In a CFD the input signal gets split into three equal components. A *zero-crossing discriminator (ZCD)* releases a trigger exactly at the time when the voltages from the time-delayed (some nano seconds) first component and an inverted, attenuated copy of the second component cancel each other. This signal is sent (with a delay) to the *data* input pin of a flip-flop where an additional *clock* signal is necessary to produce the final 10 ns CFD output pulse (see Fig. 2.9).
The clock signal is provided by a simple *threshold discriminator (TD)* which generates a trigger signal if the programmable threshold level is reached by the third component. For standard, dark sky VERITAS operation, the threshold is set to 50 mV (corresponding to 4 - 5 photoelectrons). By using an additional ZCD the exact trigger time of the final CFD output signal is not affected by different PMT pulse sizes as it would be the case for a simple TD.
Noise in the CFD will increase the jitter of the ZCD which can be minimized by adding a DC offset. Unfortunately a high DC offset will also decrease the trigger efficiency and so a low offset is intended every time the noise is small enough. As the NSB noise varies a lot during observations the DC offset is not fixed but changes automatically according to the ZCD trigger rate. This *rate feedback loop (RFB)* is not a general feature of a CFD but was developed especially for the VERTAS-L1-Trigger [Hall *et al.* (2003)].

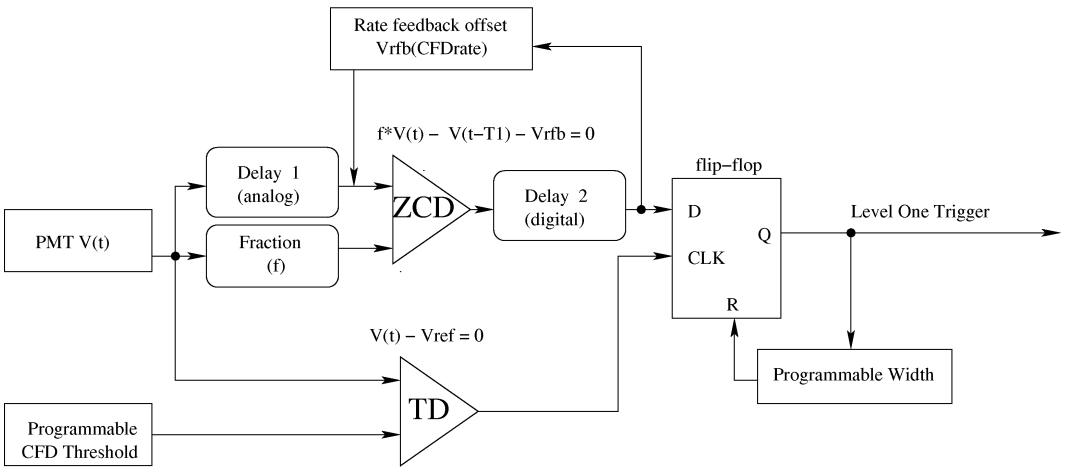

Fig. 2.9: *A block diagram of the VERITAS first-level trigger. Taken from [Hall et al. (2003)]*

After the CFD triggered, the signal is sent as input to the second-level trigger (L2). This trigger operates on the camera level and generates an output pulse when at least three adjacent pixels release a CFD pulse within a coincident time window that is set to 5 ns [Zitzer (2013)]. Its components are located in the Trailer next to each telescope.
This pattern-selction trigger successfully rejects fluctuations due to NSB and PMT afterpulsing as these events usually trigger only one or two adjacent pixels within such a short coincidence window. The projection of the Cherenkov photons from an air shower, however, results in a compact image of several adjacent pixels. The time spread of the triggering in adjacent CFDs is related to the temporal evolution of an air shower, which is in the order of nanoseconds. If the trigger time of the CFDs is very accurate, then a coincidence window of 5 ns in the L2 is sufficient wide enough to trigger three adjacent pixels that are part of an air shower image.
The necessary time accuracy is the reason why a ZCD is preferred over a simple TD. An exact timing in the CFDs facilitates a smaller L2 coincidence window, which leads to a smaller false-trigger rate as the NSB is suppressed. If the false-trigger rate is low enough, one is able to decrease the CFD threshold, which improves the detection of low-energy air showers.

In case the L2 trigger decision is positive, its output pulse is sent to the array-level trigger L3 (see Fig. 2.10). During standard operations this trigger requires a L2 signal from two or more telescopes within 50 ns before it forms the final trigger, that initiates the readout of the data. The L3 is located inside the control room building and connected to the L2 of each telescope by cables.
The purpose of this trigger logic is the rejection of local muons, which dominate the low energy background and are able to produce images in the camera similar to those of gamma-ray air showers. Fortunately the Cherenkov light from local muons will only impinge on an area large enough to trigger just a single telescope, which is not enough for a positive L3 trigger decision. By reducing the background contribution of local muons one is able to lower the CFD threshold much more and gain a better sensitivity in the low-energy range.
For the L3 trigger it is important to account for the different delays of the L2 signal due to differences in the cable transmission, the telescope positions and their pointing directions. The larger the zenith angle, the higher is the delay because the Cherenkov wavefront hits the telescopes at different times. The *Pulse Delay Module (PDM)* is the component in the L3 responsible for the correct delay calculation and equalizes the different L2 signals by adding a proper delay to each of them.
The delay-adjusted L2 signals are then fed into the *Sub-Array Trigger (SAT)* board which issues a command to the data acquisition system to record the event. As the signal needs time to propagate back to the telescopes, the SAT will stop for 10 μs after an event decision. Via a combination of outgoing PDM delays and internal compensation on the SAT board, the array trigger ensures that an L3 trigger is received at the telescope a fixed time after the corresponding L2 trigger was produced. Also the readout of the data takes some time. Altogether, after a L3 trigger, the system will be busy for $\sim$ 300 - 400 μs which results in a deadtime of 6 - 8% at a trigger rate of 150-170 Hz or 10-11% at a rate of 225 Hz [Weinstein (2007)].
Apart from providing the final trigger signal, the whole L3 system provides event numbers, event masks and log rates, timing and diagnostic information to disk.

Since the PMT upgrade in summer 2012 the L3 rates are much higher than before. At the moment typical rates during normal operations with four-telescope at 80 degrees elevation are about $\sim$ 450Hz. Before the upgrade, the rates had been much lower under the same conditions: $\sim$ 250 - 270Hz. As a consequence, also the deadtime increased after the upgrade to values of 14 - 17 % (at trigger rates of $\sim$ 390 - 450 Hz).

Data Acquisition System

A positive L3 trigger decision will result in the data acquisition of the photon pulses caused by the air shower in the camera. The whole data acquisition process and the necessary trigger operations are shown in Fig. 2.10.

Parallel to the trigger path a second copy of the PMT pulse is continuously digitized by a 500 Mega-sample per second *flash analog to digital converter (FADC)* with a 8-bit range. This corresponds to a dynamic range of $2^8 (= 255)$ digital counts (d.c). A 16 kB ring buffer holds the digitized information while awaiting an L3 trigger signal. As the width of a single sample is 2 ns and its size is one byte, the ring buffer can record up to 32 μs. During this time a trigger decision has to be made, including the signal propagation from the telescopes to the L3 and back.
As soon as the L3 trigger signal is received by the telescopes, the FADC stops the digitization, sends a BUSY signal to the L3, which stops triggering, and waits for an additional signal from the L3 that defines the event type and provides the event number. Depending on the event type the amount of samples that get readout (*readout window*) are different. During normal operations only 20 samples (40 ns) are readout to reduce the dead-time of the whole system.
As there is some time between the pulse digitization and the stop induced by the L3 signal, the position of the pulse inside the buffer is found several samples after the current start position of the buffer. Due to the fixed time between the L2 trigger production and the reception of the L3 signal also the position of each recorded pulse is located a fixed number of samples behind the current buffer position. These so-called *look-back times* are fixed to 3000 samples for all telescopes (but can be changed manually). If one wants to fine tune the position of the pulse inside the readout window one can simply change the PDM delays in the L3 system.

In case the pulse is too large, it will saturate at 255 d.c. and the information about the true pulse size is lost. As this affects the energy measurement, the problem is avoided by using two channels with different gains. If the pulse is small enough each signal coming from the pre-amplifiers is further amplified by a factor of 7.25 at the high-gain channel (default scenario). Otherwise the low-gain channel gets connected to the FADC for a short moment, right after the high-gain pulse went through. Along this channel, a delayed copy of the analog signal is amplified just by 1.25. The FADC buffer will then record the saturated high-gain pulse, followed by the delayed low-gain pulse, for which the full shape is preserved as it doesn't exceed the range. The look-back time is decreased by 20, shifting the readout window to the position of the delayed pulse. Also an additional *HiLo-bit* is set in the datastream,

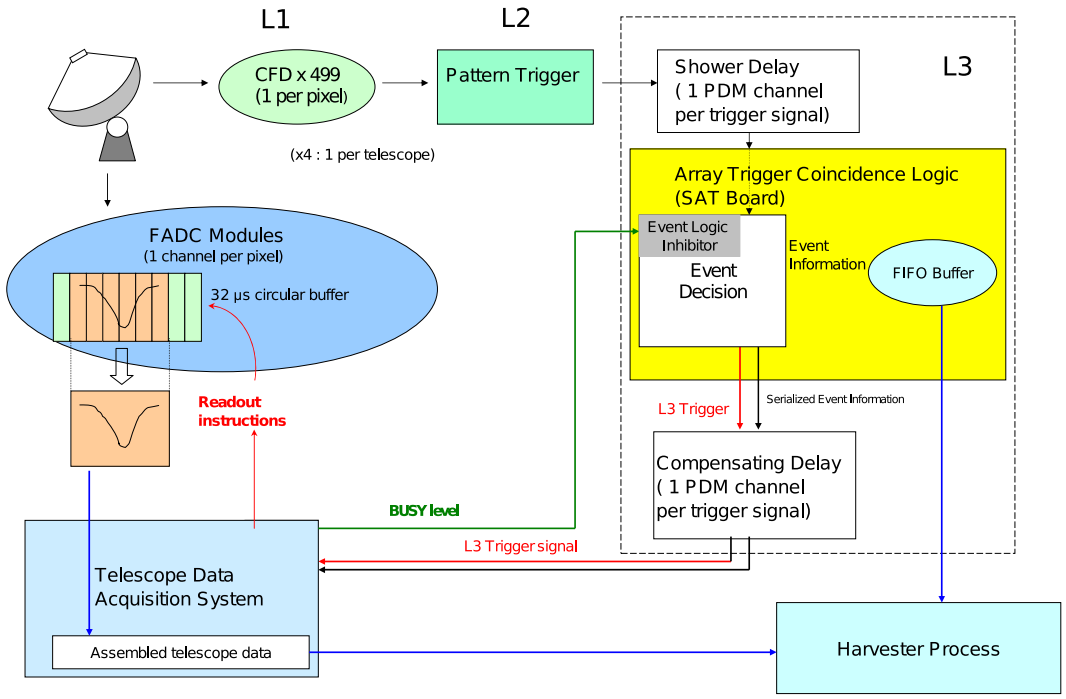

Fig. 2.10: *Illustration of the data acquisition process and the trigger operations. Taken from [Weinstein (2007)]*

indicating that the pulse has to be multiplied by a factor of $7.25/1.25 = 5.8$ during the offline analysis [Aune (2012)].

The 50 custom built FADC boards (10 channels each) of a single telescope are distributed across 4 VME crates [Buckley *et al.* (2003)]. By knowing the exact position inside each FADC buffer and the size of the readout window the data is readout by the VME crates and sent to a server next to the telescope. There, the fragments of the event, coming from different FADCs, get combined to a single telescope event. This so-called *event builder* has to arrange the fragments according to the event number, given by the L3, and stores them in a memory buffer. Additionally each telescope event gets assigned a timestamp, which is provided by a GPS clock, that has an accuracy of 1 μs.
In the following step the stored telescope event is sent via ethernet to the central *harvester* server. The harvester program receives the data from the event builders of each telescopes and forms array level events. These events also include supplementary information, provided by the L3 system, that have been transferred directly to the harvester. The final array level events are saved in a custom designed binary format named VERITAS Bank Format (VBF) [Hays (2007)].
Events are not stored separately. A sequence of array level events recorded during a specific observing period is called a *run*. The duration of a run is manually defined by the observer. In a last step, the harvester combines all the array level events produced in this period and adds some additional information about the run and the telescope configuration. Once the data run is complete, the files are compressed and transferred to local and remote archival machines.

2.3.3 Observations and GRB follow up

Normal operations with VERITAS usually get performed during clear, dark nights. As there is also a total shut down in the summer months of July and August due to local monsoon, a typical observation time per year is ca. 980 hours. There exist different observing modes where the telescopes either point directly at the source or right beside it. The *wobble mode* is such a technique, where the offset between the source position and the camera center amounts to 0.5°. This is the preferred method as it allows for simultaneous background measurements within the same run. A typical run duration is about 20-30 minutes after which the wobble position is changed to another cardinal direction, or the telescopes are pointed to another source. All these operations are executed by a local observer via a GUI of the *Array Control* program running on a server next to the control room. This program controls all necessary lower-level programs responsible for the telescope pointing, triggering, data acquisition, calibration and monitoring.
In order to explore a wide range of science topics and open questions, many different objects are observed by VERITAS. Those include active galactic nuclei (AGNs) like blazars and radio galaxies; possible dark matter targets like the Galactic center and spheroidal dwarf galaxies; cosmological distant sources like gamma-ray bursts (GRBs), galaxy clusters, and distant AGNs; and galactic sources like pulsars, pulsar wind nebulae, supernova remnants and binary systems. Most of these source classes have already been detected by VERITAS and show a large variety of photon fluxes and spectral behavior.

The main interest of this work was to study different analysis techniques for fast transient sources like GRBs. Due to their sudden, unpredictable appearance, special observing procedures are necessary. For all other sources there is usually enough time to schedule the observations in advance. This observation plan is subordinated to the observations of GRBs because it is important to observe them as fast as possible.
The dedicated GRB follow-up observation procedure starts with an notification of the *the Gamma-ray bursts Coordinate Network (GCN)* obtained by a computer at the VERITAS site that is constantly connected to the GCN via a TCP/IP socket connection. The GCN notifications are the result of information received in real-time by the GCN system from the various spacecraft, processed into a standard format and automatically distributed to various ground-based instruments and observatories. The response to GRBs in most of the satellite missions and the final GCN process are fully automated and no human interaction is required. The computer at VERITAS is also running an automated program which is configured to process only the GRB location notifications from the Swift, Fermi, AGILE, and INTEGRAL missions. This program rejects all GRB notifications of sources with a declination of less than -30° (too far south for a successful VERITAS detection) or if the 68% containment radius of the localization by the satellite is greater than 10° (much larger than the VERITAS FOV). As Fermi and Swift missions also calculate the likelihood of the triggered event actually being a GRB, a third rejection criteria is a likelihood below 50%.
If all filters haven been passed, then the relevant informations about the GRB and its

position are transmitted to the Array Control program which prepares all necessary steps for a repointing. An audio alert is played at the control room, notifying the observers that a possibly-observable GRB has been detected and a pop-up window appears in front of the Array Control GUI (if the burst is above 20° elevation) asking the observer to confirm the repointing of the telescopes by a single click. This way, the time delay between the beginning of a GRB flare and the start of the repointing is minimized which is necessary, as this process is the most time consuming in the whole chain due to a slewing speed of 1°/s. If there is enough time during the repointing, the observers can start a new run. Otherwise they should extend the current run duration for an additional 20 minutes.
The maximum amount of observation time spend on a GRB depends on the localization accuracy of the satellite missions. If it is smaller than the FOV of VERITAS, the observing window lasts for maximum 3 hours after the burst trigger. If it is wider but still better than 10° (68% containment radius), VERITAS observes the center of the error circle for maximum 1 hour. However, in both cases the observing duration will stop before it reaches its maximum if the elevation declines below 20°. More information about the GRB observing procedures can be found here [Aune (2012)].

2.4 Analysis of VERITAS data

The software package that had been used during this work to analyze the VERITAS data is called `eventdisplay`. Originally, it was designed as a display for the VERITAS prototype data by Gernot Maier (DESY) and Jamie Holder (University of Delaware), but evolved into a full analysis package.
In the following sections the whole analysis chain is explained, which includes the reconstruction of the air-shower direction, the estimation of its energy, the distinction of gamma-ray showers from the hadron-induced background and the determination of their significance.

2.4.1 Image parametrization

At the beginning of the analysis the different images of the same shower event in the different telescope cameras have to be parametrized. The orientation, the centroid position, the shape and the size of the images are necessary input parameters for the reconstruction algorithm. A first step of the image parametrization is the analysis of the FADC traces in each camera. In a preceding procedure, the offset and the noise in the FADC of each channel have to be measured.

FADC Pedestal

The FADC records the negative voltage output of the preamplifiers, located at the base of each PMT, with a rate of 500 MHz. The voltage signal is converted to digital counts (dc) with a conversion factor of 7.85 mV/dc. It is also possible to associate the value in dc to a number of photoelectrons (pe).

Due to the AC coupling, each constant contribution of the PMT pulse to the FADC trace is suppressed and the baseline should be at zero. Then the amount of NSB light can only be measured by the magnitude of the trace fluctuation around zero. As positive voltage values cannot be digitized by the FADC, a negative voltage, corresponding to approximately 16 dc, is added to the AC coupled PMT output. Hence, the value of each sample in a FADC trace without any Cherenkov light contribution will vary around a mean value close to 16 dc with a standard deviation that depends on the amount of the NSB. Because the artificial offset is not exactly the same for each channel and also the NSB can vary over the duration of a run, it is necessary to do some calibrations during the data taking.
An important calibration task is the readout of FADC traces without any Cherenkov light. As these traces don't exceed the CFD threshold, the readout is triggered externally during special time slices (every 3 min) with a rate of 1-3 Hz. The mean value of such a trace is called the *pedestal*. It is determined either by taking into account all the special pedestal trace samples readout during the whole run or only those ones readout during a single time slice.
For the estimation of the amount of light contained in a Cherenkov pulse, measured by a single channel, the values of all the trace samples belonging to the integration window get add together. In the next step, the previously calculated pedestal, multiplied by the size of the integration window, is subtracted from this sum.

The significance of a measured signal pulse depends on the background fluctuation which is the result of the NSB. If one calculates the sum of the samples inside the integration window of the externally triggered pedestal traces and builds an distribution over all the traces readout in a single time slice, one can determine the standard deviation for this specific integration window in this time slice. This standard deviation is also called *pedvar*. It is determined for different integration windows giving the opportunity to chose the optimal one during the offline analysis later on. If the excess, calculated over a certain integration window, is similar to the pedvar of the same integration window, it is likely to be just a background fluctuation due to NSB without any Cherenkov signal contribution.

Both values, pedestal and pedvar, have to be calculated before the FADC trace analysis is performed. However, the necessary information is contained in the same data file. It stores the FADC pulses from Cherenkov events and the separately triggered pedestal events whose readout is forced at certain times during a run.

FADC trace analysis

A typical PMT pulse produced by Cherenkov photons from an air-shower will result in a FADC trace similar to those in Fig. 2.11. It is characterized by a fast rise to a negative maximum and a slightly slower decay back to the pedestal value.
A necessary parameter, required by the offline analysis at a later stage, is the integrated charge of each FADC trace minus its pre-measured pedestal. The integration window (summation window) is smaller than the whole readout window. An ideal integration window should start where the pulse begins to rise and it should stop

after the pulse's decay back to pedestal level. This way the error introduced by the pedestal (and its fluctuation) is minimized.
Unfortunately, the trigger signal, that initiates the readout, doesn't reach every FADC at the same time. Hence, due to the fixed lookback time, the pulse appears at different positions in the readout window, even if the photons hit the PMTs exactly at the same time. Therefore a good time calibration is necessary to adjust the start of the integration window in each FADC separately. The arrival time of each pulse is determined at the rising edge when the trace exceeds half of the maximum pulse height. This parameter is called T_0.

By measuring this value in special calibration runs (*flasher* runs) [Hanna *et al.* (2010)], executed once each night, one is able to determine the temporal offsets of the trigger between different channels induced by hardware issues (i.e. cable length) and environmental effects (i.e. temperature) which can change from night to night. During a flasher run, a LED light source in front of the camera produces light pulses with a rate of 300Hz. As the light is uniformly distributed over the whole camera, the pulses reach each PMT at the same time. The uniform light intensity is also necessary to measure the differences in the gain of each PMT, which is very important as the integrated charge of each FADC channel needs to be comparable.

Besides the temporal differences, caused by the hardware, there can be also a gradient in the pulse arrival time between adjacent pixels belonging to the same air-shower image. This is due to the temporal shower evolution and the different distances between the location of the Cherenkov emission inside the shower and the camera. Therefore an additional shift, besides the offset given by the flasher run, will help to optimize the integration window's position in channels where the pulse arrives later due to the gradient.

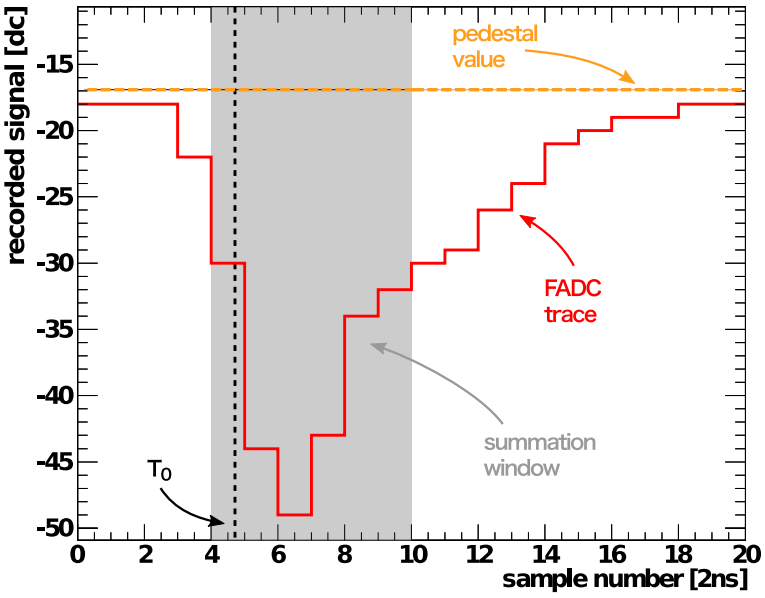

Fig. 2.11: *A typical FADC trace of a PMT pulse induced by Cherenkov photons. The dashed orange line represents the pedestal value while the vertical dashed lines indicate the arrival time T_0. The grey area visualizes the width and the position of the summation window used in the analysis for the charge integration.*

Estimating the optimal shift is done by the so-called *double-pass* methode [Holder (2005)]. In a first pass, all FADC traces belonging to the same event get integrated over a large summation window of 18 samples. This window starts at a fixed position and is only shifted by the offset measured with the flasher runs. Besides the integrated charge, also the T_0 is determined of each FADC trace. After the image cleaning and the reconstruction of the image axis, described in the following section, a linear fit of the T_0 versus the distance of the PMT from the image center along the image axis is determined. With this information in hand, the start time of each FADC pulse can be estimated more accurately according to the position of the PMT in the camera. In a second pass the same traces get integrated again, but this time over a smaller summation window of 6 samples. This window is placed at the position where an pulse is supposed to occur including the information of the flasher runs and the linear fit of the first pass.

Image cleaning & parameterization

Before a shower image can be parameterized, all pixels that measured solely photons from NSB have to be removed from the compact shower image. The cuts used during the cleaning are based on the signal-to-noise ratio in each pixel as the noise in each trace is not constant and changes with the NSB. The signal is the integrated charge of each FADC trace minus its pedestal and the noise is given by the pedvar value calculated according to the size of the integration window. In case the signal is 5 times larger than the pedvar, this pixel forms an *image pixel*. After all pixels, fulfilling this criteria, have been detected, a second pass is executed which accepts all those pixels whose signal is just 2.5 times the pedvar if at least one of their neighboring pixels is already identified as an image pixel. These pixels, detected during the second pass, form the *border pixels*. If at the end of the cleaning procedure an image pixel does not have any neighbor image or border pixels, it is removed as well. All remaining pixels form the image of the air shower.

When all pixels that belong to the shower image are found, its parametrization is the next step in the analysis chain. It is based on a moments analysis of the elliptical image formed by an typical gamma-ray shower and was first mentioned by [Hillas (1985)]. The parameters determined during this process are called the *Hillas parameters*. Today, not all of the original Hillas parameters are still under usage. Instead some other parameters have been developed. Here, only the frequently used ones are presented (see Fig. 2.12).

The summation of the integrated charge of all image pixels will define the *size* (in dc) of an image. It is the zeroth order moment and one of the most important parameters. The first order raw moment is the center of gravity of the image, also called *centroid*. This leads directly to the determination of another parameter, which is the *distance* between the camera center and the centroid, measured in degrees. Images very close to the expected source position tend to have a circular shape, making it difficult to determine its orientation. Images far away, at the edge of the camera, get not fully recorded. If the telescopes point at the source (or at least very close to it), then the expected source position is near the camera center and the distance parameter can be used to reject both kind of images.

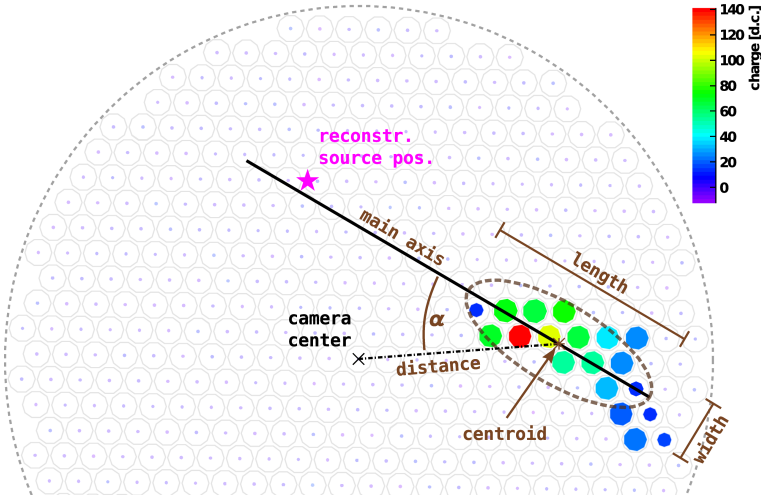

Fig. 2.12: *A shower image in the camera after cleaning. Only the colored pixels survived the cleaning cuts and the color represents the integrated charge of each pixel. During the parameterization process all the important parameters (brown) are determined. The source position (magenta) is reconstructed with the help of the shower images from the other telescopes (see next section).*

After calculating the second order central moments a covariance matrix is constructed which is used to determine the orientation and shape of the image. The eigenvector of the highest eigenvalue corresponds to the direction of the image's *main axis* and its eigenvalue represents the variance of the image along this axis. It is called the *length* (in degree) of the image. The second highest eigenvalue marks the *width* (in degree) of the image which is the variance perpendicular to the main axis. With these information in hand more parameters can be calculated, like the angle *alpha* between the main axis and the line connecting the centroid with the camera center. Further, one is able to calculate the intersection angle between the major axes of two telescope images plotted in the same camera coordinate system. A small angle indicates images whose main axes are almost parallel to each other. In such case a minor error in the orientation of the axes will result in a large error in the position of the intersection point.
Another important parameter is the fraction of image size contained in pixels at the camera edge, which is also called the *loss* parameter. A high loss value indicates images at the edge of the camera exceeding its boundaries. Hence, a large part of the image is not recorded which would lead to an incorrect image parametrization. Due to this problem another image parametrization procedure had been developed besides the geometrical one introduced by Hillas. This newer method assumes a two-dimensional normal distribution to describe the shower images and applies a log-likelihood fitting algorithm. This way also some of the truncated images at the edge can be recovered.
While some of the mentioned parameters get used to reconstruct the shower direction, impact position and its energy (size, centroid, main axis), others will be used to distinguish between hadronic and leptonic shower images (length, width) or to reject images whose parametrization will be error-prone (distance, loss).

2.4.2 Event reconstruction

After the images of a single shower event had been parametrized for each telescope separately, these information get combined to reconstruct the direction of the shower, its impact parameter and its energy. To improve the quality of the reconstruction, images who are not fully covered by the camera, whose main axis is too parallel to other image axes or whose elliptical shape is less pronounced, will not be taken into account. The cut values used during this study to reject these kind of images are: size $>$ 100 dc, number of image pixels $>$ 4, loss $<$ 0.2 and an angle between two image axes of more than 10°. If at least two images from different telescopes survive these cuts the analysis program continues with the geometrical reconstruction.

Geometrical reconstruction

The reconstruction of the direction of the shower event is based on the stereoscopic approach explained in section 2.2.1. The principle is illustrated in Fig. 2.13,a. Theoretically the axes of all accepted images, superimposed into a single camera plane coordinate system, should intersect all at the same point which represents the direction of the shower. In reality each pair of major axes produce their own intersection point. If there are N images passing the cuts, the number of intersection points will be $N \cdot (N-1)/2$.
The algorithm used by `eventdisplay` determines the source position from a weighted average of all intersection points, which is in principal the same method as *Algorithm 1* in [Hofmann *et al.* (1999)]. The weights include the size of the images, the ratio of width-over-length from each image, and the sine of the angle between two axes. In this way more weight is given to high quality (i.e. brighter and more elongated) image pairs.

After the source position has been found, an axis, connecting the centroid with the source position, is constructed for each image and projected onto the shower plane. The position of the plane can be chosen arbitrarily, important is just the fact that it is perpendicular to the reconstructed shower direction (source position). The intersection points of the different axes in the shower plane are determined and the shower core position is then given by the weighted average of all the intersection points. The weighting is done in the same way as during the determination of the source position. In Fig. 2.13,b the shower core is determined under the usage of four shower images.
Now all necessary informations are available to reconstruct the three-dimensional shower axis and determine the point where it hits the ground, which is the so-called *shower core*. The distance of this point to the telescope positions, is the *impact parameter* of each telescope. As far distant showers tend to produce parallel images, the angular resolution worsens, which can be avoided by applying a cut on the shower core position of 250 m away from the array center.

Besides the shower direction and the shower core the third parameter that is determined during the reconstruction, is the *emission height* of the shower maximum [Aharonian *et al.* (1997)]. The shower maximum is mapped onto the camera close to the position of the image's centroid. With at least two images in two different

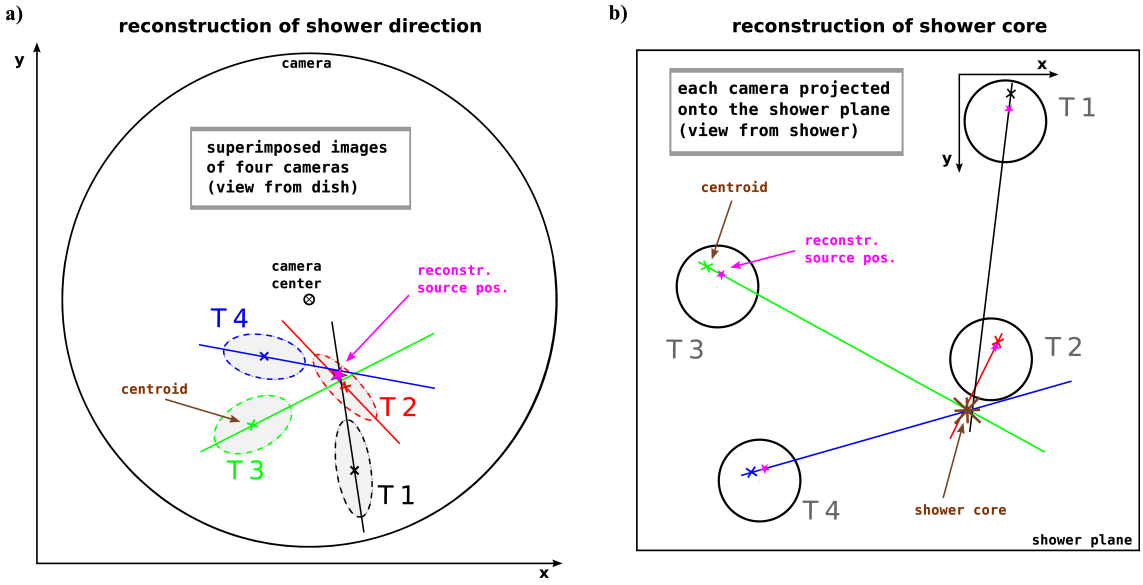

Fig. 2.13: a) *Reconstruction of the shower direction (source position) by superimposing the different camera images and their main axes. The source position (magenta star) is the weighted average of all intersection points.*
b) *Reconstruction of the shower core. The centroids and source position from each camera are projected onto the shower plane. The weighted intersection of the lines, connecting source position and centroid, provides the shower core position.*

telescopes, the software is able to estimate the emission height by simple trigonometric relations. Necessary informations are just the angular distance d between the centroids of two images, superimposed in one camera coordinate system, and the spatial distance r between the two telescope positions, perpendicular to the pointing direction of the telescopes. Then the following relation $r/d \approx h$ delivers the emission height h of the shower maximum with respect to the orientation of the camera plane. As the error on h is larger than the size of the array, the fact is ignored that the four camera planes are not contained in a single plane if they are not pointing towards zenith.
If more than two telescopes reconstruct an image, again a size-weighted mean value of h is calculated. Additionally, the χ^2-value is determined. Both parameters, the mean value and the χ^2-value, can be used to reduce the amount of background events since hadronic showers and single muons penetrate deeper into the atmosphere than gamma-ray initiated showers.

Energy reconstruction

As the energy of a gamma particle is proportional to the amount of Cherenkov photons emitted by the air shower, it is related to the total charge contained in the shower image (*size*). Because it is not possible to measure the instrumental response with a test beam the usage of Monte Carlo simulations of gamma-ray showers is required. Furthermore the size of an image also depends on the shower direction (zenith, azimuth, wobble offset), the impact parameter and the NSB level. Therefore a wide parameter space has to be covered by the MC simulations.
For each set of simulated showers with a specific zenith angle, azimuth range, wobble

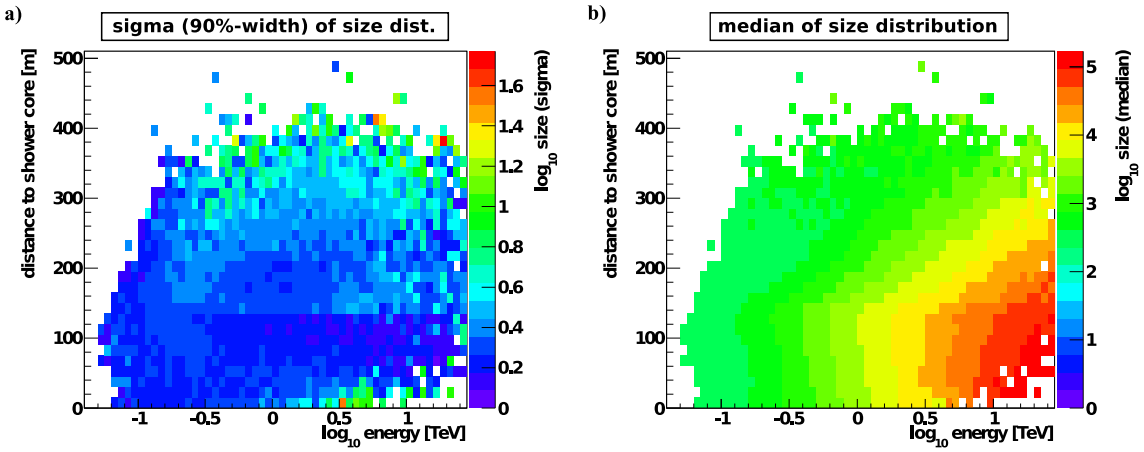

Fig. 2.14: *Lookup tables for the sigma value (left) and the median (right) are shown for showers at 20° zenith angle, with a wobble offset of 0.5° and a NSB level similar to that observed in the Crab Nebula FoV.*

offset and NSB level a separate table is produced that contains the median and the 90%-width (σ) of the image size distribution (logarithmic scale) for each pair of simulated primary energy and impact parameter (see Fig. 2.14). The table is produced for each telescope separately.

During the analysis of a certain air shower, its primary energy is estimated by inverting that lookup table of the mean size which was generated for this specific shower direction and NSB level. The program searches in the table row, that corresponds to the reconstructed impact parameter of the shower, for a bin whose value fits best the measured image size. By knowing that bin and its position also the corresponding energy is given (= x-value of bin position) together with the 90%-width (σ) value which is also stored in the same bin. As the shower parameters are usually in between those values used to generate the lookup tables, the final results are obtained by interpolation.
For each telescope the estimated energy and σ-value of the same shower will differ from the results of the other telescopes. The final shower energy is therefore derived by averaging the energy estimates from all telescopes, weighted by one over σ^2.

2.4.3 Gamma-hadron separation

After the reconstruction and parametrization of an air shower the next step in the analysis chain is the distinction between gamma-ray showers and the cosmic-ray background.

Shape cuts

The most effective distinction procedure between cosmic-ray and gamma-ray showers is a hypothesis test based on the usage of the width w and length l parameter measured for each contributing telescope image separately.
As it was mentioned before, the images of cosmic-ray showers are wider and longer than those of gamma-ray showers with the same image size. The hypothesis that the shape corresponds to a gamma-ray shower is the null hypothesis. The used test

statistics, which are called *mean reduced scaled width - MSCW* and *mean reduced scaled length - MSCL*, are defined in the following way:

$$MSCW = \frac{1}{\sum_{i=1}^{N} W_{\mathrm{i},w}} \sum_{i=1}^{N} \left(\frac{w_i - \overline{w}_{\mathrm{MC}}(R,s)}{\sigma_{w,\mathrm{MC}}(R,s)} \right) \cdot W_{\mathrm{i},w} \quad ; \; W_{\mathrm{i},w} = \frac{\overline{w}^2_{\mathrm{MC}}(R,s)}{\sigma^2_{w,\mathrm{MC}}(R,s)} \tag{2.5}$$

$$MSCL = \frac{1}{\sum_{i=1}^{N} W_{\mathrm{i},l}} \sum_{i=1}^{N} \left(\frac{l_i - \overline{l}_{\mathrm{MC}}(R,s)}{\sigma_{l,\mathrm{MC}}(R,s)} \right) \cdot W_{\mathrm{i},l} \quad ; \; W_{\mathrm{i},l} = \frac{\overline{l}^2_{\mathrm{MC}}(R,s)}{\sigma^2_{l,\mathrm{MC}}(R,s)} \tag{2.6}$$

with: N = No. of images passing the quality cuts ($\leqslant 4$)

where $\overline{w}_{\mathrm{MC}}(R,s)$ and $\overline{l}_{\mathrm{MC}}(R,s)$ are the median width and length, retrieved from the same MC simulations used to generate the energy lookup tables, while $\sigma_{w,\mathrm{MC}}(R,s)$ and $\sigma_{l,\mathrm{MC}}(R,s)$ are the corresponding 90%-widths. Those values are stored in lookup tables whose y-axis represents the impact parameter R and the x-axis represents the image size s. Both parameters, the width and length of a gamma ray shower, depend on the shower direction, NSB level and impact parameter. Hence, there exists a table for each telescope, each simulated shower direction and each simulated NSB level.

If data is examined and the null hypothesis is true, then the test statistics of the width (MSCW) and the length (MSCL) are almost normal distributed around zero. The alternative hypothesis is the hypothesis that the shower is induced by a cosmic-ray particle. The test statistic distribution of cosmic-ray showers is skewed and shifted towards positive values for MSCW and MSCL (see Fig. 2.15).
The cut values for both mean scaled parameters are chosen in a way that the fi-

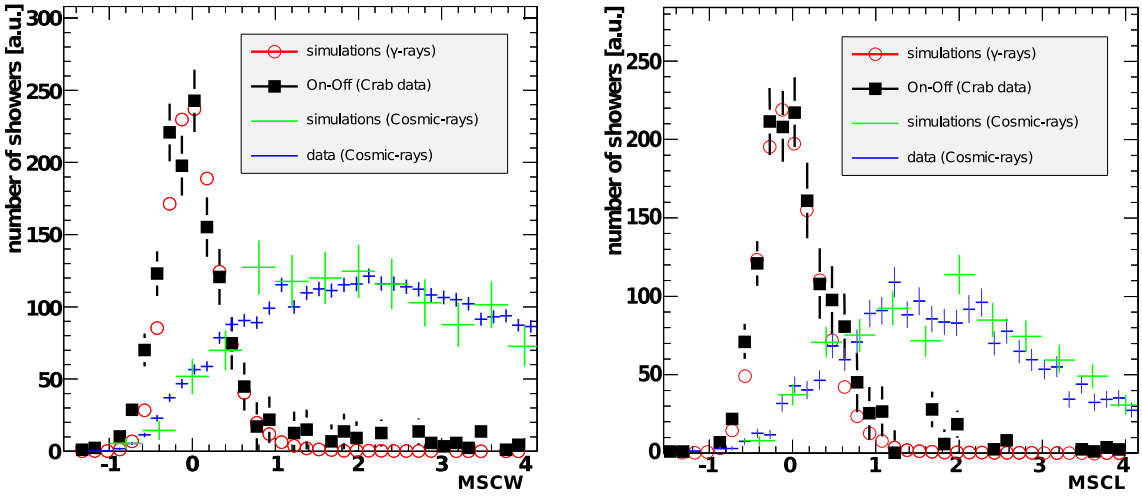

Fig. 2.15: *Comparison of the mean scaled parameters (MSCW: left; MSCL: right) for gamma-ray and background data from simulations and Crab-Nebula observations done in 2007 (3 telescope data) by Gernot Maier [Maier (2007)]. In the data the cosmic-ray events, measured in the* OFF-region, *get subtracted from the events in the* ON-region *to determine the gamma-rays (for explanation of ON- and OFF-region see 2.4.4). All distributions have been scaled to similar fluxes.*

nal probability of accepting a cosmic-ray shower (type 2 error) is very low, while the probability of rejecting a true gamma-ray shower (type 1 error) is not too high. The cut ranges used during this study are: -1.2 < MSCW < 0.35 and -1.2 < MSCL < 0.7.

Theta square cut

Because even the shape cuts can not completely remove all background events from the dataset, one has to take into account the reconstructed position of each event. As the direction of cosmic-ray air showers is isotropic, most of them can be rejected by accepting only events whose direction is close to the expected gamma source position. The angular distance of the reconstructed direction to the expected source position is called θ. However during the analysis usually the square of this value is used.
Depending on the type of source (point-like or extended) and its spectrum, which affects the quality of the reconstruction and the event statistics, different maximum cut values of θ^2 are used. For point-like sources with a moderate spectrum, all events with $\theta^2 \geqslant 0.008$ deg^2 get rejected. In case of a soft spectrum source, for which the determination of the shower direction is less accurate due to smaller images, even events with θ^2-values up to 0.02 deg^2 are accepted.

2.4.4 Background estimation

The final goal is the measurement of a significant excess in the number of gamma-like events caused by gamma rays from an observed source. For visualization all reconstructed positions of gamma-ray-like events are transformed into right ascension and declination and filled into a two-dimensional *sky map*. By looking at the *radial acceptance* curve in Fig. 2.16 one can see that the systems ability to reconstruct events decreases at larger distances from the camera center (pointing direction). Therefore all events with a distance of more than 2° are removed from the sky map.
In general, those maps are smoothed and each bin contains the number of events N_{on} found in the circular *ON-region* around that bin (see also A.1). By this procedure, the error in the reconstruction of a source position is taken into account. Therefore the radius of this area is the same as the θ-cut value. A sky map for the ON-region events is called *ON-map*.
Lots of bins in the ON-map contain background events from the irreducible isotropic cosmic-ray showers. In case their positions are close to a gamma-ray source, the bins also contain signal events. To determine the number of signal events N_{S} for each bin in the sky map it is necessary to know the number of background events N_{B} for that bin. Then

$$N_{\mathrm{S}} = N_{\mathrm{on}} - N_{\mathrm{B}}.$$

As N_{B} cannot be measured directly like N_{on}, several different estimation procedures had been developed for IACTs. For this study it is sufficient to concentrate on just two of these methods. The idea for both methods is to use the same dataset that was used to generate the ON-map. The difference is, that now each bin contains the number of events N_{off} found in dedicated *OFF-regions* for this bin. Such a sky map is called *OFF-map*.

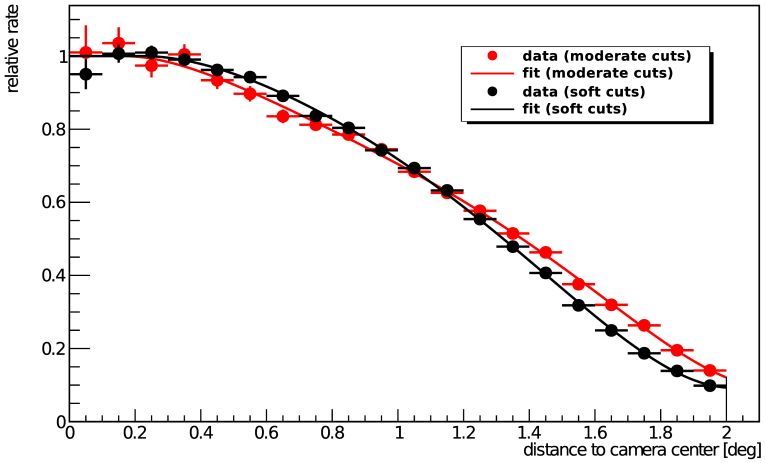

Fig. 2.16: *Radial acceptance curve of the VERITAS camera. It is obtained by analyzing data from a part of the sky with no strong gamma-ray source in the FOV. In this example two different sets of cuts are applied on the data: soft-spectrum cuts (black) and moderate-spectrum cuts (red). The relative rate is calculated with respect to the weighted mean of the first 4 bins. It is assumed, that the acceptance in the camera is symmetric in azimuth.*

These OFF-regions should not contain any gamma-like events from other potential sources in the FOV to insure only contribution from background events to N_{off}. These sources are bright stars (V magnitude > 7), other gamma-ray emitters and the observed target itself. The user is able to specify the size of the circular exclusion regions around those objects. Events measured in those areas are not taken into account for the calculation of N_{off}
As the OFF-regions of each bin have other locations and sizes than its ON-region, N_{off} has to be multiplied by a normalization factor α to estimate the number of background events N_{B} in this bin: $N_{\mathrm{B}} = \alpha N_{\mathrm{off}}$. The α is different for each bin position and is therefore stored in a map as well, the so-called α-*map*.

Ring-background method

In the *ring-background method* the OFF-region is defined as a ring placed around the ON-region (see Fig. 2.17,a). The user defines its radius and its width. Usually it is chosen in a way that the area of the ring is 10 times larger than the size of the ON-region. For the determination of α it is necessary to take into account the decreasing acceptance of the IACT at positions several degrees away from the pointing direction (see Fig. 2.16). So the α for each bin is the ratio of the cumulative acceptances in the ON-region and the OFF-region of that bin. It is required that regions around known gamma-ray emitters and bright stars are excluded from the background regions to avoid possible over- and underestimation.
With this background method one is able to estimate the N_{B} at each bin in the sky map. However it is necessary to generate acceptance predictions for each different cut-set under the usage of MC simulations. Depending on the cuts used and the accuracy of the simulations the error on the acceptance, especially at the edge of the sky map, is not negligible.

Reflected-regions method

To avoid the necessity of an acceptance simulation the *reflected-regions method* can be used. Here the OFF-region of a single bin is divided into several circular areas (same size as the ON-region), arranged on a ring around the pointing position (see Fig. 2.17,b). The radius of the ring is equal to the distance of the bin from the pointing position. In doing so, no correction for the relative camera acceptance is required. The α-value is just the inverse of the number of OFF-areas along the ring. Again, it is necessary to avoid possible over- and underestimation. Therefore an OFF-area will be removed from the list if it intersects with an exclusion region. The ON-region and some of its surrounding area are excluded as well from the OFF-region.
The user is able to specify the minimal and maximal amount of OFF-areas and also the minimal distance from the ON-region to the nearest OFF-areas along the ring. The algorithm will then try to fit the highest possible amount of OFF-areas into the ring, taking into account the exclusion regions. In case the highest possible number of OFF-areas is larger than the maximum required number of OFF-areas, the algorithm starts to randomly remove some of the redundant OFF-areas. In case it is lower than the minimal required amount of OFF-areas, the algorithm is not able

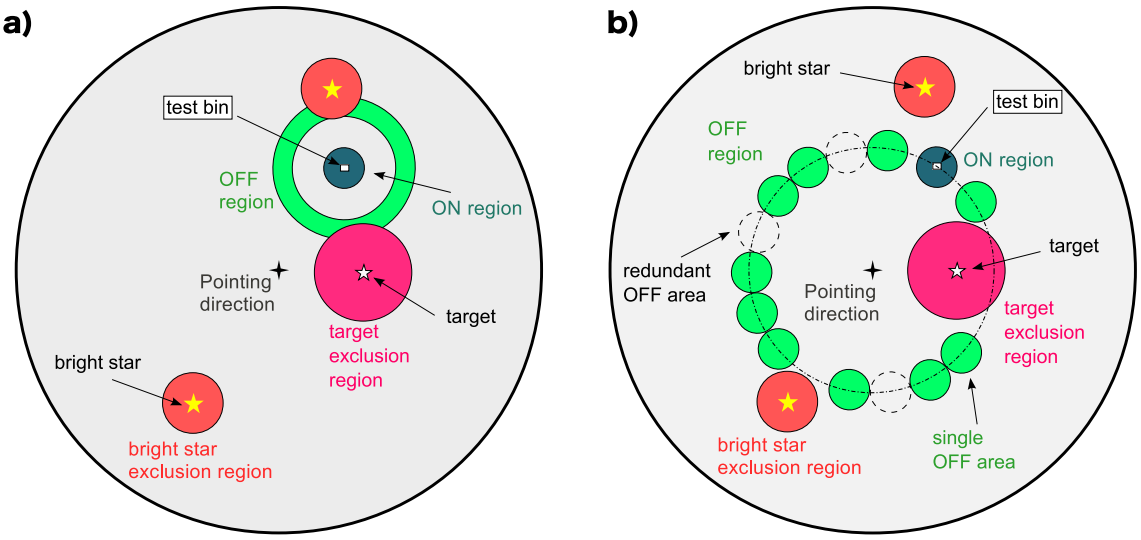

Fig. 2.17: *Comparison of two different background estimation methods applied on data from the same section of the sky. These examples show the the different OFF-regions (light green) used to calculate N_{off} for the test bin (white). They also show the different treatment of the exclusion regions around the observed target (magenta) and around bright stars (orange). The exclusion regions affect only the OFF-regions, not the ON-region.*
a) *The OFF-region of the ring-background method is a ring around the test-bin. The algorithm sums up all events inside the OFF-region to get N_{off} except those ones that also enter an exclusion region.*
b) *The reflected-regions method tries to fit as many OFF-areas as possible onto a ring around the pointing direction, taking into account the deletion of every OFF-area that intersects with an exclusion region. If the pre-defined maximum number of OFF-areas (here it's 10) is exceeded, randomly some redundant OFF-areas get deleted as well. All events that enter one of the remaining OFF-areas add up to N_{off}*

to provide a background estimation for that bin. This is always the case for bins very close to the pointing position in the center. Hence, this method can only be used if the telescopes point slightly next (usually 0.5°) to the putative source position, which is the so-called *wobble-mode*. During a run, a wobble position is fixed, but it is attempted to change the wobble position for each run. Possible positions are north, east, south and west from the source.

Chapter 3

Transient gamma-ray sources

In gamma-ray astronomy and in astronomy in general many of the observed sources show a transient behavior. Depending on the source type there are various reasons why its flux is variable. The measurement of its temporal evolution will contribute a lot to the informations an observer can gain about the physics behind an astronomical object. In this chapter different, transient source types are presented and it is explained what can be learned about the emission mechanisms of a source by determining its temporal evolution. The focus is on objects that are potentially able to emit very-high-energetic (VHE) photons in the GeV-TeV range ($\geqslant$ 100 GeV) and whose flux variations are in the order of seconds to minutes.

3.1 Emission of very high-energetic (VHE) gamma-rays

At the beginning of this chapter we will briefly review some general non-thermal emission mechanisms that cause VHE gamma-rays and are valid for all astronomical objects we are dealing with in the following sections.

3.1.1 Acceleration of charged particles

In this section we want to explain briefly the process of charged particle acceleration in the vicinity of astronomical objects. Being able to emit VHE photons the kinetic energies of charged particles need to be even higher which makes an efficient acceleration mechanism necessary. The *Fermi acceleration* [Fermi (1949)] is such a process and plays a very important role in many astrophysical models. There are two different types of Fermi acceleration which depend on the structure of the plasma. In case of randomly moving magnetized interstellar clouds we are dealing with the *second order Fermi acceleration*. The acceleration mechanism at shock fronts is called *first order Fermi acceleration*. We will describe both processes in short while much more details can be found in [Drury (1983), Blandford *et al.* (1987), Bell (1978)].

Second order Fermi acceleration: Consider a cloud with velocity $\boldsymbol{v}_c$ relative to an average rest frame for the interstellar medium. The magnetic field in the cloud can reflect a cosmic ray due to scattering of the particles by magnetohydrodynamic

waves [Schlickeiser (2002)] or due to the magnetic mirror effect [Longair (2011)]. If the particle gets reflected from an approaching cloud it will gain energy while it will lose energy during a reflection with a receding surface.
To prove this, we first make a Lorentz transformation into the frame where the moving cloud is at rest. The transformed parameters are marked with an apostrophe. In this frame, the energies before and after the reflection (E'_{b} and E'_{a}) are the same while the components of the particles's momentum $\boldsymbol{p'}$ (with $\boldsymbol{p'} = m\gamma_{v'}\boldsymbol{v'}$) parallel to $\boldsymbol{v}_{\mathrm{c}}$ ($p'_{\mathrm{b}\,\parallel}$ and $p'_{\mathrm{a}\,\parallel}$) just change their sign:

$$E'_{\mathrm{a}} = E'_{\mathrm{b}}\ ; \quad p'_{\mathrm{a}\,\parallel} = -p'_{\mathrm{b}\,\parallel} \implies \boldsymbol{p'_{\mathrm{a}}} \cdot \boldsymbol{v}_{\mathrm{c}} = -\boldsymbol{p'_{\mathrm{b}}} \cdot \boldsymbol{v}_{\mathrm{c}} \tag{3.1}$$

After the transformation back to the laboratory frame with $\Gamma = (1 - v_{\mathrm{c}}^2/c^2)^{-1/2}$ one can calculate the energy difference ΔE:

$$E_{\mathrm{a,b}} = \Gamma(E'_{\mathrm{a,b}} + \boldsymbol{p'_{\mathrm{a,b}}} \cdot \boldsymbol{v}_{\mathrm{c}})\ ; \qquad \boldsymbol{p'_{\mathrm{a,b}}} \cdot \boldsymbol{v}_{\mathrm{c}} = \left(E_{\mathrm{a,b}} \frac{v_{\mathrm{c}}^2}{c^2} - \boldsymbol{p}_{\mathrm{a,b}} \cdot \boldsymbol{v}_{\mathrm{c}} \right) \tag{3.2}$$

$$\Delta E = E_{\mathrm{a}} - E_{\mathrm{b}} = -2\Gamma(\boldsymbol{p'_{\mathrm{b}}} \cdot \boldsymbol{v}_{\mathrm{c}}) = -2\Gamma(m\gamma v'_{\mathrm{b}\,\parallel} \cdot v_{\mathrm{c}}) \tag{3.3}$$

In the last step we have already used the relations from Equ. (3.1). Now one can determine the conditions necessary to make a particle gain energy during a refelction:

$$\text{if } \Delta E > 0: \quad v'_{\mathrm{b}\,\parallel} < 0 \quad \Rightarrow \quad v_{\mathrm{b}\,\parallel} < v_{\mathrm{c}} \quad \text{with:} \quad v'_{\parallel} = \frac{v_{\parallel} - v_{\mathrm{c}}}{1 - v_{\parallel} v_{\mathrm{c}}/c^2} \tag{3.4}$$

$$\text{if } \Delta E < 0: \quad v'_{\mathrm{b}\,\parallel} > 0 \quad \Rightarrow \quad v_{\mathrm{b}\,\parallel} > v_{\mathrm{c}} \tag{3.5}$$

It is clear that energy gains result from head-on collisions which happen when the parallel component of the particles relative speed measured inside the cloud $v'_{\mathrm{b}\,\parallel}$ is negative. Contrary to this, the particle loses energy when this velocity component is positive in the proper frame. Back in the laboratory frame one can state that the energy gain occurs if the parallel velocity component $v_{\mathrm{b}\,\parallel}$ is smaller than the speed of the cloud v_{c}.
If the incidence angle $\alpha = \angle(\boldsymbol{v}_{\mathrm{b}}, \boldsymbol{v}_{\mathrm{c}})$ between the particle and the cloud is completely arbitrary, then the probability for the case: $v_{\mathrm{c}} > v_{\mathrm{b}\,\parallel}$ ($= |\boldsymbol{v}_{\mathrm{b}}| \cos\alpha$) is always higher than for the case: $v_{\mathrm{c}} < v_{\mathrm{b}\,\parallel}$. So the net effect after several scatterings at different clouds with random α is a gain in energy. That the mean energy change is positive, can be also shown by substituting the second equation of (3.2) into (3.3). We find that ΔE depends on $\boldsymbol{p}_{\mathrm{b}} \cdot \boldsymbol{v}_{\mathrm{c}}$ and v_{c}^2/c^2. For arbitrary α at different scatterings the sum of all $\boldsymbol{p}_{\mathrm{b}} \cdot \boldsymbol{v}_{\mathrm{c}}$ terms average to zero and the remaining energy gain results from the second order term: v_{c}^2/c^2.

While this second order term represents the fact that a collision between particle and cloud on average leads to an increase in energy, there is another second order effect which takes into account the rate ν of collisions inside a volume with several random moving clouds. Let the mean distance traveled between clouds be L. Then the rate of collisions is

$$\nu = \frac{|\boldsymbol{v}_{\mathrm{b}} - \boldsymbol{v}_{\mathrm{c}}|}{L} \tag{3.6}$$

One can see that the rate for head-on collisions ($\boldsymbol{v}_\mathrm{b} \cdot \boldsymbol{v}_\mathrm{c} < 0 \Rightarrow v_{\mathrm{b}\,\parallel} < 0$) is higher than that for overtaking collisions ($\boldsymbol{v}_\mathrm{b} \cdot \boldsymbol{v}_\mathrm{c} > 0 \Rightarrow v_{\mathrm{b}\,\parallel} > 0$). As the head-on collisions are responsible for the energy gain of the particle and the probability of $\boldsymbol{v}_\mathrm{b} \cdot \boldsymbol{v}_\mathrm{c} < 0$ is exactly 1/2 for particles inside the volume the sum of all energy changes after several collisions is positive.

First order Fermi acceleration: A more efficient particle acceleration than the second order Fermi acceleration is the *first order Fermi acceleration*. As a simple example one can assume the same environment as for the second order Fermi acceleration but this time the movement of the magnetized clouds is not arbitrary. Instead they are approaching each other and a particle bouncing back and forth between them is always reflected head-on. Hence the first order change ($\boldsymbol{p} \cdot \boldsymbol{v}_\mathrm{c}$) in energy is always positive and doesn't cancel out.

A realistic environment with similar conditions is found in an astrophysical *shock wave* which is a discontinuity between two media moving relative to each other. An example of a shock wave would be a supernova where the explosion expels much or all of a star's material into the surrounding interstellar medium. The interstellar medium ahead of the shock front is called the *upstream* while the swept up material behind the shock front is the *downstream* region. In the frame where the shock wave is at rest the speed of the upstream and the downstream plasma is u_1 and u_2 while $u_1 > u_2$ (see Fig. 3.1). So the speed of the shock wave in the laboratory frame is always faster than the speed of the downstream.

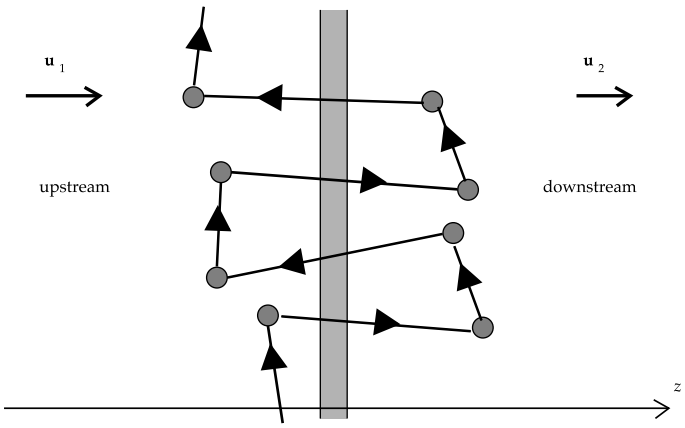

Fig. 3.1: *Diffusive shock acceleration in the frame of the shock front: the shaded vertical region indicates the shock, the circular blobs denote different scatterings, and the solid line with arrows indicates the path of an idealized fast particle. The coordinate z and the velocities $\boldsymbol{u_1}$ and $\boldsymbol{u_2}$ are shown for the case of a parallel shock. In a laboratory frame, where the upstream medium is at rest, the shock wave moves from right to left in this example.*

On each side of the shock wave there are magnetohydrodynamic (MHD) waves that scatter the particles and change their momentum direction but not its modulus. As those MHD waves convect along with the plasma a particle gains energy if it enters the plasma head-on and gets reflected after several scatterings.

Imagine a particle inside the upstream region (the interstellar medium). The shocked material behind the shock front (the downstream) approaches the particle with a relative velocity of $v_{\mathrm{rel}} = u_1 - u_2$. Hence, in the reference frame where the interstellar medium is at rest, the particle gains energy as it collides head-on with the approaching downstream plasma. After several scatterings inside the downstream plasma, the particle will eventually move back to the upstream plasma with a higher speed than it had at the beginning. If also a reflection happens in this region, the whole process starts again but with a higher particle energy. Repeating this cycle several times will efficiently increase the energy of the particle.
A more quantitative approach, used in various text books (e.g. [Longair (2011)]), reveals that the average gain in energy after one cycle is proportional to the relative speed v_{rel} between the upstream and downstream fluid. This is why it is called *first order Fermi acceleration*. Further calculations take into account the probability that the particle remains within the acceleration region after one collision. It can be shown that the distribution of high energy particles accelerated by this process follows a power law:

$$N(E)\mathrm{d}E \propto E^{-q+2}\mathrm{d}E \qquad \text{(for fully ionized gas: } q = 4\text{)}$$

3.1.2 Non-thermal radiation mechanisms

In the previous section, the mechanisms of particle acceleration are described. It is now necessary to discussion the processes by which the accelerated, charged particles lose energy in the form of VHE radiation.

Accelerated charged particle

By solving the Maxwell equations for a single charged particle in free space, one can see that a propagating electric field $\boldsymbol{E}_{\mathrm{rad}}$ is created only if the particle is accelerated. If one is interested in situations, where the particle has a relativistic velocity and the distances between the particles position $\boldsymbol{r_0}$ and the measurement of the electric field at $\boldsymbol{r} = \boldsymbol{r_0} + \boldsymbol{R}$ is very large ($R \to \infty$), one has to use this equation for the electric field:

$$\boldsymbol{E}_{\mathrm{rad}}(\boldsymbol{r}, t) = \frac{q}{4\pi R \epsilon_0 c} \underbrace{\left[\frac{\boldsymbol{n} \times [(\boldsymbol{n} - \boldsymbol{v}/c) \times \dot{\boldsymbol{v}}/c]}{(1 - (\boldsymbol{n} \cdot \boldsymbol{v})/c)^3} \right]}_{:= \boldsymbol{f}(\boldsymbol{R}, t_{\mathrm{ret}})} \Bigg|_{\mathrm{ret}} \tag{3.7}$$

Here the vector $\boldsymbol{n} = \boldsymbol{R}/R$ is the unit vector from the charged particle to the point of observation and $\boldsymbol{v}$ is the velocity of the particle. For both vectors we have to use retarded times ($t_{\mathrm{ret}} = t - R/c$) due to the propagation duration between the observer and the position of the particle.
Another important parameter to calculate, is the magnitude of the Poynting vector, measured at the position of the observer: $S = E^2_{\mathrm{rad}}(\boldsymbol{r}, t)\epsilon_0 c$. It describes the energy flux per unit area. We use this value to calculate the energy loss rate $\mathrm{d}W/\mathrm{d}t$ ($= \mathrm{d}P$) per solid angle $\mathrm{d}\Omega$: $\mathrm{d}P/\mathrm{d}\Omega = S \cdot R^2 = |\boldsymbol{f}(\boldsymbol{R}, t_{\mathrm{ret}})|^2 \cdot q^2/(16\pi^2\epsilon_0 c)$. We are especially interested in the equation that describes the spectral distribution. By the usage of

Fourier transformation and the application of the Parseval's theorem we derive the following:

$$\int_{-\infty}^{+\infty} \frac{\mathrm{d}P(t)}{\mathrm{d}\Omega}\mathrm{d}t = \frac{q^2}{16\pi^2\epsilon_0 c}\int_{-\infty}^{+\infty} |\boldsymbol{f}(\boldsymbol{R}, t_{\mathrm{ret}})|^2\mathrm{d}t = \frac{2q^2}{16\pi^2\epsilon_0 c}\int_{0}^{+\infty} |\hat{\boldsymbol{f}}(\boldsymbol{R}, \omega)|^2\mathrm{d}\omega \quad (3.8)$$

$$\text{with:} \quad \frac{\mathrm{d}W}{\mathrm{d}\Omega} = \int_{-\infty}^{+\infty} \frac{\mathrm{d}P(t)}{\mathrm{d}\Omega}\mathrm{d}t = \int_{0}^{+\infty} \frac{\mathrm{d}I(\omega)}{\mathrm{d}\Omega}\mathrm{d}\omega$$

$$\Rightarrow \quad \frac{\mathrm{d}I(\omega)}{\mathrm{d}\Omega} = \frac{2q^2}{16\pi^2\epsilon_0 c}|\hat{\boldsymbol{f}}(\boldsymbol{R}, \omega)|^2 = \frac{q^2}{16\pi^3\epsilon_0 c}\left|\int_{-\infty}^{+\infty} \boldsymbol{f}(\boldsymbol{R}, t_{\mathrm{ret}}) \cdot \mathrm{e}^{i\omega t}\mathrm{d}t\right|^2 \quad (3.9)$$

(see [Longair (2011), Jackson (1998)]). In the end we get the spectral energy distribution per solid angle by calculating the Fourier transformation of the vector function $\boldsymbol{f}(\boldsymbol{R}, t_{\mathrm{ret}})$, which is just a placeholder for the long term between the brackets in Equ. (3.7). One has to know the particle's trajectory, its temporal change in velocity and the position of the observer. Hence, also the possible directions and the spectrum of the emitted radiation depend on these characteristics.

Synchrotron radiation

As *synchrotron radiation* is one of the most important non-thermal radiation mechanisms we describe briefly its characteristics and results. For detailed information please read [Longair (2011)].
The particle acceleration, necessary to produce radiation, is created by strong magnetic fields close to the astronomical objects that emit relativistic electrons. Those electrons are bound to the magnetic fields and travel along spirals around the direction of those field lines. After choosing a sophisticated coordinate system all necessary informations are available to calculate $\boldsymbol{f}(\boldsymbol{R}, t_{\mathrm{ret}})$. At the beginning of the derivation one assumes only one electron traveling along a spiral with a fixed pitch angle $\alpha = \angle(\boldsymbol{v}, \boldsymbol{B})$ which emits light that is observed under a specific angle $\theta = \angle(\boldsymbol{n}, \boldsymbol{v})$. In the end one has to integrate over all the fixed parameters, if one wants to know the total energy loss. It is not necessary to repeat the whole derivation but to state just some important steps:

- one has to take into account the real three-dimensional curvature, whose radius a is larger than the *gyroradius* $r_{\mathrm{g}} = \gamma m_{\mathrm{e}} v/eB$ if the pitch angle α of the particle is lower than $90°$ $\longrightarrow$ $a = r_{\mathrm{g}}/\sin\alpha$

- as the radiation is highly beamed along $\boldsymbol{v}$, if $v \approx c$, it is only visible for an observing direction close to $\boldsymbol{v}$ ($\theta \leqslant 1/\gamma$) and only during a short fraction of a whole electron orbit around the field lines $\longrightarrow$ using the approximation of small θ and small t_{ret}

- $\boldsymbol{E} \perp \boldsymbol{n}$ with $\boldsymbol{E} = \boldsymbol{E}_\perp + \boldsymbol{E}_\parallel$ $\longrightarrow$ $\mathrm{d}I(\omega)/\mathrm{d}\Omega$ get split into two components: $\mathrm{d}I_\perp(\omega)/\mathrm{d}\Omega$ for $\boldsymbol{E}_\perp \perp \boldsymbol{B}$-$\boldsymbol{n}$ plane and $\mathrm{d}I_\parallel(\omega)/\mathrm{d}\Omega$ for $\boldsymbol{E}_\parallel \parallel \boldsymbol{B}$-$\boldsymbol{n}$ plane $\longrightarrow$ different dependencies on t and θ between both components lead to different polarisations: linear if $\theta = 0$; elliptical if $\theta \neq 0$

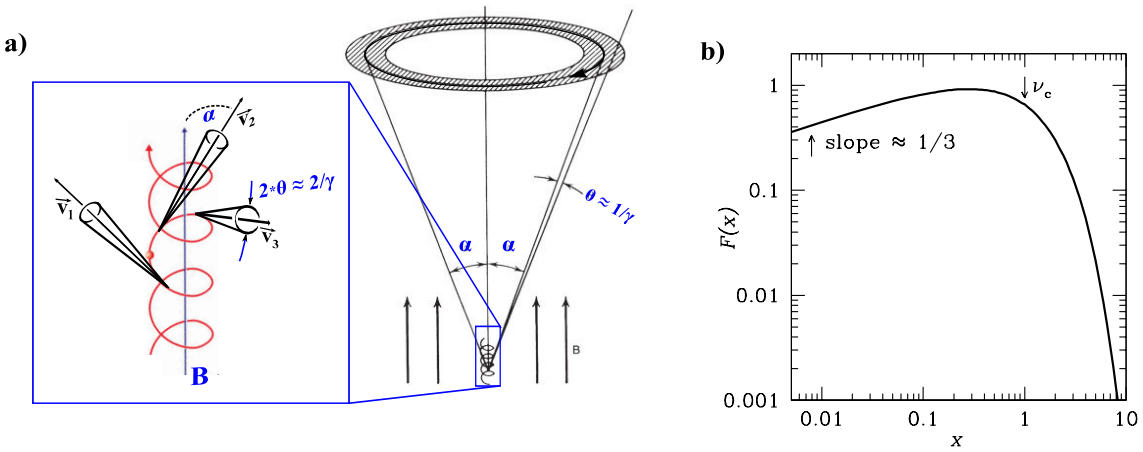

Fig. 3.2: *a) Beamed emission of a single electron moving with relativistic speed along a spiral trajectory around a magnetic field. The pitch angle between* $\boldsymbol{v}$ *and* $\boldsymbol{B}$ *is* α *and the opening angle of the beamed emission is* $2\theta \approx 2/\gamma$*. As an example, the emission of the same electron is shown at three different times in the detailed plot on the left side. Only the direction of* $\boldsymbol{v}$ *is changing but not its modulus. The grey shaded circle at the edge of the* velocity cone *in the bigger picture on the right side marks the area where the cone of the beamed emission slips over during a single orbit of the electron. So at each observing position that is inside the grey area, one can only observe pulsed emission.*
b) Plot of function $F(x)$ *with* $x = \omega/\omega_\mathrm{c} = \nu/\nu_\mathrm{c}$*.*

- transformation of the equations in a way that parts of them can be replaced by modified Bessel functions $K_{2/3}$ and $K_{1/3}$

- integration over the solid angle $\mathrm{d}\Omega$ for one period of gyration (grey area in Fig. 3.2) to get $I_\perp(\omega)$ and $I_\parallel(\omega) \longrightarrow \mathrm{d}\Omega = 2\pi \sin\alpha \, \mathrm{d}\theta$

As the radiation is concentrated in a small angular space ($\theta \leqslant 1/\gamma$) around $\boldsymbol{v}$, if $v \approx c$, the emission pattern of a single electron on a spiral trajectory will be the envelope of a so-called *velocity cone* (see Fig. 3.2,a) with an opening angle that is equal to 2α and with an envelope thickness of $\theta \approx 2/\gamma$. The beamed radiation will precess together with $\boldsymbol{v}$ about the direction of magnetic field lines in the center of the velocity cone. As it is necessary to determine the intensity emitted per time by one electron, one has to divide the emitted radiation $I(\omega)$ $(= I_\perp(\omega) + I_\parallel(\omega))$ during one gyration period by the time of that period $T_\mathrm{r} = \nu_\mathrm{c}^{-1} = 2\pi\gamma m_\mathrm{e}/eB$. The final result is the following:

$$j(\omega) = \frac{I_\perp(\omega) + I_\parallel(\omega)}{T_\mathrm{r}} = \frac{\sqrt{3}e^3 B \sin\alpha}{8\pi^2 \epsilon_0 c m_\mathrm{e}} \cdot \underbrace{x \int_x^\infty K_{5/3}(z)\mathrm{d}z}_{:= F(x)} \tag{3.10}$$

$$\text{with:} \quad \omega_\mathrm{c} = 2\pi\nu_\mathrm{c} = \frac{3c\gamma^2 eB \sin\alpha}{2v m_\mathrm{e}} \quad \text{and:} \; x = \frac{\omega}{\omega_\mathrm{c}}$$

and for the mean energy loss rate per electron one has to integrate over ω and an isotropic distributed pitch angle α:

$$-\left(\frac{\mathrm{d}W}{\mathrm{d}t}\right)_{\mathrm{sync}} = \int_0^{\infty}\int_0^{\pi} j(\omega)\mathrm{d}\omega\,\frac{1}{2}\sin\alpha\,\mathrm{d}\alpha = \frac{4}{3}\sigma_{\mathrm{T}}cU_{\mathrm{mag}}\left(\frac{v}{c}\right)^2\gamma^2 \tag{3.11}$$

$$\text{with:}\quad \sigma_{\mathrm{T}} = \frac{e^4}{6\pi\epsilon_0^2 m_{\mathrm{e}}^2 c^4} \qquad \text{and:}\quad U_{\mathrm{mag}} = \frac{B^2}{2\mu_0}$$

In a next step, the asymptotic behavior of $F(\omega/\omega_{\mathrm{c}})$ is studied in the limits of high and low frequencies:

$$\begin{aligned} j(\nu) &\propto \nu^{1/2}\mathrm{e}^{-\nu/\nu_{\mathrm{c}}} \quad &&\text{for } \nu \gg \nu_{\mathrm{c}} \\ j(\nu) &\propto \nu^{1/3} &&\text{for } \nu \ll \nu_{\mathrm{c}} \end{aligned} \tag{3.12}$$

That these asymptotic equations are true can be seen by looking at the plot of the function $F(\omega/\omega_{\mathrm{c}})$ in Fig. 3.2,b. So for high frequencies an exponential cut-off is expected.

Now one knows the emission spectrum of a single electron at a certain energy entering the magnetic field under a certain pitch angle. This study concentrates on cosmic ray electrons that are accelerated by astrophysical shock waves. So one has to deal with a large amount of electrons at different energies E and with arbitrary pitch angels. For these scenarios one can assume that the pitch angle will be isotropically distributed and that the energy distribution of the electrons is dominated by the process of a first order Fermi acceleration: $N(E)\mathrm{d}E = \kappa E^{-p}\mathrm{d}E$.
One has to multiply the energy distribution with $j(\omega)$ from Equ. (3.10) and integrate the result over the energy E. This is because also $j(\omega)$ is affected by the value of the energy due to the internal parameter $\omega_{\mathrm{c}} \propto \gamma^2 \propto E^2$. After a final integration over the isotropic pitch angle distribution, the resulting emission spectrum will look like this:

$$J_{\mathrm{sync}}(\nu) \propto \kappa B^{(p+1)/2}\nu^{-(p-1)/2} \tag{3.13}$$

A detailed derivation can be found in [Longair (2011)].

Inverse Compton scattering

The interaction of relativistic electrons with low-energy photons through *inverse Compton (IC) scattering* is one of the main important gamma-ray production processes in astrophysical objects. During this process energy gets transferred from high-energy electrons towards the isotropic distributed photons. Due to relativistic aberration, this photon field is extremely anisotropic inside the comoving frame of the relativistic electron (see Fig. 3.3). In this reference frame almost all ambient photons approach the electron within a small angle of $\approx \gamma^{-1}$.

If $\hbar\omega \ll m_{\mathrm{e}}c^2$ inside the comoving frame, it is a good approximation if we treat the scattering as *Thomson scattering*. In this classical approach, the electric field E_{rad} of an incident radiation will cause the electron to oscillate with an acceleration of:

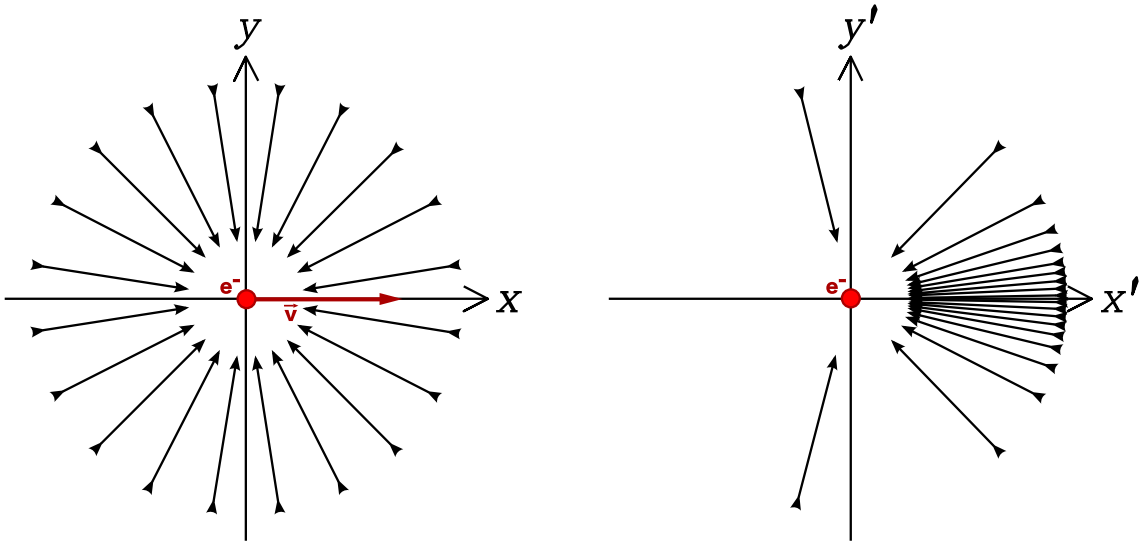

Fig. 3.3: *Relativistic electron moves through isotropic photon field. LEFT: laboratory frame. RIGHT: rest frame of the electron*

$\ddot{r} = eE_{\mathrm{rad}}/m_{\mathrm{e}}$. As we know already from the section above, an accelerated electron will lose energy by emitting radiation with a loss rate $\mathrm{d}W/\mathrm{d}t$ that is proportional to $|\ddot{r}|^2$:

$$-\left(\frac{\mathrm{d}W}{\mathrm{d}t}\right) \propto |\ddot{r}|^2 \propto |E_{\mathrm{rad}}|^2 \qquad \Rightarrow \qquad -\left(\frac{\mathrm{d}W}{\mathrm{d}t}\right) = \sigma_{\mathrm{T}} S = \sigma_{\mathrm{T}} c u_{\mathrm{rad}} \tag{3.14}$$

$$\text{with:} \qquad \sigma_{\mathrm{T}} = \frac{e^4}{6\pi\epsilon_0^2 m_{\mathrm{e}}^2 c^4} = 6.653 \times 10^{-29} m^2 \tag{3.15}$$

Here σ_{T} is the cross section of the Thomson scattering and u_{rad} is the energy density of the radiation.
The goal is to calculate the energy loss inside the rest frame of the electron because $\mathrm{d}E'/\mathrm{d}t' = \mathrm{d}E/\mathrm{d}t$ will directly lead to the result valid for the laboratory frame. Therefore we need to transform u_{rad} into u'_{rad}. After some algebra, involving the relativistic Doppler shift formula and some geometrical considerations (see [Longair (2011), Blumenthal *et al.* (1970)]) we end up with the following relation:

$$u'_{\mathrm{rad}}(\theta) = [\gamma(1 + (v/c)\cos(\theta))]^2 u_{\mathrm{rad}} \tag{3.16}$$

u_{rad} doesn't depend on θ if the energy density is isotropic in the laboratory frame. If we integrate over the all θ, assuming that each direction has equal probability, we

will find the global U'_{rad} which we can insert in the equation for $\mathrm{d}E'/\mathrm{d}t'$:

$$-\left(\frac{\mathrm{d}E}{\mathrm{d}t}\right)_{\mathrm{rad,gain}} = -\left(\frac{\mathrm{d}E'}{\mathrm{d}t'}\right)_{\mathrm{rad,gain}} = \frac{4}{3}\sigma_{\mathrm{T}} c u_{\mathrm{rad}} \left(\gamma^2 - \frac{1}{4}\right) \tag{3.17}$$

$$-\left(\frac{\mathrm{d}E}{\mathrm{d}t}\right)_{\mathrm{IC}} = -\left[\left(\frac{\mathrm{d}E}{\mathrm{d}t}\right)_{\mathrm{rad,gain}} - \left(\frac{\mathrm{d}E}{\mathrm{d}t}\right)_{\mathrm{rad,loss}}\right] =$$

$$= \frac{4}{3}\sigma_{\mathrm{T}} c u_{\mathrm{rad}} \left(\gamma^2 - \frac{1}{4}\right) - \sigma_{\mathrm{T}} c u_{\mathrm{rad}} = \frac{4}{3}\sigma_{\mathrm{T}} c u_{\mathrm{rad}} \left(\frac{v}{c}\right)^2 \gamma^2 \tag{3.18}$$

This equation describes the energy loss per time of the relativistic electron. The energy transfer to the photon field is always positive with an average boost per photon of $4/3 \cdot (v/c)^2\gamma^2$. The maximum energy a scattered photon can acquire is $4\gamma^2 h\nu_0$. This happens when an incoming photon, with frequency ν_0, collides with the electron head-on and gets reflected back on its original path.
There is also a remarkable similarity of the result in Equ. (3.18) to the expression for the energy loss rate of the synchrotron radiation in Equ. (3.11). Therefore we can assume that the intensity spectrum of the IC-scattered photons, produced by the same power-law distribution of electrons that was used in Equ. (3.13), will show the same functional behavior between ν and the spectral index p of the power-law:

$$J_{\mathrm{IC}}(\nu) \propto \nu^{-(p-1)/2} \times \int \nu_0^{(p-1)/2} n(\nu_0)\mathrm{d}\nu_0 \tag{3.19}$$

with $n(\nu_0)$ which is the density of photons before the scattering. This assumption is proven to be correct in a long, but straightforward equation (see [Blumenthal *et al.* (1970)], Equ. 2.64).
However Equ. (3.19) is only valid for the Thomson regime. In general the cross section for Compton scattering is the *Klein-Nishina cross-section* taking into account quantum electrodynamic effects. This cross section is not constant anymore but proportional to $1/(\hbar\omega)$ for large energies. In such a scenario the power law of $J_{\mathrm{IC}}(\nu)$ is steeper: $J_{\mathrm{IC}}(\nu) \propto \nu^{-p}$

Synchrotron-self Compton radiation

Actually the *synchrotron-self-Compton radiation (SSC)* is not a different kind of non-thermal radiation process. It is a combination of both processes described above. It occurs when relativistic electrons produce low energy synchrotron radiation which in turn provides the seed photon field for inverse Compton scattering by the same electrons. As long as the energy of the photons before the inverse Compton scattering is low enough ($\sigma \approx \sigma_{\mathrm{T}}$) the following equation is valid:

$$\eta = \frac{(\mathrm{d}E/\mathrm{d}t)_{\mathrm{IC}}}{(\mathrm{d}E/\mathrm{d}t)_{\mathrm{sync}}} = \frac{u_{\mathrm{rad}}}{B^2/2\mu_0} \tag{3.20}$$

This is the ratio between the two different energy loss rates. Where u_{rad} is the photon energy density around the relativistic electrons and B is the magnetic flux

density in this area. Observing the synchrotron radio flux density and the X- and γ-radiation from the same source region will then make it possible to estimate the magnetic flux density at the source region. Of course only under the assumption that electrons of nearly the same energies are responsible for the different emissions.

As long as the upscattered photons stay close to the relativistic electrons further inverse Compton processes can occur. This way the high-energy photons will again increase their energy until ultra-high energy γ-rays are produced. However the cross section will decrease with $1/(\hbar\omega)$ because we are now in the Klein-Nishina regime. Therefore, higher order scatterings result in much lower luminosities. For more details about the SSC radiation see [Longair (2011)].

Bremsstrahlung

This process also based on the fact that accelerated charged particles will emit radiation. The difference is that this time the acceleration happens in the electrostatic field of another charged particle when an electron moves at a high velocity past the stationary nucleus. As the focus of this work is on astrophysical emission methods of VHE γ-rays, we need to concentrate only on Bremsstrahlung of relativistic electrons entering a ionized plasma. Details on the exact derivation of the necessary equations can be found in [Blumenthal *et al.* (1970)]. Here I just want to state that the emitted intensity spectrum follows the power-law form of the accelerated particles with the same spectral index [Longair (2011)]. Therefore it is possible that ultra-high-energy electrons emit a measurable flux of bremsstrahlung in the TeV regime [Atoyan *et al.* (2000)].

Neutral pion decay

Besides the already mentioned leptonic induced γ-ray emission mechanisms there is also the possibility of hadronic interactions that produce VHE photons. If protons are accelerated to sufficient high energy to reach the threshold for proton-photon interactions of $\simeq$ 145 MeV [Kelner *et al.* (2008)], the high-energy protons would interact with synchrotron photons to produce pions. The decay of the neutral pion would result in high-energy γ-ray emission up to the TeV energy [Cao *et al.* (2014)]. For this interaction, the energy transferred from the incident proton to the secondary product is usually around 10% or more.

$$p + \gamma \longrightarrow \begin{cases} p + \pi^0 \\ n + \pi^+ \end{cases} \tag{3.21}$$

$$\pi^0 = \gamma + \gamma \tag{3.22}$$

3.2 Transient gamma-ray emitters

In this section we will describe different astronomical objects that are known to produce transient ultra-high energetic γ-radiation. We will concentrate on objects whose variability in this spectral range is of the order of minutes.

3.2.1 X-ray binaries

Binary stars are astronomical objects that contain two stars which orbit around their common center of mass. Roughly 33% of all star systems in our galaxy are binary systems. A special class of binary stars are *X-ray binaries (XRB)* that are luminous in X-rays. In our galaxy and the nearest neighbor galaxies there are a few hundred sources of this kind.

General characteristics of X-ray binaries

In general, X-ray binaries are made up of a star, which emits optical light (optical companion), and a compact object (a white dwarf, neutron star, or black hole). Usually they originate from a binary system with a large mass ratio between the two stars. The more massive star will evolve faster until it explodes in a supernova by which a neutron star or black hole is produced. When the mass is too low there will be no supernova but a white dwarf instead.
X-ray binaries are characterized by a high X-ray luminosity (10^{34} to 10^{38} erg/s), hard spectra, and a high degree of variability of different nature. In case of an accretion-powered binary the necessary energy is coming from the released gravitational potential energy of infalling matter. This accreted matter stems from the companion star and is transferred by stellar wind or by *Roche lobe* overflow (see Fig. 3.4). The Roche lobe is a region defined in a coordinate system that rotates together with the binary star. This teardrop-shaped space marks the area around a star within which orbiting material is bound to that star taking into account the centrifugal and the gravitational force [Longair (2011)].
An other mechanism for non-thermal emission at binary systems is the collision of streams of matter ejected by both objects and the acceleration of particles in the accrued shock fronts.

High-mass vs. low-mass companion

Besides those general characteristics, valid for almost all XRBs, any further property can differ a lot from one XRB to another. By todays knowledge there is a large set of subgroups in which we can separate different XRB with different characteristics. A fundamental property, however, is the mass of the companion star which is used to subdivide the XRB into two classes: *High-Mass X-ray Binaries (HMXBs)* and *Low-Mass X-ray Binaries (LMXBs)*. In HMXB the optical companion is a Be star ($M \geqslant 5M_{\odot}$) or OB supergiant ($M \geqslant 15M_{\odot}$). They usually have long orbital periods (days to tens of days) and mass transfer is by stellar wind. If the system contains a Be star, it tends to have orbits with strong eccentricity and the mass transfer is connected to the circumstellar disk of these fast rotating stars. In the case of LMXB the companion is of spectral type A or later ($M \leqslant 2M_{\odot}$), the orbital periods are shorter (hours to days) and the mass transfer is by Roche Lobe overflow which occurs through the inner Lagrangian point, L1.(see Fig. 3.4).
In Table 3.1 we compare all important properties of the two different types of XRBs. Detailed information about each parameter, and XRBs in general, can be found in [Trümper *et al.* (2008)]

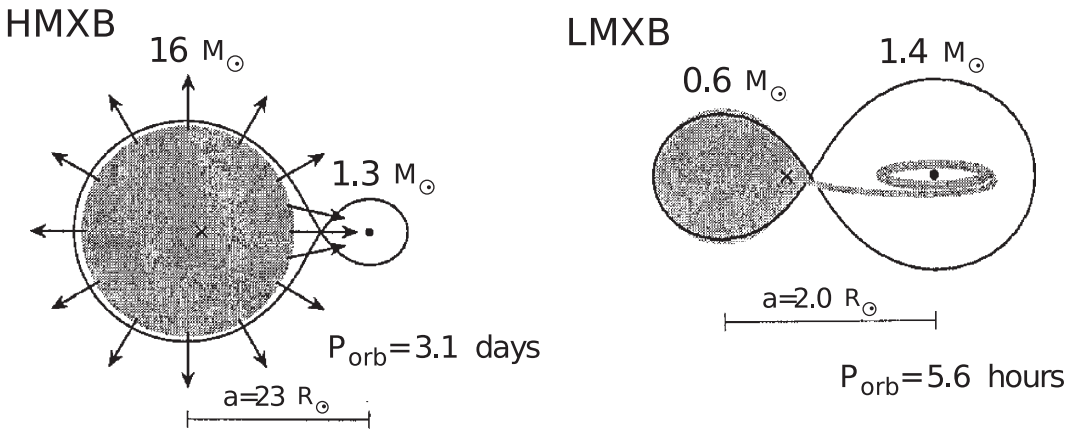

Fig. 3.4: *Two representative examples for mass transfer in a HMXB (stellar wind) and in a LMXB (Roche lobe overflow) [Trümper et al. (2008)].*

Properties	HMXB	LMXB
donor star	O-B ($M \geqslant 5M_{\odot}$)	A-M ($M \leqslant 2M_{\odot}$)
$L_{\mathrm{X}}/L_{\mathrm{opt}}$	0.001 - 10	100 - 1000
optical spectrum	stellar-like	reprocessing
mass transfer	stellar wind	Roche lobe overflow
accretion disk	yes, small	yes
X-ray spectrum	hard (kT $\geqslant$ 15 keV)	soft (kT $\leqslant$ 15 keV)
orbital period	1 h -100 d	10 min - 10 d
X-ray eclipses	common	rare
magnetic field	strong ($\sim 10^{12}$ G)	weak ($\leqslant 10^{9}$ G)
X-ray pulsation	common (0.1 - 1000 s)	rare (1 - 100 s)
X-ray bursts	absent	common

Table 3.1: *Comparison of HMXB with LMXB. $L_{\mathrm{X}}/L_{\mathrm{opt}}$ is the ratio of X-ray to optical luminosity. All values and informations taken from [Trümper et al. (2008)]*

X-ray and optical/UV Emission

The dominant emission mechanisms inside a XRB strongly depend on its type and its composition. In case there is no strong wind ejected by the compact object, that prevents material from falling into the gravitational potential, an accretion disk will form around that object if the transferred matter has large angular momentum. This is especially the case for Roche lobe overflow (i.e. LMXBs) but also happens rarely during stellar wind accretion (i.e. HMXBs), however, the size of the disk is much smaller in this situation.
The disk has differential rotation, and generates shear which heats the gas. By this effect, energy will be transferred from a gravitational potential towards blackbody radiation. The temperature is large enough to produce optical and UV-light and even X-rays. This is also the dominating X-ray source of black-hole XRBs. For non-black-hole XRBs, however, the energy release of the infalling matter, when hitting the surface of the compact object, is the main source of X-ray emission. The radiation mechanism is mostly thermal Bremsstrahlung and black body emission with temperatures in excess of 10^7 K.

In case of HMXB with a neutron star and a strong magnetic field the accretion disk will be distorted and charged particles funnel along the field lines towards the polar caps where they create a X-ray hot spot. Therefore the X-ray emission will be pulsed if the dipole axis of the rotating neutron star is inclined and the hot spot moves around the rotation axis. A consequence of accretion is that infalling material close to the poles shorts out the electric field which is necessary for radio emission. Therefore HMXBs are usually not radio pulsars.
The optical and UV light are coming from the companion star. In HMXBs, where the massive companion star is still young and very bright, the luminosity is in the same order as those from the X-ray radiation.

For the LMXB the dominating emission mechanisms are slightly different. As the magnetic fields are not strong enough matter gets accumulated over larger parts of the NS surface for some time until a nuclear burning flash may ignite, giving rise to X-ray bursts.
Any optical/UV emission of the late type companion star in a LMXB is too weak. It will be outshone by optical and UV light generated by reprocessing of the X-ray photons. This happens when X-rays, produced at the compact object, get intercepted by the accretion disk and the star. After the absorption of the X-ray photons by hydrogen and helium atoms a subsequent emission process will be initiated during which optical and UV photons are produced.

The flux variations observed in different ranges of the XRB spectrum, if periodical or burst-like, are the crucial measurements to associate an astronomical object with a rotating binary system and provides indications of the nature and mass of the compact object and the mechanisms that lead to photon emission. Further details and more informations about the emission processes inside a XRB can be found in [Trümper *et al.* (2008), Israel *et al.* (2001)].

Transient gamma-ray emission

While the emission of X-rays is a fundamental fact of all XRBs, the emission of gamma rays, and especially VHE gamma rays, was measured only for a tiny fraction of all XRBs. Today there is only a handful of binaries detected by one of the IACTs HESS, MAGIC or VERITAS which cover the spectrum above 100 GeV. Some of them are XRBs in which accretion feeds relativistic radio jets and powers the non-thermal emission (i.e., *microquasars*). In another scenario the wind of a young pulsar provides the necessary energy instead of accretion. Although the power mechanism in these systems is different (accretion vs pulsar wind), all of them are radio, X-ray and gamma-ray emitters, and belong to the class of HMXBs. The high-mass bright companion (O or B) star will then deliver the seed photons for IC scattering and the target nuclei for hadronic interactions [Paredes (2011)]. A visualization of the different models of gamma-ray emitting binaries is shown in Fig. 3.5 which is taken from [Mirabel (2012)]

A *microquasar* is a XRB which launches and collimates relativistic jets. The compact object can be a neutron star or a black hole. The important fact is, that there is no wind streaming away from the compact object and an accretion disk can form. An accretion disk is supposed to be a necessary ingredient to build a relativistic jet. Old neutron stars with a weak magnetic field and black holes fulfill that criterion. Because this phenomena is, on a much smaller scale, similar to that seen in quasars, these type of XRBs are called microquasar [Mirabel (2010)].
The spectrum of a microquasar is usually very broad. It ranges from radio to X-ray emission and in some cases they are expected to even emit VHE gamma-rays. The different parts of the spectrum have different spatial origins inside the microquasar. The donor star, for example, can emit thermal radiation from the infrared to the ultraviolet while the hot accretion disk produces thermal soft X-rays. It is also expected that there is a hot plasma surrounding the compact object very closely, the so-called *corona*, which is responsible for the hard X-rays and soft gamma rays generated by the Comptonization of soft disk photons to higher energies [V. Bosch-Ramon *et al.* (2006)]. The jet is usually responsible for synchrotron radio emission but there are also models claiming that the jet can produce the high-energy emission observed in some of the microquasars, like Cygnus X-1 (VHE detection needs to be confirmed) and Cygnus X-3 (no detection in VHE, just in HE)[Dubus (2013)]
One of these models is based on a freely expanding magnetized jet, whose internal energy is dominated by a cold proton plasma extracted from the accretion disk. Due to velocity variations in the ejected matter internal shocks form all along the jet and effectively accelerate the electrons inside the jet up to relativistic speeds. Besides synchrotron radiation and Bremsstrahlung the electrons will also lose energy by IC scattering of the ambient radiation fields provided by the star, the disk and the corona [V. Bosch-Ramon *et al.* (2006)]. Another possible particle interaction is a proton-proton collision of a relativistic jet proton with a proton from the stellar wind. This reaction can produce a neutral pion which decays into two gamma-rays [Romero *et al.* (2007)]. Both mechanism will deliver photon energies up to the TeV range.

The other XRB scenario able to produce VHE gamma-rays requires a pulsar wind streaming away from the compact object and colliding with the stellar wind of the high-mass companion. Hence, these XRBs build a subclass of HMXBs with a pulsar as compact object. Currently there are five sources with measured VHE emission that possibly belong to this class of objects: PSR B1259-63, LS 5039, LS I +61 303, HESS J0632+057 and 1FGL J1018.6-5856 [Dubus (2013)] However, only the compact object of PSR B1259-63 has been firmly identified as a pulsar, while the natures of the compact objects in the other systems have not yet been unambiguously determined.
Pulsars are fast rotating young neutron stars with a large magnetic dipole fields that are inclined with respect to the rotation axis. Due to large electric fields at the polar caps charged particles will be accelerated and move along the magnetic field lines. The corotating field lines from the polar caps intersecting with the light cylinder and are not closed. Charged particles moving along those field lines will drift away from the pulsar and escape its magnetosphere
When this pulsar wind collides with the strong stellar wind from the massive com-

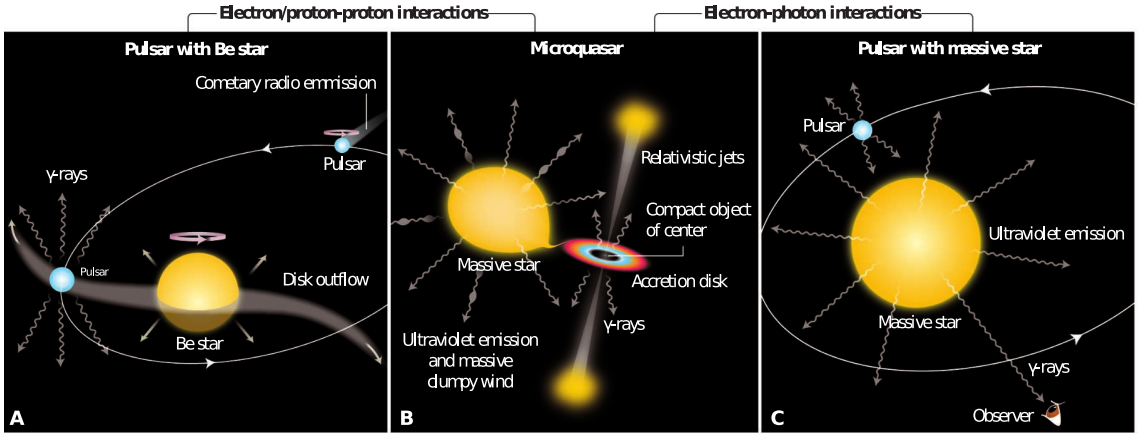

Fig. 3.5: *Types of possible gamma-ray emitting binaries: (A) Pulsar wind collides with the disk or envelope of a Be star and generates shock front. Accelerated particles at shock produce VHE emission by IC scattering of photons from Be star or by proton-proton interactions (e.g., PSR B1259-63 and LS I +61 303). (B) Microquasars with relativistic jets that are able to up-scatter photons from accretion disk, corona or companion star by IC scattering. (C) Same as (A) but pulsar wind collides with stellar wind from massive star. Up-scattering by IC is most effective when it happens head-on (e.g., LS 5039 and 1FGL J1018.6-5856) [Mirabel (2012)].*

panion star shock fronts will form. Depending on the momentum ratio of the two colliding winds the shock fronts can have different shapes. If the stellar wind is dominant, the termination shock of the pulsar wind will warp around the pulsar forming a comet-like shape that can be measured as elongated radio emission at the XRBs.
Inside the shocks charged particles are accelerated either by Fermi acceleration, if the magnetic field is small inside the shock, or by magnetic reconnection (plus additional "Fermi-like" acceleration). Both mechanisms lead to a power law distribution of the relativistic particle energies. The charged particles will lose their energy by synchrotron radiation and by IC scattering. UV photons inside the photon field around the massive companion or especially inside the equatorial disk of a Be star serving as seed photons and get up-scattered to TeV energies [Dubus (2013)].

Both types of gamma-ray emitting XRBs depend on the ambient photon (or proton) field and so the orientation of the binary with respect to the observer is very crucial and explains measured variability in the scale of orbital periods. Besides that, it is also know that the X-ray spectrum of microquasars switches between different states (low/hard $\leftrightarrow$ high/soft) on timescales in the order of minutes [Mirabel *et al.* (1998)]. If and how VHE gamma-ray emission is correlated to that sudden change in X-rays can only be measured if IACTs improve their significance on short time variability and especially their detection of short time flares.
In case of pulsar-wind binaries clumpy winds from the companion star can be a potential source of non periodic short time variability. Due to the interaction of clumps with the pulsar-wind, the dominant radiative loss mechanism at the shock front can vary between synchrotron radiation or IC scattering. Hence, also the luminosity of the VHE radiation will vary according to the duration of clump-wind

interaction, which can be in the order of minutes to hours [Bosch-Ramon (2013)]. Investigations of this phenomenon will then also require an improvement of the short time significance of IACTs.

3.2.2 Active Galactic Nuclei

An *Active Galactic Nuclei (AGN)* is a compact region around a supermassive black hole (SMBH) at the centre of a galaxy located at large distances. The average redshift of an AGN is $z = 1$ - 3 but even redshifts above 7 have been observed. Due to their very high luminosity (10^{45} to 10^{48} erg/s) over almost all of the electromagnetic spectrum, they can still be observed at earth which made them ideal objects to probe the evolution and formation of galaxies in the Universe [Krawczynski *et al.* (2013)], [Beckmann *et al.* (2013)b]. Besides these studies it is as well of great interest to understand their structure and the mechanisms that enables them to radiate away such large amounts of energy. Determining the spectrum and the variability of AGN in the VHE range is one part in the process of improving the theoretical model of these objects and of the universe in general.

General properties and model

The current believe is that there is an accretion disk of matter spiraling towards the SMBH ($10^4 - 10^{10} M_\odot$) in the center of an AGN. It is supposed that the AGN and its host galaxy have been formed in a merger of gas-rich galaxies which stimulated the mass accretion process inside the center region of the newly formed galaxy [Beckmann *et al.* (2013)b, Hopkins *et al.* (2006)].
In about 10% of the cases energetic particle beams are emitted along the rotation axis of the black hole. AGN with these well collimated radio jets, powered by the accretion flow, belong to the class of so-called *radio-loud AGN*, while those ones without jet are called *radio-quiet AGN* [Sol *et al.* (2013)]. Separating AGN by their radio emission is just a first step in the classification of the large variety of observational characteristics. Today it is assumed that the various AGN sub-classes are connected to each other and that the different observed characteristics can be attributed according to the different viewing angle θ, the different power of the central engine and the fact wether a jet is produced or not (see Fig. 3.6). In the top half of the circle all sub-classes that belong to the radio-loud AGN can be subdivided into two categories: *Fanarof-Riley Galaxy type 1 - FR1* and *Fanarof-Riley Galaxy type 2 - FR2*. FR1 are best known for their distorted, not well collimated, jets that appear disrupted and two-sided. Hence they must emit subsonic jets. FR2, however, are supposed to house powerful supersonic jets that appear smooth, un-distorted and as one-sided [Urry *et al.* (1995)].

Now, the different parts of the AGN model in Fig. 3.6 and their emission characteristics are briefly described but the explanation of all different sub-classes is avoided. Detailed information on those, and on AGN in general, can be found in textbooks like [Beckmann *et al.* (2013)a] and [Rosswog *et al.* (2007)].
The SMBH with a typical Schwarzschild radius of $\sim 10^{-4}$ pc (for $M = 10^9 M_\odot$) in the center of an AGN is surrounded by an optical thick *accretion disk* (~ 0.01

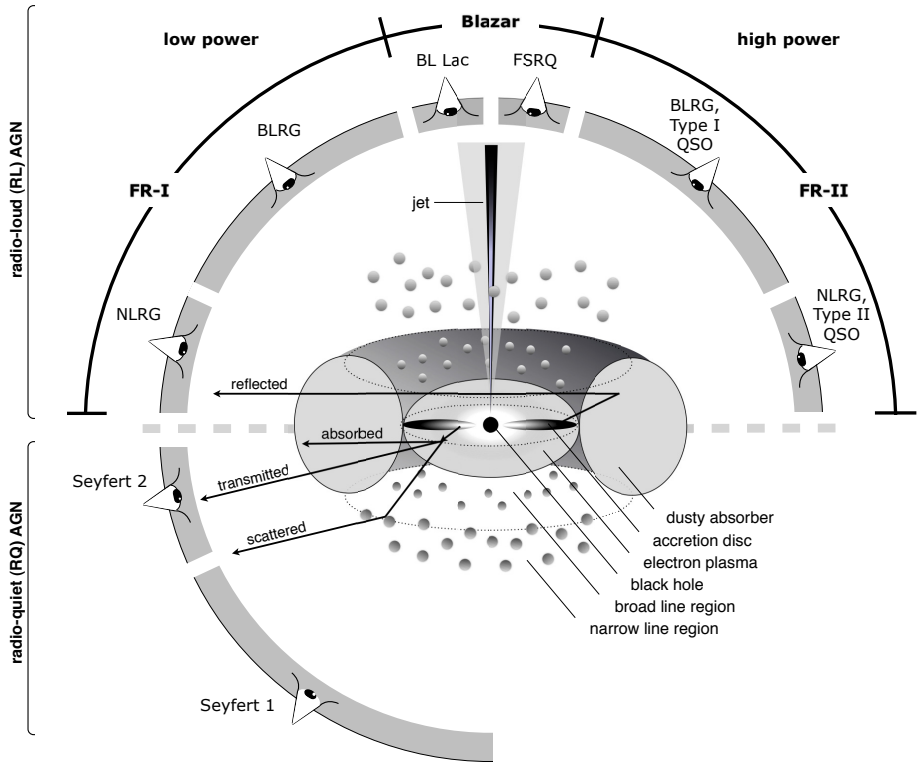

Fig. 3.6: *Schematic representation of the different observed AGN classes taken from [Beckmann et al. (2013)a]. It shows their dependance on the viewing angle, on the fact whether or not the AGN produces a significant jet and on how powerful the central engine is. In general it is thought that the radio-loud AGN also emit a jet in the opposite direction, which is just not drawn here, in favor of having a representation of the radio-quite sub-classes in the bottom half of the same picture as well.*

pc) which glows brightly at ultraviolet and perhaps soft X-ray wavelengths due to viscous or turbulent processes that heat up the disk. Above and below the disk eventually a *corona* of hot electron plasma is formed that is able to produce hard X-ray emission by the Comptonization of photons from accretion disk. Further away, but still close to the disk and the black hole (at $\sim$ 1 pc) one supposes to find the *broad-line region (BLR)*. It contains rapidly moving gas clouds that produce strong optical and ultraviolet emission lines, stimulated by photons from the central region. As the clouds permanently change their direction (with respect to the observer) the emission lines are broadened by the Doppler effect. A thick *dusty torus* (inner radius $\sim$ 10 pc), filled with cold gas, obscures the BLR, the corona and the accretion disk when the AGN is seen from the side. Especially the optical and ultraviolet radiation gets absorbed. The narrow emission lines, however, are produced in much slower clouds further away from the central source ($\sim$ 1000 pc). These *narrow-line regions (NLR)* are located beyond the torus which made them the dominant emission regions for observations at large θ. In case of radio-loud AGN there will be an additional relativistic outflow of energetic particles along the poles of the disk or torus. Depending on the matter distribution of the host galaxy (or galaxy cluster) those collimated *radio-emitting jets* (extending to about 10^6 pc) can interact with material which leads to shock fronts at and large radio lobes at both ends of the jet.

VHE Gamma ray emission and variability

When discussing the emission of VHE gamma rays we have to concentrate on radio-loud AGN with small θ between the jet and the line-of-sight. According to the unified model these AGN belong to the *blazar* class which can be subdivided into *flat spectrum radio quasars (FSRQ)* and *BL Lacertae objects (BL Lacs)*. The sample of AGN detected at VHE by the middle of 2013 includes 49 published sources, spread in redshifts from z = 0.0018 to z = 0.536, with 45 blazars and four Fanaroff-Riley type 1 radio galaxies [Sol *et al.* (2013)]. The FR1s are supposed to have θ-values larger but still close to those ones of blazars. This why they are called *misaligned BL Lac* [Aleksić *et al.* (2013)].
The most prominent observational features of a blazar are its rapid variability (down to minute time scale), its luminous, non-thermal, broadband (from radio to TeV γ-rays) continuum emission and the apparent *superluminal motions* of radio components in its jets [Sol *et al.* (2013)]. The phenomenon of superluminal motion, which is observed typically at radio wavelengths, occurs when the photon emitting sources move relativistically and almost directly towards the observer (= small θ). Hence, the time interval separating any two events in the observer's frame is strongly reduced which gives the impression that the apparent transversal motion of the sources is faster than light. All the observational features, mentioned above, indicate that the non-thermal continuum emission of blazars is produced in $\lesssim$1 light day sized emission regions, propagating relativistically with velocity $\beta_\Gamma c$ along a jet whose direction is very close to our line of sight. The Doppler factor $D \equiv [\Gamma(1-\beta_\Gamma \cos\theta)]^{-1}$, which has then to be taken into account, will affect the observed energy flux $F_{\rm obs}$, frequency $\nu_{\rm obs}$ and variability time scale $\Delta t_{\rm obs}$ as can be seen in the following relations [Boettcher (2012)]:

$$F_{\rm obs} = D^3 F_{\rm em} \tag{3.23}$$

$$\nu_{\rm obs} \propto D\nu_{\rm em} \tag{3.24}$$

$$\Delta t_{\rm obs} \propto D^{-1}\Delta t_{\rm em} \tag{3.25}$$

The luminosity will then be boosted by a factor of D^4 which explains the domination of the non-thermal radiation of the jet over the emission of the other parts (e.g. disk, corona, host galaxy).

A generic spectral energy distribution (SED) of a blazar will have a double-bumped structure as can be seen in the example Fig. 3.7. The low-energy component typically ranges from radio to UV/X-rays, while the second, high-energy component peaks between X-rays and gamma rays.

In the most common models (see [Boettcher (2007)], [Boettcher (2012)] and [Sol *et al.* (2013)]), it is expected that the first bump is produced by synchrotron radiation of ultrarelativistic electrons, injected instantaneously into a spherical emitting volume (a plasma blob) which moves along the jet at relativistic speeds. The mechanism that ejects the plasma and the process that accelerates the particles inside the blob are both still under investigation but it is assumed that shock acceleration plays an important role. This is why in the simplest models, the underlying lepton (electrons and/or positrons) distribution is ad-hoc pre-specified, either as a single

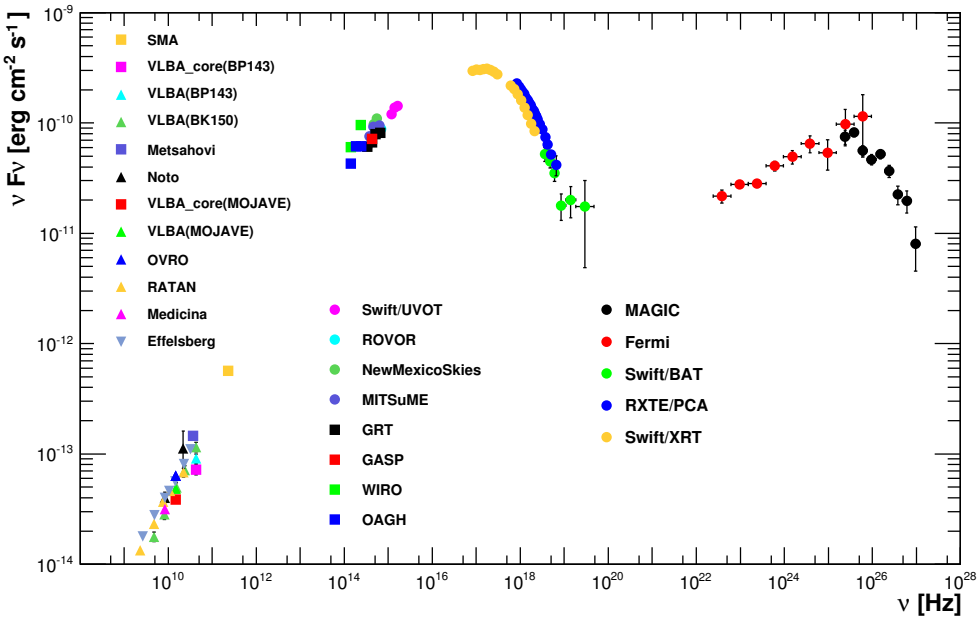

Fig. 3.7: *Spectral energy distribution of Mrk 421 during multi-wavelength campaigns with the participating instruments indicated in the figure [Abdo et al. (2011), Fig.8]. On can clearly see the two-bump structure, that is typical for blazars.*

or broken power-law with a low- and high-energy cut-off.
The second bump of the SED can be described within these models in two different ways. In *leptonic models* the high-energy component arises from inverse Compton scattering of the soft photons off the same ultrarelativistic electrons which are producing the synchrotron emission. Both, the synchrotron photons produced within the jet (*Synchrotron Self-Compton (SSC)* model) and the external photons (*External Compton (EC)* model) can serve as target photons for Compton scattering. In both cases, it is the same particle population within the jet that is responsible for the non-thermal emission. Therefore, a correlation between X-ray and VHE gamma-ray variability would support a SSC scenario. On the other hand, one-zone models are not favored if a hard spectra is observed in VHE because of the model limitation due to the Klein-Nishina regime.
In *hadronic models* the gamma-ray emission in the second bump is explained by synchrotron emission of charged particles, produced in pair cascades that are initiated by the interaction of ultra-relativistic protons with the matter and photons inside the jet. Also the direct proton-synchrotron emission has to be taken into account as potential gamma ray source. In those scenarios large magnetic fields of several tens of Gauss (much higher than in leptonic models) are required inside the moving plasma blob to accelerate the protons to the necessary ultra-relativistic energies ($E_{\mathrm{p,max}} \geqslant 10^{19}$ eV).
Those two models (leptonic and hadronic) just represent the two extreme cases. In a realistic model one has to take into account contributions from both effects. For further details and information about those models and even more complex ones please read [Boettcher (2012)].

It is well known that blazars are far from being steady sources. They exhibit strong flares in all frequency bands. Flux variability of blazars has been detected on all time scales from years, months, and days. Most rapid variability in the VHE regime has been observed at PKS 1222+216 [Tavecchio *et al.* (2011)], at BL Lac [Arlen *et al.* (2013)], Mrk421 [Galante (2011)], at Mrk 501 [Albert *et al.* (2007)] and at PKS 2155-304 [Aharonian (2007)], which exhibit flux variations down to timescales of several minutes.
Further investigations of PKS 2155-304 by [Biteau *et al.* (2011)] show that the power spectral density (PSD) of the outburst is well described by a power law $P_\nu \propto \nu^{-2}$ up to a maximum frequency $\nu_{\max}$, above which the spectrum is dominated by the measurement uncertainty power. Under the assumption that the PSD is a continuous power law, even for frequencies above $\nu_{\max}$, an inverse Fourier transformation of this power law extension was calculated and used in combination with the existing light curve to figure out which substructures in the temporal space ($<$ 1 min scale) had been missed due to the limited sensitivity of the detector.
Such short flux variations pose severe problems to those simple models explained above. For example, the size of the causally connected emission region (blob) would have to be much smaller than expected to induce such short time variability. Short rise/decay times of a flux change constrain the size of its possible origin by causality arguments: $R_{\rm blob} \lesssim ct_{\rm rise}D/(1+z)$. The measured variability time scales are also much shorter than the cooling times of the relativistic particles in those models, especially in the hadronic case. Due to those recent observations of minute scale variability in VHE blazars, it is necessary to extend and improve the simple models that have been working so far [Boettcher (2012), Sol *et al.* (2013)]. Possible extensions to the existing models could be small subregions within a jet (jets-in-jet) [Giannios *et al.* (2009)], stratified structures (compact region moving faster than the rest of the jet) [Boutelier *et al.* (2008)], the recollimation of the jet [Bromberg *et al.* (2009)] or its deceleration [Levinson (2007)].

By measuring the exact duration of a VHE flare and the delay time with respect to a potential correlated flare in the X-ray regime, one is able to constrain the set of models (and their parameter space) that are currently under development. In case of low VHE rates it is difficult to measure flux changes in the order of few minutes with IACTs. Particularly the exact rise and decay times of a short flare would be very interesting. It is therefore necessary to improve current statistical methods used in in TeV astronomy.

3.2.3 Gamma Ray Bursts

Gamma-Ray Bursts (GRBs) are the most luminous sources in the Universe, apart from the Big Bang, and their angular distribution on the sky is completely isotropic. Detecting their short and intense bursts of non-thermal radiation, emitted at cosmological distances, allows us to probe the evolution of stars in the early Universe at high redshift and to test several aspects of the latest theoretical models in cosmology.

Generic characteristics and origin

GRBs are able to release 10^{52} - 10^{54} erg of isotropic-equivalent energy during a brief period of 0.01-1000 s [Inoue *et al.* (2013)]. Over this relatively short timescale they emit a spectrum at gamma-ray energies (keV - MeV) that is fit well by the so-called *Band function* [Band *et al.* (1993)]. This function can be described by two power-laws smoothly joined by an exponential at an energy of $E_\mathrm{p} \approx 0.1$ - 1 MeV. E_p represents the peak energy, because most energy is emitted in this part of the spectrum (see Fig. 3.8,b).

$$N(E) = \begin{cases} N_0 \left(\frac{E}{E_\mathrm{ref}}\right)^{\alpha} \mathrm{e}^{-E/E_0} & \text{if: } (\alpha-\beta)E_0 \geqslant E \\ N_1 \left(\frac{E}{E_\mathrm{ref}}\right)^{\beta} & \text{if: } (\alpha-\beta)E_0 \leqslant E \end{cases} \qquad (3.26)$$

$$\text{with: } E_0 = E_\mathrm{p}/(\alpha+2).$$

These erratic, gamma-ray (or hard X-ray) prompt emission phase is accompanied by afterglows that span the radio to X-ray bands and gradually decay over hours to days or more while they are softening from x-rays to optical to radio. A light curve of a typical GRB with its prompt and afterglow phase can be seen in Fig. 3.8,a.

Since 1991 there exist satellite observatories, covering the energy range from keV to GeV, dedicated to search for GRBs due to their wide field of view. Today the number of detected GRBs is above 5000 [Bloom (2011)]. The detection rate of GRBs with the current observatories like *Fermi* (gamma ray regime; low angular resolution) and *Swift* (X-ray regime; high angular resolution; follows GRB position) is $\sim$ 160/year and $\sim$ 90/year respectively [von Kienlin *et al.* (2014), Sakamoto *et al.* (2011)]. A more detailed description of both instruments is given in subsection 6.3.1. Follow up observations of GRBs by optical telescopes, triggered by satellite experiments

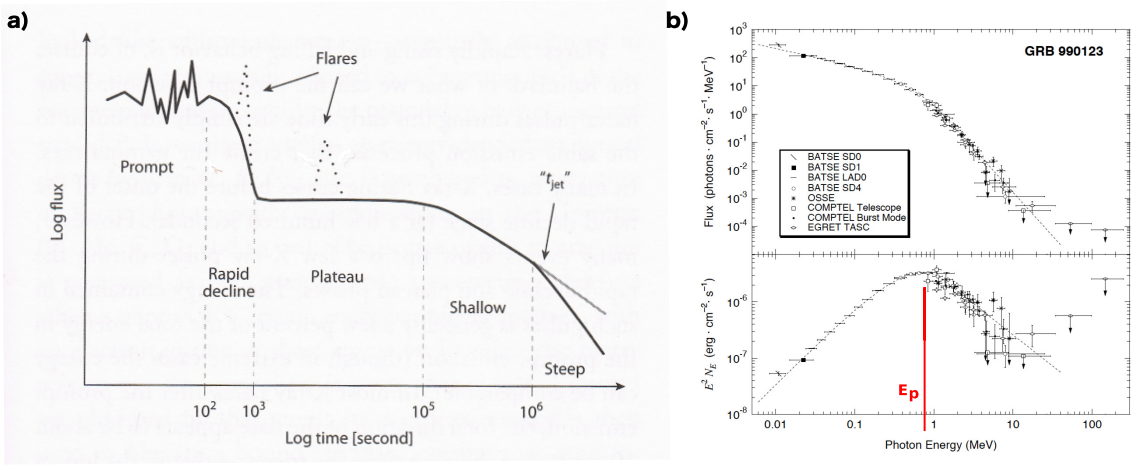

Fig. 3.8: a) *Canonical X-ray light curve showing the temporal evolution of the flux after the GRB trigger time. The afterglow phase starts in this example at ~100 seconds. There are many variations on this general picture. Especially the flares don't have to occur in every GRB. Adapted from [Bloom (2011)].*
b) *Example of a GRB's high energy spectrum shown both as photon counts N_E and in $E^2 N_\mathrm{E}$ units, where E is the energy of detected photons. The quantity $E^2 N_\mathrm{E}$ tells us the amount of energy emitted in certain energy band. Adapted from [Briggs et al. (1999)]*

with high angular resolutions, made it possible to measure a redshift for some of the GRBs. The mean value of the redshift distribution is around $z = 2.5$ (for all Swift detections) [Sakamoto *et al.* (2011)] but there are also extreme GRBs detected with a redshift of $z = 9.4$ [Cucchiara *et al.* (2011)].
Measurements of the duration T_{90} of the prompt emission also revealed that one can divide GRBs into two groups: short ($T_{90} < 2$s) and long ($T_{90} > 2$s) GRBs. T_{90} is defined as the time over which the central 90% of the counts (between 10 and 500 keV) above background from a GRB are detected. In general the properties of GRBs belonging to one group are systematically different to those from GRBs of the other group which indicates two different formation scenarios.
Due to the energies and the short durations a natural candidate for GRB progenitors are either corecollaps supernovae of a Wolf-Rayet star (long GRBs) or the merger of two compact objects, like neutron stars or a black holes, trapped in a binary system (short GRBs). In both scenarios, it is expected that a black hole forms, which is surrounded by a temporary debris torus whose accretion can provide a sudden release of gravitational energy, sufficient to power a burst. It is supposed that a small fraction of this energy is converted into electromagnetic radiation, through the dissipation of the kinetic energy of a collimated relativistic outflow, a *fireball* with bulk Lorentz factors of $\Gamma \gtrsim 300$, expanding out from the central black hole [Ghisellini (2010), Meszaros (2006), Meszaros (2013)]. The fireball model and its emission mechanisms will be described in the following section.

GRB standard model - "Fireball model"

The development of a canonical GRB model started with the advent of the *compactness problem*. It arises due to the necessity of combining the three main characteristics of a GRB: strong emission of high energy photons , short-time variability and non-thermal spectrum. The short variability timescales imply that the emission region must be very small due to causality: $D \leqslant c \cdot \Delta t$. Taking into account the very high luminosity emitted from this compact region and the fact that the energy of the emitted photons exceeds the pair production threshold, it should lead to an opaque plasma from which no energetic non-thermal radiation is expected [Piran (1999), Vedrenne *et al.* (2009)]. As such a scenario contradicts the observations, a relativistic expansion at high Lorentz factors Γ along the line-of-sight of an observer had been added to the model. The relativistic Doppler effect and the Lorentz transformation will then lead to a much larger (less denser) emission region and a lower photon energy at the plasma than expected from measurements. So in the comoving frame the plasma is not optical thick and photons can be emitted. The optical depth of the plasma is in fact Γ^6 times smaller than in the observer frame [Vedrenne *et al.* (2009), Gomboc (2012)].

A necessary condition for a relativistic expansion is a high energy/mass ratio ($\eta = E_0/M_0c^2 \gg 1$) at the central object where M_0 represents the baryon load. The energy E_0, which is emitted by the central engine, creates a very hot plasma consisting of $e^{\pm}$, photons and baryons inside a compact volume with $r = R_0$. Since this so-called *fireball* is initially optically thick, it undergoes adiabatic expansion and cools.
At the beginning of the expansion the Lorentz factor of each particle is $\gamma' \sim \eta$ while

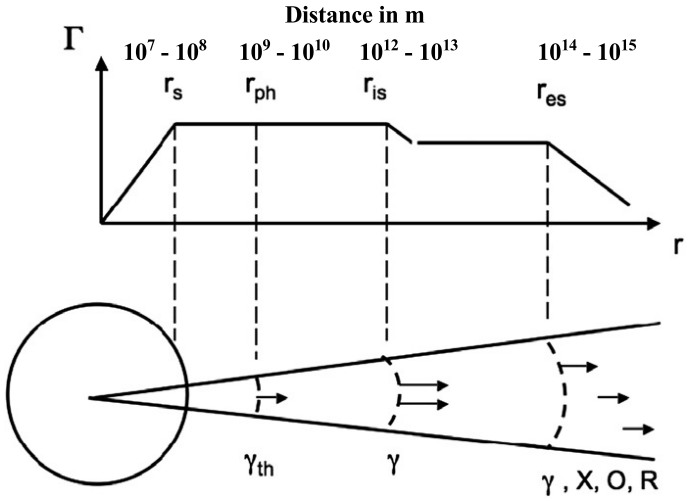

Fig. 3.9: *Schematic behavior of the bulk Lorentz factor* Γ *together with the locations of the of the saturation radius* $r_{\rm s}$*, photospheric radius* $r_{\rm ph}$*, internal shock (or magnetic dissipation) radius* $r_{\rm is}$ *and external shock* $r_{\rm es}$*. The photosphere produces thermal* γ*-rays, the internal shock/dissipation region produces the non-thermal* γ*-rays and the external shock region produces the afterglow. Adapted from [Vedrenne et al. (2009)]*

the direction of each velocity vector is completely isotropic. Therefore the bulk Lorentz factor of the fireball is $\Gamma \sim 1$. During the adiabatic expansion the velocity vectors are more and more aligned with the radial vector the further the particles have moved away from their initial position. Hence, they form an expanding shell whose radial bulk Lorenz factor increases proportional to the radius ($\Gamma \propto r$) while the comoving Lorentz factors γ' decrease anti-proportional. The bulk acceleration stops at a radius $R_{\rm s}$ of $\sim 10^7$ - 10^8 m when the Lorentz factor has saturated ($\Gamma_{\rm max} \sim \eta$ and $\gamma' \sim 1$). Beyond that radius the shell coasts with a constant Lorentz factor until it sweeps up enough interstellar medium and begins to decelerate.

During the constant coasting phase the ejected plasma keeps on cooling until its optical depth becomes 1. At this radius $R_{\rm ph}$ ($\sim 10^9$ - 10^{10} m) the emission of thermal photons is expected. If the initial central engine produces a fast moving ejecta (particle wind), rather than an explosive fireball, it is supposed that time-varying outflow leads to several small shells with different Γ. Every time a fast one overtakes a slower shell transient collisionless shocks will appear which are able to produce the erratic non-thermal prompt emission. Therefore the measured variability during the prompt phase reflects the activity of the central engine. The emission has to happen after the fireball has become optical thin because high-energy photons are observed. A typical region for those *internal shocks* begins at a radius $R_{\rm is}$ of $\sim 10^{12}$ - 10^{13} m.
The end of the GRB evolution marks the appearance of the slowly decaying (up to days), smooth afterglow phase. The main fraction of the injected energy E_0 is lost during this process. It is caused by the deceleration of the ejecta when it sweeps up enough of the surrounding material, which usually happens at $R_{\rm es} \sim 10^{14}$ - 10^{15} m. In general two *external shocks* form: the forward shock and the revers shock which propagates back into the relativistic outflow. Both shocks produce electro-

magnetic radiation at lower frequencies compared to the prompt emission. While the relativistic forward shock is still energetic enough to emit X-ray photons the much weaker reverse shock produces typically optical photons. In Fig. 3.9 one can see an example of a typical fireball model with its different emission regions and the corresponding bulk Lorentz factors. More detailed information can be found in [Vedrenne *et al.* (2009), Piran (1999), Meszaros (2006)]

As this model was first intended to describe a spherical expansion, one can also use it, if the outflow is strongly collimated. In such a scenario, the emission is not isotropic. Hence, the initial energy, required to produce a certain luminosity, is much smaller than the one predicted by a model with isotropic emission. In some GRBs, the observed luminosity is so high that its initial energy would exceed the binding energy of the sun, if isotropic emission is assumed. Such a high energy is difficult to describe within models that suppose stellar mass progenitors. Therefore a jet scenario is favored. It would also increase the number of existing GRBs because all of them whose relativistic ejecta is not moving towards the earth can not be observed. An explanation for the emergence of collimated outflow could be a the accretion of material with angular momentum. Only matter along the rotation axis are not held back from immediate infall, which leads to a matter free funnel along which a subsequent fireball ejecta can expand [Vedrenne *et al.* (2009), Gomboc (2012)].

High and very high energy emission

The fireball model describes several occasions where non-thermal radiation is produced. The internal and external shocks accelerate electrons and protons to relativistic speeds which cool under the emission of synchrotron radiation and/or by inverse Compton scattering. Other possible acceleration mechanisms, besides the shocks, are magnetic reconnection and hydromagnetic turbulence [Rees *et al.* (1994)].
The non-thermal emission produced by such processes can contain high energetic photons detectable by *Fermi/LAT*. The *LAT (Large Area Telescope)* is an imaging high-energy gamma-ray telescope and the principal scientific instrument on the Fermi spacecraft. It covers the energy range from about 20 MeV to more than 300 GeV [Atwood *et al.* (2009)].

The measured GeV prompt emission can be described by a simple extrapolation of the Band function towards higher energies. In some cases, however, an additional hard power-law component is necessary to fit the data (see Fig. 3.10). It has also been measured that for some GRBs the GeV emission during the prompt phase is delayed (up to a few seconds) and longer lasting than the keV to MeV emission. In the right example of Fig. 3.10 one can see that the high-energy power-law component appears several seconds after the GRB trigger. Further it is visible that during high flux phase an additional exponential cut has to be introduced to describe the GeV data [Meszaros (2013)].
While this is an example of VHE emission during the prompt phase there exist also GRBs with GeV photons detected minutes to hours after the trigger during the afterglow phase [Fan *et al.* (2013)].

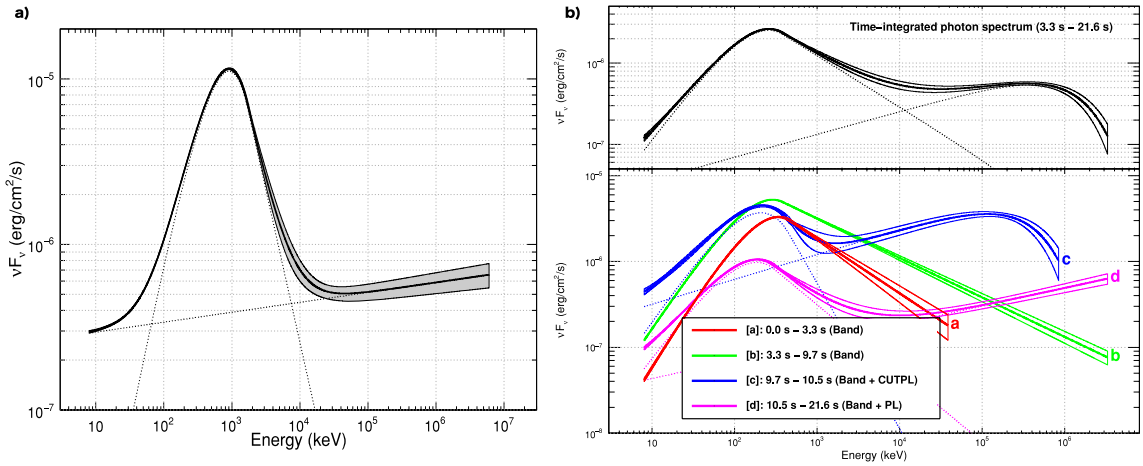

Fig. 3.10: a) *The joint Fermi-GBM-LAT unfolded νF_ν spectrum of GRB090902B showing the extra power-law component which is dominant at both high and low energies. Adapted from [Abdo et al. (2009)].*
b) *The integrated (top) and time-resolved (bottom) spectra showing the evolution of the power-law component during the prompt phase of the GRB 090926A. Adapted from [Ackermann et al. (2011)].*

Depending on the spectral characteristics and the temporal appearance of those high-energy (HE) emissions different models had been developed. In general it is assumed that inverse Compton (IC) scattering is responsible for the HE emission. The seed photons could come from the photosphere ($R_{\rm ph}$) or from the synchrotron emission at the shocks. The IC scattering of the photons can happen at the external or the internal shocks. For the long lasting HE emission in general IC scattering at the external shocks is favored. Rapid and large amplitude variability, however, would favor internal shocks or photospheric emission.
Besides the leptonic models there are also HE emission mechanisms possible that involve hadrons. This includes proton synchrotron emission or $p\gamma$ and pn collisions which lead to pions, including π^0, resulting in ultra-high energetic photons which cascade down to the GeV range by IC emission of secondary $e^{\pm}$ [Inoue *et al.* (2013), Meszaros (2006)].
A spectral cutoff could be the result of a huge optical depth to pair production ($\gamma\gamma \rightarrow e^- e^+$). But also a cooling break, a maximum energy cutoff of synchrotron emission or a Klein-Nishina break of inverse Compton emission could be the reason [Inoue *et al.* (2013)].
To describe the delayed onset of the GeV emission mentioned above two- or multiple zone models are favored, which typically involve an inner softer source whose photons are up-scattered by electrons in a different region further out [Meszaros (2013)].
So depending on the external medium and the origin of the central engine activity a large variety of spectral shapes and lightcurves are possible.

The highest photon energy from a GRB until now was measured at GRB 130427A (redshift = 0.34). Besides this energetic photon at 94 GeV in total 19 photons above 5 GeV have been measured by the Fermi/LAT [Fan *et al.* (2013)]. Extrapolating the

spectra of GRBs like this, leads to the expectation of numerous photons in the VHE range (up to several TeV). This depends of course on the model of the *extragalactic background light (EBL)* and the redshift of the GRB as VHE photons coming from cosmological distances are attenuated by pair production with EBL photons. Only if the number of VHE photons is high enough IACTs are able to detect the GRB. Unfortunately such a detection is still lacking. Reasons are the duty cycle, the small field of view and the slow slewing speed of IACTs. After a trigger signal is received from a satellite experiment that detected the GRB, it can take up to several minutes until the telescopes accurately pointing at the source. Of course this is only true for trigger signals arriving at dark, cloudless nights. During the day, or during bright moonlight no sensitive observations are possible with IACTs and one has to wait until the conditions are acceptable to start the GRB observation. However, if the VHE emission is produced in the afterglow, follow up observations are still reasonable after several hours [Inoue *et al.* (2013)].

Possible observation scenarios are the detection of VHE emission during the afterglow or during the prompt phase of a long GRB. The second case will be quite difficult as one has to reduce the duration between the GRB trigger and the start of the IACT observation to a minimum of $\sim$ 10 - 100 sec. It is not expected to detect more than one GRB per year during its prompt phase, even with the new generation of IACT instruments.
However, there are many physical aspects that can be tested by GRB observations in the VHE regime. For example, one is able to constrain the different parameters used in the GRB models, especially the limitation of the value for the bulk Lorentz factor is a very crucial point. Further one can test the different EBL models if the VHE photons come from a distant GRB ($z \gtrsim 1$). GRBs at cosmological distances are also ideal sources to test the *Lorentz invariance violation*. As this theory predicts an energy dependance of the speed of light, an observational delay between the different energy regimes of the GRB emission could be a hint that such a theory is true. Obviously on has to exclude any internal delays due to the emission mechanisms inside a GRB which will be the most difficult part [Inoue *et al.* (2013)].
Because the durations of GRB VHE emissions are very short, when comparing with flares of Blazars or other VHE emitting sources, it was not possible to make a significant detection with IACTs. This is due to the low numbers of signal photons which lead to a small sigma when the standard Li&Ma method is applied. In this work we will test different statistical methods which are sensitive to variability. Our approach is the detection of a GRB due to its fast variability and not due to the number of the observed photons. A positive side effect of one of these methods is the determination of the rise and fall time of the VHE flare from a GRB which provides valuable information of the temporal evolution of the VHE emission and helps to constrain the existing models.

Summary

As it was shown in the previous sections, there exist several source types (e.g. XRBs, GRBs and AGN) for which the occurrences of very short ($\sim$ minutes) flux variations in the VHE regime are expected or, at least, theoretically possible. The purpose of

this thesis is the search for such abrupt flux changes in the VHE data of AGN and GRBs, taken by VERITAS. Therefore it is necessary to improve the current analysis procedure by applying some advanced statistical methods, that are optimized for the detection of significant variations in the event rate. A detailed description of these methods and their application to Monte-Carlo simulations and VERITAS data are the topics of the following chapters.

Chapter 4

Statistical methods to detect transient gamma-ray sources

In this chapter I discuss advanced statistical methods regarding the evaluation of the probability that a detected γ-ray signal deviates from background expectations. Furthermore I compare them with the standard methods, currently used by VERITAS, which are also explained in the following sections. It is necessary to mention that the main feature of the advanced methods is the fact that the time is used as an additional input parameter.

4.1 Significance calculation in γ-ray experiments

Unfortunately even after gamma hadron separation the number of events in our signal region is still interspersed by so called gamma-like background events. Getting a significant detection of a γ-ray source observed with an IACT is a statistical effort due to the limited number of events. Here I describe three different formulas which are used in current analysis software of IACTs to calculate the significance S of an excess. We will see that only one of them provides a good approximation to the expected normal distribution of S even for small numbers.

Each of the three different calculation methods requires the same input parameters, which are the number of events in the ON region, the number of events in the OFF region and the α parameter. As we have seen in subsection 2.4.4 the ON region corresponds to our estimated signal region while the OFF region is an area in the sky where we expect just background events. The quantity α is the ratio of the on-source exposure and the off-source exposure which depends on the the chosen background estimation method (see subsection 2.4.4).
The estimated number of γ-ray like background events contained within the measured on-source counts are:

$$\hat{N}_{\mathrm{B}} = \alpha N_{\mathrm{off}} \quad .$$

Then the observed signal photons can be estimated as follows [Li *et al.* (1983)]:

$$\hat{N}_{\mathrm{S}} = N_{\mathrm{on}} - \hat{N}_{\mathrm{B}} = N_{\mathrm{on}} - \alpha N_{\mathrm{off}} \quad .$$

4.1.1 Standard deviation of signal

Let us start with a simple assumption of two individual Poisson processes when calculating the standard deviation σ of N_S. Because N_{on} and N_{off} are measured independently one can just add their variances and does not have to take into account the covariance:

$$\sigma^2(N_S) = \sigma^2(N_{on}) + \sigma^2(\alpha N_{off}) = \sigma^2(N_{on}) + \alpha^2\sigma^2(N_{off}) \tag{4.1}$$

$$\rightarrow \quad \sigma(N_S) = \sqrt{N_{on} + \alpha^2 N_{off}} \quad \text{with:} \quad \sigma^2(N_{on/off}) = N_{on/off} \tag{4.2}$$

This last condition is valid under the assumption that the on- and off-source counts follow a Poisson distribution with a true mean value $\lambda_{on/off}$ ($= \sigma^2_{on/off}$) that is equal to the measured values $N_{on/off}$.
Now, one can calculate the significance S as the ratio between N_S and $\sigma(N_S)$:

$$S = \frac{N_S}{\sigma(N_S)} = \frac{N_{on} - \alpha N_{off}}{\sqrt{N_{on} + \alpha^2 N_{off}}} \tag{4.3}$$

In the paper by Li and Ma [Li *et al.* (1983)], where an extensive Monte Carlo study was made to compare these different methods, one can see that this formula provides a good estimation for S but only if $\alpha \approx 1$.

To improve the evaluation of S it would be better to assume that there is just background in the data so that the measured N_{on} doesn't include any signal events. Estimating the probability that any observed excess is just compatible with background fluctuations should be the goal of a significance calculation. Under this assumption λ_{on} will be $\langle N_B \rangle$ and λ_{off} will be $\langle N_B \rangle / \alpha$. Equ. (4.1) can then be written as:

$$\sigma^2(N_S) = \sigma^2(N_{on}) + \alpha^2\sigma^2(N_{off}) = (1+\alpha)\langle N_B \rangle \tag{4.4}$$

$$\rightarrow \quad \sigma(N_S) = \sqrt{(1+\alpha)\langle N_B \rangle} = \sqrt{\alpha(N_{on} + N_{off})} \tag{4.5}$$

The last equation is true if one estimates $\langle N_B \rangle$ not only by using N_{off} but also by using N_{on}, taking into account the different exposures: $\langle N_B \rangle = \alpha(N_{on} + N_{off})/(1+\alpha)$
Finally one ends up with the following equation for S:

$$S = \frac{N_S}{\sigma(N_S)} = \frac{N_{on} - \alpha N_{off}}{\sqrt{\alpha(N_{on} + N_{off})}} \tag{4.6}$$

For $N_{on} \geqslant 10$ and $N_{off} \geqslant 10$ counts N_S is approximately normally distributed around 0, under the assumption of no signal. This leads to a normal distributed variable S whit a variance of one and a mean value of zero (see LiMa 1983 [Li *et al.* (1983)]).

4.1.2 Likelihood ratio method

Another method to estimate the significance is the usage of a hypothesis test. The idea is to compare the date (N_{on}, N_{off}) with two different hypothesis to figure out

which one fits better the data. These two hypothesis are usually described as the same likelihood function but with two different sets of parameters. In the present problem those parameters are the expectation values of the signal and the background counts: $\langle N_S \rangle$ and $\langle N_B \rangle$. Assuming no signal but just background data leads to the so called "null hypothesis" with the parameter values $\langle N_S \rangle_0 = 0$ and $\langle N_B \rangle_C$ is equal to a conditional maximum likelihood estimate, which is a value that leads to the highest possible probability of fitting the data under the condition of no signal counts: $\langle N_B \rangle_C = \alpha(N_{on} + N_{off})/(1+\alpha)$. One can now calculate the ratio between the likelihood of the null hypothesis and the maximized likelihood, whose parameters are not restricted by any conditions: $\langle N_S \rangle_{max} = N_S = N_{on} - \alpha N_{off}$ and $\langle N_B \rangle_{max} = N_B = \alpha N_{off}$ (see [Li *et al.* (1983)] for further details).

$$\begin{aligned}
\lambda = \frac{\mathcal{L}(N|\mu_0)}{\mathcal{L}(N|\mu_{max})} &= \frac{P\left[N_{on}, N_{off}|\langle N_S\rangle_0, \langle N_B\rangle_C\right]}{P\left[N_{on}, N_{off}|\langle N_S\rangle_{max}, \langle N_B\rangle_{max}\right]} \\
&= \frac{P\left[N_{on}|\langle N_{on}\rangle = \langle N_S\rangle_0 + \langle N_B\rangle_C\right] \cdot P\left[N_{off}|\langle N_{off}\rangle = \langle N_B\rangle_C/\alpha\right]}{P\left[N_{on}|\langle N_{on}\rangle = \langle N_S\rangle_{max} + \langle N_B\rangle_{max}\right] \cdot P\left[N_{off}|\langle N_{off}\rangle = \langle N_B\rangle_{max}/\alpha\right]} \\
&= \frac{P\left[N_{on}|\langle N_{on}\rangle = \frac{\alpha}{1+\alpha}(N_{on}+N_{off})\right] \cdot P\left[N_{off}|\langle N_{off}\rangle = \frac{1}{1+\alpha}(N_{on}+N_{off})\right]}{P\left[N_{on}|\langle N_{on}\rangle = N_{on}\right] \cdot P\left[N_{off}|\langle N_{off}\rangle = N_{off}\right]}
\end{aligned} \tag{4.7}$$

Under the assumption of a Poisson distribution, $P(k|\mu) = \frac{\mu^k}{k!}e^{-\mu}$, the result of this *maximum likelihood ratio* is:

$$\lambda = \frac{\mathcal{L}(N|\mu_0)}{\mathcal{L}(N|\mu_{max})} = \left[\frac{\alpha}{1+\alpha}\left(\frac{N_{on}+N_{off}}{N_{on}}\right)\right]^{N_{on}} \left[\frac{1}{1+\alpha}\left(\frac{N_{on}+N_{off}}{N_{off}}\right)\right]^{N_{off}} \tag{4.8}$$

According to *Wilk's theorem* (see [Wilks (1962)]) the variable $-2\ln\lambda$ follows a χ^2 distribution with r degrees of freedom, if the null hypothesis is true, whereas r corresponds to the number of parameters that are fixed during the null hypothesis. In the case described here $r = 1$ because one fixes only one parameter: $\langle N_S \rangle = 0$. The behavior of $-2\ln\lambda$ is equal to that of a squared normal variable. Therefore one can assume that the value $\sqrt{-2\ln\lambda}$ follows a standard normal distribution and that this value is a direct measurement for the significance S.

$$\begin{aligned}
S &= \sqrt{-2\ln\lambda} = \\
&= \sqrt{2}\left\{N_{on}\ln\left[\frac{1+\alpha}{\alpha}\left(\frac{N_{on}}{N_{on}+N_{off}}\right)\right] + N_{off}\ln\left[(1+\alpha)\left(\frac{N_{off}}{N_{on}+N_{off}}\right)\right]\right\}^{1/2}
\end{aligned} \tag{4.9}$$

It is clear from the previous calculations that λ cannot be negative. Hence, either an excess ($N_S > 0$) or a lack of signal ($N_S < 0$) is represented with a positiv value of S. For visualization reasons it is therefore useful to multiply S with -1 if $N_{on} < \alpha N_{off}$ and get negative significance values, as well. In the aforementioned Monte Carlo studies of Li and Ma it was shown that the last equation (Equ. (4.9)) provides the best approximation to a Gaussian probability distribution, which makes it easy to translate the significance value directly into a probability.

In the sections above I have shown several methods to calculate the significance of an excess under the assumption that there are just background events in the data. On

the basis of the outcome of these methods the decision is made whether to declare a detection of a signal or not. The usual convention is, that a signal is detected, if one measures a significance greater than five ($S \geqslant 5$). In this case one wants to present the value of N_S together with its error $\sigma(N_S)$. The calculation of the error was already described in Equ. (4.2).

4.2 Event times in significance calculation

In the methods presented in the previous sections the number of photons in the signal region (ON region) and the number of background photons, measured in dedicated sidebands (OFF region), are the necessary input parameters while the measured times of each single gamma-like event are completely ignored. In this section I will explain methods dedicated to detect variability during a period of measured single event times.

4.2.1 Motivation

The detection of gamma rays with a Cherenkov telescope array is a time consuming process due to the low rate of high-energetic photons and the large background fraction of gamma-like air showers. Depending on the source it can take up to several hours to accumulate enough statistics for a significant deviation from background. For the calculation of the significance we use the equations that had been explained in the previous sections (see Equ. 4.9). In case of a short flare these methods won't work very well if the analyzed data period is much longer than the time scale of the flare. Extending the duration of data taking will just increase the number of OFF events which will lead to a less pronounced signal excess. If the exact time of the flare is known a simple solution is to analyze just this specific time period. But what happens if one does not know the exact timing of the flare? One could split the data into arbitrary blocks, hoping to catch the flare exactly with one of these blocks, and analyze each of them separately. This procedure has the disadvantage of introducing trials if one changes the splitting several times in order to find the best block for the flare that leads to the largest deviation from background.
In this section I describe some existing statistical methods that take these trials into account. They improve the detection of short signals and help to discover variability in a data set. Instead of comparing the numbers of events from different regions in the skymap these methods make use of the time information of each single event. They are therefore not restricted to specific ON and OFF regions and work in the whole field-of-view.
Now, I concentrate on the description of the two different methods, which I applied to data sets with minute-scale flares measured by the VERITAS Cherenkov telescope system. The first was invented by J. Prahl [Prahl (1999)] and has already been used to measure variability in data from the HEGRA telescope system [Aharonian *et al.* (2004)] while the second, which was invented by J. D. Scargle [Scargle (1998), Scargle *et al.* (2013)], has never been applied to data from IACTs but to data from gamma-ray satellite experiments like *Fermi* instead.

4.2.2 The *exp-test*

In this section I explain in detail how the method of Prahl [Prahl (1999)], the so-called *exp-test*, is derived. I also highlight the advantages of this method compared to other variability analysis procedures. The focus of this thesis, is the analysis of temporal sequences of measured gamma-ray photons. But the method is not restricted to the time domain it can be used on spatial or frequency data as well.
Assuming an uniform temporal acceptance of the detector, the sequence of reconstructed events follows Poisson statistics if there is no variability in the data. This fact applies to both background events and events from a steady source. Therefore this case defines the null hypothesis in the framework of the described test on variability.

Distribution of time differences

One calls a monotone sequence of event times a *Poisson process*, if the numbers n of independent events per equally sized time interval are Poisson distributed with the same expectation value λ for all of these intervals. It is clear that λ is proportional to the size of the interval Δt. Together with a constant factor $1/C$, which can be interpreted as the event rate, λ can be write as: $\lambda = \Delta t/C$. However, for the exp-test it is not the number of events in an interval with fixed size that is important but the time difference between two consecutive events. To get from poisson distributed events inside an interval a distribution of time differences, one has to do the following:

$$P_\lambda(n) = \frac{\lambda^n}{n!}\mathrm{e}^{-\lambda} = \frac{(\Delta t/C)^n}{n!}\mathrm{e}^{-\Delta t/C} = P_{\Delta t/C}(n) \tag{4.10}$$

Fixing the value of n to zero one will get the probability that an interval with Δt contains no events. Now, one can calculate the joint probability that there is no event in the interval Δt and one event in the very short interval $\mathrm{d}\Delta t$ right after the first interval. This is exactly the probability of finding the time difference x inside a small range $[\Delta t, \Delta t + \mathrm{d}\Delta t]$. Due to the fact that the events are independent the joint probability is just a multiplication of two Poisson probabilities:

$$\begin{aligned} &P[\Delta t < x \leqslant \Delta t + \mathrm{d}\Delta t] = P_{\mathrm{joint}}[n_{\Delta t} = 0, n_{\mathrm{d}\Delta t} = 1] \\ &= P_{\Delta t/C}(0) \cdot P_{\mathrm{d}\Delta t/C}(1) \approx P_{\Delta t/C}(0) \cdot \big(1 - P_{\mathrm{d}\Delta t/C}(0)\big) \\ &= P_{\Delta t/C}(0) - P_{(\Delta t+\mathrm{d}\Delta t)/C}(0) \end{aligned} \tag{4.11}$$

The last step is only valid for the Poisson distribution at n=0 due to the fact that one has to multiply two single exponential functions without any pre-factors.

The remaining step will be the calculation of the probability density function (pdf) $f_C(\Delta t)$ of Δt:

$$f_C(\Delta t)\,\mathrm{d}\Delta t = P[\Delta t < x \leqslant \Delta t + \mathrm{d}\Delta t] \tag{4.12}$$

$$\begin{aligned} \Longrightarrow\ f_C(\Delta t) &= \frac{P_{\Delta t/C}(0) - P_{(\Delta t+\mathrm{d}\Delta t)/C}(0)}{\mathrm{d}\Delta t} = -\frac{\mathrm{d}\,P_{\Delta t/C}(0)}{\mathrm{d}\Delta t} \\ &= -\frac{\mathrm{d}\left(\mathrm{e}^{-\Delta t/C}\right)}{\mathrm{d}\Delta t} = \frac{1}{C}\cdot e^{-\Delta t/C} \end{aligned} \tag{4.13}$$

This is an *exponential distribution* of Δt with the true mean value C ($= \overline{\Delta t}$) and with an integral equal to one over $[0,\, \infty]$.

If a random sequence of event times follows a Poisson distribution with a constant rate of $1/C^*$, then the distribution of the discrete time intervals between consecutive events $\{\Delta T_i\}_{i=1\ldots N}$ is described by $f_{C^*}(\Delta t)$. Here, the true mean value C got replaced by the actually obtained mean value $C^* = \overline{\Delta T}$. The pdf $F(\Delta t)$ of a random probe with discrete event times will look like this:

$$F(\Delta t) := \frac{1}{N}\sum_{i=0}^{N} \delta(\Delta t - \Delta T_i) \tag{4.14}$$

Comparison of the discrete event distribution with the ideal distribution

The goal is now to compare this distribution with the ideal distribution $f_{C^*}(\Delta t)$. Like the well known distribution tests from Kolmogorov and Smirnov, Prahl developed its own test which is especially sensitive to excesses of the ΔT_i and takes into account the constant mean value C^*. This way it will only depend on variability in the data and not on the magnitude of its overall rate.
Prahl starts with the comparison of the 0. and 1. moment of $f_{C^*}(\Delta t)$ and $F(\Delta t)$:

$$\int_0^\infty f_{C^*}(\Delta t)\,\mathrm{d}\Delta t \quad = \int_0^\infty F(\Delta t)\,\mathrm{d}\Delta t \qquad = 1 \tag{4.15}$$

$$\int_0^\infty \Delta t \cdot f_{C^*}(\Delta t)\,\mathrm{d}\Delta t \ = \int_0^\infty \Delta t \cdot F(\Delta t)\,\mathrm{d}\Delta t \quad = C^* \tag{4.16}$$

It follows that:

$$\int_0^\infty \left(1 - \frac{\Delta t}{C^*}\right)\cdot f_{C^*}(\Delta t)\,\mathrm{d}\Delta t \ = \int_0^\infty \left(1 - \frac{\Delta t}{C^*}\right)\cdot F(\Delta t)\,\mathrm{d}\Delta t \ = \ 0 \tag{4.17}$$

One can define a new function $H(x)$

$$H(x) := \int_0^x \left(1 - \frac{\Delta t}{C^*}\right)\cdot f_{C^*}(\Delta t)\,\mathrm{d}\Delta t \tag{4.18}$$

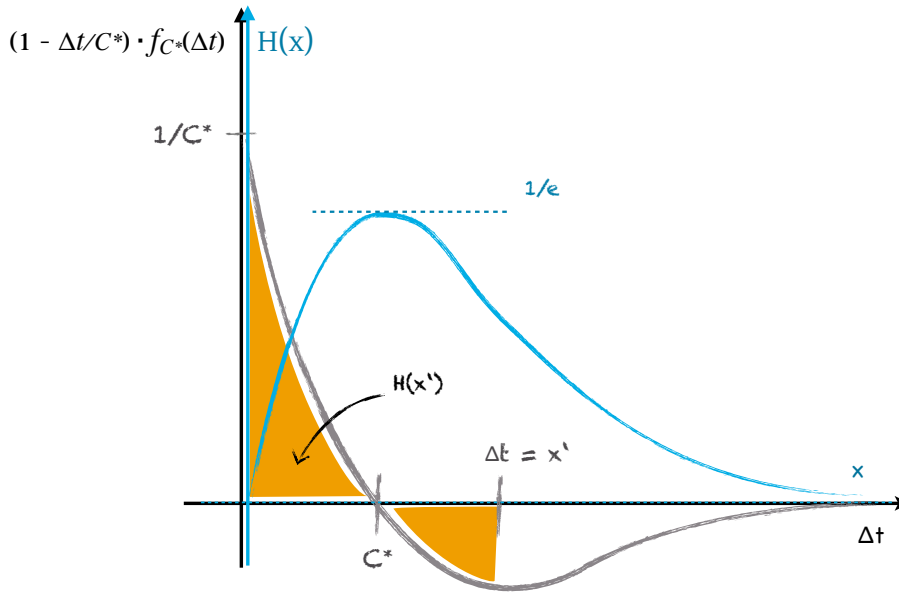

Fig. 4.1: *A sketch of the theoretical distribution $f_{C^*}(\Delta t)$ multiplied by $1-\Delta t/C^*$ (grey) and the function $H(x)$ (blue) which is the corresponding integral. The orange area is equal to the value of $H(x')$. The usage of $F(\Delta t)$ instead of $f_{C^*}(\Delta t)$ would lead to a curve with discrete steps and a maximum that is different from 1/e.*

which has the following properties (see Fig. 4.1):

- $H(0) = H(\infty) = 0$
- $H(C^*) = 1/\mathrm{e}$, this is the global maximum of $H(x)$

If one replaces $f_{C^*}(\Delta t)$ by the discrete distribution $F(\Delta t)$ of the random probe all the properties still hold with the exception of a global maximum which is not exactly 1/e but varies around a mean value μ near 1/e. The maximum can be calculated like this:

$$M(F) := \int_0^{C^*} \left(1 - \frac{\Delta t}{C^*}\right) \cdot F(\Delta t)\,\mathrm{d}\Delta t = \frac{1}{N} \sum_{i \in I_{C^*}} \left(1 - \frac{\Delta T_i}{C^*}\right) = \frac{1}{N} \sum_{i \in I_{C^*}} a_{i,C^*} \quad (4.19)$$

$$\text{with:} \qquad I_{C^*} := \{\, i \mid \Delta T_i \leqslant C^* \} \quad \text{and} \quad a_{i,C^*} = \left(1 - \frac{\Delta T_i}{C^*}\right)$$

The reason for the deviation of μ from 1/e is the difference between C^*, which will be used in the equations, and the true, but unknown, mean value C. C^* varies around C with a spread of $\sigma_{\Delta t}/\sqrt{N}$. This leads to a slightly lower maximum than 1/e. Hence the mean value μ of many different random probes is also smaller than 1/e.

One can see that the global maximum $M(F)$ is a suitable value for testing the random distribution against the ideal exponential distribution. Due to the discrete nature of the $F(\Delta t)$ the integral in Equ. (4.19) transforms into a summation. On the basis of two extreme examples I will show the range of possible solutions for $M(F)$:

1. distribution with a untypical regular structure:
   $\Delta t = const.$ (like a heartbeat)
   $F_H(\Delta t) := \delta(\Delta t - C^*) \quad \Rightarrow \quad M(F_H) = 0$
   if all ΔT_i are equal to C^* the summation in Equ. (4.19) will be 0

2. distribution of events appearing almost all at the same time:
   $\Delta t \approx 0$ for almost all $(N-1)$ events (like a needle peak)
   $F_N(\Delta t) := \lim_{N\to\infty} \left((1-\frac{1}{N})\cdot\delta(\Delta t) + \frac{1}{N}\cdot\delta(\Delta t - N\cdot C^*)\right)$
   almost all ΔT_i are zero and smaller than C^*
   $\Rightarrow \; M(F_N) = \frac{1}{N}\sum 1 = \frac{1}{N}(N-1) \xrightarrow[N\to\infty]{} 1$

Now it is clear that $M(F)$ can only attain values between 0 and 1. If the distribution is too regular $M(F)$ will be lower than μ ($\approx 1/\mathrm{e}$) but not lower than 0. If the distribution indicates an untypical variability compared to a Poisson process $M(F)$ will be higher than μ but still lower than 1.

Result of exp-test and the normal distribution

To use $M(F)$ as a statistical test for variability it is necessary to know its distribution function under the zero hypothesis. This task is not trivial and would be considerably expensive if one would try to find an analytically exact solution. Therefore Prahl's approach was semi-analytical.
One can see that $M(F)$ is dimensionless and that C^* only scales the time. So the distribution will not depend on C^* but on the number of time differences N instead. Therefore $M(F)$ will be called M_N from now on. Regarding equation 4.19 it is clear that M_N is the sum of a_{i,C^*} divided by N. The probability distribution of a sum is usually the convolution of the probabilities of all the variables a_{i,C^*} that have been added together. In such a case the variances ($= \sigma^2$) of each variable are summed. Because the variance of a_{i,C^*} has the same value for all i, the overall variance is just proportional to I_{C^*}, which is proportional to N (for large N). Taking also into account the division by N mentioned in Equ. (4.19), the variance, which is related to M^2, additionally scales by $1/N^2$. So at the end the scale factor will be asymptotically $N/N^2 = 1/N$. Hence, for the standard deviation $\sigma \propto 1/\sqrt{N}$ is valid

The convolution of probabilities is also the reason for the expectation value μ of M_N to tend towards the expectation value of the positive a_{i,C^*}. As the value of a_{i,C^*} depends on ΔT_i it is possible to replace Δt in Equ. (4.13) by a term $(1-a_{C^*})C^*$. Hence, the resulting equation represents the pdf of a, which can be used to calculate its expectation value between 0 and 1. For the equation of the expectation value, which is a function of C^*, a Taylor series can be derived for $C^* = C$. When $C^* - C$ is replaced by $\pm\sigma_{\Delta t}/\sqrt{N}$, one can see that the asymptotic value of μ will be 1/e subtracted by a second order term that is proportional to 1/N while the first order terms average out for large N due to the $\pm$-sign.

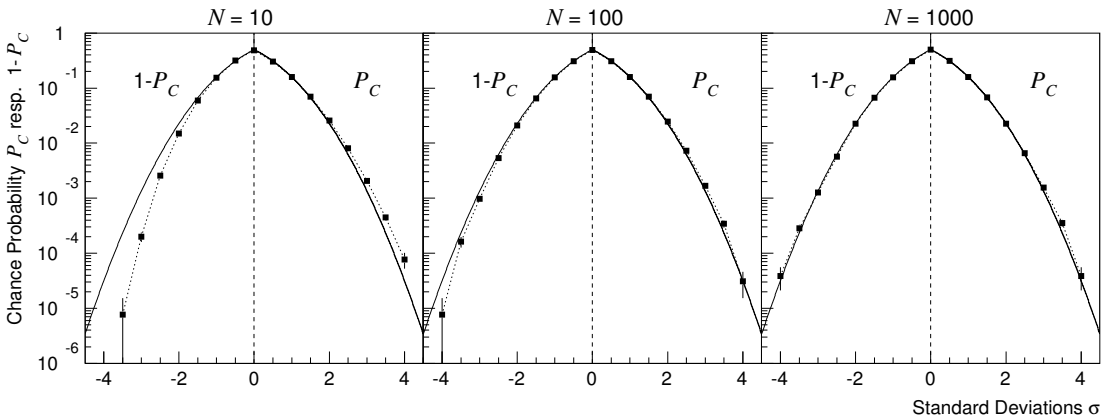

Fig. 4.2: *Comparison of the normal distribution $\mathcal{N}(1/\mathrm{e} - \alpha/N, \beta/N)$ with the M_N distribution for different N. For $\sigma \geqslant 0$ the points on the dashed lines represent the relative frequencies of all the Monte Carlo generated M_N for which $M_N - \mu \geqslant \sigma$ is valid. As comparison the inverse cumulative distribution function (cdf) of the normal distribution is plotted (solid lines). For $\sigma < 0$ the dashed curves show the frequencies of $M_N - \mu \leqslant \sigma$ which can be compared to the standard cdf of the normal distribution. The number of tests for each N is $1.3 \cdot 10^5$. [Prahl (1999), p.4, Fig.2]*

According to the central limit theorem one expects further that not only the mean value and the variance reach a common value for large N but also the whole distribution of M tends towards a *normal distribution*. Therefore the last step will be the determination of only two parameters: the difference between μ and $1/\mathrm{e}$ and the standard deviation. Because their dependencies on N had been already explained above, it only remains to find two constants α and β for which the following equations are true if N is large enough ($N \gtrsim 10$):

$$\mu(M_N) = \frac{1}{\mathrm{e}} - \frac{\alpha}{N} \qquad \text{and} \qquad \sigma(M_N) = \frac{\beta}{\sqrt{N}} \tag{4.20}$$

In extensive Monte Carlo simulations of Poisson distributed event times Prahl constrained α and β to the following values:

$$\alpha = 0.189 \pm 0.004 \qquad \beta = 0.2427 \pm 0.0002 \tag{4.21}$$

That the distribution of M_N is close to a normal distribution $\mathcal{N}(1/\mathrm{e} - \alpha/N, \beta/N)$ can be seen in Fig. 4.2 . Here Prahl compares the *cumulative distribution function (cdf)* of the normal distribution with the relative frequencies of Monte Carlo simulated M_N. Only for event numbers $N \leqslant 10$ a small deviation from normal distribution can be seen but this will just make the result for low N more conservative due to a slightly smaller β.

Comparison with other methods and dead time treatment

The sensitivity of this method was compared with the Kolmogorov test and with the standard method using just the event counts. It could be shown, that the exp-test results in an improved significance which can be up to 50% higher than that of

the standard method. Of course this depends on the relative duration of the excess compared to the whole measured time. Only if this tends to zero, which corresponds to a sharp spike, the significance of the exp-test will reach the 50% improvement. The comparison with the Kolmogorov test revealed that the *exp-test* is better suited to find some or many short bursts while the Kolmogorov test is more sensitive for comparable long states of increased rates [Prahl (1999), p.8, sec.5].

As a last remark about the *exp-test*, I would like to refer to the treatment of varying temporal acceptance of the detector. If this is known, one just has to replace the variable t by a scaled effective time. Unfortunately in most experiments this is not precisely known enough. Therefore Prahl developed a slightly modified method on the basis of the procedure described above. Hereby one uses background events measured in dedicated off regions (see subsection 2.4.4). The number of these off-source events (so called *Inter-Events*) recorded between two consecutive on-source (signal) events can be used as a substitute for the scaled effective time. Less acceptance of the detector reduces the number of detected on-source and off-source events equally. Hence the mean number of the Inter-Events stays constant even for a varying acceptance.
In the work presented here, the purpose was to be independent of different background estimation procedures (see subsection 2.4.4). Hence, only data with almost constant acceptance will be used for the analysis with the original exp-test (see Equ.4.19).
It remains to explain how the dead time t_d is taken into account. One can treat the dead time as several short switch-offs during data taking. This usually happens directly after a triggered event, no matter if it is an event in the signal region or in the background region. This leads to a different distribution of the signal Δt, which will be a summation of the pdfs $f_{k,C'}(\Delta t)$ [Müller (1973), Müller (1967)] of finding k events (signal or background) in the interval Δt, multiplied by the probability that the first $k-1$ are just background and only the kth event is a signal event.

$$f_s(\Delta t) = \sum_{k=1}^{\infty} f_{k,C'}(\Delta t) \cdot p_{\text{sig}}(1-p_{\text{sig}})^{k-1} \qquad \text{with:} \quad p_{\text{sig}} = \frac{\Lambda_{\text{sig}}}{\Lambda_{\text{sig+bkg}}} = \frac{C_{\text{sig+bkg}}}{C_{\text{sig}}}$$

$$= \sum_{k=1}^{\Delta t/t_d} \frac{(\frac{1}{C'}(\Delta t - kt_d))^{k-1}}{C'(k-1)!} \mathrm{e}^{-\frac{1}{C'}(\Delta t - kt_d)} \cdot \frac{C_{\text{sig+bkg}}}{C_{\text{sig}}} \left(1 - \frac{C_{\text{sig+bkg}}}{C_{\text{sig}}}\right)^{k-1} \tag{4.22}$$

With C' representing the unknown true mean time difference of the combined signal and background events without any dead time influence. And with $C_{\text{sig}}$and $C_{\text{sig+bkg}}$ that denote the mean ΔT of the measured signal and the measured signal plus all background events respectively. Therefore it is valid to write $C_{\text{sig+bkg}} = C' + t_d$. If t_d tends towards zero it follows that $C' = C_{\text{sig+bkg}}$ and equation (4.22) transforms to:

$$f_s(\Delta t) \overset{t_d \to 0}{=} \frac{1}{C_{\text{sig}}} \mathrm{e}^{-\frac{\Delta t}{C'}} \sum_{k=1}^{\infty} \frac{\left(\frac{\Delta t}{C'} - \frac{\Delta t}{C_{\text{sig}}}\right)^{k-1}}{(k-1)!} = \frac{1}{C_{\text{sig}}} \mathrm{e}^{-\frac{\Delta t}{C_{\text{sig}}}} \tag{4.23}$$

So in case the dead time is infinitely small the distribution of the Δt between two signal events is the same even if there are many background events occurring in between. Otherwise one has to deal with Equ. (4.22) which has the same characteristics as the simple exponential distribution (see Equ. (4.15) and Equ. (4.16)) but results in a different maximum when one applies the $H(x)$ function to it (see Equ. (4.18)). Plotting Equ. (4.22) with a dedicated plotting program one can see that the resulting curve is similar to an exponential distribution Equ. (4.23) with a shift of t_d towards positive Δt. The smaller t_d is compared to $C_{\text{sig+bkg}}$ the better the shape will be approximated by the exponential distribution. To be still able to use the exp-test as derived above on has to take care of the t_d shift by subtracting this amount from each measured ΔT_i in the data and from the mean value C^*. Due to the fact that $t_d/C_{\text{sig+bkg}} = \alpha_{\text{dt}}$ which is the overall dead time fraction, it is reliable to use the approximation for the signal time difference distribution as long as $\alpha_{\text{dt}} < 30\%$.

4.2.3 The *Bayesian Blocks* method

The method invented by Scargle is an analysis of time series addressing the detection of intensity variations using Bayesian statistics. In contrast to the *exp-test* the input data has to be in a quantized format, so the method is not fully unbinned. However the bin size is not fixed and can be as small as required. Another difference is the form of the output. While the *exp-test* is just able to provide a fast answer to the question if there is variability in the data or not, Scargles method delivers the most probable segmentation of the observed time into smaller intervals during which the data rate will have no significant variations. Thus, it delivers not only a statement about the variability but also an information about the exact times when the variations happen. These times are called *change points*.
In this section I will explain the method and its useful features. For a more detailed explanation see [Scargle (1998)] and [Scargle *et al.* (2013)]

Bayesian approach

Using Bayesian statistics to find change points is not a new idea, as was already reported by Scargle in [Scargle (1998), sec 1.3.]. The difference in this approach here is the search for change points by comparing likelihoods of different models and not by comparing the likelihoods of their different parameters. Thus, one takes automatically into account the fact that more complex models are less desirable. Firstly, let's briefly summarize Bayes's theorem, which is the basic relation of determining parameter inference:

$$P(\theta|D,\mathcal{M})P(D|\mathcal{M}) = P(D|\theta,\mathcal{M})P(\theta|\mathcal{M}) \tag{4.24}$$

where D is some data and $\mathcal{M}$ indicates a model with the parameter θ. If there is more than one parameter θ can just be treated as a vector. With this relation one can estimate the probability that a specific model is correct and one can learn something about the most likely parameter solely on the basis of the data measured and some prior information one might have. Both sides of the equation above are just different ways of describing the same combined probability of getting a certain parameter θ for the observed data D under the assumption of a model $\mathcal{M}$.

Model comparison

In the case described here the main goal is the comparison of different models for a given set of event times observed during a time interval T. Basically one is interested in two different models:

1. $\mathcal{M}_1$: constant intensity over T
2. $\mathcal{M}_2$: two subintervals ($T_1 + T_2 = T$) with different intensities

Using the Bayes's theorem one can create the ratio $R_{k,j}$ of the conditional probabilities that a specific model $\mathcal{M}_k$ fits the measured data D:

$$R_{k,j} = \frac{P(\mathcal{M}_k|D)}{P(\mathcal{M}_j|D)} = \frac{P(\mathcal{M}_k|D)P(D)}{P(\mathcal{M}_j|D)P(D)} = \frac{P(D|\mathcal{M}_k)P(\mathcal{M}_k)}{P(D|\mathcal{M}_j)P(\mathcal{M}_j)} \tag{4.25}$$

Now one has to derive a formula for the quantity $P(D|\mathcal{M}_k)$ which is the same as the likelihood $\mathcal{L}(\mathcal{M}_k, D)$. It describes the probability of observing data D under the assumption of model $\mathcal{M}_k$ without requiring a specific value for the parameter θ_k. Because one has to take into account all possible solutions for θ_k then, the formula will be an integration over $\mathrm{d}\theta_k$. This can be proven as well by integrating equation (4.24):

$$P(D|\mathcal{M}_k) \cdot \underbrace{\int P(\theta_k|D, \mathcal{M}_k)\,\mathrm{d}\theta_k}_{=1\,!} = \int P(D|\theta_k, \mathcal{M}_k)P(\theta_k|\mathcal{M}_k)\,\mathrm{d}\theta_k \tag{4.26}$$

As it is a required feature of a probability density function, the integral of $P(\theta_k|D, \mathcal{M}_k)$ over all possible θ_k is 1. Together with this relation and equation (4.25) it follows:

$$R_{k,j} = \frac{\int P(D|\theta_k, \mathcal{M}_k)P(\theta_k|\mathcal{M}_k)\,\mathrm{d}\theta_k}{\int P(D|\theta_j, \mathcal{M}_j)P(\theta_j|\mathcal{M}_j)\,\mathrm{d}\theta_j} \cdot \frac{P(\mathcal{M}_k)}{P(\mathcal{M}_j)} = \frac{\mathcal{L}(\mathcal{M}_k, D)}{\mathcal{L}(\mathcal{M}_j, D)} \cdot \rho \tag{4.27}$$

$$\text{with:} \quad \mathcal{L}(\mathcal{M}_k, D) = \int P(D|\theta_k, \mathcal{M}_k)P(\theta_k|\mathcal{M}_k)\,\mathrm{d}\theta_k \quad \text{and} \quad \rho = \frac{P(\mathcal{M}_k)}{P(\mathcal{M}_j)}$$

So the important part of the model comparison is the calculation of the likelihood ratio $\mathcal{L}(\mathcal{M}_k, D)/\mathcal{L}(\mathcal{M}_j, D)$. If one believes in an equal probability for all possible models ($\rho = 1$) one simply needs to search for the maximum likelihood, to find the best fitting model.
More complex models with more parameters always increase the maximum likelihood but are usually not the best ones to chose. Bayesian analysis automatically takes this fact into account by integrating over all model parameters.

Constant Poisson rate models

In the next step one has to define a distribution function $P(D|\theta_1, \mathcal{M}_1)$ for the constant rate model $\mathcal{M}_1$. This depends on Poisson statistics and the data format of the experiment. While Scargle describes the distributions for 3 different data formats [Scargle (1998), sec 2.2.] I will concentrate on just 2 different distribution models.

The basis of all distribution models is the Poisson process with a constant rate λ over the observed time interval T. The number of events X_m in a short subinterval δt_m will then be:

$$P(X_m|\Lambda, \mathcal{M}_1) = \frac{\Lambda^{X_m}}{X_m!} \cdot \mathrm{e}^{-\Lambda} \qquad \text{with:} \quad \Lambda = \lambda \delta t \tag{4.28}$$

One can assume that the arrival of photons in different subintervals is independent of that in adjacent intervals. Therefore the model distribution of the data in an interval T will be the product of the Poisson distributions for each subinterval m:

$$P[D|\mathcal{M}_1(\Lambda, T)] = \prod_{m=1}^{M} P(X_m|\Lambda, \mathcal{M}_1) \qquad \text{with:} \quad T = \sum_{m}^{M} \delta t_m \tag{4.29}$$

Depending on the experiment, the output can be the exact arrival times of each single photon or the number of photons during some discrete time bins. There are also some other data formats which I will omit in this section because there are not important here.

Time-tagged event (TTE) data: If the output contains the exact arrival times of N photons, Scargle calls this mode the *time-tagged event (TTE) data*. Due to the finite time resolution ($\delta t \neq 0$) one can interpret the data period as M time bins with a size small enough that the number of photons in it is just zero or one ($X_m = \{0, 1\}$). As shown in Equ. (4.29) one has to multiply all the Poisson probabilities which can attain only two different values $p_0 = P(X_m = 0)$ and $p_1 = P(X_m = 1) \approx 1 - p_0$. The entire probability for the observed data will then look like this:

$$P[D_{TTE}|\mathcal{M}_1(p_0)] = \prod_{m=1}^{M} P(X_m|p_0) = p_1^N p_0^{M-N} = (1-p_0)^N p_0^{M-N} \tag{4.30}$$

The equation reduces to a binomial distribution with the parameter p_0, which depends on the constant Poisson mean Λ. What is missing to calculate the full likelihood for the constant rate model $\mathcal{L}(\mathcal{M}_1, D_{TTE})$ is the prior of the parameter p_0 given the model $\mathcal{M}_1$. Assuming that the probability is uniformly distributed over all physical realizable values of p_0 one can express this with the following function:

$$P(p_0|\mathcal{M}_1) = \begin{cases} 1 & \text{for } 0 \leqslant p_0 \leqslant 1 \\ 0 & \text{otherwise} \end{cases} \tag{4.31}$$

Together with Equ. (4.30) one can finally calculate the likelihood:

$$\begin{aligned} \mathcal{L}(\mathcal{M}_1, D_{TTE}) &= \int P[D_{TTE}|\mathcal{M}_1(p_0)] P(p_0|\mathcal{M}_1) \mathrm{d}p_0 = \int_0^1 p_0^{M-N} (1-p_0)^N \mathrm{d}p_0 \\ &= \frac{\Gamma(M-N+1)\Gamma(N+1)}{\Gamma(M+2)} = \frac{N!(M-N)!}{(M+1)!} \end{aligned} \tag{4.32}$$

Binned data: A slightly different likelihood will be the result if the data doesn't provide the single photon times but the number of events in M evenly spaced time intervals instead. This case will be called *binned data* and the only difference to the time-tagged data is the larger bin size with X_m being usually much bigger than one. According to Poisson statistic the distribution of the data given the model $\mathcal{M}_1$ with the constant mean Λ will be:

$$P[D_{BIN}|\mathcal{M}_1(\Lambda)] = \prod_{m=1}^{M} P(X_m|\Lambda) = \prod_{m=1}^{M} \frac{\Lambda^{X_m}\mathrm{e}^{-\Lambda}}{X_m!} = \frac{\Lambda^N \mathrm{e}^{-M\Lambda}}{\prod_{m=1}^{M} X_m!} \tag{4.33}$$

where $N = \sum_{m=1}^{M} X_m$ is the total number of photons in the entire dataset.
In the next step one can omit the denominator in Equ. (4.33) because the product of all $X_m!$ stays the same even if we split the data into more parts with different probability distributions $P[D_{BIN}|\mathcal{M}_2] = \prod_j P[D_{BIN,j}|\mathcal{M}_1(\Lambda_j)]$ with $D_{BIN,j} \subseteq D_{BIN}$. Thus the denominator cancels out if one calculates the likelihood ratio between the constant rate model $\mathcal{M}_1$ and the model for several subintervals $\mathcal{M}_2$.
Again one needs to define a prior for the parameter Λ before one can derive the likelihood for this kind of data format. Scargle chose the nonuniform but normalized prior:

$$P(\Lambda|\mathcal{M}_1) = \begin{cases} \mathrm{e}^{-\Lambda}/(1-\mathrm{e}^{-C}) & \text{for } 0 \leqslant \Lambda \leqslant C \\ 0 & \text{otherwise.} \end{cases} \tag{4.34}$$

With this prior one has the advantage to express the belief that the mean value Λ cannot exceed a specific value C due to instrumental limitations. A possible limiting factor could be the dead time. In this case the mean value cannot be larger than $C = T_{\mathrm{sig}}/t_{\mathrm{dead}}$ $(= \Lambda_{\max})$ with the time in a bin T_{sig} during which a signal event can be detected and the average dead time of a single event t_{dead}. Note that T_{sig} can be smaller than the bin width T_{bin}. This is due to all the background events not appearing in the data of the signal region but being responsible for a non negligible amount of dead time during which no signal detection is possible.

$$T_{\mathrm{sig}} = T_{\mathrm{bin}}(1-\alpha_{\mathrm{dead}}) \qquad \text{with:} \quad \alpha_{\mathrm{dead}} = \text{dead time fraction} \tag{4.35}$$

Of course the fraction α_{dead} includes also the dead time of the signal events that we don't want to take into account for the calculation of T_{sig}. However the dead time induced by background events is nearly 100% compared to the dead time of the rare events in the signal region.
With all this information one can derive the formula for the likelihood:

$$\begin{aligned} \mathcal{L}(\mathcal{M}_1, D_{BIN}) &= \int_0^{\Lambda_{\max}} \frac{\Lambda^N \mathrm{e}^{-(M+1)\Lambda}}{1-\mathrm{e}^{-\Lambda_{\max}}}\,\mathrm{d}\Lambda \\ &= \frac{N!}{(M+1)^{N+1}} \cdot \frac{1-\sum_{k=0}^{N}(\Lambda_{\max}^k/k!)\cdot \mathrm{e}^{\Lambda_{\max}}}{1-\mathrm{e}^{-\Lambda_{\max}}} \\ &= \frac{N!}{(M+1)^{N+1}} \cdot \underbrace{\frac{P_{\mathrm{Pois}}(k>N|\Lambda_{\max})}{1-\mathrm{e}^{-\Lambda_{\max}}}}_{\substack{\approx 1 \\ \text{(if: } \Lambda_{\max}\to\infty \text{ and } N\ll\Lambda_{\max})}} \end{aligned} \tag{4.36}$$

In case of measurements with ground-based gamma-ray telescopes the number of events N is much lower than $\Lambda_{\max}$. Further the dead time after an event t_{dead} is relatively low compared to the distance between two signal events which is in the order of seconds. Hence a bin width of $T_{\text{bin}} \approx 1$ sec is a reasonable choice. Even after subtraction of the background dead time is T_{sig} still much larger than t_{dead} and therefore it is valid to use the approximation of $\Lambda_{\max} \to \infty$ and $N \ll \Lambda_{\max}$ in the last line of Equ. (4.36).

An interesting point about all these likelihoods is that they just depend on the number of events N and the total number of time bins M but not on the single event times. So completely different datasets have the same likelihood of being described by a constant rate model if their numbers N and M are identical.

Segmented Poisson rate model and likelihood ratios

After explaining the constant rate models it is now just a small step to the segmented model. Basically one assumes a break in the data where the photon rate suddenly changes and one analyzes each of those two subintervals D_1 and D_2 with durations T_1 and T_2 separately under the assumption of a constant rate model. The point separating the two segments with different rates Λ_1/T_1 and Λ_2/T_2 is called a *change point in time series* and will be labeled t_{cp}. Further it is valid to replace the duration T_1 of the first subinterval by t_{cp} and T_2 by $T - t_{\text{cp}}$. The probability distribution of the entire dataset D is then the combined probability of the two subintervals which is, if we assume independence between those intervals, just the product of the two constant rate distributions:

$$P[D(T)|\mathcal{M}_2(\Lambda_1, \Lambda_2, t_{\text{cp}})] = P[D_1|\mathcal{M}_1(\Lambda_1, t_{\text{cp}})] \cdot P[D_2|\mathcal{M}_1(\Lambda_2, T - t_{\text{cp}})] \tag{4.37}$$

Again one has to integrate over all the parameters and their prior probabilities to get the formula for the global likelihood:

$$\begin{aligned}\mathcal{L}(\mathcal{M}_2, D) = \int \mathrm{d}t_{\text{cp}}\ P_{\text{cp}}(t_{\text{cp}}) \int \mathrm{d}\Lambda_1\ P_\Lambda(\Lambda_1) \int \mathrm{d}\Lambda_2\ P_\Lambda(\Lambda_2) \\ \cdot P[D_1|\mathcal{M}_1(\Lambda_1, t_{\text{cp}})] \cdot P[D_2|\mathcal{M}_1(\Lambda_2, T - t_{\text{cp}})]\end{aligned} \tag{4.38}$$

For the prior distributions of the different Λ_i one chooses those from above according to the data type that is used. The prior of the change point is assumed to be uniform because there is no reason to favor some t_{cp} over other possible values. Furthermore it is more useful to denote the change point location by the integer m_{cp} instead of t_{cp} due to the discrete time measurement in each of the different data types. All together the integral in Equ. (4.38) will reduce to a sum over all possible constant

rate likelihood combinations multiplied by the constant $P_{\mathrm{cp}} = 1/(M-1)$:

$$\mathcal{L}(\mathcal{M}_2, D) = \sum_{m_{\mathrm{cp}}=1}^{M-1} \mathcal{L}[\mathcal{M}_1(m_{\mathrm{cp}}), D_1] \cdot \mathcal{L}[\mathcal{M}_1(M - m_{\mathrm{cp}}), D_2] \cdot \frac{1}{M-1} \tag{4.39}$$

$$\approx \sum_{n_{\mathrm{cp}}=1}^{N-1} \mathcal{L}[\mathcal{M}_1(m_{n_{\mathrm{cp}}}), D_1] \cdot \mathcal{L}[\mathcal{M}_1(M - m_{n_{\mathrm{cp}}}), D_2] \cdot \frac{\Delta m_{n_{\mathrm{cp}}}}{m_{N-1}} \tag{4.40}$$

Through this approximation one assumes the likelihood product to be constant for all the change points located between the arrival of two consecutive signal photons $[N_j, N_j + 1]$ which are separated by $\Delta m_{n_{\mathrm{cp}}}$ time bins. Therefore one parametrizes the change point as $m_{\mathrm{cp}} = m_{n_{\mathrm{cp}}}$ and reduces the summation over m_{cp} to one over the photon index n_{cp}.

Finally one has to divide the likelihoods of the different models according to Equ. (4.27) to get the final odds ratio:

$$R_{2,1} = \frac{\mathcal{L}(\mathcal{M}_2, D)}{\mathcal{L}(\mathcal{M}_1, D)} = \frac{1}{M-1} \sum_{m_{\mathrm{cp}}=1}^{M-1} \frac{\mathcal{L}[\mathcal{M}_1(m_{\mathrm{cp}}), D_1] \cdot \mathcal{L}[\mathcal{M}_1(M - m_{\mathrm{cp}}), D_2]}{\mathcal{L}(\mathcal{M}_1, D)}$$

$$= \frac{1}{M-1} \sum_{m_{\mathrm{cp}}=1}^{M-1} \mathrm{e}^{\ln\left(\mathcal{L}[\mathcal{M}_1(m_{\mathrm{cp}}), D_1]\right) + \ln\left(\mathcal{L}[\mathcal{M}_1(M - m_{\mathrm{cp}}), D_2]\right) - \ln\left(\mathcal{L}[\mathcal{M}_1, D]\right)} \tag{4.41}$$

If the data favors a constant rate model the value of $R_{2,1}$ should be lower than 1 while in the other case it should be much bigger. Due to the very low values and the large differences between each other it is more convenient to use the logarithms of the likelihoods. This makes it much easier for numerical calculations especially because some likelihood values can go down to very low values. Values so low, that they even can't be stored in a standard 64 bit double format.

Data example and block separation

To make it more clear how the whole algorithm works I will show a plot of the exponent of Equ. (4.41)

$$\begin{aligned}\psi_{M,N}(m_{\mathrm{cp}}, n_{\mathrm{cp}}) &= \ln\left(\mathcal{L}[\mathcal{M}_1(m_{\mathrm{cp}}), D_1]\right) + \ln\left(\mathcal{L}[\mathcal{M}_1(M - m_{\mathrm{cp}}), D_2]\right) \\ &\quad - \ln\left(\mathcal{L}[\mathcal{M}_1, D]\right) \qquad \left(\text{with: } n_{\mathrm{cp}} = n(m_{\mathrm{cp}}, D)\right) \\ &= \ln\left(\frac{n_{\mathrm{cp}}!}{(m_{\mathrm{cp}}+1)^{n_{\mathrm{cp}}+1}}\right) + \ln\left(\frac{(N-n_{\mathrm{cp}})!}{(M-m_{\mathrm{cp}}+1)^{N-n_{\mathrm{cp}}+1}}\right) \\ &\quad - \ln\left(\frac{N!}{(M+1)^{N+1}}\right)\end{aligned} \tag{4.42}$$

taking into account the likelihood distribution of the binned data type (see Equ. 4.36).

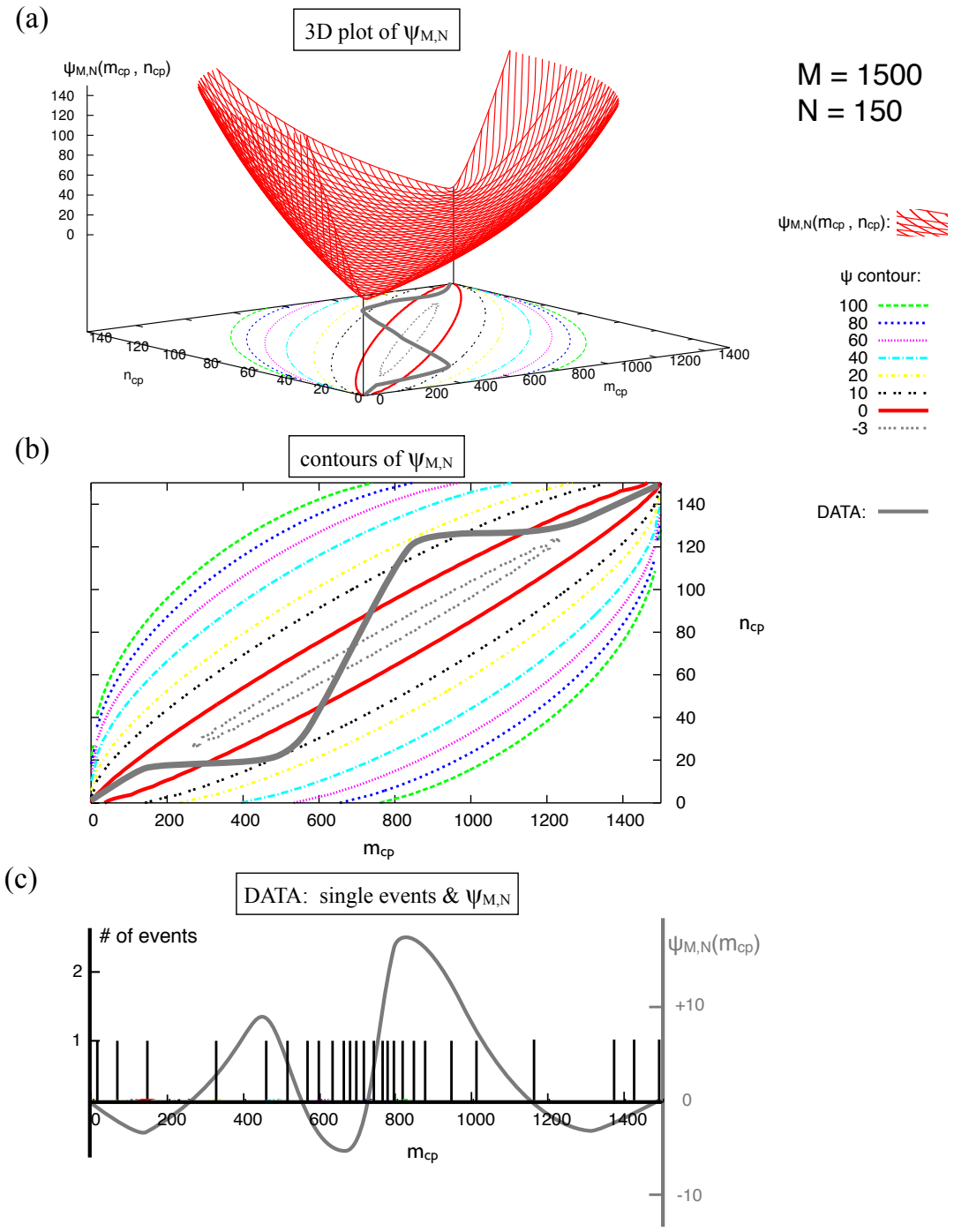

Fig. 4.3: *Two dimensional function of the exponent $\psi_{M,N}(m_{\mathrm{cp}}, n_{\mathrm{cp}})$ for $M = 1500$ and $N = 150$. In (a) the surface of the function is shown in a 3D plot. The x-axis accounts for the discrete time bins m_{cp} and the y-axis for the number of events n_{cp} inside the interval $[0, m_{\mathrm{cp}}]$. Additional the contours of $\psi_{M,N}(m_{\mathrm{cp}}, n_{\mathrm{cp}})$ are drawn in the x-y-plane (see also (b)) together with a grey curve that visualizes some arbitrary data D of distinct events. According to this data D an example is shown in (c) of how these single events could be distributed (black) over the time bins m_{cp} and how the corresponding $\psi_{M,N}(m_{\mathrm{cp}})$ would look like (grey). This is a projection of the $\psi_{M,N}(m_{\mathrm{cp}}, n_{\mathrm{cp}})$-values of the grey curve in (a, b) to the m_{cp}-axis.*

As one can see in Fig. 4.3 (a,b) the lowest values of the two-dimensional function of $\psi_{M,N}(m_{\mathrm{cp}}, n_{\mathrm{cp}})$ can be found on a diagonal in the m_{cp}-n_{cp}-plane from (0,0) to the the maximal possible point (M,N). In this example the following values have been used: $M = 1500$ and $N = 150$. Furthermore one can see a gray curve in the m_{cp}-n_{cp}-plane. With this curve I want to visualize all possible m_{cp}-n_{cp}-combinations of a certain dataset (see Fig. 4.3 (c)). If this monotonically increasing curve stays close to the diagonal, inside the red contour line, which denotes the area where $\psi_{M,N}(m_{\mathrm{cp}}, n_{\mathrm{cp}}) \leqslant 0$, the summation over all m_{cp}, as in Equ. (4.41), will then lead to a result for $R_{2,1}$ that is smaller than one and thus expresses a preference of the constant rate model $\mathcal{M}_1$. This makes perfectly sense because all points (m_{cp}, n_{cp}) on the diagonal have the same ratio as N/M and therefore have the same rate at every time bin m.
Further it is visible in the contour plot (Fig. 4.3 (b)) that a distribution of events concentrated at the beginning or at the end of a measured data period would lead to a strong deviation from the diagonal and therefore to a much higher odds ratio $R_{2,1}$. While if all the events are concentrated in a short time interval right in the middle of the measured duration the odds ratio would still be bigger than one but less dominant.
During the computation of the sum in Equ. (4.41) given the data D one will automatically find the point m_{cp} where $\psi_{M,N}(m_{\mathrm{cp}}, n_{\mathrm{cp}})$ is at its maximum. Splitting D at this change point leads to the highest possible likelihood. If one is interested in splitting the data in more than just two blocks one can repeat the whole method for each of the two subintervals separately ending up with three change points and up to four subintervals. This procedure can be continued until one reaches the desired split level or until the subintervals are too small and disfavor any further splitting.

Last remarks

The *Bayesian Blocks* method provides the time of the change points in rate and an estimate if the data follows a poisson distribution with a constant rate over the whole period or not. Due to the small statistics in case of ground-based gamma-ray astronomy there will be almost always a deviation from the constant rate model even if the data consists solely of background evens with a constant rate. As I will show later, the expectation value of the odds ratios, computed for datasets without variability, is much smaller than one and depends on M and N. It was therefore necessary to perform Monte Carlo tests. During each test some predefined number N of events were uniformly distributed over M time bins. This represents the case of the constant rate poisson distribution. By calculating the odds ratio for each of those Monte Carlo tests one gets the distribution of $R_{2,1}$ under the assumption of a constant rate model. Any significant deviation from this distribution will then be a proof of a fluctuation in the rate of some measured data.

Finally I will mention briefly the fact that Scargle already increased the efficiency of his method [Scargle *et al.* (2013)]. Especially the technique of finding several change-points was improved and makes it now possible to find them during data taking.

The idea is to iterate over all measured time bins and calculate at each bin m the probability of a constant rate model $\mathcal{M}_1$ between this bin m and the last measured bin M. Afterwards, one has to multiplying this probability with the best block separation found in the interval between the first time bin and bin $m-1$. The best block separation is computed during an earlier iteration step and its overall fitness at bin $m-1$ is stored in the program. It is now the goal to find that bin m where the combined probability of the best block separation before m and the constant rate model after m reaches its maximum. This value of m is then stored in the program as the change-point of M together with the overall probability which will than represent the best block separation at bin M. Repeating this procedure for $M+1$ bins after a new bin was added to the data will result in a different change-point and and a different overall fitness.
Beginning at bin $M = 1$ one can determine the best block separation for each bin until the last measured bin. This even works during data taking when the number of the last measured bin is much smaller than the unknown final bin number M_{final}, which marks the end of observing. When this is reached, one can get the separation of the best fit by searching backwards trough the list of stored change-points. Starting at M_{final}, one gets the corresponding change-point and jumps to this bin $cp(M_{\text{final}}) = m_{\text{cp}_1}$. At this bin one looks again for the corresponding change-point which leads to the next lower change-point $cp(m_{\text{cp}_1}) = m_{\text{cp}_2}$. Continuing this recursive procedure until the first bin $m = 1$ is reached will then lead to the full recovery of all the change-points of the best fitting block separation for the whole dataset with M_{final} time bins.

Chapter 5

Test of statistical methods

After understanding the differences of the methods described in chapter 4 my goal was their comparison on the basis of Monte Carlo generated events in the field of view of a VERITAS camera. Therefore we wrote a program[1] to simulate skymaps with or without some variable source and to test the different methods on these simulations. Further it is also capable of accepting output from standard event analysis to search for variability in VERITAS data. In this chapter I will present the outcome of the Monte Carlo measurements and the results of the methods after applying them on data.

5.1 The analysis program - *timingSignificance*

In this section I will describe its basic functions and the procedure of analyzing data or Monte Carlo events.

5.1.1 Mode of operation

As a starting point for the test setup we generate events with time differences Δt following the above-mentioned exponential distribution (see sec.:4.2.2, Equ. (4.13)) assuming a mean value $1/\lambda$. The events are generated until a predefined duration $T = \sum_i \Delta T_i$ is reached. We also take into account a certain dead time t_d. By dead time, we mean the time of detector inefficiency between two consecutive incoming events due to the readout process initiated by the first event. In case of VERITAS the dead time is around $0.3 \pm 0.02 \cdot 10^{-3}$ sec. So in our simulation, the time difference has to be at least as large as the dead time which is achieved by shifting the exponential distribution to the right by t_d. This way also the mean value gets shifted by t_d
When we simulate solely background, we use the background rate as input for λ. When we simulate background events with additional signal events, we use the sum of those two rates (signal rate and background rate) as input. As we generate one event after another, we then have to decide after each event if it should belong to the background events or to the signal events. This is done randomly in a way that in the end the overall number of the signal events and the number of the background events represent the rates specified by the user when executing the program. It is

[1] c++ program on the basis of existing EVENTDISPLAY and ROOT libraries.

clear that the rate of events, readout by an IACT like VERITAS, will be smaller than the triggered rates due to the mutual dead time influence of consecutive events, no matter if they are of the same type or not.
Before further processing the simulated events, it was necessary to throw away a large fraction of the readout background events to match the quality cuts, the radial acceptance and the gamma-hadron filtering in the VERITAS analysis chain. As a rough estimate, we choose a fraction f_{loss} of 98.9% (for *post-upgrade*) or 99.7% (for *pre-upgrade*). We will describe these cuts later in this chapter. For the generated signal events, however, we use the value of the rate after all cuts instead of the trigger rate as the input parameter. Of course this is a simplification because the signal rate at trigger level would be larger, but in the end we only need a value of the signal rate after cuts for our further study. The true value of the triggered signal rate is only necessary for the correct dead time treatment. However, compared to the much larger trigger rate of the background events this correction would be only marginal. This is why we just use the signal rate after cuts for our simulation.

After the generation and the filtering of an event in time one has to assign a random position (x, y) somewhere in the VERITAS field-of-view. Here with the values x and y the deviation of the direction of an incoming event from the central axis is given in degrees. In case of a background event the position is distributed across the whole field-of-view according to the radial acceptance $A(x, y)$ of the VERITAS system (see Fig. 2.16). But if an event should represent a signal photon from a point source the idea was to use a two-dimensional Gauss distribution instead, which is centered around a mean position that has been randomly generated somewhere in the VERITAS field-of-view at the beginning. Of course, the effect of the radial acceptance will be also taken into account for those signal events. The result of this procedure represents a random signal position with a spread due to reconstruction errors, the so-called *signal region* (= 68% containment radius). This kind of signal simulation is sufficient for our purpose in which we don't want to restrict ourselves to a specific location in the field-of-view where we expect a flaring signal with a sudden rate change.
Due to the independence between the position of an event and its time, the temporal distribution of all the events found in a small area ΔS_i compared to the full size of the observable part of the sky S will be still Poisson distributed. The only difference will be the rate λ_i which is then proportional to $\Delta S_i \cdot A(x, y)$.

Finally one has to store all these informations in an easy-to-handle way. In this program, a two-dimensional array with fixed length and fixed bin width was chosen to represent the position of an event. Further, each bin of this array contains a non-fixed, scalable array to keep the exact time information of each single event assigned to that position bin. This was done because we don't now from the beginning how many events will occur in each position bin and we don't want to waste to much computer memory by reserving unused space.
Looping over the two-dimensional array, the program is now able to analyze each bin separately by obtaining the time array of this position bin and applying the different methods on it. While the two methods dedicated to find rate changes require the vector from each position bin, the standard method just needs the amount of events

in this bin together with an additional array of OFF-region events. This procedure is completely handled by existing classes and libraries from the standard analysis package and was already described in an earlier chapter (see subsection 2.4.4). Here we use the *reflected region* background estimation for the standard method. The output of each method in the form of multiples of the standard deviation σ is then visualized bin by bin in the form of a two-dimensional map. Additionally a distribution of the standard deviation of all the bins is plotted for each method separately.

5.1.2 Implementation of time-sensitive methods

exp-test (Prahl): The Method relies on the time difference ΔT_i of each event with respect to the following one and the mean time difference C^* between all adjacent events in the whole observing period.
In the program, we use for each position bin the corresponding list of times of all events belonging to this position bin. After sorting this list, the program iterates over each entry and subtracts from this time the time of the previous entry and the deadtime t_d to get the deadtime corrected time differences ΔT_i. In the end, one will compute $N-1$ different ΔT_i, where N is number of all entries in the list. Two additional ΔT will be calculated which are the ΔT_start between the first event and the start of the data taking period, and the ΔT_end between the last event and the end of the measurement. Then the value of C^* is just the sum of all deadtime corrected ΔT_i divided by the number of all calculated time differences $N+1$.
After calculating C^* a second iteration over the same list is done but this time the algorithm sums up all $1-\Delta T_i/C^*$ for which $\Delta T_i \leqslant C^*$ is true (see Equ.: 4.19). Again, this sum is divided by $N+1$ to get M_N which is the normal distributed result of the exp-test. Because the mean value $\mu(M_N)$ is not at zero and the standard deviation $\sigma(M_N)$ is not equal to one (see Equ.: 4.20), the final step of the exp-test algorithm is a transformation of the result M_N into a value following the standard normal distribution ($\mu = 0$, $\sigma = 1$). In doing so, we subtract $\mu(M_N) = \frac{1}{\mathrm{e}} - \frac{\alpha}{N}$ from M_N and divide this difference by $\sigma(M_N) = \frac{\beta}{\sqrt{N}}$.
In the end, one has a normal distributed result which serves as an indicator of the variability of the event sequence in the list. A result of 5, for example, will then represent a significance of 5σ that the underlying sequence cannot be described by a random Poisson distribution with a constant rate. A result of 0, however, would be in perfect agreement with events from a constant source.

Bayesian-blocks method (Scargle): In contrast to the exp-test the event times data has to be binned for the Bayesian-block methods. We chose a bin size of 1 second because this is small enough to keep the amount of entries per bin reasonable low in case of high gamma-ray rates, but it is also wide enough to reduce the amount of empty bins in case of low gamma-ray rates. As the event times are given in seconds but in decimal numbers, the program has to round off each time to integer numbers. In the end each event got assigned to a specific time bin and each time bin can hold more than one event. During the analysis of the data, we get the information on the duration of the observing period, and we can calculate the number of time bins that represent this duration. A typical observation with

VERITAS takes 1200 or 1800 seconds, so the number of time bins will be 1200 or 1800. As already explained before, we want to apply the algorithm on each bin in the position map. Therefore we have to retrieve the sorted list of the times belonging to all the events that get reconstructed at this position bin.

The computation of Equ. (4.41) is split into several steps. An important part is the numerical calculation of the log-likelihood of a single-block model (see Equ.4.36). Because the deadtime of the VERITAS experiment is very low we can apply the same approximation as it was done in Equ. (4.36) which will result in the following term:

$$\ln(\mathcal{L}_1(M,N)) = \ln\left(\frac{N!}{(M+1)^{N+1}}\right) = \ln\left(\frac{1}{M+1}\right) + \sum_{i=1}^{N} \ln\left(\frac{i}{M+1}\right) \tag{5.1}$$

So we just need the number of events N and the number of time bins M for that block. If the block represents the whole event sequence of the analyzed list, M is just the number of all time bins in the observing period and N is the number of all events that are found in the list. The time information of each event is not important during the computation of the single-block log-likelihood.
Because M can reach values up to 1800 this logarithm will be a large negative number. When this is solved numerically it is crucial to use the term on the right side of this equation and calculate the logarithm of each $i/(M+1)$ separately in a loop and sum up all the results. It is not possible to compute the left side of the equation with a computer program directly due to the limited accuracy of standard computer variable types which results in the calculation of the undefined $\ln(0)$. Each single $n/(M+1)$, however, is not too small so that the logarithm delivers reasonable values which can be handled by the code.

In a next step, which is illustrated in Fig. 5.1, the algorithm has to iterate over almost all time bins $m_{\mathrm{cp}} = \{1, 2, ..., M-1\}$, split the event sequence into two blocks at that bin (events in time range $[1, m_{\mathrm{cp}}]$ and events in range $[m_{\mathrm{cp}}+1, M]$) and calculate the two-block log-likelihood. This is just the sum of both one-block likelihoods:

$$\ln\left(\mathcal{L}_2(m_{\mathrm{cp}}, M, N)\right) = \ln\left(\mathcal{L}_1(m_{\mathrm{cp}}, n_{\mathrm{cp}})\right) + \ln\left(\mathcal{L}_1(M - m_{\mathrm{cp}}, N - n_{\mathrm{cp}})\right) \tag{5.2}$$

During one loop, we add the number of events, belonging to a time bin, to the sum of events found in all the time bins before. This will result in the number of events n_{cp} at this changepoint.
According to Equ. (4.41) it is necessary to subtract the log-likelihood of the one-block model from the $\ln\left(\mathcal{L}_2(m_{\mathrm{cp}}, M, N)\right)$ before starting the new loop at the next time bin $m_{\mathrm{cp}}+1$. This difference was called $\psi_{M,N}(m_{\mathrm{cp}}, n_{\mathrm{cp}})$ in the preceding chapter (see Equ.4.42). If one wants to calculate the odds ratio as a fraction between two likelihoods instead, as it is indicated by the second term of Equ. (4.41), one will suffer again from the limitations of standard variable types which are not able to store such large values accurately. Therefore we us $\psi_{M,N}(m_{\mathrm{cp}}, n_{\mathrm{cp}})$.
In the final step we use the result of the difference $\psi_{M,N}(m_{\mathrm{cp}}, n_{\mathrm{cp}})$ between the log-likelihoods as an exponent over e and calculate the mean of all those outcomes

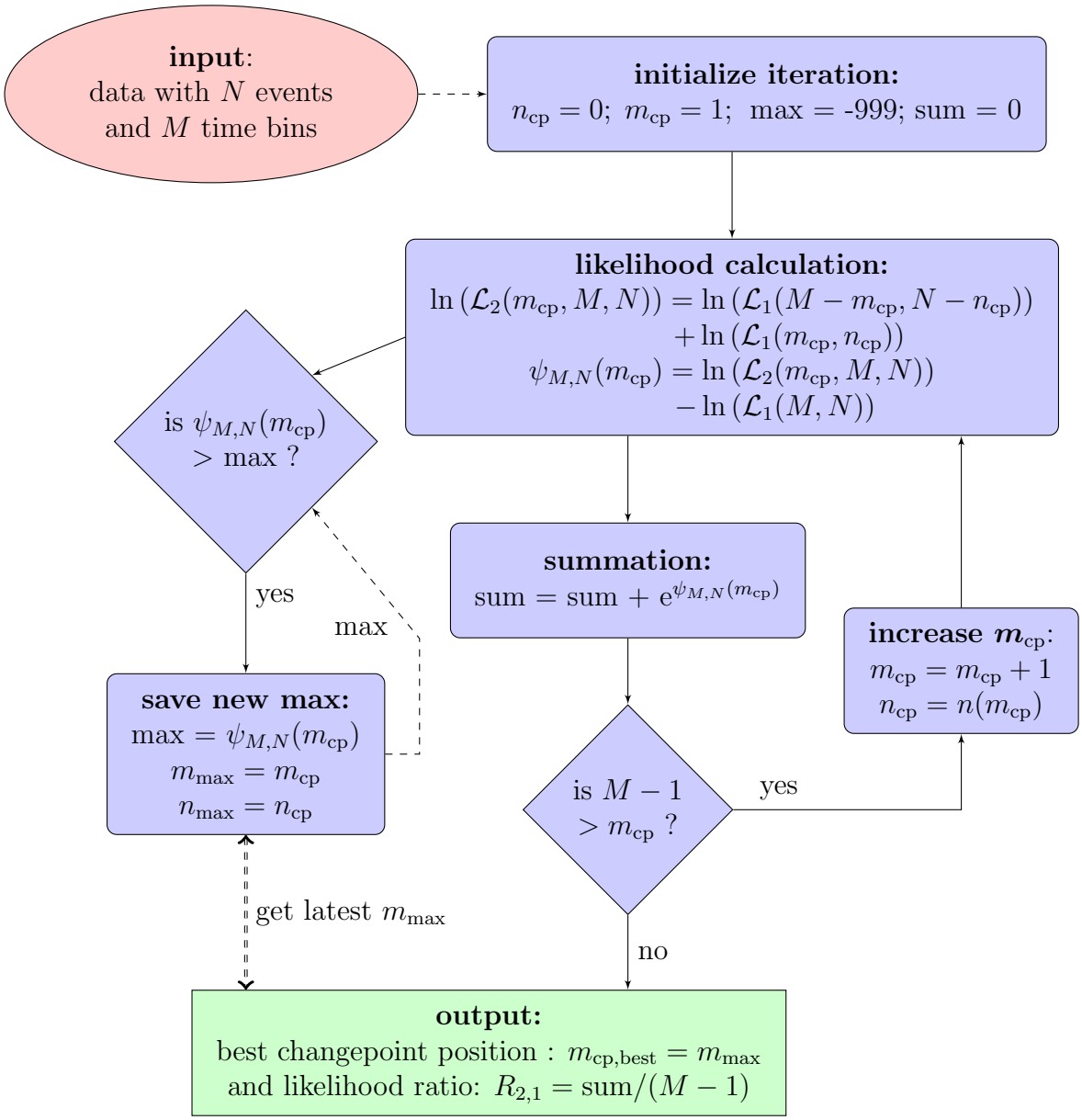

Fig. 5.1: *Flowchart of the iteration processes inside the Bayesian-blocks mechanism: Give an event sequence with N events in M time bins these processes determine the likelihood ratio $R_{2,1}$ and the time bin $m_{\mathrm{cp,best}}$ where splitting the data in two blocks is most probable. The solid lines show the direction of the process sequence, the dashed lines show the transfer of values from one process to another and the double dashed line represents a readout of a stored value.*

during the iteration over $M - 1$ time bins. This mean value represents the final odds ratio between the two different models. Due to the large values it was more convenient to use the logarithm of the odds ratio as final result. Unfortunately this value doesn't follow a standard normal distribution which is reason why we have to examine its distribution for random event sequences simulated with a constant rate which will be described later.

An additional feature of the Bayesian-blocks method is the ability to determine the time bins where the rate changes. This is done during the iteration over the time bins and the calculation of each $\ln(\mathcal{L}_2(m_{\mathrm{cp}}))$. If this value was bigger than the largest one calculated so far during one of the preceding loops the actual $\ln(\mathcal{L}_2(m_{\mathrm{cp}}))$ will be stored in the code as the new maximum and the according time bin m_{cp} as the new best separating changepoint $m_{\mathrm{cp,best}}$. After iterating over all bins, there will be a remaining $m_{\mathrm{cp,best}}$ which represent the point where a separation of the event sequence into two blocks, described by different rates, would be most probable.
When the first iteration, over all time bins, is finished the outcome covers the logarithm of the odds ratio and the bin number of the best block separation: $m_{\mathrm{cp,best}}$. To find two additional changepoints the event sequence gets split into two blocks at $m_{\mathrm{cp,best}}$ and the whole procedure is repeated for each block separately.

After the execution of the whole Bayesian-block algorithm one will obtain the best block separation bin $m_{\mathrm{cp,best}}$ together with the odds ratio calculated for the whole event sequence. Furthermore the output includes the two additional changepoints ($m_{\mathrm{cp,best,1}}$, $m_{\mathrm{cp,best,2}}$) together with two odds ratios, calculated for each of the resulting blocks that have been determined by the $m_{\mathrm{cp,best}}$ during the first iteration. As additional information we keep the information of the number of events in each of the three blocks, their duration in units of time bins and the number of events before the best block separation bin inside that block.

5.1.3 Input parameters and options

Rate and duration of signal and background: As input parameters, one can choose the duration T and the rate of the background events λ_{bkg} triggered, but not necessarily getting readout, by the telescope system from arbitrary directions as well as the rate λ_{sig} and the duration $T_{\mathrm{sig}}(< T)$ of signal events getting reconstructed in a narrow but random area of the field-of-view.
Because the goal of this study was to compare different statistical methods in case of a transient source, T_{sig} will always be chosen to be much smaller than the duration of the background events. While the duration T_{sig} is defined, the start time of the first signal event will be picked randomly by the program because we aren't interested in a particular time when a flare occurred, but just by its duration compared to the overall observing time. A typical distribution of events in time, where an additional transient signal has been added, is shown in Fig. 5.2 (bottom). In this figure we show two examples representing two different signal durations T_{sig} (150 sec and 350 sec) while the remaining input parameters are the same.

Signal spread and background efficiency: The size of the signal area will be defined by the signal spread parameter which takes account of the limited angular resolution. The default value is 0.14° which represents the average resolution at a energy of 200GeV. In Fig. 5.2 (top) we compare the effect of different signal spreads by looking at the position maps, whose bins contain the number of all gamma-ray-like events getting reconstructed at the position of that bin. This map is also known as the *ON-map* (see subsection 2.4.4)
The background efficiency parameter is the same as 1-f_{loss}. With this parameter

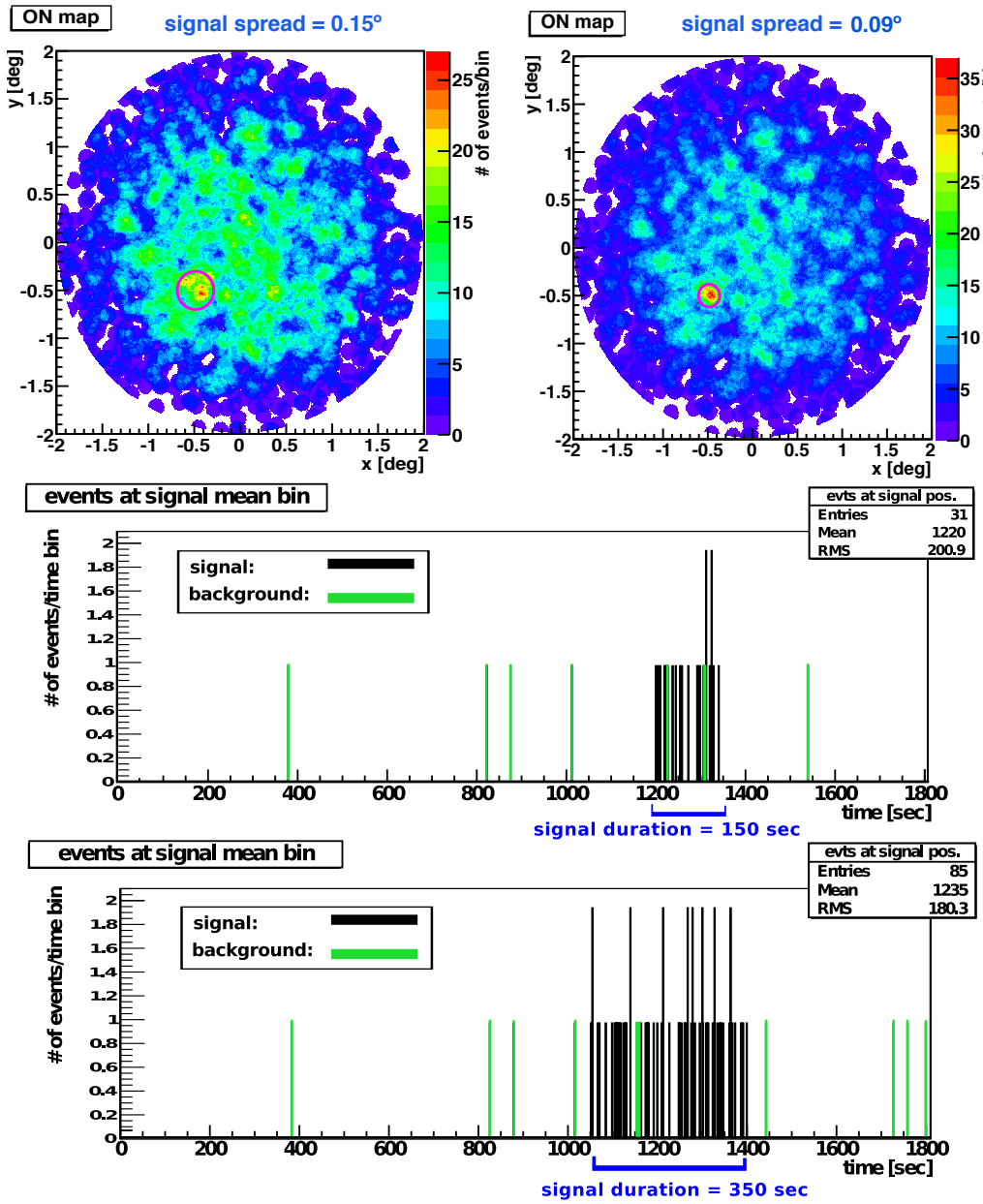

Fig. 5.2: *Comparison of different angular resolutions (top) and different signal durations (bottom). For both ON-maps we chose:* $T = 1800$ *sec,* $\lambda_{\rm bkg} = 500$ *Hz (true rate* $\gg$ *gamma-like rate),* $f_{\rm loss} = 99.7\%$*,* $\lambda_{\rm sig} = 0.4$ *Hz and* $T_{\rm sig} = 150$*sec. The magenta circle represents the position of the simulated signal and the simulated spread. One can see that the signal peak in left plot is less pronounced compared to the case of a smaller spread (*$= 0.09°$*) in the right map. The two bottom plots show the times of all transient signal events (black) and of all continuous background events (green) together, coming from the same position bin at the center of the magenta circle.*

one adjusts the number of background events in the final ON-map. By doing so, we simulate the process of background separation which is performed by the application of cuts on data. The effect of the cuts depends on the data and of course on the values of the cuts used in the analysis program. As a default value we use 0.011 for the background efficiency which represents the effect of typical cuts optimized for sources with a soft spectrum and used during the analysis of actual VERITAS data.

Different Bayesian-block algorithms: Further options are the choice between the Bayesian-blocks method looping over each possible time bin (*continuous method*) or jumping just from filled bin to the next filled one (*discrete steps method*) assuming there is no change of the likelihood in between (Fig. 5.3). See also Equ. (4.39) and Equ. (4.40). The first method is of course faster but not as accurate as the second one. If the number of events in the time vector of each position bin is small the difference in the processing time is also small. The larger the number of events gets, the larger will be the effect of saving some processing time. If one analyzes a strong and non variable source where almost each time bin contains one or more events ($N \geqslant M$) the two methods are equal and there is no time saving. But usually only the bins at the position of a self generated Monte Carlo signal or at the position of a real source (= center of ON-map) are filled with lots of events.

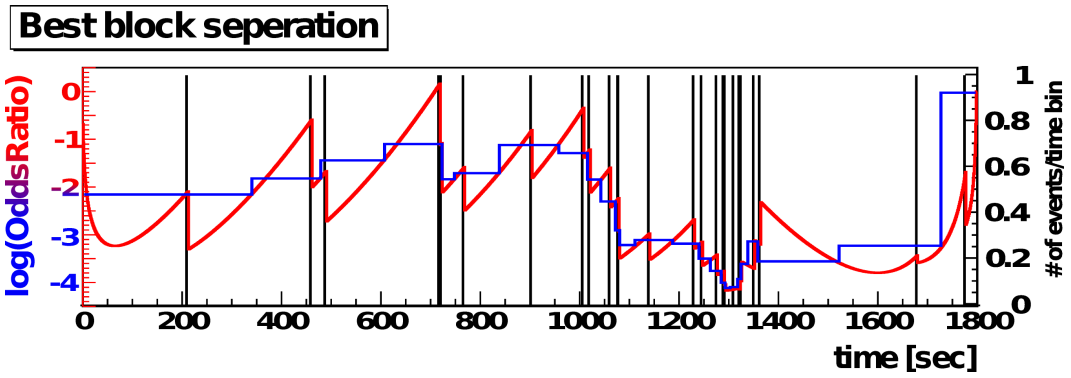

Fig. 5.3: *This plot shows the two different Bayesian-block algorithms with the y-axis representing the logarithm of the odds ratio $\psi_{M,N}(m_{\rm cp}, n_{\rm cp})$ (see Equ. (4.42)). The vertical black lines mark the exact times of all events that got assigned to the same position bin. Assuming each time bin on the x-axis could be a possible change point $m_{\rm cp}$ separating the sequence of events in two parts, the red curve shows the continuous $\psi_{M,N}(m_{\rm cp}, n_{\rm cp})$-function calculated at all time bins (see Equ. (4.39)). The spikes mark the times when there is an event. The blue curve, however, is produced under the usage of Equ. (4.40), assuming that the only relevant changes in the odds ratio occur between two events. This procedure is less accurate but faster. In this example both algorithms found the changepoint ($\psi_{M,N}(m_{\rm cp}, n_{\rm cp}) = max.$) at the same time bin ($m_{\rm cp} \approx 720$ sec).*

Some further parameters and options dedicated to read external data files and to improve the processing speed will be explained in detail in A.

5.2 Output of test statistic and best block separation

5.2.1 p-value of Bayesian-blocks method

Before we compare the different methods it is necessary to point out that the results of the Li&Ma equation (Equ. 4.9) and the exp-test (Equ. 4.19) calculated at all position bins is distributed like a normal distribution ($\sigma = 1$) if there is no signal.

Hence, each result with a value of more than five will be considered as a signal detection, depending on what is defined as a the signal one is looking for - number of events (Li&Ma) or variability (exp-test). The result of the Bayesian-block algorithm, however, is the logarithm of a likelihood ratio: $\ln(R_{2,1})$ from Equ. (4.41) with a distribution that cannot be described by a Gauss curve, even if the null hypothesis is true and there is no transient signal in the tested dataset. For this reason it is not possible to compare the output of the Bayesian-block method directly with the ones from the other two methods and we have to use the *p-value* instead.
The p-value is a measure of how likely the outcome of a statistical test, the so-called *test statistic TS*, occurred by chance, assuming that the tested dataset just contains background events and no signal. It is the probability of finding a TS value equal or larger than the currently measured one under the condition that the null hypothesis is true (no signal) [Bender *et al.* (2007)].
If the distribution is known, which is true for the Li&Ma test and the exp-test, it is easy to calculate the p-value in advance just by integrating the related function from the measured TS value towards infinity. Unfortunately in the Bayesian-blocks case we don't know the function that describes the distribution. The goal is therefore the determination of the distribution and the related p-values by analyzing a sufficiently large set of Monte Carlo test samples. Each of those samples consist of events generated at random times but with a constant rate and time differences larger than the dead time of 0.0003 sec. In the end we get a p-value p_{BB} for each possible outcome of the Bayesian-block algorithm (= the TS_{BB} value). We store them in a histogram with a fine binning in the x-axis, which represents the TS_{BB}, and use it as a lookup table. In doing this, we are then able to read for each TS_{BB} value, measured during the analysis of an unknown dataset, the related $p_{\mathrm{BB}}(TS_{\mathrm{BB}})$ from the lookup table. For small TS_{BB}-values this is done by picking the corresponding bin from the histogram and reading its bin content. In the region of high TS_{BB}-values the estimation of the p-value is not very accurate due to low statistics. In this case we use an extrapolation to estimate the p-value. Therefore we fit an exponential function to the p-value histogram between the test-statistic values 2 and 4. The p-values for all $TS_{\mathrm{BB}} > 5$ will then be evaluated by this function.
The determined $p_{\mathrm{BB}}(TS_{\mathrm{BB}})$ can then be used to find the corresponding TS_{norm} value belonging to a normal distribution. Basically the whole procedure is a transformation of the TS_{BB} value from the Bayesian-block algorithm into a normal distributed TS_{norm} value, like the ones we get from the other two statistical tests. The calculation of the normal distributed TS_{norm} value related to a certain p_{BB} is done with the following equation:

$$TS_{\mathrm{norm}} = \sqrt{2} \cdot \mathrm{erf}^{-1}\Big(1 - 2 \cdot p_{\mathrm{BB}}(TS_{\mathrm{BB}})\Big), \tag{5.3}$$

$$\text{with: } \mathrm{erf}(x) = \frac{2}{\sqrt{\pi}} \int_0^x \mathrm{e}^{-x'^2} \mathrm{d}x'$$

and with $\mathrm{erf}^{-1}(x)$ which is the inverse of the *error function* $\mathrm{erf}(x)$.

Analyzing a small set of test samples we realized that the distribution of the TS_{BB} and the related p_{BB}-histogram depend on the choice of the input parameters. Therefore it was inevitable to perform the Monte Carlo tests for all possible combinations of N (= number of events) and M (= number of time bins) and get a different p-value histogram for each combination: $p_{\mathrm{BB;\,N,M}}$.

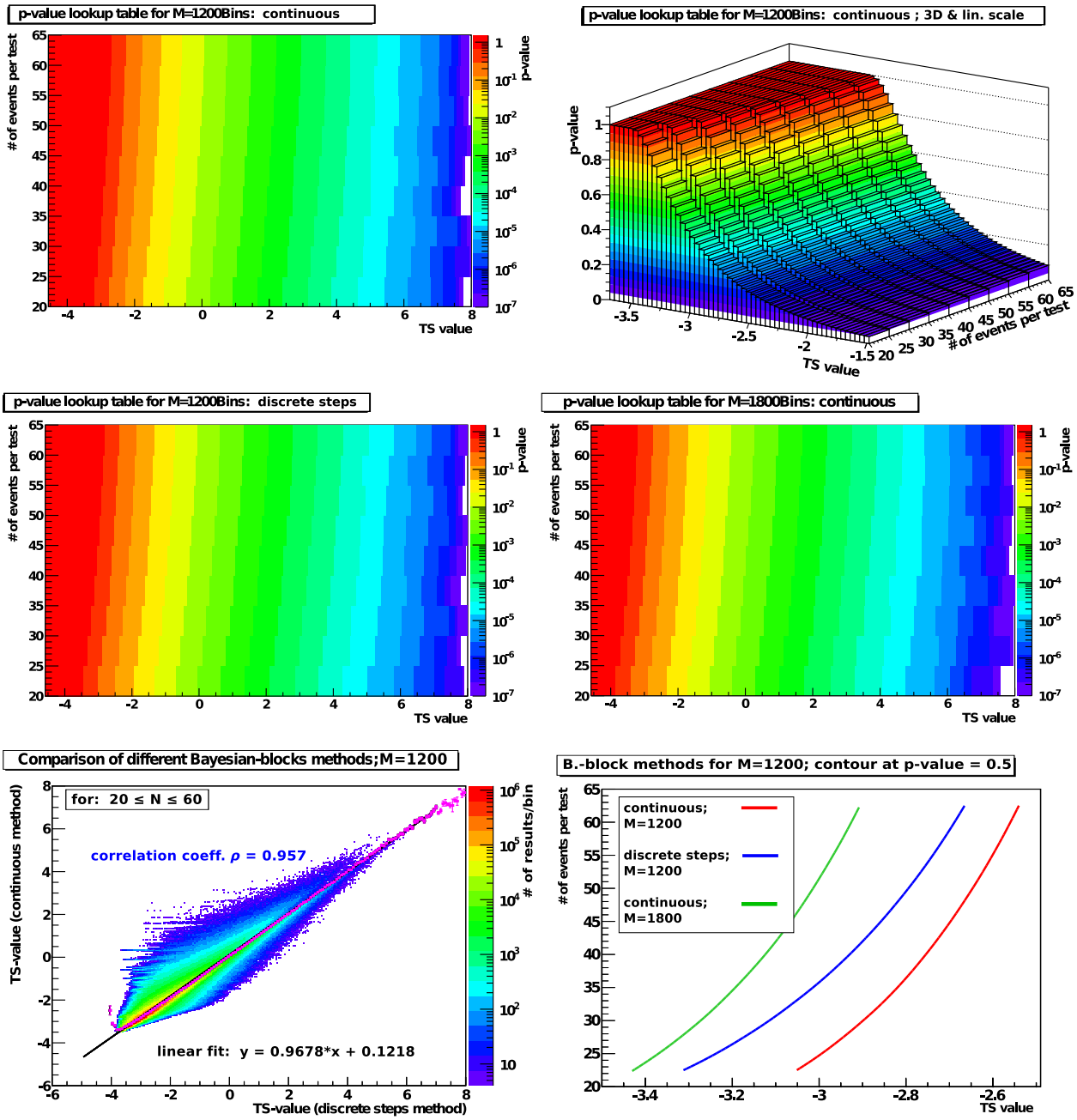

Fig. 5.4: *Comparison of different p-value lookup tables generated for* $20 \leqslant N \leqslant 60$. *In the top section of the figure two representations of the same lookup table (M=1200; continuous method) are pictured: two-dimensional with a logarithmic color scale representing the p-value (right side) and a 3D plot of a small TS-value range with a linear p-value on the z-axis (left side). The middle section shows the 2D lookup table for the same N range but generated under different conditions: M=1200 and the discrete steps method (left side) and M=1800 together with the continuous method (right side). For a better comparison the contour at p-value=0.5 of all those three lookup tables is drawn together in the diagram on the bottom left. On the bottom right is a 2D histogram showing the correlation between the two different Bayesian-block methods for each tested event sequence. The y-axis represents the TS value of the continuous method and the x-axis represents the TS of the discrete steps method. Due to the strong correlation* ($\rho \approx 1$) *we can assume a linear relationship between the two TS-values and fit the means of the y-bins (magenta dots) for each x-bin with a linear function (black line).*

Due to the fact that we want to obtain a high statistic, even for large TS_{BB} values, we generate 10^7 test samples per N-M-combination. Hence, if N is large ($\approx 400-800$) the duration of all 10^7 tests for just one combination can take up to a day even if the process is parallelized. To reduce the amount of processing time we limit the available values for M to 1200 and 1800. With a bin width of 1 sec these values represent the typical durations of a VERITAS run. Further reductions are achieved by not simulating each N, especially if they are large. If during the analysis of a unknown dataset a sequence of events occurs with a number N_{test} for which there is no suitable $p_{\mathrm{BB;\,N,M}}$-histogram available in the lookup table file, two other p-value histograms got selected: $p_{\mathrm{BB;\,N',M}}$ and $p_{\mathrm{BB;\,N'',M}}$ with N' and N'' being the next higher, respectively the next lower N referred to N_{test} and an interpolation is performed between them. It was therefore useful to store the p-value histograms of several consecutive N-values, calculated for the same M, together in a two-dimensional histogram to create a lookup table as can be seen in Fig. 5.4.
In the end we generated several lookup tables covering N-values in the range from 1 to 600. This is enough when we analyze data from the experiment, because the number of events during a run of 1800 seconds is rarely above 600 if the observed source is not exceptionally strong. Because we have the option of two different Bayesian-block algorithms: the continuous changepoint calculation (=default option) or the discrete steps method, we also have to produce different lookup tables for both algorithms.
In Fig. 5.4 one can see how the lookup tables change between different methods and numbers of time bins. Especially when we use a lookup table that was generated for a higher bin number M than the actual data was measured with. This is visible at the bottom right plot which shows the contour of the lookup table at the same p-value but for different M and different methods. The shape of the lookup table and the underlying distribution of the TS_{BB} for $M = 1800$ is equal to those generated for $M = 1200$ but with a shift of ca. 0.4 towards lower TS-values. Thus, for each TS-value calculated by the bayesian-block method for a specific M_{true} one will find a lower p-value than expected if one uses the lookup table generated for a higher M than M_{true}. This leads to an overestimation of the corresponding TS_{norm} which results in a distorted normal distribution making the comparison with the other statistical tests impossible.
With the diagram on the bottom left of Fig. 5.4 one is also able to probe the correlation between the outcome of both Bayesian-blocks methods. It is a two-dimensional histogram with the x-axis representing the TS-values from the discrete steps method and the y-axis representing the TS-values from the continuous method. In each bin we count the number of all those Monte Carlo tests for which the resulting pair of different TS-values correspond to the x- and y-values of this bin. By calculating the correlation coefficient ρ of this two-dimensional distribution we get $\rho \approx 0.957$ which represents almost perfect correlation ($\rho = 1$). It is therefore valid to describe the relationship between both TS-values by a linear equation. The parameters of this equation can be found by fitting a linear function to the mean values calculated for each x-bin taking into account the contents of all the bins along the y-axis that belong to the same x-value. We can see that the slope is almost one while the y-intercept is close to zero which means that most of the time the TS-value from the continuous method and the one from the discrete steps method are very similiar.

Later we will see if the relation between the exp-test results and the Bayesian-blocks results is also that strong or not.
Another important fact is the usage of extrapolations for TS_{BB}-values larger than 5. With increasing N all TS_{BB}-distributions, and therefore all p-value histograms, get shifted towards higher TS-values. We assume that this behavior is true for all TS_{BB} but due to limited statistics it cannot be expressed by the lookup table in the region of large TS-values as can be seen in the three two dimensional lookup tables in Fig. 5.4 . The idea is to fit the p-value histogram of each N separately between $TS_{\mathrm{BB}} = 2$ and $TS_{\mathrm{BB}} = 4$ with an exponential function and extrapolate this curve if it is necessary to get the p-value of a high TS_{BB}.

5.2.2 significance maps and distributions

After explaining the transformation of the TS_{BB} into a normal distributed test statistic we can describe the output of *timingSignificance* program. It is intended to provide an easy way of comparing the two different time-sensitive statistical tests with each other and with the standard sensitivity calculations (Li&Ma method, see sec. 4.1.2). Therefore the output consists, for each statistical method, of a two-dimensional significance map, containing the test result calculated at each position bin in units of standard deviations σ, and the one-dimensional distribution of the test results of all bins, also in units of σ. The test results measure the deviation from the null hypothesis, which is the assumption that there is no signal in the analyzed position bins. It is necessary to understand that the hypothesis of "no signal" has diverse definitions for the different statistical tests. While for the standard method "no signal" has the meaning of measuring a number of events per position bin that is consistent with the number of background events at that position, the idea of "no signal" in the context of the time-sensitive tests is a sequence of events in time with a constant rate. Measuring a large value of the test result ($\geqslant 5\sigma$) will then also have different meanings. In case of the time-sensitive tests it tells us that the events coming from a source cannot be described by a constant rate and that the source has to be variable, if all other conditions during measurement stay constant. In case of the standard counting method a large test result just tells us that the number of events is too large to be made up by background events alone.

In Fig. 5.5 we show the ON-map that contains all the simulated events in the whole field-of-view, the temporal distribution of all events found at the position bin where the signal was generated and the output of the three different statistical methods used to analyze a simulated transient signal and its background. For the generation of the Monte Carlo events we use the following parameters: $T = 1800$ sec (and a time-bin width of 1 sec $\Rightarrow M = 1800$), $\lambda_{\mathrm{bkg}} = 330$ Hz, $f_{\mathrm{loss}} = 98.9\%$, $T_{\mathrm{sig}} = 150$ sec and $\lambda_{\mathrm{sig}} = 0.4$ Hz.
On the left side of the figure there are all the significance maps displaying the test results measured at each position bin and on the right side there are the corresponding distributions of these test results. The black histogram shows the test result distribution of all bins in the significance map while the red histogram just takes the bins inside the signal region around the signal position (black circle) into account. The size of this region corresponds to the signal spread for which we choose a value

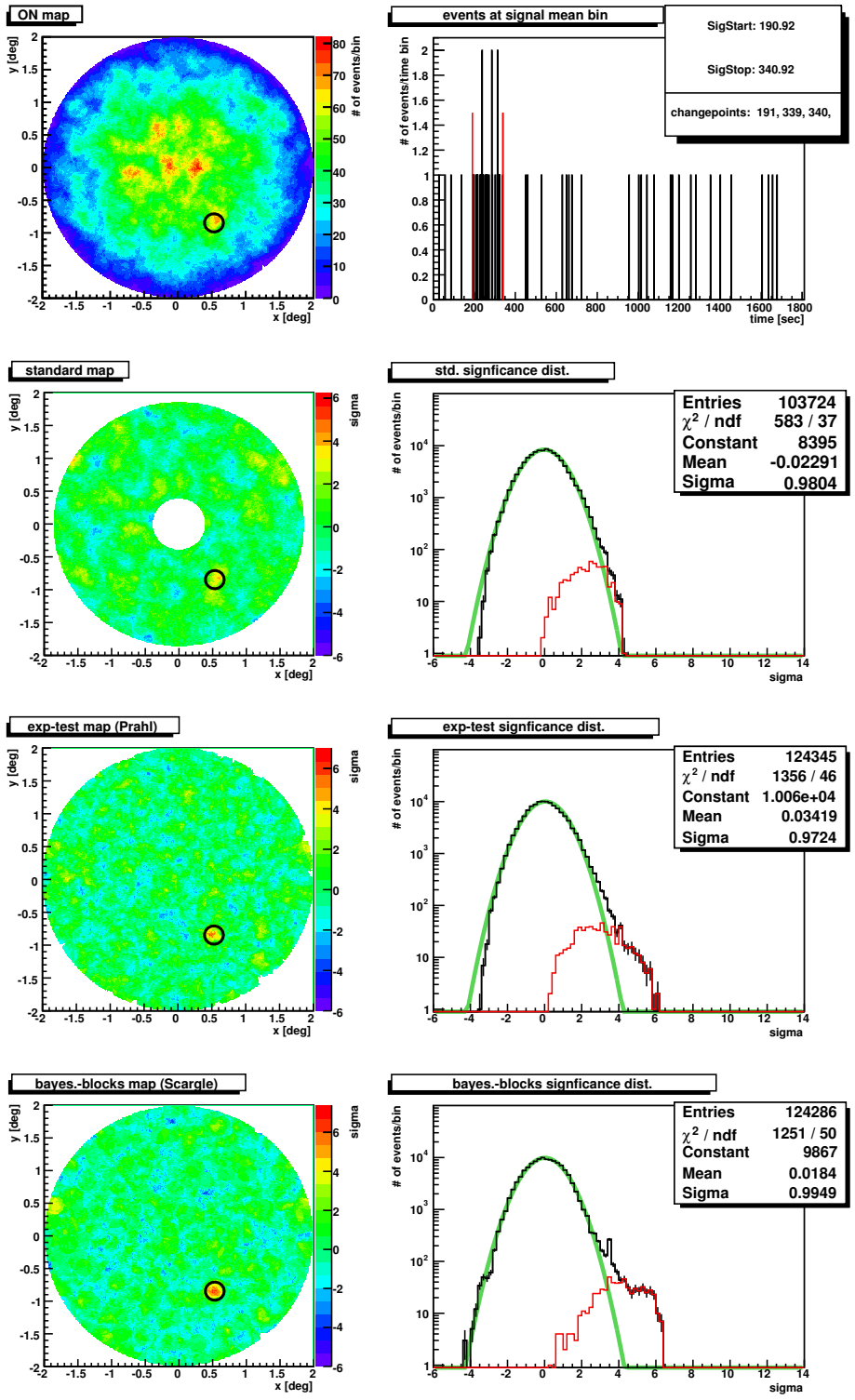

Fig. 5.5: *The two plots on top show the ON-map containing all the events (left) and the distribution of all the events of the central MC-signal position bin along the time axis (right). Below the output of the three different statistical tests is shown: standard on-off method (top), exp-test (middle) and Bayesian-blocks test (bottom). On the left side the significance maps can be seen which display the significance calculated at each position bin in units of standard deviation. The x- and y-value define the deviation of the incoming photon from the optical axis in degrees. The black circle marks the signal region and represents a signal spread of* $0.14°$*. On the right side there are the corresponding one-dimensional histograms representing the distribution of the TS-values of all bins in the significance map (black) and the distribution of solely the bins in the signal region (red).*

of 0.14°. This represents the angular resolution of a source with a soft spectrum. Additionally we allow correlation[2] between bins closer than $\theta = 0.141°$ to each other. The square of this distance is $\theta^2 = 0.02(°)^2$ which corresponds to the value of the θ^2-cut used during former standard analysis of soft spectrum gamma-ray sources to distinguish the concentrated signal events from the background events with arbitrary directions. It also defines the size of the OFF-region areas necessary for the reflected region background estimation during the standard significance test.
One can convince oneself by looking at the green fit function in each of the three black histograms that the TS-values (in units of the standard deviation σ) are normally distributed for all bins in the map besides those ones that are inside the simulated signal region. All TS-values in this region deviate from the normal distribution as can be seen in the red histogram where all bins with TS-values higher than 5 are considered as a signal detection.

For the standard method a detection means that the amount of events at the signal position bin is significantly ($> 5\sigma$) higher than the number of events estimated as background at this position. This is not the case in Fig. 5.5 where the highest value inside the signal region is only around 4σ. Obviously the duration of the signal is too short to provide a large enough number of events to get detected with the standard method.
The time-sensitive tests however don't compare the number of signal events against the background events but looking for rate fluctuations instead. Getting high TS-values is therefore not a detection of a significantly larger amount of gamma-rays but a detection of fluctuations stronger than expected for background with constant rates. In our case here we are able to detect the signal with both time-sensitive methods due to its strong fluctuation and not due to the number of events. The strength of the fluctuation depends on how short the signal duration T_{sig} is compared to the overall duration T and how much the rate changes due to the additional signal events. Contrary to this, observing a strong source that has a constant rate during the time of measurement T will of course be detected by the standard method but will not lead to a detection by the time-sensitive methods. Therefore one goal of this study was to measure the detection capability of the three methods for different combinations of signal rate and signal duration.

5.2.3 Change points from Bayesian-blocks method

An additional feature of the Bayesian-blocks method is the possibility to find the times, the so-called *changepoints*, when there are sudden changes in the rate due to additional events coming from a flare. In the top plot of Fig. 5.6 one can see the sequence of events occurring in the central signal position bin together with three red marks representing the changepoints found by the algorithm.
During this study we make the simplifying assumption that the rate of events coming from a transient source is constant as long as the flare is active and that the rate of the background events during the rest of the time is constant as well but much lower. Therefore it would be enough to look for not more than two changepoints

[2]for further details on correlation/smoothing read section A.1

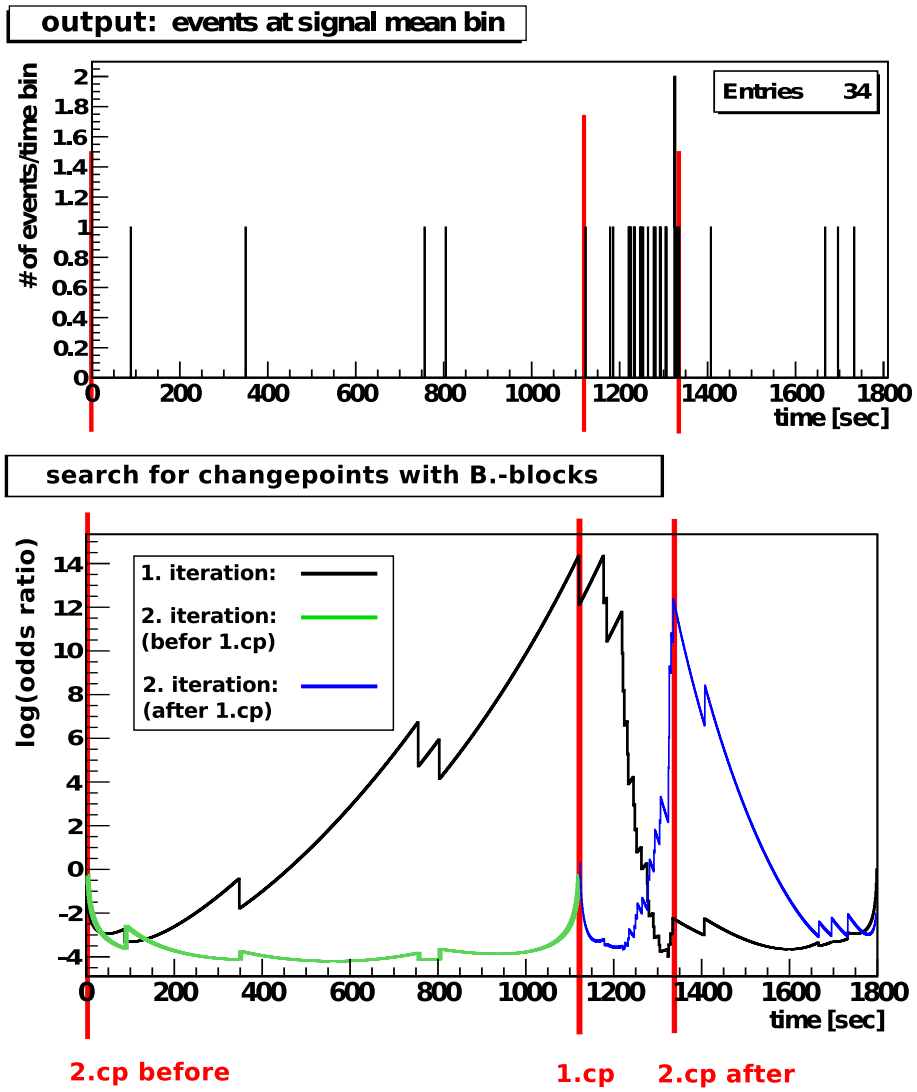

Fig. 5.6: *Representation of the best block separation. In top plot one can see typical output from the analysis program showing the times of all events assigned to the position bin at the center of the signal region. The red marks define the changepoints which divide the event sequence into three blocks. In the bottom plot it is visualized how the algorithm finds these changepoints: During the first iteration of the continuous Bayesian-block algorithm the logarithm of the odds ratio is calculated for each time bin being the potential separator (black curve). The value of this curve can be interpreted as the probability to split the data in two parts at this time bin. The bin where the probability reaches its maximum is then called the first changepoint (**1. cp**). In a second iteration the Bayesian-block algorithm is used again for each of the two subintervals, before (green curve) and after the 1.cp (blue curve), separately to search for additional changepoints:* ***2.cp before*** *and* ***2.cp after****.*

marking the start and the end of the flare and separate the whole measured time into three blocks: just background before the flare starts, background and signal during the flare and just background after the flare.
By looking at the black curve in the bottom plot of Fig. 5.6 one can see the logarithm of the odds ratio calculated for each time bin during a first iteration of the

continuous Bayesian-blocks analysis over the whole event sequence. The maximum of this curve would define the position in time where a separation into two blocks would be most probable. In this example the signal rate is 0.4 Hz and the randomly generated start and end time of the signal are 1196 sec and 1346 sec while the background starts at 0 sec and ends at 1800 sec. The maximum is found at 1122 sec which then defines the first changepoint that separates the event sequence into two blocks. To find more changepoints our approach is now to repeat the Bayesian-block algorithm for each block separately. The output of these second iterations, before and after the first changepoint, are presented by the green and the blue curve in the same plot. Again two different maximums, at 1 sec and 1336 sec, are found marking the positions of the two changepoints from the second iteration.
In the end one gets three changepoints splitting the event data into four blocks. But as we analyzed a simulated event sequence here that had a constant high signal rate a block separation of not more than the above mentioned three blocks is enough. Therefore two of the three changepoints confine the block that contains the signal events while the third one just marks the beginning or the end of the overall background time T. In this example the block containing the simulated flare is supposed to be between 1122 sec and 1336 sec which is quite close to the actual start and end time (1196 sec, 1346 sec).
How good the changepoint estimation works depends on the strength of the fluctuation. If there is almost no sharp change in rate due to a weak source or a flare with a long raise and fall time it will be difficult to find the correct changepoints. In most of these cases they will be close to $t = 0$ sec and $t = T$, meaning that the best block separation would be just one big block containing all M time bins. Another problem occurs if the overall rate of events is so low that the algorithm will try to create blocks around the large areas of empty time bins, not regarding the whole sequence as a single block.

5.3 Analysis of Monte Carlo simulations

Within this section we will compare the different statistical test by applying them to simulations of transient sources as it was described in 5.1.1. The parameters concerning the signal event simulation, like λ_{sig} and T_{sig}, will be varied to figure out which of the three tests works best for which signal characteristics. The examined interval for λ_{sig} is [0.05 Hz, 0.5 Hz] and the one for T_{sig} is [10 sec, 420 sec]. The other parameters which describe the detector, the background and the analysis behavior are fixed in such a way that the position maps (= ON-map) will be as close as possible to the ones used during the standard event analysis of a real source.

5.3.1 Adjust simulation parameters

With the standard event analysis we mean the filtering of the data by cuts optimized for a source with a soft spectrum (i.e GRB, Blazar). For the soft source analysis simulation we adjust the size of the signal area to a value of 0.14° which represents the reconstruction error of gamma rays in the low energy range (E > 200 GeV). Further we set the correlation distance to $\theta = 0.141°$ ($\theta^2 = 0.02(°)^2$) which is the

θ^2-cut that is used during the analysis of soft sources. This parameter is also used as the size of the OFF regions in the reflected region background estimation.

It remains to choose the values for the total measured time T, the rate of background events λ_{bkg} and the background loss fraction f_{loss}. As there was an upgrade of VERITAS which took place in summer 2012 the number of triggered background events is much higher for measurements taken after the upgrade than for ones taken before the upgrade. For low elevations, between 30° and 50°, an average trigger rate after the upgrade is 330 Hz, while before it was around 180 Hz. We concentrate on low elevations because transient sources like GRBs appear more likely under a low elevation due to the larger fraction of sky that is observable.
Also the loss fraction is different for different VERITAS states. While 99.7% background events get removed from data that was taken before the upgrade it is only 98.9% for post-upgrade data taking into account the same cut values for both datasets. However, these loss fractions are just estimates, which we determine by comparing several ON-maps generated during simulations with the ones we get from the analysis of different data (pre- and post-upgrade) under usage of the same soft spectrum cuts: Number of triggered telescopes $\geqslant 2$; $\theta^2 = 0.02(^\circ)^2$; MSCW $\leqslant 0.35$; MSCL $\leqslant 0.7$; size of the second largest image $\geqslant$ 400d.c.; distance of reconstructed impact from array center $\leqslant$ 250m.
The last parameter that has to be adjusted is the background duration which is the same as the duration of the run. During pre-upgrade times a typical run duration was 1200 sec. After the upgrade we took longer runs and the new standard is 1800 sec.
In the end we have two different parameter selections accounting for two different VERITAS states:

- pre-upgrade: T = 1200sec, $\lambda_{\text{bkg}} = 180\text{Hz}$, $f_{\text{loss}} = 99.7\% \rightarrow \lambda_{\text{bkg,S}} \approx 0.003\text{Hz}$
- post upgrade: T = 1800sec, $\lambda_{\text{bkg}} = 330\text{Hz}$, $f_{\text{loss}} = 98.9\% \rightarrow \lambda_{\text{bkg,S}} \approx 0.018\text{Hz}$

The value for the average background rate at the signal position $\lambda_{\text{bkg,S}}$ is calculated by subtracting the loss fraction from the rate and by multiplying this result with the fraction of the signal area compared to the whole field-of-view:

$$\lambda_{\text{bkg,S}} = \lambda_{\text{bkg}} \cdot (1 - f_{\text{loss}}) \cdot \theta^2/(2^\circ)^2$$

Finally we have to set the optimization parameters, which are responsible for the process splitting and for the choice between the two Bayesian-blocks methods. We select the equal process splitting and the continuous bayesian blocks method because the overall time T and the amount of signal events are relatively small so by using the discrete steps method instead we would just gain a little bit in processing time but definitely lose some accuracy on the other hand. Because we are only interested in the outcome of the time sensitivity tests applied to events inside the signal region we use the parameter dedicated to restrict the analysis to a small area around the signal position which reduces the overall processing time.

5.3.2 Simulation of different signal characteristics

As it was mentioned at the beginning of this section we chose one of the two parameter-sets and vary only the signal rate λ_{sig} and the signal duration T_{sig}. The idea was to choose the range [0.05 Hz, 0.5 Hz] with a step size of 0.01 Hz for λ_{sig} and the range [10 sec, 420 sec] with a step size of 10 sec for T_{sig}. For each of the 1600 different λ_{sig} and T_{sig} combinations we repeat the simulation 20 times with a different random seed before we move on to the next combination. As an example on can see in Fig. 5.5 the output of a single simulation for a specific combination of λ_{sig} and T_{sig}.

From each of those simulation outputs one is able to extract the calculated significance at the bin of the simulated signal position, which is of course also randomly distributed. As we use three different methods we get three different significance measurements from the same simulation output. We visualize the significance as

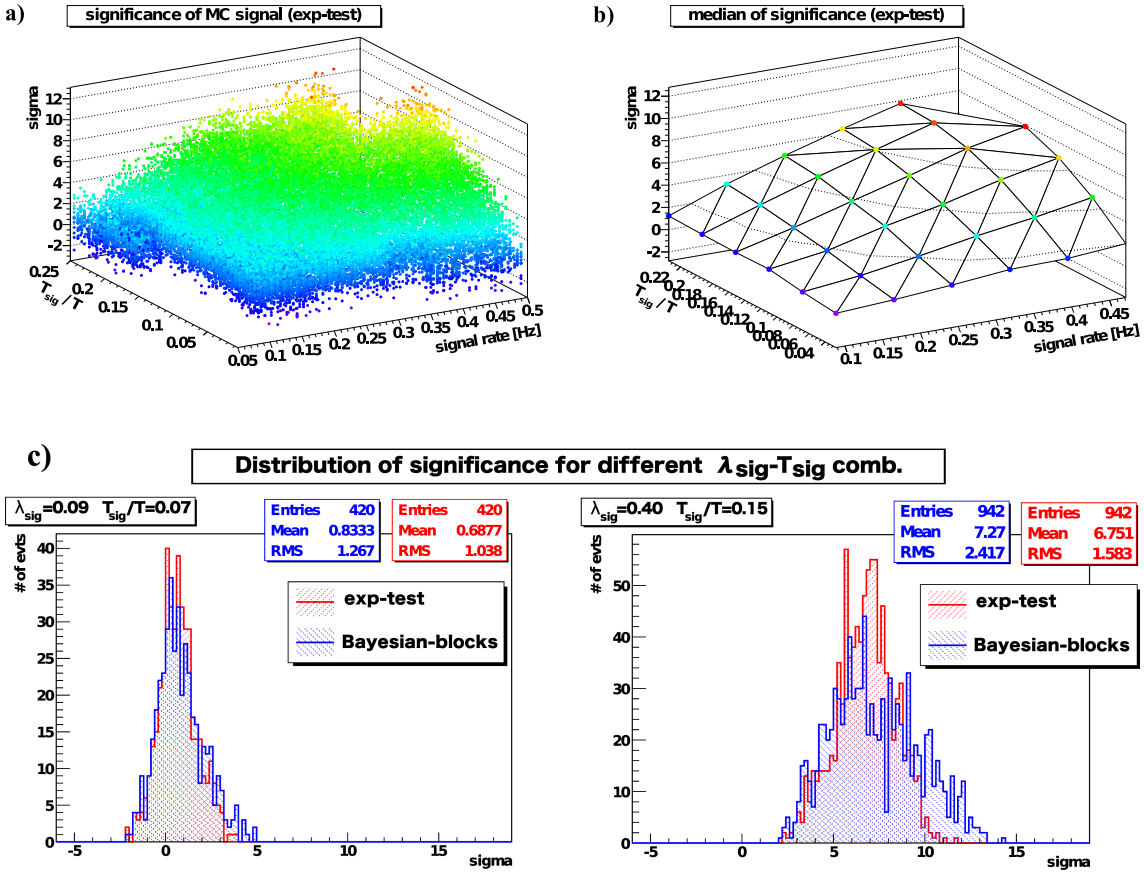

Fig. 5.7: *Significance calculations by the exp-test applied to 32 000 Monte Carlo simulations of 1600 different λ_{sig}-T_{sig}-combinations (a) and the median of the distribution along the z-axis for different λ_{sig}-T_{sig}-combinations merged into larger bins (b). The signal duration is presented in the form of a ratio T_{sig}/T on the y-axis. This makes it easier to compare different scenarios with different observing durations T.*
The two bottom plots (c) show the distribution of all significance values (exp-test = red; Bayesian-blocks = blue) belonging to a certain point in the plot on the top right of this figure. We choose the two examples of ($\lambda_{\text{sig}} = 0.09$; $T_{\text{sig}}/T = 0.07$) and ($\lambda_{\text{sig}} = 0.40$; $T_{\text{sig}}/T = 0.15$)

multiples of standard deviations σ on the z-axis of a three dimensional diagram where the x- and y-axis represent the input parameters used to generate this simulation: the signal rate λ_{sig} on the x-axis and the ratio of T_{sig}/T as the y-axis. For each method we get a separate diagram.
In Fig. 5.7,a one can see the significance calculated with the exp-test method of all simulated signals. For the background generation we use the parameters simulating the post-upgraded state (see 5.3.1). The significances for signals with the same rate and same duration are stacked on top of each other along the z-axis. For comparison reasons we determine the median of the significance distribution along the z-axis for different combinations of rate and duration. To get higher statistics we combine the results of different λ_{sig}-T_{sig}-simulations in larger bins. Each bin covers an area in the λ_{sig}-T_{sig}-parameter space with a size of $\Delta\lambda_{\text{sig}} = 0.08$ Hz and $\Delta T_{\text{sig}} = 70$ sec. In the end we have 6×6 measurements of the median as is shown in Fig. 5.7,b. We use the median instead of the mean because the distribution of significance measurements is not always close to a normal distribution and can be asymmetric for some areas in the parameter space, which can be seen in the two plots at the bottom of Fig. 5.7. For the calculation of the median and its 68% confidence interval we refer to appendix B.4. Besides the diagram in Fig. 5.7,b we will then also create two more diagrams: one for the upper confidence limit and one for the lower confidence limit.

Contrary to our initial idea the number of signal simulations is not evenly distributed over the whole λ_{sig}-T_{sig}-parameter space. This is because we reduced the amount of simulations for regions of the parameter space with significance results much lower than 5σ or much higher than 5σ and concentrate more simulations on the part of the parameter space whose significance measurements will be close to 5σ. At the end this whole simulation procedure will be repeated for a different background simulation representing the pre-upgrade state.

5.3.3 Comparison of methods

Correlation between methods

In the section above we described our test setup to compare the three different methods. For each simulated signal we get three different significance measurements. If we take now several signals and plot for each signal the significance of one method against the significance of another method we are able to measure the correlation of the different methods. Therefore we select all the simulations that had been used to calculate one of the points in Fig. 5.7,b , plot them in a two-dimensional histogram, where each axis represents the significance measurement of one of two different test methods, and calculate the correlation coefficient ρ. We repeat this procedure for all points in the parameter space of Fig. 5.7,b and end up with a set of two-dimensional histograms as can be seen in Fig. 5.8.
In this example we compare the Bayesian-blocks method (y-axis) with the exp-test method (x-axis) in case of the post-upgrade state. The diagonal line, which represents the situation when both methods lead to the same significance measurement for a simulated signal, is plotted as well to guide the eye. If a large fraction of points

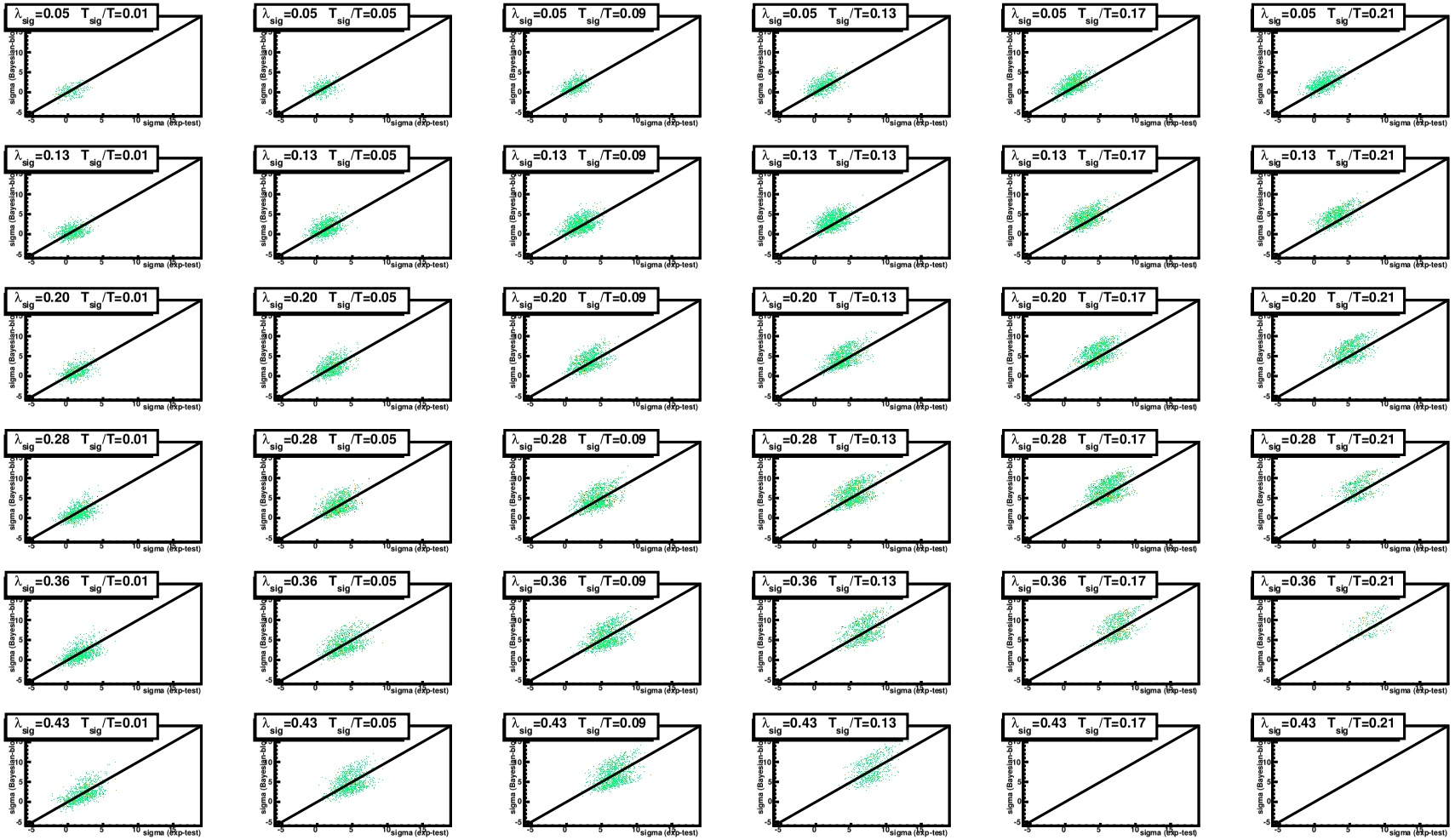

Fig. 5.8: *Correlation between Bayesian-blocks method and exp-test method tested on Monte Carlo simulations of different signal characteristics. The signal varies in* λ_{sig} *and* T_{sig} *while the remaining simulation input parameters stay fixed as described in subsection 5.3.1 (soft spectrum cuts & post-upgrade state* $\Rightarrow T = 1800sec$*). Each histogram contains the information of all the simulations inside the parameter space that is centered around the* λ_{sig}*-*T_{sig}*-combination written in the histogram title. The x-axis in each histogram represents the significance (in* σ*) calculated with the exp-test while the Bayesian-blocks significance is represented by the y-axis.*

is above that line one can say that on average the Bayesian-blocks method results in a higher significance than the exp-test for this part of the λ_{sig}-T_{sig}-parameter space. If a large fraction is below then the exp-test method is better. This can be also visualized by printing the difference between the medians of each method for that part.
By looking at Fig. 5.8 we further notice that the spread of both time-sensitive methods increases with higher significance medians. Also the correlation between both methods worsens when the median increases. On can also see that in average the Bayesian-blocks leeds to higher significance measurements when the signal rate λ_{sig} is small and the duration T_{sig} is quite long while the exp-test is slightly better for high λ_{sig} and low T_{sig}. But in the end it is very difficult to predict the output of an individual measurement by just knowing its input parameters.
For a better visualization we plot the values of the correlation coefficient and the difference between the medians for the different areas in the parameter space in separate histograms (see middle and bottom plots in Fig. 5.9). On the left side we simulated the VERITAS system before the upgrade and on the right side we simulated the conditions after the upgrade. The empty bins in the histograms represent the areas in the parameter space for which we didn't generate simulations. By looking at those histograms we see that on average there is a small correlation between the different methods. But together with the information of the median differences, which are plotted in the bottom histograms, we can conclude that the output of one method can never be predict by the output of the other method, which is why we keep on using both methods during the analysis of data in the next section.

Flare detection capability

The contour plots: As we are especially interested in the detection capability of the different methods we will concentrate more on the parameter space where the medians of each method is close to 5σ. Therefore we use the information from the right diagram in Fig. 5.7 and determine the contour of this distribution in the x-y-plane for a z-value of 5σ. When we do this for all three diagrams of the three different methods we get for each method a different contour which makes it easy to compare the detection capability of the methods in the parameter space (see top plots in Fig. 5.9). The upper right (shaded) part of these plots mark the parameter space where the methods on average detect a signal. Because we are working with the median the exact meaning is that in this region the significance measurements of more than 50% of the simulations of each bin exceed 5σ.
Of course we also want to estimate the error on the contour we determined for each method. Therefore we repeat the procedure with the confidence limits instead of the median values. It was explained in the preceding section how we calculate the 68% confidence interval of each median and that we stored the upper limits and the lower limits in separate diagrams. The three solid lines, or put it in another way, the three filled thin areas in the top plots of Fig. 5.9 define for each method the areas between the contour of the upper limit diagram and the contour of the lower limit diagram at a significance value of 5σ. The contour of the median lies inside these areas but is not displayed.
We will now analyze the contour plots in Fig. 5.9. The black shaded region defines

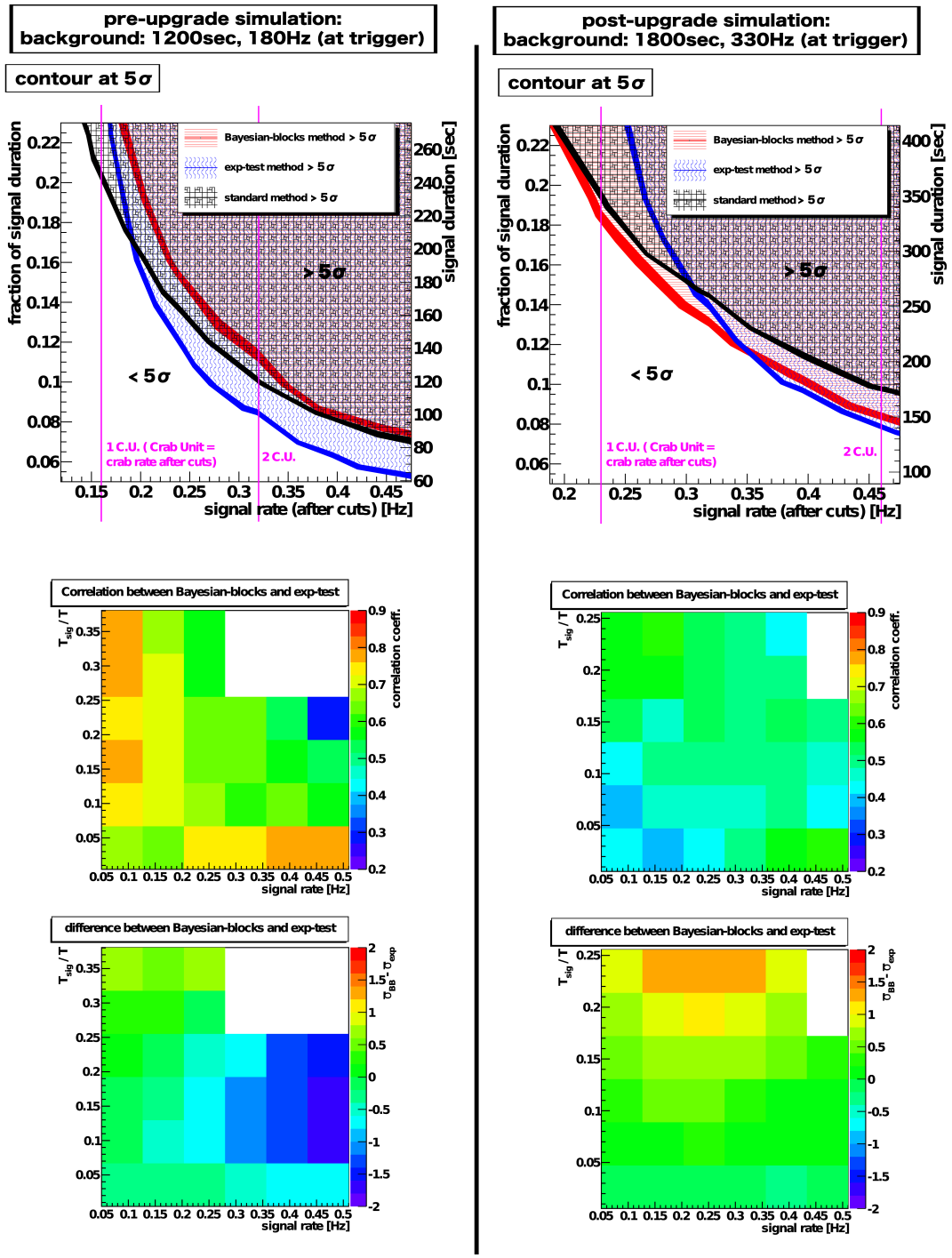

Fig. 5.9: *On the left side we see the results of simulations for a pre-upgrade conditions and soft spectrum cuts. On the right side the results for the same cuts and the post-upgrade simulation. Top: areas between the 5σ-contours of the upper limit diagram and the lower limit diagram for Bayesian-blocks (solid red), exp-test (solid blue) and standard method (solid black). The limits correspond to a 68% confidence interval around the median. The magenta vertical lines mark the typical rate of the crab source after cuts: 1 C.U. = one Crab unit. This rate is different for different VERITAS states.*
Middle: The color plots show the correlation coefficients between Bayesian-blocks and exp-test for each bin in parameter space (see Fig. 5.8) for which we generated MC simulations.
Bottom: Histograms displaying the difference between the medians of the Bayesian-blocks and exp-test significance in each bin.

the parameter space where a simulated signal is on average detected just due to its number of events which is significantly higher than the number of background events. The red and blue shaded areas mark the parameter spaces where the fluctuation in the event sequence, due to a short period of additional signal events, is on average strong enough to deviate significantly from the initial event sequence, simulated with a constant rate (= background). It is clear that for a large part of the parameter space both criteria are fulfilled by the same signals. Thats the area where all shaded areas overlap.
One has to keep in mind that the contour for each method just separates the parameter space in two regions. In the shaded one the probability of a detection is larger than 0.5 and in the white one the probability is 0.5 or lower. But even in the white area is a detection possible.
We can see that all methods detect a signal much better when we increase its rate λ_{sig}. It leads to more events, which is useful for the standard method, and to a sharper rate changes which is good for the time-sensitive tests. While the standard method will also detect a signal much better when we increase its T_{sig}, due to the growing number of events, the time-sensitive methods will reach their best performance for $T_{\text{sig}} < T$, because there would be no fluctuation if the signal is active during the whole observing duration. But this is not shown here because we just concentrate on the parameter space of flares much shorter than the entire run, like it would be the case for GRBs, Magnetars or some Blazars.

Compare different methods: Now we want to look closer at the regions where the methods show differences. In the pre-upgrade simulation plot, we see that the exp-test method performs better than the other methods in a region of larger signal rate and a short duration. So in this parameter space we detect a signal due to the fluctuation it causes and not by its number of events. However, for small rates and long durations the standard method is still better because the rate change is not significant enough to be detected by the time-sensitive methods. In this state the Bayesian-blocks method is worser than the other two methods and covers the smallest parameter space with its 5σ-contour.

If we look at the post-upgrade simulations the situation is quite different. Here the Bayesian-blocks method performs on average better than the standard method and the exp-test. Only in the region of high rates and short durations the exp-test is slightly more sensitive than the Bayesian-blocks method.
One information we can also get from both plots is the width of each contour. As explained above it describes the area between the two contour lines of the two confidence limits. Because the width of the Bayesian-blocks is larger than the one of the other methods in both plots, pre- und post-upgrade, we know that the spread of the Bayesian-blocks calculation in the parameter space along the contour is wider than for the other methods. This is due to the fact that this method will produce different results if the signal starts in the middle of a run or at the beginning or at the ending of a run (see sec.4.2.3 and Fig. 4.3). So if the whole event sequence stays the same and we would just move all events that belong to the simulated signal from the mid of a run to one of its edges we would change the output of the Bayesian-blocks method while the other two methods won't be affected. As we don't specify in our simulations when the signal should start and create this value randomly this leads to the additional spread of the Bayesian-blocks method.

Compare different VERITAS states: After comparing the single methods with each other, we also want to compare the detection performance for both VERITAS states in general. If we just look at the actual rates the situation for all methods appears to be much worser in the simulations of the post-upgrade state due to the higher background rate. But this is not true because we also expect a higher signal rate after cuts in the upgraded system. Therefore we print the magenta lines to visualize the Crab rate after cuts measured for these two VERITAS states. If a source has the same flux than the Crab nebula it will lead to the same rate as the position of the left line indicates and we say that the source has a flux of *1 Crab unit (= 1 C.U.)*.
If one compares just the area framed by the 1 C.U. and 2 C.U. mark (see Fig. 5.10) one will notice that the shape of the contour of the standard method and the exp-test is nearly the same for both VERITAS states. That means a signal with a strength of, e.g. 1.5 C.U., needs to be active for the same fraction of the whole run duration: T_{sig}/T (in this example: ca. 0.13) in both VERITAS systems to produce enough events to deviate significantly from the background. On can conclude that the benefit of a higher signal rate in the upgraded system got equally compensated by an also higher background rate.
We have to mention that both rates scale differently. While the signal rate λ_{sig} increases by a factor of 1.5 between the pre-upgraded state and the post-upgrade state, the background rate λ_{bkg} of the upgraded system is six time higher. This is due to the lower energy threshold that has been achieved by the upgrade and the fact that the amount of gamma-ray-like photons increases towards lower energies much more than the photons of a VHE gamma-ray source. As the different algorithms just

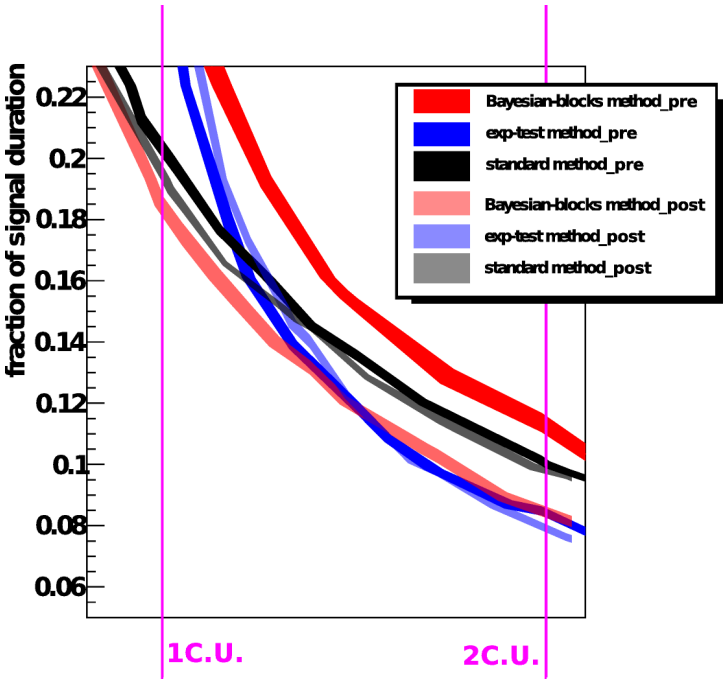

Fig. 5.10: *Combine all contours from different methods and different background simulations and scale it to the Crab flux. Contours are taken from Fig. 5.9 (top) with the same color code. The transparent lines mark the contours of the post-upgrade simulations.*

base on general Poisson statistics without including any special conditions that are related to the VERITAS system, it is a rather lucky coincidence, that the five-sigma contour-lines of the same method, but for different VERITAS states, are similar.

That we can not expect the same contour line ($\sigma = 5$) for different background simulations in general, can be explained easily on the basis of the standard Li&Ma method. If the background rate and the overall data taking duration T is fixed, which means the number of background events N_{bkg} is fixed, the number of signal events N_{sig} has to stay constant as well to provide the outcome of a certain significance value (see Equ. 4.9). In a simplification the contour of $\sigma = 5$ can than be described by $T_{\mathrm{sig}} = N_{\mathrm{sig},5\sigma}/\lambda_{\mathrm{sig}}$. To preserver the significance value the N_{sig} has to change according to N_{bkg} if this value varies for different background simulations. However the relationship between both numbers is not linear. We describe now both contours for different VERITAS states and figure out which condition has to be fulfilled that both curves are equal:

$$\text{fixed values: } \sigma = 5 \; ; \; N_{\mathrm{bkg}} = \lambda_{\mathrm{bkg}} T \tag{5.4}$$

$$\Rightarrow N_{\mathrm{sig}} = N_{\mathrm{sig}}(\sigma, \lambda_{\mathrm{bkg}}, T) \tag{5.5}$$

$$\frac{T_{\mathrm{sig}}}{T} = \frac{N_{\mathrm{sig}}(\sigma, \lambda_{\mathrm{bkg}}, T)}{\lambda_{\mathrm{sig}} T} \tag{5.6}$$

These are the equations for a certain simulation. Now we want to write down the equation for a simulated state where λ_{bkg},T and λ_{sig} have different values and also scale differently:

$$\lambda'_{\mathrm{sig}} = b \cdot \lambda_{\mathrm{sig}}; \quad \lambda'_{\mathrm{bkg}} = d \cdot \lambda_{\mathrm{bkg}}; \quad T' = c \cdot T; \tag{5.7}$$

$$\frac{T'_{\mathrm{sig}}}{T'} = \frac{N_{\mathrm{sig}}(\sigma, \lambda'_{\mathrm{bkg}}, T')}{\lambda'_{\mathrm{sig}} T'} = \frac{a(\lambda'_{\mathrm{bkg}}, T') \cdot N_{\mathrm{sig}}(\sigma, \lambda_{\mathrm{bkg}}, T)}{b \lambda_{\mathrm{sig}} c T} \tag{5.8}$$

$$\text{only if: } a(d\lambda_{\mathrm{bkg}}, cT) = bc \quad \Longrightarrow \quad \frac{T'_{\mathrm{sig}}}{T'} = \frac{T_{\mathrm{sig}}}{T} \tag{5.9}$$

We introduce a scale factor a which is a non-linear function of λ'_{bkg} and T'. One can see that the last equation Equ. (5.9) is only true when the three scale factors b,c and d have exactly the right values. Because there is no linear correlation between these three scale factors the last equation will be $T'_{\mathrm{sig}}/T' \neq T_{\mathrm{sig}}/T$ in general. In our special case all parameters fit perfectly by accident. If an other data taking period than 1200 sec and 1800 sec ($\Rightarrow c$ is different) had been chosen, both contours wouldn't be on top of each other in the combined plot of Fig. 5.10.
One can also obtain an equation for the scale factors b and c of the signal duration and the signal rate in case of the exp-test method under the condition that T_{sig}/T and the significance stay constant. This time the derivation is much more elaborate why we omit showing the equations. However, the final result is that the scale factors b and c follow a non-linear function similar to $a(d\lambda_{\mathrm{bkg}}, cT)$ in Equ. (5.9). So the same set of scale factors that has been used for the standard Li&Ma method (b,c and d) will also fulfill the condition of $T'_{\mathrm{sig}}/T' = T_{\mathrm{sig}}/T$ in case of the exp-test.

Only the relation between T_{sig} and λ_{sig} is different from the standard method which is why the different methods have differently shaped curves.

The Bayesian-blocks method, however, shows a different acceptance for the different VERITAS states. It is much more sensitive in the upgraded system. Its contour intersects with the 1 C.U. line at a much lower signal duration fraction value than in the pre-upgrade plot. Meaning that a source with a same flux (measured in C.U.) has to be active a much shorter time fraction in the upgraded system to be detected. It is also not possible to derive a mathematical condition for the scale factors of T_{sig}, λ_{sig}, T and λ_{bkg} as we did for the standard method and the exp-test above. There the approach was the usage of a general distribution function of the event times for a specific set of T_{sig}, λ_{sig}, T and λ_{bkg}. This is not suitable for the Bayesian-blocks method because it critically depends on the exact time of each event. Therefore we have to rely on the Monte Carlo simulations. We can at least argue that due to a longer data taking duration T and higher background rates also the number of time bins M and the number of events N are larger. In case of larger M and N also the exponent $\psi_{M,N}$ in Equ. (4.41) and Equ. (4.42) will be larger for each deviation from a constant rate which can be seen in Fig. 5.11. At the end of the iteration process, looping over all time bins, the result will then be also a higher likelihood ratio.

Of course if we compare the absolute signal durations T_{sig} the methods will always perform better within the pre-upgraded simulations because the run duration T is

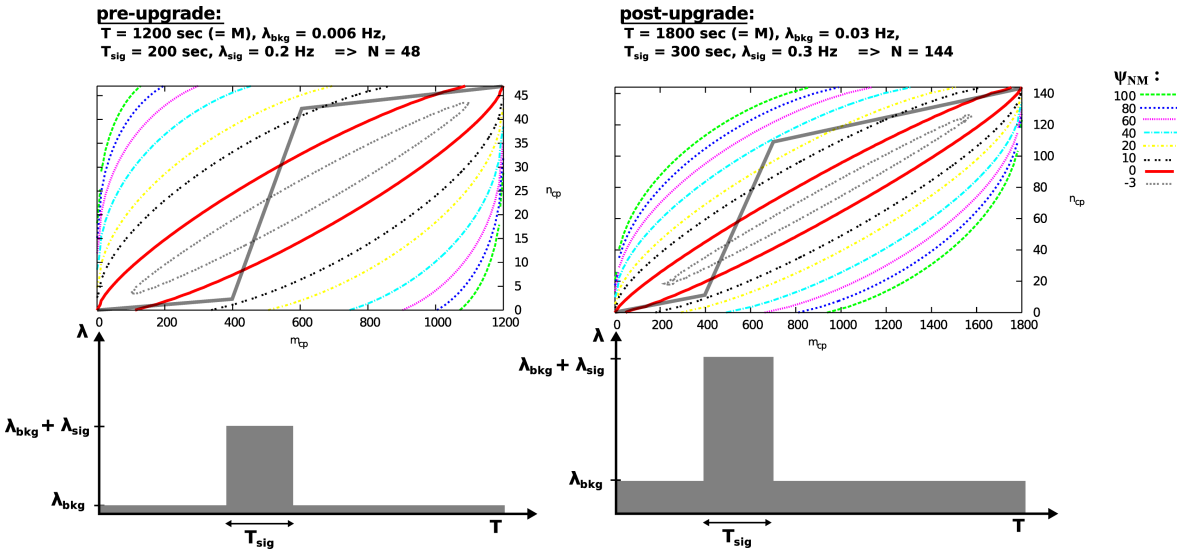

Fig. 5.11: *Comparison of Bayesian-blocks algorithm applied to two different simulations of the VERITAS state. On the left side we simulate an event sequence of the system before the upgrade and on the right side we do the same for the post-upgrade state. The value of λ_{bkg} is of course the rate at the signal region and not the rate of the whole field of view. The plots show the contours of the $\psi_{M,N}(m_{\text{cp}}, n_{\text{cp}})$ (see also Fig. 4.3) and a gray line which represents the sequence of events with different rates. It corresponds to the histogram below showing a simplified assumption of a transient signal at high rate together with a constant background. A higher rate will result in a higher slope of the gray line in the contour plot. An event sequence with no change in rate but with the same number of events would correspond to a diagonal line from (0,0) to (M,N).*

smaller and also the number of background events. By reducing our observation time during measurements with the upgraded system we can also improve our sensitivity for signals with smaller durations. But to be sure we would have to re-run all our simulations of the post-upgrade system for a duration of $T = 1200$ sec instead of 1800 sec, which was not done during this work.

Concluding remarks: If we assume a random sequence of background events described by a constant rate λ over a certain duration T we define a signal as a sudden generation of additional events with a constant rate λ_{sig} and a sudden ending after a duration of $T_{\text{sig}} < T$. In this case we can use both time-sensitive methods to measure such a signal. We analyzed only two different sets of fixed parameters describing the expected background for two different conditions. Much more different conditions have to be simulated to give recommendations which method performs best for which state of VERITAS. Here we can just say that for our definition of a signal an exp-test, in addition to the standard method, would increase the detectable parameter space for both VERITAS states while the Bayesian-blocks method improves the detection only during post-upgrade conditions. The additional parameter space covered only by the time-sensitive methods is the region of high signal rates (above 1 C.U.) and short signal durations.

5.4 Summary

In this chapter we explained the implementation of the time-sensitive methods and the features of a program which we used to test the methods. On could see that both methods, exp-test and Bayesian-blocks, are able to detect variability of a gamma-ray flux. Hence, those methods are also useful to detect sources that are active only for a short period of time if the whole observation duration is much longer. Sources with a constant high flux over the entire observation run, however, won't lead to a high-significant detection by those methods.
The advantage is that we don't have to estimate the number of background events as it is the case for the standard Li&Ma method. It is just necessary to provide the exact times of each measured photon and its reconstructed position in the sky. Another feature of the Bayesian-blocks method is the determination of the begin and end of the enhanced flux phase. The disadvantage is that for the Bayesian-blocks method we get as a result a test-statistic that depends on external conditions like the observing duration and the number of events. We have to produce p-value lookup tables for each different condition if we want to compare the results of the Bayesian-blocks method with the other methods. Up to now, only tables for durations $T = 1200$ sec and $T = 1800$ sec and event numbers from $N = 1$ to $N = 800$ are produced. Much more tables have to be produced to cover all possible observing durations. Another disadvantage, valid for both methods, is the fact that the combined analysis of several observing periods is not trivial because one has to be sure that there are no sharp rate changes between two consecutive runs
We compared the sensitivity of both methods with the sensitivity of the standard method under different simulated conditions. We chose some behavior that rep-

resents two different VERITAS states, pre- and post upgrade. For the simulated signal we assumed that it has a constant rate when its flaring and that it shows no smooth transition between quite state and flaring state. By varying the signal rate and its duration we found out that the time-sensitive methods improve the detection potential of the analysis especially for short flares where the difference in flux between quite state and active state is in the order of 1 to 2 C.U.s. But even for signals that could easily be detected by the standard method, the usage of time-sensitive methods can still be useful to detect if, and at which time, a flare occurs during a single run. A lot more observing conditions have to be simulated to find out which method works best for which set of data. Especially much longer observing periods and longer flare durations could help if one wants to study the variability over several runs.
The simulations also revealed that the performance of the methods depend on the external conditions like the background rate or the observing duration. A change of the external conditions has different effects on the different methods, therefore also different VERITAS states will change the performance of each method. For the comparison between the two states we have to use crab units instead of absolute rates. While the standard method and the exp-test method show almost no changes between both VERITAS states, the Bayesian-blocks method performs better in the upgraded state. The reason for that, is the Bayesian-block algorithm. It is less sensitive to deviations from a constant rate if the number of events in a sequence is small (see left side of Fig. 5.11). This makes sense when we imagine a case where only 5 events are randomly distributed over 1200 time bins. Almost every possible outcome would then lead to a significant deviation from a constant rate if the algorithm would be too sensitive. Therefore the algorithm is more sensitive when the overall number of events is higher, which is the case for the upgraded state.
In general one can say that the exp-test method is a good choice for short flares or repeating fluctuations. It doesn't matter when the phase of enhanced flux starts as long as it is fully covered by one observation run. The Bayesian blocks is a good choice if the phase of the enhanced rate happens at the beginning or the end of a run. In between there has to be a larger difference in rate to give the same significance.

Chapter 6

Data analysis of variable sources

6.1 Sources from the *Fermi LAT Second Source Catalog*

After the analysis of simulations we want to test the methods on data of known variable high-energy gamma-ray sources. Therefore we search inside the *Fermi LAT Second Source Catalog - 2FGL catalog* [Nolan *et al.* (2012)] for variable sources that could have been observed with the VERITAS system and check afterwards the VERITAS archive if that source region was actually exposed. Because we require the sources to be at least above 50° elevation at the culmination we constrain the possible declination range from −8° to 72°. As they should also be measurable with the VERITAS telescopes we accept only those sources with a integral photon flux for the 10 to 100 GeV range above 10^{-10} photon/cm^2/s and a power law index not steeper than 3. An additional parameter in the catalog indicates the variability of a source. This so-called *variability index* is 2 times the logarithm of a likelihood ratio which compares the null hypothesis of a flat light curve over the full 2-year catalog interval against the alternate hypothesis where the flux is optimized for each month. If this value exceeds 41.6 than the chance of being a steady source is less than 1%. So, we allow only sources in our dataset with a variability index of at least 50. The sources that meet all these criteria are mainly BL Lac type of blazars or FSRQs and their total number is 113.
We will now search in the archival data of VERITAS how many of those sources

ra	dec	assoc name 1	powerlaw index	flux 10 100 gev	flux 10 100 gev error	variability index	source type
02 22 38.8	+43 02 09	3C 66A	1.9119	2.16964e-09	1.74735e-10	358.641205	BZB
03 19 51.7	+41 30 45	NGC 1275	2.0304	1.09574e-09	1.26610e-10	277.424103	rdg
05 21 47.8	+21 13 14	VER J0521+211	1.9290	8.43534e-10	1.16553e-10	118.715668	bzb
05 34 31.6	+22 01 11	PSR J0534+2200	2.1889	7.44553e-09	3.29898e-10	86.224548	PSR
07 19 18.6	+33 06 28	B2 0716+33	2.0632	3.28463e-10	7.17785e-11	302.965363	bzq
11 04 28.8	+38 12 48	Mkn 421	1.7706	4.23130e-09	2.45710e-10	112.768120	bzb
12 17 52.1	+30 06 33	1ES 1215+303	2.0194	3.71287e-10	7.87137e-11	96.197243	bzb
12 21 29.8	+28 14 21	W Comae	2.0186	3.87170e-10	7.80661e-11	111.495537	bzb
12 24 54.3	+21 22 48	4C +21.35	2.2314	9.38423e-10	1.19916e-10	13030.349609	BZQ
13 03 06.3	+24 35 51	MG2 J130304+2434	2.1145	1.25676e-10	4.58675e-11	207.955688	bzb
14 27 02.3	+23 47 42	PKS 1424+240	1.7784	1.58398e-09	1.54874e-10	77.722694	bzb
16 53 55.5	+39 45 47	Mkn 501	1.7377	1.24574e-09	1.34160e-10	72.325722	BZB
20 32 10.5	+40 49 41	Cyg X-3	2.4820	1.69910e-10	0.00000e+00	121.210594	HMB
22 02 49.7	+42 16 03	BL Lacertae	2.2609	2.30335e-10	5.95948e-11	266.983032	bzb

Table 6.1: *List of variable high-energy gamma-ray sources covered by VERITAS under good observing conditions (see text).*

have been covered by observations. The sources don't have to be the primary targets of an observation but should be near the actual pointing direction ($< 2°$) otherwise too many gamma-ray events will be missed due to the limited radial acceptance. The number of observed sources will then reduce to 29.
In the final step only good quality data is accepted, that was taken after the movement of telescope T1 to its actual position in the VERITAS array. This still includes runs of the pre-upgraded and post-upgraded state. The meaning of "good quality" is that all telescopes take part and that the whole system works properly during the observation. Also the weather conditions have to be good and stable during that time. It is really important that there prevail no external conditions causing the measured rate to be fluctuating. A cloud moving through the field of the camera during a run would be such a scenario which could falsely trigger the time-sensitive methods, as those methods also react on drops in rate. Further we decide to use only those runs with elevations of 70° or larger because the rate of incoming photons will then be higher and we can increase our statistics. Because the production of p-value tables for the Bayesian-blocks method is very time consuming and cpu intensive, we only produce tables for $T = 1200$ sec and $T = 1800$ sec. Therefore we also have to restrict the allowed duration of a single run to a value of 1200 sec or 1800 sec. If we use a p-value table, generated for a specific duration T, during the analysis of data runs with longer durations than T, we will underestimate the significances calculated with the Bayesian-blocks method. If the run duration is shorter than T we overestimate the significance. In the end we find 450 runs that fulfill all these criteria and cover 14 of the 29 sources (see Table 6.1).

6.1.1 Measure variability at source position

Now each run is analyzed with the standard analysis software by applying the soft spectrum cuts mentioned in subsection 5.3.1. Afterwards we use both time-sensitive methods and create for each one their significance map. Then one can determine the significance exactly at those bins in the map, where the sources are. As the sources show some variability in the Fermi LAT energy range, the hope was to significantly detect also variability in the energy range of VERITAS. But one has to keep in mind that the variability in Fermi LAT was measured in monthly bins and with our method we search for minute scale flux changes. A source that is in a flaring state for more than a run will not be detected if its rate stays constant during a whole run. The only possibility would be a sudden increase of the rate inside a run when the flare begins and a sudden decrease in a run much later when the flare ends. A smooth increase and decrease of the rate over several run durations won't be detected by the time-sensitive methods applied on single runs. Of course there is also the possibility of combining several runs and apply the methods on the combined event sequence. The challenges here will be the fact that one has to assure that there are no rate changes between different runs due to external issues, like the weather or the elevation of the telescopes, which can be quite difficult if one tries to combine runs from several nights. Another problem will be the fact that, if one wants to use the Bayesian-blocks method, one has to generate p-value tables for those long duration observation periods which is a very time consuming process. Due to the several iterations in the generation code this process doesn't scale linearly with the

amount of time bins M, it is more like M^2, and you have to do it for each individual observation duration you want to analyze. So do those methods work for combined run analysis - Yes! Is the application easy and well tested - No!

Some data runs contain more than one source, e.g. runs taken on the source W Comae cover also the source 1ES 1215+303 from the list in Table 6.1. The measured significance of each source in each run will be plotted in a common histogram, one for the exp-test and one for the Bayesian-blocks significance values. The idea is not to study each source separately but to examine more in general if the methods show a tendency towards positive significances. The result can be seen in Fig. 6.1.
The distribution for both methods can be approximated by a standard normal dis-

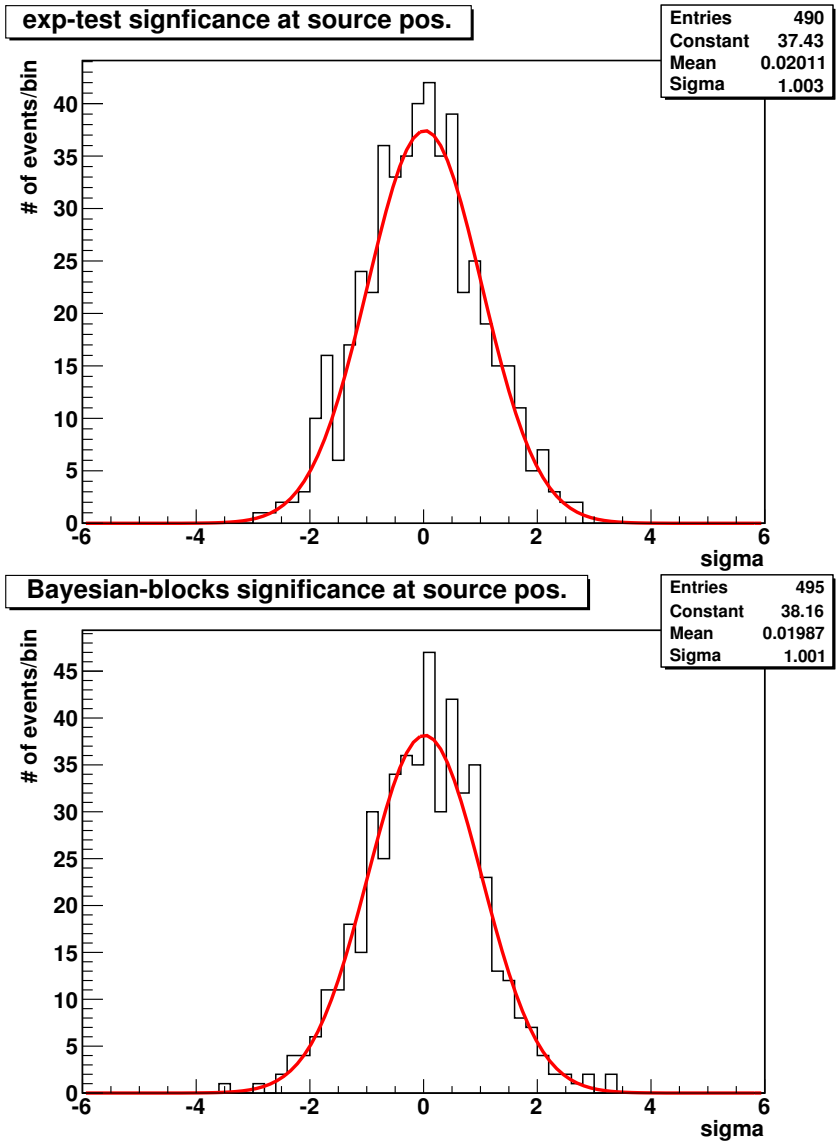

Fig. 6.1: *Distribution of significance measurements at known source positions which we get from the* Fermi LAT Second Source Catalog. *The red curve is the gaussian fit to the distribution and the resulting fit-parameters are shown in the box in the upper right of each plot. The histogram on top presents the significance measurements of the exp-test while the bottom histogram shows the result of the Bayesian-blocks method.*

tribution. The difference of the entries between the histograms of both methods is due the fact that the exp-test method requires at least 3 events at the bin of the source position to calculate a significance value while the Bayesian-blocks methods works already for 2 events. So if some source positions are close to the edge of the radial acceptance the number of events per bin can be less than 3 and in this case only the Bayesian-blocks method provides a result.

So in the end by looking at the histograms we cannot detect a tendency towards positive significance measurements for both methods. This leads to the conclusion that the high-energy gamma-ray emissions measured by VERITAS for the 14 different sources in Table 6.1 don't show flux changes during single runs, as long as we assume parameters for the flux changes like the ones inside the shaded areas (red and blue) of the contour plots in Fig. 5.9. The duration of the increased flux period will then be described by the signal duration parameter in the contour plot and the difference between the increased rate during this period and the lower rate in the constant emission phase during the rest of the run is then represented by the signal rate parameter. The rate during the time of the constant emission phase will then correspond to the background rate in the simulations. Roughly saying none of the tested data runs show enhanced fluxes (with a flux change of more than the Crab flux) over time periods of $\sim$2 to $\sim$15 min length. An increased flux over a duration as long as a data run (20 min or 30 min) can not be detected by the advanced methods, hence it is also not possible to exclude long flares in timescales of hours and days.
But we have to be a little bit careful with the conclusion concerning the strong high-energy gamma-ray emitters in our data set e.g. Mrk 421, Mrk 501 and the Crab Nebula around the pulsar. Their rates during their constant emission phase are much higher than the rates of the background simulated during the generation of the contour plots: 0.003 Hz (pre-upgrade) and 0.018 Hz (post-upgrade). For such a case we don't know exactly the size of the parameter space for which the methods will be sensitive. It tends to be smaller than the ones in Fig. 5.9 and so the excluded time periods are smaller than 15 min and larger than 2 min and/or the flux change is larger than the Crab flux.

An additional study of light curves taken simultaneously at other wavelengths for these objects can help to estimate the variability expected in the VHE range. Based on this information it would be possible to set an upper flux limit for the flares.

6.1.2 Search in the whole sky map

However the situation is different when we search in the whole sky map of a run for variability signals. Here the background rate is similar to the one in the simulations. The hope is to find unknown sources which produce short but strong flares in a way that the time-sensitive methods are able to detect them within a run, while the standard method suffers from the small number of events due to the short duration and is not able to detect the source in one run. By looking at the contour plots in Fig. 5.9 the parameters for such flares are in the blue and red shaded areas not covered by the black ones.

So we start to search for the highest significance that was measured with one of the time-sensitive methods in the whole skymap of each run. In Fig. 6.2 and Fig. 6.3 we show the significance maps of both methods for all those runs where the highest significance exceeds 5σ without taking into account trials. The stars mark the positions of sources from the catalog covered by that run and the center of the colored rings mark the bin with the highest significance. If the ring is purple it means that the exp-test calculated a significance larger than 5σ for that bin and if it is magenta than the Bayesian-blocks measurement exceed 5σ. For comparison reasons we print the ring in both significance maps. If both rings are on top of each other than both methods found variability for the same bin. Next to the ring we print also the position of that bin in right ascension and declination but only in the map of that method that detected the bin with a significance of more than 5σ.
In the end we found 15 runs in the list of 450 runs that contain a bin with a significance above 5σ measured by one of the time-sensitive methods. All of those bins have been detected solely by one method and could not be confirmed by the other method. For nearly all runs it was the exp-test method that measures a significance above 5σ. Only in the last two runs in Fig. 6.3 the Bayesian-block method found a bin with a high enough significance. This makes sense when we realize that the last three runs have been taken during the upgraded state and when we remember the contour plots in Fig. 5.9. For the post-upgrade state it is the Bayesian-blocks method that performs in general a little bit better than the exp-test method while during the pre-upgrade phase the exp-test method works better.

We started to compare the positions of the bins with the sources found in the 0.1-2.4 keV x-ray energy band derived from the all-sky survey performed during the first half year of the ROSAT [Voges *et al.* (1999)]. As those sources can show some sharp increases in rate it could be potentially behave the same way in the gamma-ray regime and we could detect a flux change within a VERITAS run. Unfortunately, none of the sources coincide with the detected bin positions.
Finally we have to take into account the trial factor as no bin positions was known before due to other experiments. Our probability of finding a signal somewhere in the map is of course much larger than if we just look at a predefined bin. If we want to declare a detection of a signal somewhere in the map with a significance of at least 5σ the significance of the single bin has to be larger to compensate for the additional possibilities of accepting a signal in any other bin. So we have to determine the significance level α_{bin} that a p-value of a single bin has to come under to ensure that the global probability $P_{>1}$ of finding at least one such a bin in the whole map by chance is the same or lower as the α-value corresponding to 5σ: $\alpha \approx 2.87 \cdot 10^{-7}$. The calculation is done as shown in the following equation where we start with the probability P_0 of not detecting a signal at a significance level of α_{bin} in any bin:

$$P_0 = (1-\alpha_{\text{bin}})^N \quad \Rightarrow \quad P_{>1} = 1 - P_0 = 1 - (1-\alpha_{\text{bin}})^N \tag{6.1}$$

$$P_{>1} \leqslant \alpha \quad \Rightarrow \quad \alpha_{\text{bin}}(N) \leqslant 1 - (1-\alpha)^{\frac{1}{N}} \tag{6.2}$$

In this example N is the number of bins where we try to find a signal. Each bin will then represent one trial, which is true if there is no correlation between different bins and their results are independent. Of course this is not true in our case where we

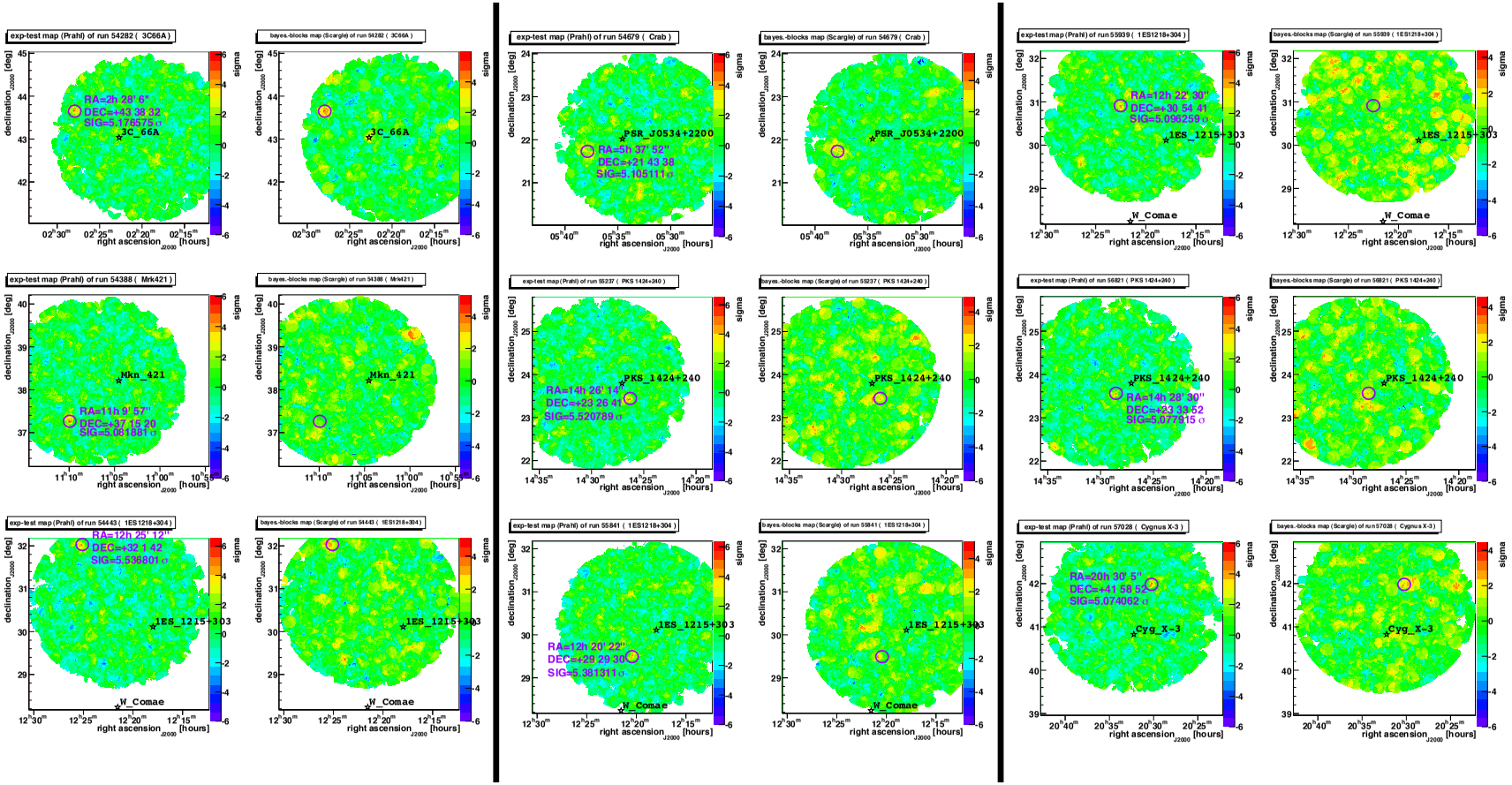

Fig. 6.2: *Significance maps of 9 different runs with a highest significance measurement without trials of at least more than 5σ calculated with exp-test method (left) and with Bayesian-blocks method (right). The position is given in right ascension (x-axis) and declination (y-axis). The title of each map contains the name of the method, the run number and the name of the source where the telescopes were pointing at (with wobble offset). The stars in each map mark the positions of the sources from the 2FGL catalog. The colored rings mark the region around the bin with the highest significance (at least $> 5\sigma$). If the ring is purple then the bins significance is $> 5\sigma$ in the exp-test, if its magenta than the Bayesian-blocks method measures a significance $> 5\sigma$ for that bin.*

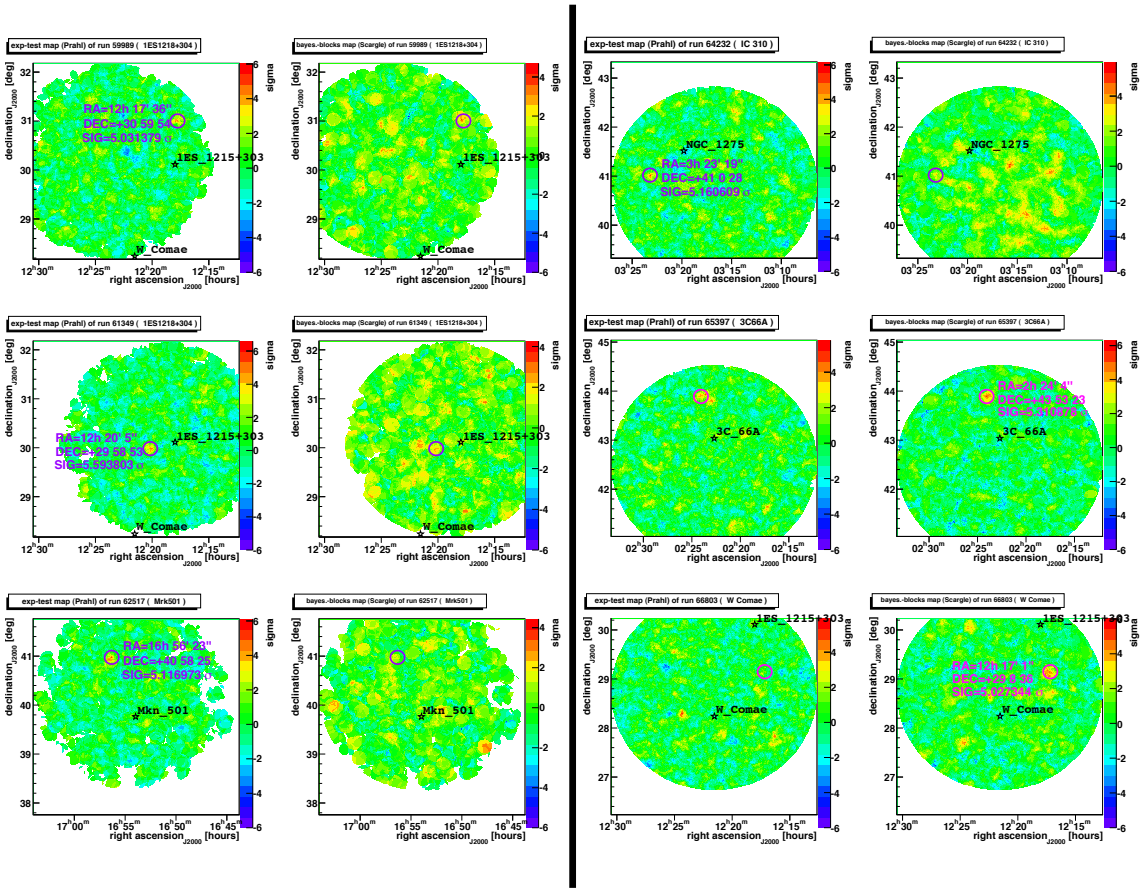

Fig. 6.3: *Significance maps of 6 different runs calculated with exp-test method (left) and with Bayesian-blocks method (right). Continuation of Fig. 6.2.*

use correlated maps as explained in section A.1. If we want to estimate the possible range of α_{bin} for a single bin we will look at two extrema:

- each bin ($= 0.01(^\circ)^2$) inside the whole sky map area $(2^\circ)^2 \cdot \pi$ is a trial $\rightarrow \; N_{\text{max}} = (2^\circ)^2 \cdot \pi / (0.01^\circ)^2 = 125664$

- all bins inside the smoothing area ($= \theta^2$) around the highest-significant bin are taken as the same trail $\rightarrow \; N_{\text{min}} = (2^\circ)^2 / \theta^2 = 200$

So the true value of α_{bin} must be in between $\alpha_{\text{bin}}(N_{\text{min}}) \approx 1.435 \cdot 10^{-9}$ and $\alpha_{\text{bin}}(N_{\text{max}}) \approx 2.284 \cdot 10^{-12}$. If we assume a normal distribution the corresponding significance values are 5.94σ and 6.92σ respectively.
From this we can conclude that the significance in one of the bins has to be at least larger than 5.94σ to be a significant detection of a transient source in the whole run. As this is not observed in our dataset we have to assume that all the bins detected in the 15 runs are just random fluctuations of the background. Hence, no unknown sources with strong ($\gtrsim 1$ C.U.) but short flares ($\lesssim 2$ min) has been detected inside the field of view during these runs.

6.2 Analysis of Makarian 421 Flare in 2010

The test on variable 2FGL sources in the section above didn't lead to any detection. The reason could be that there is no variability in the runs we analyzed or the variability is in a range where the methods are not sensitive enough because the flux change is too small ($\lesssim 1$ C.U.), too smooth ($\lesssim 0.25$ C.U./min) or the duration too short ($\lesssim 2$ min). We will therefore look inside the data of the Markarian 421 Flare observed with VERITAS on February 17, 2010. This set of runs was not included in the previous 2FGL source analysis because T1 was not operating during the flare which was a exclusion criterium.
The advantage of testing the methods on Markarin 421 is the fact that we know that there is variability in the data and also the rates are high enough to provide good statistics. The important fact is how fast and how much the rate changes. If the flux changes continuously over several run periods it is difficult to detect variability. The list of the 12 runs that have been analyzed with the standard analysis software and the corresponding results after the application of soft cuts is shown in Table 6.2.

Run Nr.	El. [deg]	Az. [deg]	Duration [min]	standard Significance [sigma]	exp-test Significance [sigma]	BayesBl. Significance [sigma]	Rates [gamma/min]	Background [events/min]
50099	75	56	20.05	73.9	-1.748	1.511	74.73 ± 1.94	0.88
50100	79	51	20.05	76.1	-1.651	-0.653	74.78 ± 1.94	0.79
50101	81	34	20.05	82.7	0.044	2.782	88.34 ± 2.11	0.94
50102	83	-2	20.05	64.8	-0.366	3.488	55.92 ± 1.68	0.79
50103	81	-31	30.07	79.1	-0.492	0.311	58.04 ± 1.40	0.79
50104	77	-57	30.07	82.0	0.188	2.612	59.13 ± 1.41	0.77
50105	71	-63	30.07	70.4	-2.223	-0.788	45.21 ± 1.24	0.79
50106	64	-66	30.07	60.5	-0.584	1.464	33.60 ± 1.07	0.62
50107	58	-66	30.07	67.6	1.508	-0.45	41.98 ± 1.19	0.52
50108	52	-67	30.07	66.0	1.042	0.665	37.87 ± 1.13	0.44
50109	47	-66	30.07	67.9	-0.350	0.637	38.95 ± 1.14	0.33
50110	41	-62	20.40	48.9	-0.855	3.033	30.14 ± 1.22	0.30

Table 6.2: *List of VERITAS runs that measured the Flare of Mrk 421 on February 17, 2010. The significance was calculated by the standard Li&Ma method, the exp-test method and the Bayesian-blocks method*

We also analyzed all runs with both time-sensitive methods like we did for the 2FGL sources and add the significance measurements to the table. Additionally we plot the distribution of their significance measurements in the figure 6.4. We can see that the exp-test results exhibits no signs of a general high variability. In contrary it even tends towards negative values which leads to the conclusion that the fluctations at the source position are even less than expected from normal background. The usage of the Bayesian-blocks method leads to a wider distribution of significance values but tends to be more positive in general. However, no method detected variability at the source position with a significance of more than 5σ.

By looking at the table we can see that there is a sudden drop in the rates between run 50101 and 50102. We can also see that the significance for variability is quite high compared to all other runs. For a better visualization of the variability of the source we plot the rates in 4-minute bins over the whole duration of all combined runs (see Fig. 6.5). The rates have been calculate exactly at the bin of the position of Mrk421 under the usage of correlated maps. The size of the correlation region is 0.02(°) by which we can guarantee to take into account 68% of the spatial spread of the source gamma-rays due to our limited angular resolution. With the two red vertical lines we mark the duration of both runs.

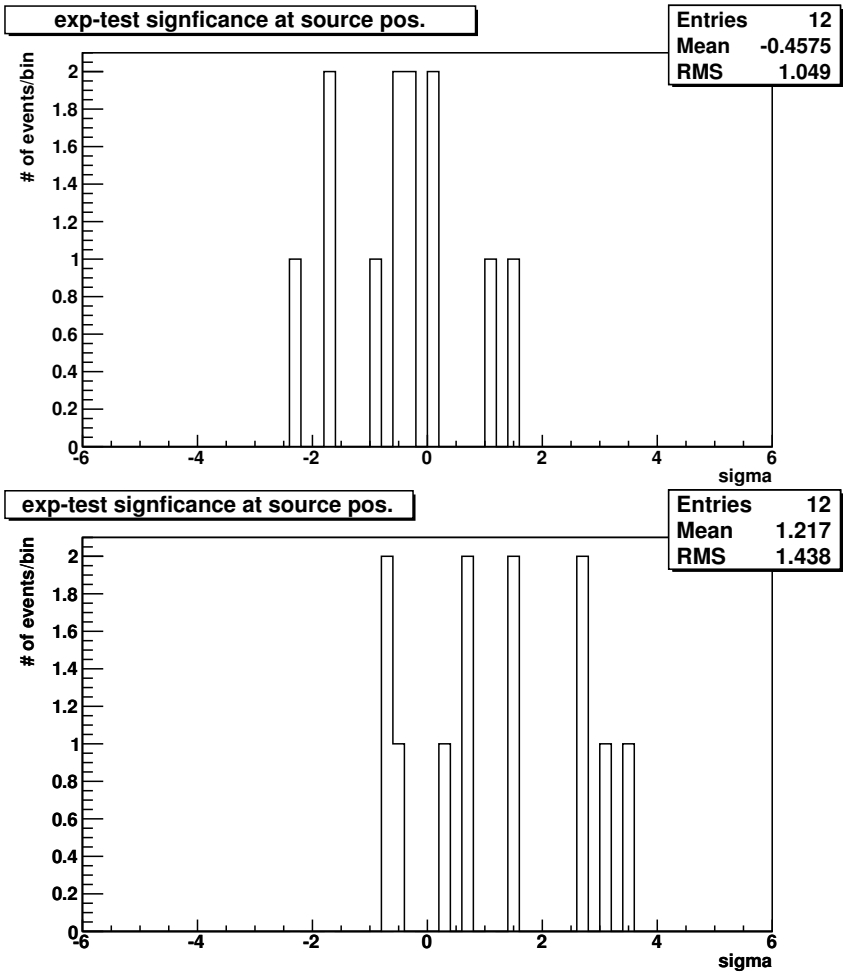

Fig. 6.4: *Distribution of significance measurements at the center positions of the maps which we get by analyzing twelve consecutive Mrk 421 runs. The histogram on top presents the significance measurements of the exp-test while the bottom histogram shows the result of the Bayesian-blocks method.*

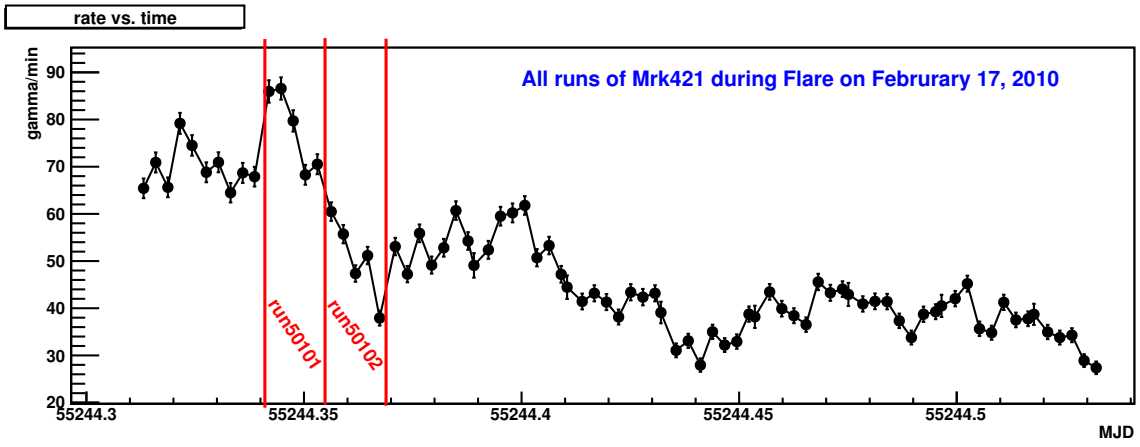

Fig. 6.5: *Rate per minute of all reconstructed gamma-rays of Mrk421 during the flare on February 17, 2010 (soft spectrum cuts). Each value represents the average over 4 minutes. The red lines mark the beginning and the end of run 50101 and of run 50102.*

One can recognize that the difference $\Delta\lambda$ between several data points of these runs is quite large compared to all other data points during the rest of the day. If we pretend that the additional rate of gamma-rays represents a flaring signal on top of the constant Mrk421 rate we can say that $\Delta\lambda = \lambda_{\text{sig}}$. Lets take run 50101 as an example: $\Delta\lambda \approx 18\gamma/\text{min}$, which is the same as $\lambda_{\text{sig}} = 0.3$ Hz. In case of low background rates, like during our pre-upgrade simulations (0.003 Hz), such a variability should be detectable by both algorithms if the flare lasts for at least 1/8 of a full run (see left contour plot in Fig. 5.9), which is true for run 50101. Unfortunately our background rate is much higher in our example here because the low flux state of Mrk 421 represents the background rate which is close to 68 γ/min ($\approx$ 1 Hz). This is the reason why the methods are not sensitive enough.

But as we have seen in Table 6.2, the Bayesian-blocks significance measurement for the second and third run give at least a hint to variability. We will therefore start to search in the whole skymap of each method for the highest significant bin whose value exceeds 5σ like we did during the analysis of the 2FGL data. We found exactly one run for which the Bayesian-block method detected (pre-trials) a bin as one can see in Fig. 6.6. It is the run with the strong variability at the source position: 50101. As it was mentioned before, the measured significance, however, is still too small to claim a detection if the trails are taken into account. Since we know already that our data is variable in this run, the question is, why does the method see such an excess with an offset from the real source while the standard method measures the largest significance exactly at the source position? The position of the highest significant bin, that we found, is inside the smoothing radius of the correlated map. Hence also this bin will be influenced by the fluctuations in the source bin.
For a better understanding of the difference between these bins we will compare the temporal events sequence of both bins. For comparison reasons we will also look at the event sequence of a bin with a distance to the source that is similar but with a significance much lower (see circle in bottom plot of Fig. 6.6). We decided to plot the number of events versus the time and choose a bin size of 100 seconds. This way it is easier to recognize the differences in the evolution of the rate. Additionally we also print the exponent $\psi_{\text{N,M}}$ [Equ. (4.42)] which is calculated during the Bayesian-blocks process for each time bin (= each second) of the run to determine the final test statistic value in a subsequent step. The resulting graphs look similar to Fig. 5.6 and are presented in Fig. 6.7. Before we start to compare the output, that was measured at the three different bin positions, we have to remind how the test statistic of the Bayesian-blocks methods is calculated. First we calculate $e^{\psi_{\text{N,M}}}$ for each time bin and add up the results. Then we divide this sum by the number of time bins and build the logarithm of this result. So in the end the sum of all $e^{\psi_{\text{N,M}}}$ has to be much larger than the number of bins to provide a large test-statistic which means that the blue $\psi_{\text{N,M}}$-curve should reach large values for a reasonable amount of time.
If we look again at the figures in the section above where we compare the Bayesian-blocks results for different VERITAS states (see Fig. 5.11), we can estimate for which distribution of events we would expect large $\psi_{\text{N,M}}$-values. For example if the grey curve, which represents the integral over the time of the events found in a run, lies on one of the contour lines in Fig. 5.11 we measure a constant $\psi_{\text{N,M}}$-value al-

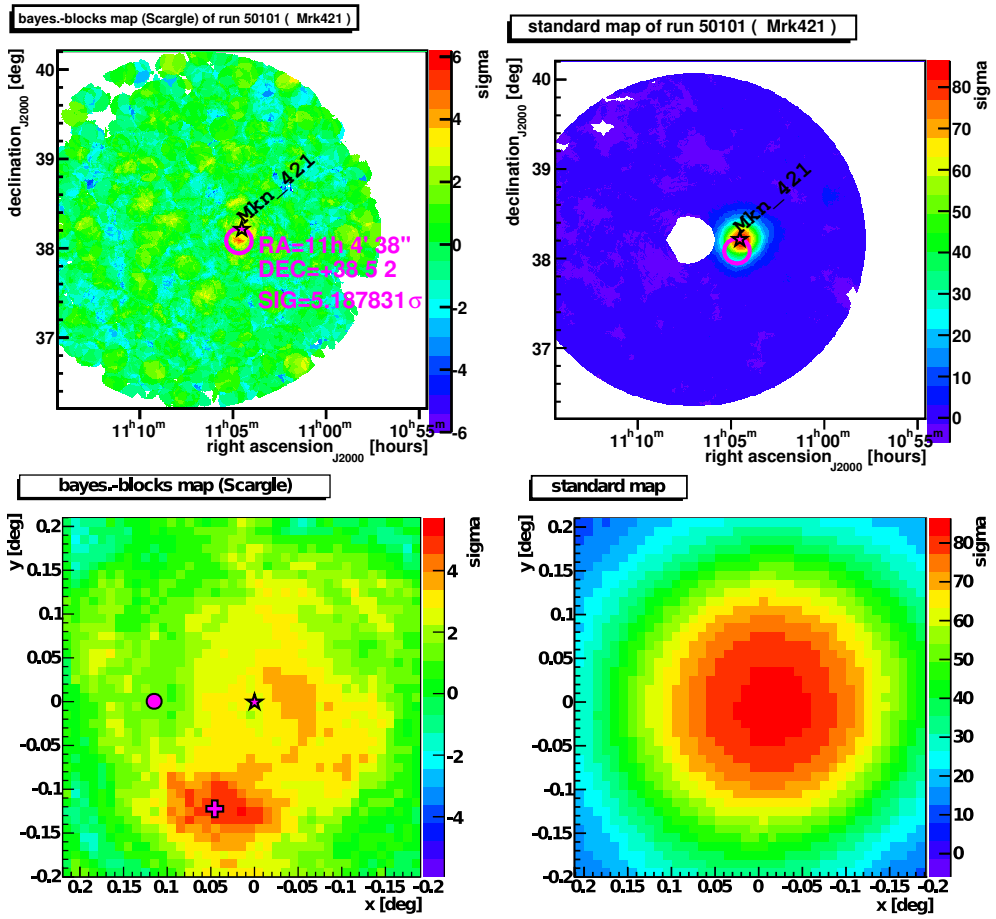

Fig. 6.6: *TOP: Significance maps of Mrk 421 run 50101 calculated with Bayesian-blocks method (left) and with the standard Li&Ma method (right). The position is given in right ascension (x-axis) and declination (y-axis). The star in each map mark the positions of Mrk 421. The colored rings mark the region around the bin with the highest significance (at least $> 5\sigma$) detected by the Bayesian-blocks method. The size of the ring represents the uncertainty of the position ($\theta = 0.14°$) respectively the size of the correlation*
*BOTTOM: Zoom of significance maps. Maps are in camera coordinates with the Mrk 421 source in the center at $x = 0°$ and $y = 0°$ (star). The cross marks the bin with the highest significance above 5σ and the circle marks a bin with a similar distance to the center but with a lower significance. (**Attention**: Due to the large uncertainty no underlying spatial structure is revealed by the plot on the left side. Reconstructed Mrk 421 events with different time stamps got spread nearly over the whole zoomed sector, causing different event sequences in each bin just by accident. The purpose of this figure is just to illustrate at which bins we were looking more closely in Fig. 6.7)*

most the entire run. An integral function with such a behavior belongs to an event distribution with an event rate that is large at the beginning of a run and decreases with a constant slope towards the end of the run (or vice versa). The modulus of this slope is the crucial point. If it is small, the integral (grey curve) will lie on top of a contour line that is close to the diagonal of Fig. 5.11 representing negative $\psi_{\mathrm{N,M}}$-values. If the slope modulus is large, the integral curve will lie on top of a contour that bends much more and represents large $\psi_{\mathrm{N,M}}$-values. In the extreme case when there is just a sharp cut-off then the integral curve will have a kink. In

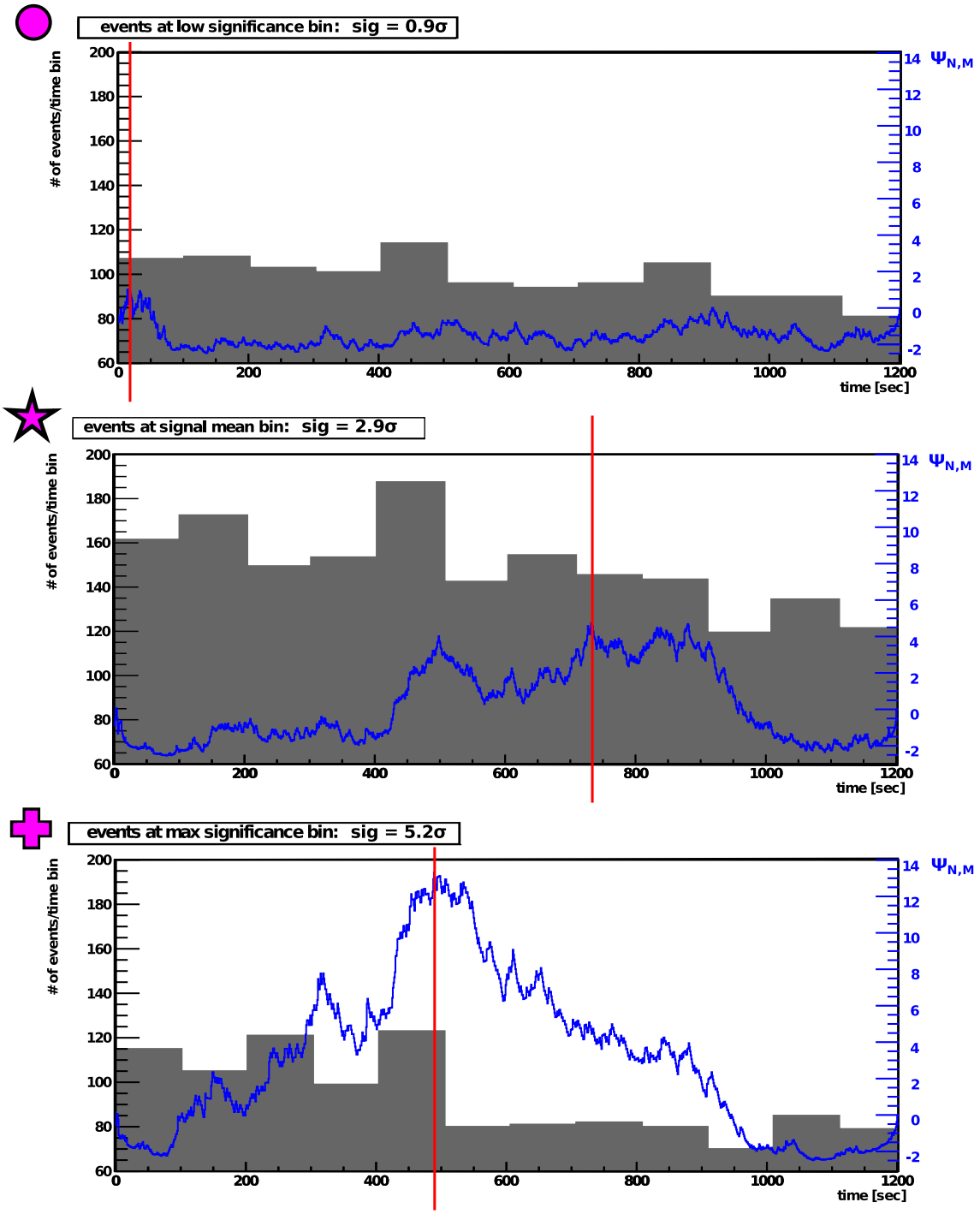

Fig. 6.7: *Number of events per time binned in 100sec wide bins (grey) and the exponent* $\psi_{\mathrm{N,M}}$ *[Equ. (4.42)] calculated during the Bayesian-blocks process for each second of the run (blue) to determine the final test statistic value in a subsequent step. The vertical red line marks the point where the separation of the data into two blocks with two different average rates is most likely (= blue curve reaches maximum). The three different figures show the events measured at three different positions in the left skymap of Fig. 6.6, which is the Bayesian-blocks skymap of run 50101*
TOP: events from the bin with low significance, marked with a circle in the skymap.
MIDDLE: events from the bin at the source position of Mrk 421, marked with a star.
BOTTOM: events from the bin with maximum significance, marked with a cross.

this case the grey curve intersects with several contour lines and hits the highest possible contour (= highest possible $\psi_{\mathrm{N,M}}$-value) exactly at the time of the sharp rate change.
So in the end one can say that a large difference between the rate at the beginning and at the end of a run, together with a monotone increase or decrease, will result in a high significance when using the Bayesian-blocks method. A sharp cut during a run will lead to a larger significance result than smooth rate changes, as long as the overall number of events, the rates at the beginning and the rates at the end are the same.

Back to the comparison of our three different event sequences. In the first example on top of Fig. 6.7 we can see that the slope of the rate change is pretty flat which leads to a small significance. In the graph in the middle the slope is much steeper but not a sharp cut-off as in the example on the bottom of the figure. Here the fast change of the rates is big enough to lead to a significance value of 5σ. As an additional feature this sharp cut-off helps to find a changepoint in the data as the cumulative integral of such a event distribution reaches the largest contour lines (= highest $\psi_{\mathrm{N,M}}$-value) only once, which is than the most probable separation point.

After this short excursion, what can we conclude about the variability detected by the Bayesian-blocks method in the vicinity of the source position? By looking at the three examples, we can see that the source bin, and also the bins around that bin, show variability but the methods are just not sensitive enough for these slowly changing rates. It was just a lucky coincidence that the events in the bin, with the large significance measurement, have been distributed in a way the Bayesian-blocks method is able to detect a significant rate change despite the large amount of background events. This makes sense as the trial factor wasn't taken into account here, which is necessary when searching for a signal in more than one bin. Therefore the required significance in a single bin would have to be larger than 5σ for claiming a detection.
The exp-test method didn't detect any variability. Not even inside the area around the source position. This method performs better on strong flares or repeating fluctuations which is not found in this set of data.

6.3 Analysis of GRB data

In a final approach we test the time-sensitive methods with some GRB data obtained by VERITAS before the upgrade. For GRB observations we expect a behavior that is close to our simulations described above. So the background rate is low at the source position and the signal should be active just for a short period of time before its rate decreases very fast. In Table 6.3 we present the list of GRBs we will use for this test.
Each GRB is analyzed with the standard VERITAS analysis software by combining all good quality runs that contain the respective GRB. The same soft cuts that were used for the analysis of the other datasets before are used again. In the last column the 99% upper limit of the flux of each GRB is shown. These values have to be

Name	RA(J2000)[i] [deg]	DEC(J2000)[i] [deg]	Delay [sec]	T_{90} [sec]	T_{obs} [min]	Discovery	Pos.Error	FluxUL [ph/cm^2/s]
GRB091123B	337.86	13.31	221	15 ± 2	60.1	Fermi GBM	4.72 deg	9.45e-12
GRB100205A	141.39	31.74	330	26 ± 4	140.3	Swift	1.7 arcsec	5.78e-12
GRB100513A	169.61	3.63	4789	84 ± 21	100.2	Swift	0.3 arcsec	3.76e-12
GRB100519A	191.18	56.87	1833	62 ± 4	20.1	Fermi GBM	2.9 deg	4.83e-11
GRB110130A	110.75	34.72	326	47 ± 2	42.1	Fermi GBM	7.43 deg	6.08e-12
GRB110522A	235.32	53.16	125	28 ± 3	25.1	Fermi GBM	6.9 deg	8.84e-12

[i] Location of Fermi GRBs is taken from the latest GBM Ground Position GCN Notice, broadcasted few seconds after the trigger

Table 6.3: *small subset of GRBs observed with VERITAS. Values in the T_{90} column define the time during which 90% of the GRBs photons got measured by the satellite that discovered it.*

calculated because no observation lead to a significant detection.

6.3.1 Satellite data of keV emission

All these GRBs were discovered either by the *Burst Alert Telescope (BAT)* or by the *Gamma Burst Monitor (GBM)*. BAT belongs to the instruments of the *Swift* satellite observatory [Gehrels *et al.* (2004)]. It is a large field-of-view (FOV = 2.0 sr) coded-aperture telescope developed to detect transient sources like GRBs over a large fraction of the sky with an accuracy of 1-3 arcmin. Hence the whole satellite with its additional narrow-FOV instruments (the *Ultraviolet/Optical Telescope - UVOT*, and the *X-ray Telescope - XRT*) is able to slew exactly to the source position in case follow-up observations are required. BAT covers an energy range of 15 to 150 keV for imaging while it is able to reach 500 keV for rate measurements over the whole FOV. Its sensitivity is high enough to trigger the GRB due to the rapid increase of the measured photon rates and also to determine its position. But it is necessary to use the XRT with its small FOV (23.6 × 23.6 arcmin) and higher sensitivity in the soft X-ray regime (0.2-10 keV) to measure the decreasing flux also during the afterglow phase. More informations about BAT and XRT can be found in [Barthelmy *et al.* (2005)] and [Burrows *et al.* (2004)].
The GBM is part of the *Fermi* satellite observatory. It consists of 12 Sodium Iodide (NaI) and 2 Bismuth Germanate (BGO) scintillation detectors mounted around the *Large Area Telescope (LAT)* [Atwood *et al.* (2009)], which is the principal scientific instrument on the spacecraft. The NaI detectors provide spectral coverage from about 8 keV to 1 MeV and have a cosine angular response. Together with their small FOVs and the different pointing directions they are used to determine the burst location by taking into account the relative rates. The accuracy, however, is much worser than the one achieved by the Swift instruments. The two BGO detectors are attached on opposite sides of the satellite and cover the energy range of ∼200 keV to ∼40 MeV. All 14 detectors combined provide a nearly full sky coverage with a FOV of ∼ 9.5 sr. For further informations about GBM see [Meegan *et al.* (2009)]

Before the results of the time sensitive analysis methods are presented it is interesting to look at the characteristics of each GRB in the X-ray and soft gamma-ray regime. GRB 100205A and GRB 100513A are detected and observed solely by the Swift observatory. On the left side of Fig. 6.8 the raw BAT rates of those two GRBs

are shown. One can see how the rates exceed the continuous background which changes according to the position and pointing direction of the satellite. Because these variations occur in general on much longer time scales than the duration of the GRB prompt emission, the trigger algorithm just has to look for a steep increase in rate. This increase is larger for GRB 100513A in comparison to GRB 100205A. Also the duration of GRB 100513A is much longer than the one of GRB 100205A. In fact it is the longest duration of all six analyzed GRBs. The exact T_{90} times of each GRB are listed in Table 6.3. The light curves of both GRBs also reveal more than just one peak with a faster rise and smaller decline which indicates that several internal shocks occur at the GRBs [Kobayashi *et al.* (1997)]. Further information about the GRBs and its afterglow are delivered by the sensitive XRT instrument. The combined light curve of BAT and XRT data is shown for each Swift GRB on the right side of Fig. 6.8. In these light curves the raw count rates already have been converted into the flux densities at 10 keV. By comparing it with the Crab flux density of $\sim$ 0,5 mJy at 10 keV [Toor *et al.* (1974)] it is visible that especially the flux density of GRB 100513A is between 0,5 and 1,5 Crab units during the first 100 seconds. If there is such a behavior also in the VERITAS energy range, these objects would be close to the detectable parameter space of the analysis methods

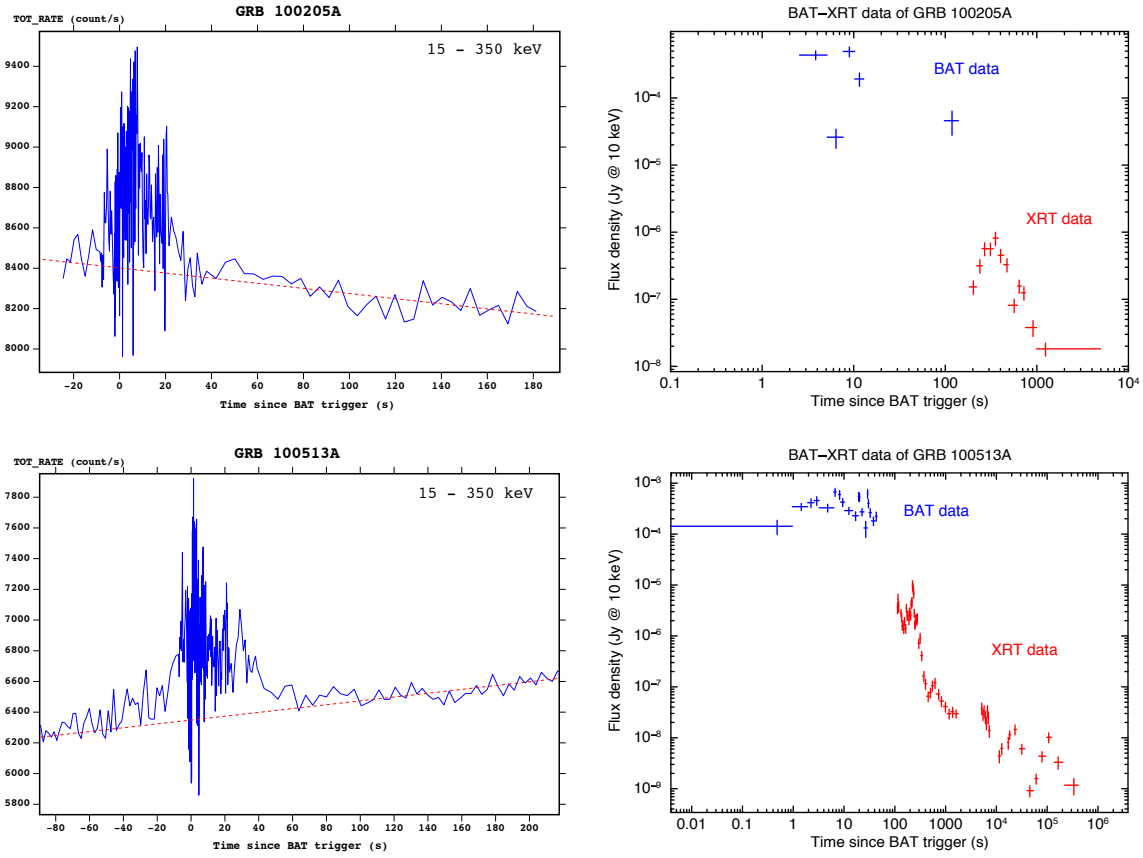

Fig. 6.8: *Light curves of the GRBs detected by Swift BAT. On the left side the raw count rates are displayed together with a dashed red line, that represents the background. The data points during the burst have smaller Δt. As there is also XRT data available, the combined light curves (at 10 keV) are shown on the right side, where the rates already have been converted into flux density. The BAT data had to be extrapolated towards the low energy of 10 keV*

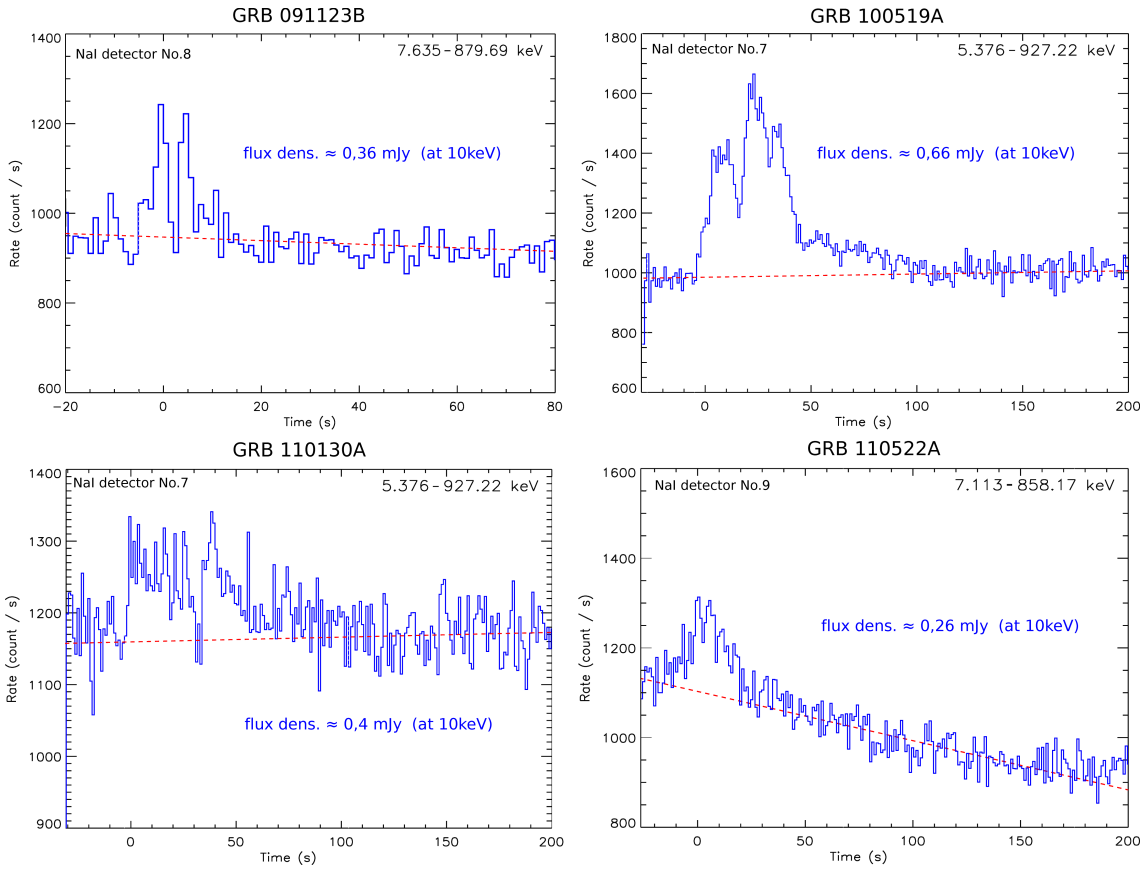

Fig. 6.9: *Light curves of the GRBs detected by Fermi GBM. Only the rates of the GBM NaI detectors with the brightest signal are shown. The dashed red line represents the background and the numbers in the upper right corner mark the accepted energy range. The signal flux density is averaged over the duration of the prompt emission.*

explained above.
Also some of the GBM detected GRBs produce flux densities during their prompt emission that are comparable to the crab flux. Their raw GBM count rates are presented in Fig. 6.9. Due to the same reasons explained before the background rate is also not a constant. One can clearly see that GRB 100519A is the strongest of all four GBM bursts. The striking features of its light curve are the 3 peaks and a slowly decaying tail. Its flux density at 10 keV exceeds the the one of Crab. Also its duration with more than 100 sec is quite long compared to the other GRBs which makes him an good object to evaluate the new analysis methods. Another candidate is GRB 110130A. Not as powerful and long as GRB 100519A but with an interesting light curve, exposing two similar shaped peaks of the same size.

6.3.2 Flares in GRB afterglow

Even if all these GRBs belong to the category of *long GRBs* their T_{90} durations are just in a range of 10 to 80 seconds. By looking at the delay of each VERITAS observation (see Table 6.3) one can see that the prompt emission of the GRB was missed by several minutes in all observations. The delay t_d is the time until the VERITAS telescopes point at the position of the GRB after it was detected by one

of the satellite experiments. But even if there was no observation during the prompt emission of the GRB it is still possible to measure VHE photons that could have been produced in the afterglow phase, which is observed by VERITAS for at least 20 min or longer (see Table 6.3).
In the combined light curve of GRB 100205A and GRB 100513A in Fig. 6.8, for example, one is able to discover several peaks at times beyond $\sim$ 100 seconds. These X-ray flares, superimposed on the underlying afterglow and sometimes also on the tail of the prompt emission, are quite common. According to [Chincarini *et al.* (2010)] $\sim$ 33 % of all detected GRB afterglows exhibit X-ray flares with an average ratio of flare width w_{X} to peak time t_{p} of ~ 0.23. They can be produced by late internal shocks which requires the central engine to be active for time scales much longer than the GRB event [Zhang (2007)]. Also a refreshed external shock is a possible explanation. At least for flares with $w_{\mathrm{X}}/t_{\mathrm{p}} \geqslant 0,25$ [Ioka *et al.* (2005), Chincarini *et al.* (2010)]. Such a flare is seen in the afterglow of GRB 100205A and its peak time of $t_{\mathrm{p}} \sim 370$ sec is covered by the VERITAS observation ($t_{\mathrm{d}} = 330$ sec, see Table 6.3).
The high-energy electrons, accelerated in the forward shock during the afterglow, can interact with the photons of the simultaneous X-ray flares via inverse Compton scattering (IC), which results in the formation of GeV-TeV flares [Wang *et al.* (2006)]. Also a synchrotron self-Compton (SSC) process in the external shock is possible to produce such VHE flares during the afterglow. Depending on which procedure is responsible for the VHE emission the light curve of the GeV-TeV flare either correlates with that of the X-ray flare (SSC model) or will become smoother and longer instead (IC at forward shock).
The widths w of the X-ray flares in our examples here are between 50 and 200 sec. A corresponding VHE flare with the same or even longer duration becomes detectable by the above-mentioned analysis methods if its flux is higher than 1 C.U. in the GeV-TeV regime. According to [Wang *et al.* (2006)] a broken power law with a peak in the GeV range is assumed for the spectrum of the IC emission. By choosing the normalization in a way that this spectrum exceeds the Crab flux density ($F_{\mathrm{Crab;0,1-0,4TeV}} = 1,6 \cdot 10^{-10}$ erg cm^{-1}s^{-1}) in the energy range of 0,1 - 0,4 TeV, one can calculate the flux density F_{IC} of the whole IC process. As a result we get $F_{\mathrm{IC}} \approx 2 \cdot 10^{-9}$ erg cm^{-1}s^{-1}. This value is in the same range as the IC flux density estimated for the afterglow flare of GRB 050502B in [Wang *et al.* (2006)]. If we assume the same parameters, the corresponding initial energy of a GRB should be $E \approx 2 \cdot 10^{52}$ ergs to produce a Crab-like flux density in the VERITAS energy range.

Hence, GeV-TeV flares during the afterglow phase and their detections with VERITAS are possible. In case of strong flares (flux $\geqslant$ 1.25 C.U.), the detection sensitivity is improved by the time-sensitive analysis methods. Now, even flares with durations down to $\sim$ 100 sec are detectable, if the flux $\gtrsim$ 1.75 C.U. Since the average delay of a VERITAS GRB observation is $\overline{t_{\mathrm{d}}} \approx 200$ sec, most of all possibly observable VHE afterglow flares at peak times of $t_{\mathrm{p}} > t_{\mathrm{d}}$ should exhibit a flare width of $w_{\mathrm{VHE}} \gtrsim 100$ sec. This is because $w_{\mathrm{VHE}} \geqslant w_{\mathrm{X}} \approx 0.23 t_{\mathrm{p}}$. Therefore the improved analysis methods are in particular useful for the delayed GRB observations performed by IACTs.

6.3.3 VERITAS analysis

To search for such flare occurrences all GRB runs are analyzed separately. These runs and their durations are listed in Tab.6.4. In addition to the standard significance calculation we also apply the time-sensitive methods to look for fluctuations in the data. The data results of the three different methods are shown in the table as well. At least for those runs for which it was possible to calculate the significance due to a sufficient amount of events at the expected position of the GRB. For a better visualization we plot the distribution of the significance values of both methods in two separate histograms (Fig. 6.10).

One can see that no significant variability at the GRB positions was measured. Both distributions are in agreement with measurements of background that can be described by a constant rate. Just the exp-test method shows a small shift towards negative significance values.
Concerning the GRB 100513A it is also obvious that we missed the first two X-ray flares, and some possibly correlated VHE flares, due to the long delay of more than 4000 sec. Also its large redshift of z = 4.8 [Cenko (2005)] can be the reason for the non-detection as the VHE flux could get attenuated by the extragalactic background light.
For GRB 100205A at least a part of the 200 sec long X-ray flare is covered by the VERITAS observation.
In case of the GBM detected GRBs it is not clear if there had been any X-ray flares, because no sensitive X-ray measurement was executed during the afterglow phase.
Since we expect in general durations of $\gtrsim$ 100 sec for flares happening during the delayed VERITAS observation, the non-detection of VHE flares for each GRB is likely due to a flux smaller than 2 C.U. in the VERITAS energy range. This can have various reasons. In case of an IC scattering at the forward shock, for example, either the X-ray flux is to low to support efficient electron cooling, the VHE flare

Run Nr.	GRB	El. [deg]	Az. [deg]	Duration [min]	standard Significance [sigma]	exp-test Significance [sigma]	BayesBl. Significance [sigma]	Rates [gamma/min]
48563	GRB091123B	71.00	-162.00	20.05	0.60	-0.455	0.241	0.16±0.25
48564	GRB091123B	68.00	-149.00	20.05	0.90	-1.024	0.318	0.21±0.24
48565	GRB091123B	66.00	-138.00	20.05	1.10	1.511	2.134	0.26±0.24
49789	GRB100205A	49.00	75.00	20.05	0.50	-0.500	-0.012	0.09±0.18
49790	GRB100205A	53.00	78.00	20.05	-2.30	-1.487	-2.463	-0.34±0.12
49791	GRB100205A	57.00	79.00	20.05	-0.20	-0.443	0.035	-0.04±0.18
49794	GRB100205A	66.00	82.00	20.05	1.90	1.263	0.664	0.45±0.27
49795	GRB100205A	70.00	82.00	20.05	1.70	-1.063	0.142	0.41±0.27
49796	GRB100205A	75.00	87.00	20.05	-1.70	-0.076	0.022	-0.39±0.20
49797	GRB100205A	79.00	86.00	20.05	0.20	-0.723	0.639	0.05±0.24
51322	GRB100513A	62.00	-170.00	20.05	-1.90	-1.393	-2.112	-0.36±0.17
51323	GRB100513A	59.00	-160.00	20.05	-0.60	-0.065	-0.640	-0.12±0.19
51324	GRB100513A	58.00	-151.00	20.05	-1.40	0.555	0.661	-0.24±0.15
51325	GRB100513A	55.00	-140.00	20.05	0.10	0.247	-1.359	0.02±0.17
51326	GRB100513A	52.00	-133.00	20.05	-0.40	-0.855	0.360	-0.07±0.18
51461	GRB100519A	61.00	-20.00	20.05	1.70	-1.118	-0.757	0.31±0.21
54686	GRB110130A	83.00	50.00	20.05	-0.30	-0.536	-0.439	-0.07±0.26
54687	GRB110130A	87.00	11.00	20.05	-3.00	0.659	-0.264	-0.74±0.20
54688	GRB110130A	86.00	-14.00	2.05	-1.00			-0.73±0.56
56737	GRB110522A	66.00	17.00	20.03	-0.90	0.472	0.354	-0.16±0.17
56738	GRB110522A	68.00	13.00	5.02	-0.60	-0.967	1.485	-0.24±0.39

Table 6.4: *List of all good quality VERITAS runs on six chosen GRBs. Significances have been measured run-wise with the standard, exp-test and Bayesian-blocks method. For run 54688 we can not calculate the significance for the time-sensitive methods because there are less than two events detected at the source position due to the short duration of the run.*

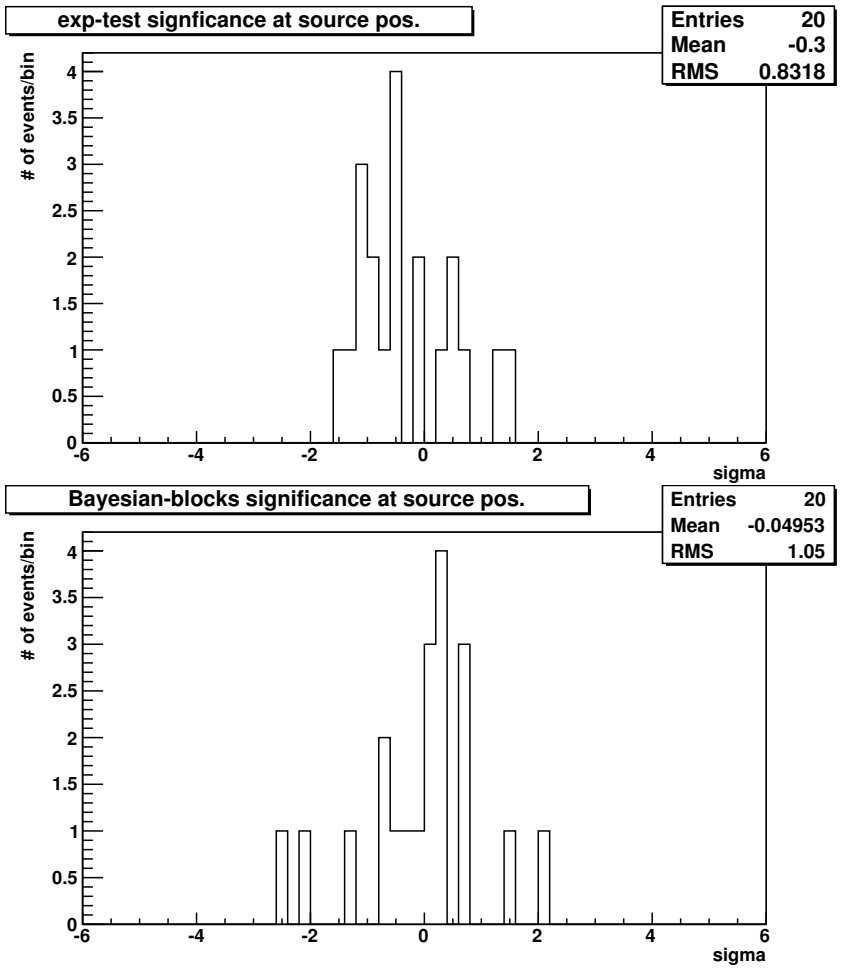

Fig. 6.10: *Distribution of significance measurements at the center positions of the maps which we get by analyzing 20 GRB runs. The histogram on top presents the significance measurements of the exp-test while the bottom histogram shows the result of the Bayesian-blocks method.*

could got smeared out by the angular dispersion of the afterglow or the Lorentz factor of the accelerated electrons is too low to shift the IC spectrum towards the GeV range.
Also the error on the source position is quite large for the GBM detected GRBs (see Table 6.3). But as mentioned above, it is still possible with the time sensitive methods to search for a flare inside the whole observed sky map. However, we then have to take the trails into account, so we won't report a detection if the significance is lower than 5.9σ. Unfortunately we even don't see an excess of more than 5σ in all the runs.

6.4 Summary

The tests of the time sensitive methods applied on data of variable sources revealed no intra-run fluctuations, neither at the source position nor somewhere in the field-of-view. At least no fluctuations distinctive enough to be detected by those methods.

Of course for some Mrk421 runs variability is even visible by looking at the rates plotted versus the time. But we can also see that in almost every run the change from a high-flux state to a low flux-state (or vice-versa) happens quite smoothly. If there are more sharp cut-offs during a run with larger variations in the rate it is possible to detect such variability with those methods. Unfortunately none of the analyzed sources exhibit such a behavior.
Especially the test on the 450 runs of mainly AGN observations revealed, that there seems to be no such sharp and strong rate changes during a run, that could trigger a detection by these two methods. This is in consistence with the theoretical models where the VHE emission is believed to originate from plasma blobs ejected along the jets of an AGN. Too short raise and decay times would imply much larger Doppler factors or much smaller radii of the blobs when compared to the respective values inferred on the basis of observations made at other wavelengths. However, such short time variability of AGNs can not completely be excluded for those objects. By choosing only a subset of all available VERITAS AGN data, it is highly probable that such flaring periods just have been missed.
In contrary to the general AGN models, such short temporal variability is typical for GRBs. Not only during the prompt emission but also during the afterglow phase one can expect flares of several minutes in different energy bands, even up to the GeV-TeV range. Therefore we analyzed 6 random GRBs and had a look at their X-ray light curves measured by the satellite experiments. Due to the delayed observation we could take VERITAS data only during the afterglow phase. The X-ray data of the Swift-detected GRBs revealed several flares during this time. However no correlated VHE flares have been discovered by the time sensitive analysis methods. With the additional information of the flare width in X-ray and the theoretical expectations based on this, one is able to constrain the flux of the non-detected VHE flares. Hence, the possible flares during the observed afterglow periods of the Swift GRBs, with expected flare durations of $\geqslant 200$ sec, are not supposed to exceed 1.25 C.U ($\approx 3,7 \cdot 10^{-10}$ erg cm^{-1}s^{-1} [0,1;10 TeV]).

Chapter 7

Conclusion and Outlook

In gamma-ray astronomy and in astronomy in general many of the observed sources show a transient behavior. Depending on the source type there are various reasons why its flux is variable. Under some circumstances these variability can be very short, in the order of seconds to minutes. Typical sources are gamma-ray bursts (GRBs), active galactic nuclei (AGNs), X-ray binaries and magnetars. While in some wavelength ranges the detection of such short flares is easy, it can be quite difficult in the very high-energetic (VHE) range ($\gtrsim$ 85 GeV) in which imaging atmospheric Cherenkov telescopes (IACTs) like VERITAS are operating. This is due to the large background and the comparable low signal rates.
This thesis discussed the investigation of advanced statistical methods, which are specialized to find deviations of a constant rate in sequences of gamma-ray like events measured with VERITAS. The name of these methods are *exp-test* and *Bayesian-blocks*. Especially their performances in case of very short and abrupt rate changes have been tested with Monte Carlo (MC) simulations. Further, the methods have been also applied on data of GRBs and AGNs observed with VERITAS.

7.1 Comparison of different methods

One goal of this work was to determine, if the advanced methods could improve the detection of weak sources that exceed the constant background only for a short amount of time ($\sim$ minutes) during a much longer period of data taking (a so-called *run*). Typical durations of a VERITAS run (T_{run}) are 20 or 30 minutes. If a significant deviation from a constant rate is measured, while all other circumstances stay the same throughout the run, then a signal is detected. The standard method, however, follows another approach and measures if the sum of all observed events during the run significantly exceeds the estimated amount of background events of that same period.
To compare the advanced methods with the standard method, it was necessary to simulate a large amount of event sequences that contain a short period where the rate is larger compared to the rest of the simulated run duration T_{run}. This should serve as a simplified model for a weak source that only exceeds the background rate during its flare. As the PMTs had been upgraded in VERITAS in 2012, two different VERITAS states had to be simulated, before and after the upgrade. By scanning the two dimensional parameter space of flare duration and flare

rate, it was revealed that the *exp-test* method, in addition to the standard method, would increase the detectable parameter space for both VERITAS states, while the *Bayesian-blocks* method improves the detection of short-flaring, weak sources only during post-upgrade conditions (see also Fig. 5.10). The area of additional parameter space covered only by the advanced methods, is found in the region of high flare fluxes (above 1 C.U.[1]) and short flare durations below $0.18 \cdot T_{\mathrm{run}}$. The integrated flux above 300 GeV corresponding to one C.U. is $F_{>300\mathrm{GeV}} \approx 1.2 \cdot 10^{10} cm^{-2} s^{-1}$ [Aleksić *et al.* (2014)]. Hence, the advanced methods are only an improvement for the detection of short flares if the flux exceeds the baseline by at least this amount.
When it's about the specific use cases for the different methods it can be concluded that the *exp-test* method is a good choice for short flares or repeating fluctuations, while the *Bayesian blocks* method is a good choice if the phase of the enhanced rate happens at the beginning or the end of a run (see Fig. 5.11). The advantage of the *Bayesian blocks* method is, that it automatically estimates the start and end time of the flare. Its disadvantage is the much longer computing process and the necessity of MC generated lookup tables.

7.2 Analysis of transient sources

After testing the methods with MC simulations, the next step of this work was to apply the methods to VERITAS data runs of transient sources. This is the first time that VERITAS data has been analyzed for these characteristics: a very high flux ($\gtrsim$ 1.C.U.) emitted over a very short duration ($\sim$ minutes). In no studies before the short time variability of a VHE source was used as a detection criterion. It was shown during the comparison process before, that the advanced methods can discover these specific kind of flaring sources, not detectable by the standard method. Therefore the goal was to detect these sources or discover some new unknown sources next to them, located in the same field of view (FOV).

Especially the test on the 450 runs of mainly AGN observations revealed, that there seems to be no such abrupt and strong rate changes within a single a run, that could trigger a detection by the advanced methods. So no variability in the order of minutes was seen in each of these runs. This is in consistence with the theoretical models where the VHE emission is believed to originate from plasma blobs ejected along the jets of an AGN. Too short raise and decay times would imply much larger Doppler factors or much smaller radii of the blobs when compared to the respective values inferred on the basis of observations made at other wavelengths. However, such short time variability of AGN can not completely be excluded for those objects. By choosing only a subset of all available VERITAS AGN data, it is highly probable that such flaring periods just had been missed in this work here. Especially as it is known that several AGN showed such an erratic behavior in the past. Examples of such AGN are Mrk421 [Galante (2011)], Mrk501 [Albert *et al.* (2007)] , PKS 1222+216 [Aleksic *et al.* (2011)], PKS 2155-304 [Aharonian (2007)] and BL Lacertae [Arlen *et al.* (2013)]. The possible explanations for the rapid TeV variability from those sources could be small subregions within a jet (jets-in-jet) [Giannios *et*

[1] C.U. = Crab unit; the rate (and flux) measured during a Crab observation

al. (2009)], stratified structures (compact region moving faster than the rest of the jet) [Boutelier *et al.* (2008)], the recollimation of the jet [Bromberg *et al.* (2009)] or its deceleration [Levinson (2007)]. Therefore it is important to discover such rapid variability more often in those sources to constrain the possible models.
By using data of a transient sources with large photon rates like Mrk 421, it was also tested if the advanced methods can detect variability in strong sources. Due to the large amount of photons, the intra-run variability of Mrk 421 was even visible by eye when the measured rates had been plotted versus the time. However, the change from a high-flux state to a low flux-state was a gradual decrease over the whole run ($\sim$ 20min) which was too smooth to trigger a detection by the advanced methods.

The last step of this work involved the application of the methods to GRB data. While it happens quite rarely in AGN, extreme short time variability is a general characteristic of GRBs. Especially during the prompt emission but also during the afterglow phase these short time variability can be measured in the X-ray and gamma-ray regime. Analyzing the VERITAS data with the newly implemented time-sensitive methods can help answering the question if the source also emits VHE photons correlated to those flares and which mechanism is responsible for their production.
The prompt emission periods of all six GRBs in this study were missed by the VERITAS observations, which all started with a delay t_d after the GRB trigger due to the slewing process and/or because one has to wait for the right observing conditions. Therefore only the afterglow phase was analyzed. During this period, however, short X-ray flares are possible, with a flare width w_X proportional to their peak time [Chincarini *et al.* (2010)]. A refreshed forward shock or late central engine activity are supposed to be the explanations [Zhang (2007)] for these flares, which have been found in the X-ray light curves of the two GRBs observed by the XRT instrument (GRB 100205A and GRB 100513A).
There also exist models [Wang *et al.* (2006)] that predict contemporaneous GeV-TeV flares, due to inverse Compton scattering of the X-ray photons, with flare widths of $w_\mathrm{V} \geqslant w_\mathrm{X}$. Therefore we expect mostly VHE flares with $w_\mathrm{V} \gtrsim 100$ sec during an averagely delayed VERITAS observation ($\overline{t_\mathrm{d}} \approx 200$ sec).
Up to now, none of these VHE flares have been detected by IACTs. The advantage of the newly implemented time-sensitive analysis methods is the improved detection performance for strong flares ($F_\mathrm{V} \geqslant 1.25$ C.U.) with short widths ($w_\mathrm{V} \leqslant 200$ sec). Which is the temporal characteristic we expect for many of the observable VHE afterglow flares, if they exist. In case of flare durations close to the VERITAS run duration ($\sim$ 1200 sec), however, the standard analysis will be the method with the better sensitivity.
Since there was no flare detected in the VERITAS data of all six GRBs, we are able to constrain the possible flare characteristics. Especially when also some additional information about the X-ray flares is provided, which is the case for GRB 100205A and GRB 100513A. By knowing the X-ray flare duration it is easy to estimate the lower limit for the potential GeV-TeV Flares to be $w_\mathrm{V;low} \approx 200$ sec. Therefore one can conclude, that the fluxes of possible afterglow VHE flares at these GRBs are not supposed to exceed 1.25 C.U ($\approx 3,7 \cdot 10^{-10}$ erg cm^{-1}s^{-1} [0,1;10 TeV]), if all the

theoretical assumptions mentioned above are correct.
Constraining flux levels and/or durations of VHE flares is important to fine tune or rule out existing afterglow models for specific GRBs. Even more exciting would be a direct detection of a flare and the determination of its parameters: w_V, t_p and F_V. This can help figuring out which acceleration mechanisms take place at which time in the environment of the GRB and how energetic they are.

In the end it should be mentioned as well, that the lack of flare detection of distant sources, like GRBs and AGN, could be also caused by the absorption of VHE photons due to the interaction with extra-galactic background light (EBL).

7.3 The Cherenkov Telescope Array - CTA

As already mentioned in the section before, it is still challenging to measure short-transient phenomena with IACTs like VERITAS. In case of GRB prompt emission an improved alert system and a faster slewing speed of VERITAS could lead to smaller delays between GRB trigger and the start of observations. This way, the end of the prompt phase could be observed. If there is VHE emission and a hard drop in the rates, the GRB could be detectable by the advanced methods and even by the standard method.

Another way of improving the detection of transient sources and variability in general would be an increase in sensitivity. This can be done by new reconstruction algorithms or by hardware improvements. Going even further, designing a completely new IACT facility is the next logical step. This next-generation IACT observatory, named *Cherenkov Telescope Array (CTA)*, is currently in the planning stages.
It is expected that CTA will improve the sensitivity at least by an order of magni-

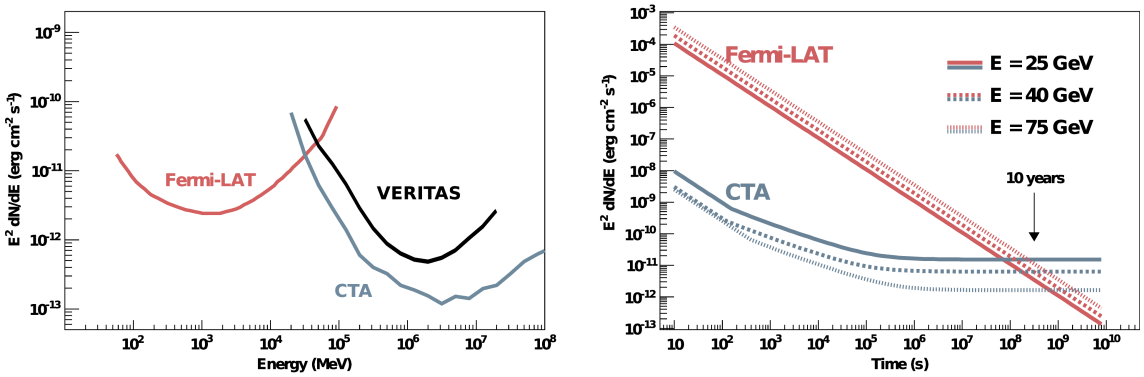

Fig. 7.1: *left: Comparison of differential sensitivities. The Fermi-LAT and the CTA curve are taken from [Funk et al. (2013)]. While the Fermi-LAT curve corresponds to a dataset of 1 year, the CTA curve represents the sensitivity of a 50 hour observation. The VERITAS curve is taken from [Prokoph (2013), Fig. 3.18] and corresponds to the 50 hour observation with the upgraded array (after summer 2012).*
right: Differential sensitivity at selected energies as a function of observation time taken from [Funk et al. (2013)]. These plots were generated for a detection significance of 5σ in the relevant energy bin and a minimum number of 25 events.

tude with respect to the current-generation IACTs (e.g. VERITAS, MAGIC, and HESS) (see Fig. 7.1, left). Especially the improvement at low energies (< 100 GeV) is important for the discovery of GRBs, as their detection at high energies is limited due to EBL attenuation. But also in general will the search for short time variability in VHE sources benefit from these improvements, as is shown in [Biteau *et al.* (2011)]. Due to higher sensitivity the sampling capabilities of CTA will increase, allowing the probe of shorter time scales.
In another study, which compared the sensitivity of CTA and Fermi-LAT in the overlapping energy range of 10 GeV to 100 GeV, it was revealed, that the discovery potential for short-transient phenomena (inside the FOV) is much larger in CTA [Funk *et al.* (2013)], which clearly can be seen in the right plot of Fig. 7.1. CTA has an advantage over the Fermi-LAT by many orders of magnitude, especially for observations below 280 hours. Longer observations don't increase the sensitivity of CTA, due to the irreducible background.
It should however be said that the FOV of CTA is much smaller than the 2.4π sr of Fermi-LAT, but it is planed to be bigger than those of current-generation IACTs. This would also increase the low probability of an accidental GRB discovery while performing a scheduled observation of another object in the same FOV.

The increased sensitivity together with the lower energy threshold of CTA will enable the detection of more distant sources. A non-detection with CTA of a distant source simultaneously detected by the Fermi-LAT could constrain the properties of the EBL at high redshifts. Further, CTA will be an ideal instrument to study timing properties of VHE emitting objects down to sub-minute time scales. Better timing information will help to determine the size and the location of the VHE emission region and give insights about the physical processes responsible for variability.

Appendix A

Additional options for the *timingSignificance* program

A.1 Correlated or uncorrelated maps - smoothing

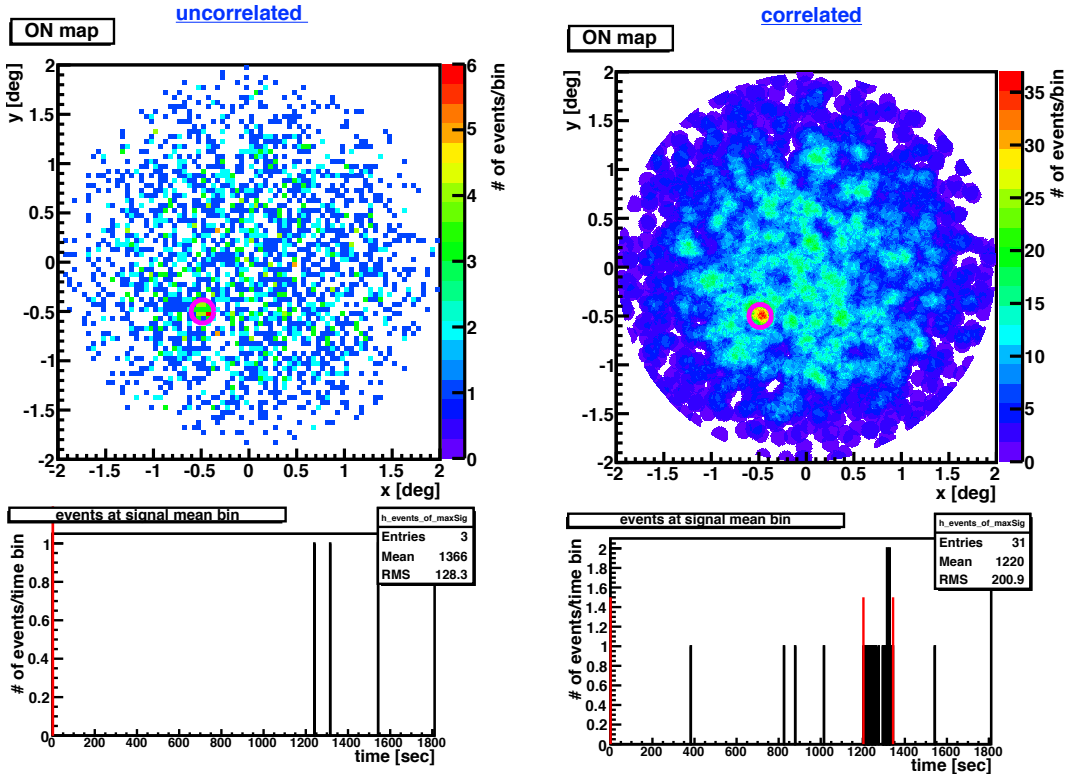

Fig. A.1: *Comparison between uncorrelated and correlated events. For all plots we chose:* $T = 1800$ *sec,* $\lambda_{\rm bkg} = 500$ *Hz,* $f_{\rm loss} = 99.7\%$*,* $\lambda_{\rm sig} = 0.4$ *Hz and* $T_{\rm sig} = 150$*sec. The position of the simulated transient signal is at the center of the magenta circle. The left side shows the effect of non-correlated events. Each bin in the position map contains just the number of events with exactly that position while in the right map each event assigned to a specific position will be also added to bins around that position* ($r \leqslant \sqrt{0.008}$)*. This leads to more events per bin as can be seen in the bottom histograms as well, showing the distribution of all events in the central signal bin over time.*

Like during the creation of significance maps using the standard on-off method, there is also a option implemented in this program to allow correlation between neighboring position bins or not. By default correlation is allowed, which results in much finer binning of the position map: 400×400. With an additional parameter (default = 0.008) on can define the size of the area of bins influencing each other: $A = 0.008 \cdot \pi$. This procedure leads to a smoother position map and a larger number per position bin. If one sets the uncorrelation option to true, the binning will reduce to 80×80. This is necessary because otherwise each position bin would contain almost no events which would make it impossible for the rate-sensitive algorithms form Scargle and Prahl to find any rate change in that bin (Fig. A.1). The default values represent the same settings that will be chosen for the analysis of a source with a medium slope in its energy spectrum.

A.2 Read data file

Instead of simulating background events as described above one also has the opportunity to use pre-analyzed data events provided in the form of an standrad analysis output file. This root-file has to contain a *TTree* with all the events surviving the gamma-hadron separation and being reconstructed inside a radius of 2°. The infor-

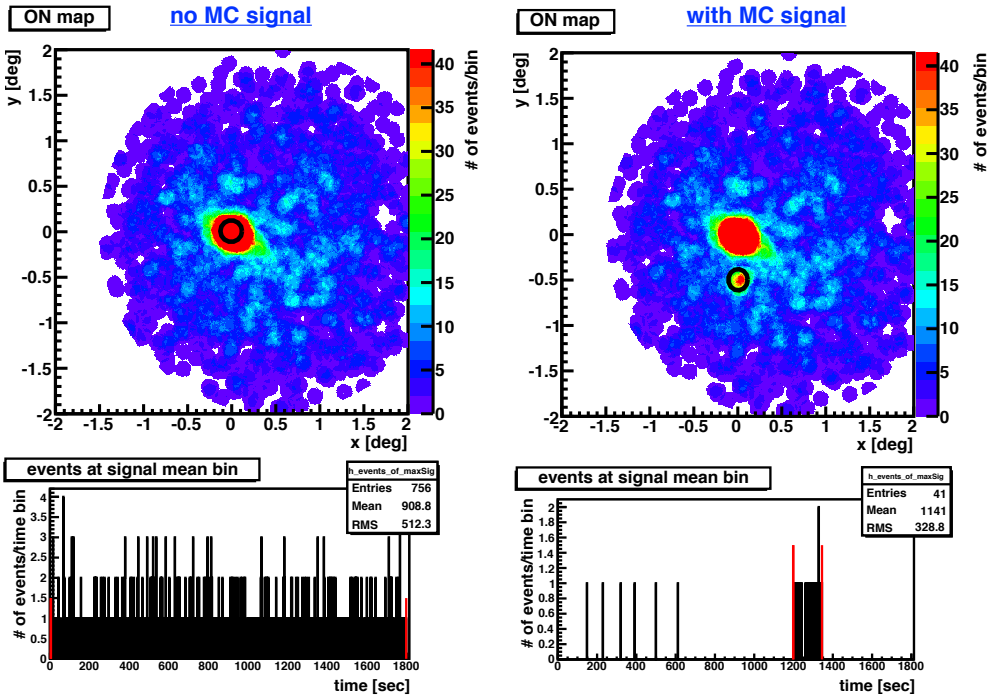

Fig. A.2: *Use of Mrk421 data file instead of MC background generation. Left side: Just events from data file (one run with wobble offset) and no MC signal. If there is no MC signal the position of the central signal bin will be set to the source position at (0,0). Bottom plot shows high but constant rate at source position. Right side: same Mrk421 events plus an additional MC signal with* $\lambda_{\mathrm{sig}} = 0.4$ *Hz and* $T_{\mathrm{sig}} = 150$*sec (exactly same as in Fig. A.1). The color scale on both sides is adjusted to see the feature of the additional MC signal on the right side. Due to this the observed point source runs into saturation (cenral bin contains 756 events) and looks extended.*

mation of each event has to cover the direction in de-rotated x- and y-coordinates and the exact measured time. It is now up to the user if he wants to specify some additional Monte Carlo transient signal events on top of these background events or not. If one wants to reveal new features of the data by analyzing them with the two dedicated methods from Prahl and Scargle it will make no sense to add some additional Monte Carlo signal appearing somewhere in the field-of-view. In this case one has to declare either the signal rate as zero or the signal duration as zero. Instead, if one wants to examine the behavior of the different methods in comparison with the standard method under most realistic conditions it will help to use the data as background and add some fake transient signal (Fig. A.2).

A.3 Analyse only signal region

If one is not interested in the analysis of all possible positions in the field-of-view but just in the outcome of the analysis at the expected signal region, there is also an option to tell the program to ignore every position outside an area of $0.6° \times 0.6°$ around the signal direction.
Analyzing a data file generated at the end of the `eventdisplay` analysis chain without any additional Monte Carlo transient signal will automatically put the signal position at the center of the position map where we would expect an observed gamma ray source to be reconstructed.

A.4 Parallel processing

The program also features parallelization under usage of the *Message Parsing Interface - MPI* [Karniadakis *et al.* (2003)]. Due to the sometimes long processing

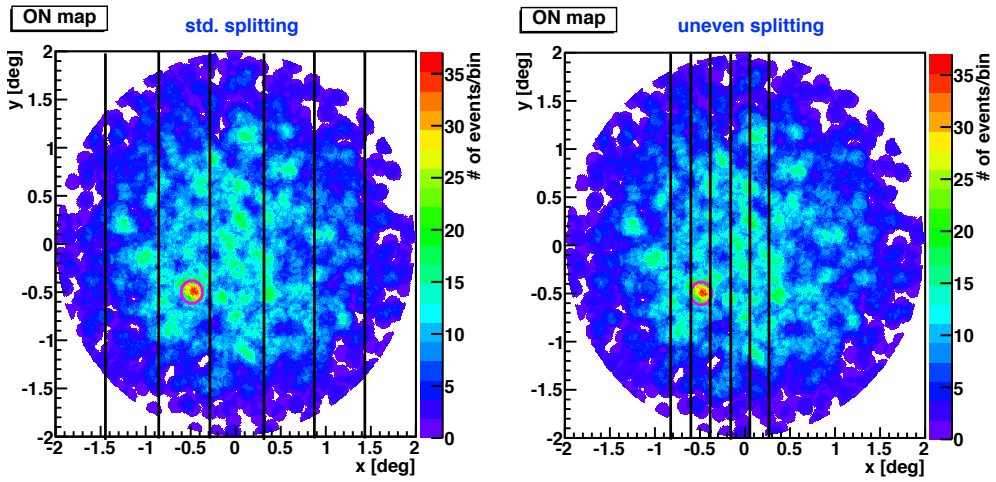

Fig. A.3: *Two different examples of splitting the analysis process. For both plots we use the same MC events and distribute the computation of the statistical tests over 7 parallel processes. While on the right side each process has to calculate the result of the same amount of position bins, the areas of bins analyzed by each process in the left plot are smaller if the bins are closer to the center of the field-of-view or to the signal position.*

time of the Bayesian-block algorithm, especially if the number of events in a position bin is very large ($\approx$ 500 - 1000), the idea was to split the process along the x-axis of the data container holding the information of each event. In doing so, many different processes running in parallel and working on a part of the data container. The number of available processes depends on the computing infrastructure of the user and can be declared at the time of program execution. By default the splitting divides the data container in equal size parts. This is not alway the most efficient way because due to the radial acceptance many events will be found in position bins close to $x = 0$ and/or close to a simulated transient signal. Using an additional option will lead to a more sophisticated splitting that divides the x-range close to the center and close to a simulated signal position in more parts than the outer region of the data container. (Fig. A.3)

Appendix B

Confidence intervalls and upper limits

The goal of each experiment is the determination of an unknown parameter. Usually one can never resolve the exact value of parameter with infinite precision. Therefore a traditional way of reporting errors on experimental results is the construction of *confidence intervals* and *upper limits*.
A confidence interval is a range of values $[\mu_{\text{low}}, \mu_{\text{up}}]$ that contains the true unknown parameter value μ with a certain probability, the so called *confidence level CL*. The CL is normally defined before the measurement started and its value α depends on the confidence one wants to achieve, which is usually 99%.

$$P(\mu \in [\mu_{\text{low}}, \mu_{\text{up}}]) = \alpha \tag{B.1}$$

The interval is different for each measurement of the same unknown μ and a CL-value of $\alpha = 99\%$ has the meaning that 99% of all measured intervals contain the unknown true value μ. This does not mean that the unknown true value has a 99% probability of being inside the interval. For each obtained interval the true value is either inside or outside [Barlow (1989), Feldman *et al.* (1998)].

B.1 Construction of a classical confidence interval

Due to the uncertainty in the experiment the measured data sample X will follow a probability distribution which depends on the unknown parameter μ. If one knows the underlying distribution function one can select an *acceptance interval* $[x_-, x_+]$ such that:

$$P(x \in [x_-, x_+]|\mu) = \alpha \tag{B.2}$$

After repeating this procedure for all possible values of μ one can draw the obtained intervals as horizontal lines in a diagram with μ over x (see Fig. B.1). This resulting *confidence belt* gives us the opportunity to retrieve the confidence interval of a measured value x. Just by drawing a vertical line through x one will find two intersection points of the line with the confidence belt. These two points correspond to μ_{low} and μ_{up}.
The reason why this construction leads to the probability mentioned above (Equ. (B.1)) is explained in detail in the original article of J. Neyman [Neyman (1937)]. It is

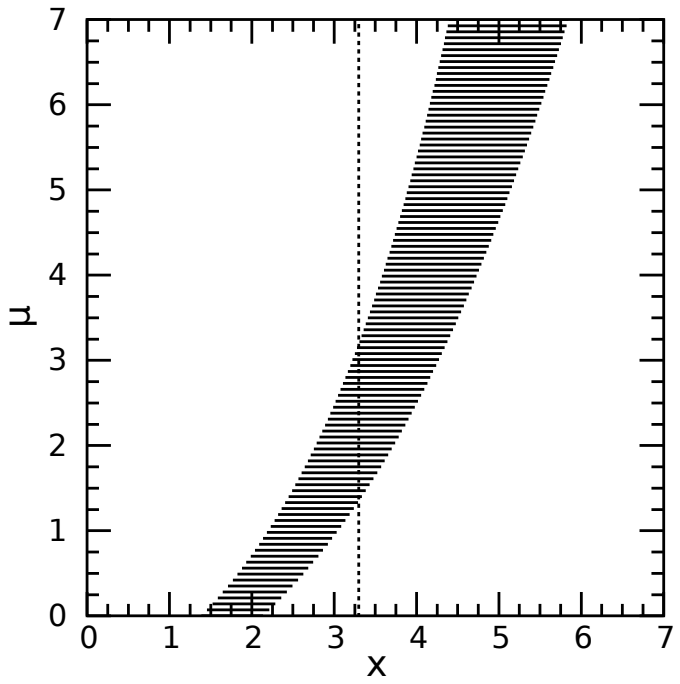

Fig. B.1: *The usage and construction of a generic confidence belt. After drawing a horizontal acceptance interval* $[x_-, x_+]$ *for each* μ *with* $P(x \in [x_-, x_+]|\mu) = \alpha$ *one can obtain the confidence interval* $[\mu_{\text{low}}, \mu_{\text{up}}]$ *by drawing a vertical line through the measured value* x*. [Feldman et al. (1998)]*

shown that the problem of constructing a system of confidence intervals is equivalent to that of selecting acceptance intervals for each μ. Every selected acceptance interval has to meet certain criteria which can be achieved by adjusting the limits in the right way depending on the structure of the underlying probability function. In case of a Gaussian distribution one valid option for the acceptance limits is the integration over a range that is symmetric to the mean value μ_{Gauss} in a way that the result will become exactly α which leads to *central confidence intervals*. Simply one adds up all the probabilities of each value x, starting from highest to lowest, until exactly α is reached. Another option, which is used quite often, one fixes x_+ at ∞ and chooses x_- accordingly to get a probability of α. This leads to *upper confidence limits*.
Due to the discreteness of a Poisson distribution it is difficult to get exactly the same value as α. Therefore a conservative approach is to use the same summation procedure as for the gaussian case but the final probability that is least equal or bigger than the CL [Barlow (1989), Feldman *et al.* (1998)].

B.2 Upper limits for small signals

In many experiments the true value μ_{true} usually represents a positive quantity. Therefore the obtained confidence intervals cannot be negative. This leads to a problem when dealing with small μ_{true}, thus small x values, as can be seen in Fig. B.1.

For measured x values smaller than 1.5 one ends up with a confidence interval that is an empty set but, according to Neyman [Neyman (1937)], there should be an interval with at least one entry for each possible x value. In this section I explain how to deal with measurements of confidence intervals if the true signal is small
A possible solution is the change of the acceptance limits x_- (n_-) and x_+ (n_+) in a way that the condition Equ. (B.2) is still true but each possible x (or n) has a confidence interval assigned to it that is not empty. This can be achieved by an ordering principle described in [Feldman *et al.* (1998)]. While in the previous section one had to choose the points x (or n) of the acceptance interval in order of decreasing $P(x(\text{or } n)|\mu)$, this time one has to order them by their likelihood ratios R.

$$R = P(x(\text{or } n)|\mu)/P(x(\text{or } n)|\mu_{\text{best}}) \qquad \text{with: } \mu_{\text{best}} = \max[0, x(\text{or } n)] \tag{B.3}$$

With this new ordering principle there will be an automatic transition from intervals to upper limits for small values of x or n. Hence there won't be any empty sets anymore.

B.3 Profile likelihood

Another approach to the construction of confidence intervals is the method of *profile likelihood* (see [Rolke *et al.* (2001), Rolke *et al.* (2005)]). Especially in the case when somebody would like to estimate the true value of a parameter μ while the distribution function contains an unknown nuisance parameter b as well this method can be very helpful. An example would be the measurement of the rate μ of a γ-ray signal under the influence of some unknown background rate b. The observables would be N_{on} and N_{off} (see section 4.1 for definition). Together with the parameter τ, which accounts for different exposures in the on- and off-region, the overall probability would look like this:

$$P_{\mu,b}(N_{\text{on}}, N_{\text{off}}) = \frac{(\mu+b)^{N_{\text{on}}}}{N_{\text{on}}!}\mathrm{e}^{-(\mu+b)} \cdot \frac{(\tau b)^{N_{\text{off}}}}{N_{\text{off}}!}\mathrm{e}^{-\tau b} \tag{B.4}$$

This is in principle the same function that has been used in subsection 4.1.1 and 4.1.2 with $\langle N_{\text{S}}\rangle = \mu$ and $\langle N_{\text{B}}\rangle = b$. For the construction of the confidence interval one can use the same likelihood ratio function as the one used for calculating the significance (see Equ. (4.7)).

$$\lambda(\boldsymbol{N}) = \frac{\mathcal{L}(\boldsymbol{N}|\mu, \hat{\mathrm{b}})}{\mathcal{L}(\boldsymbol{N}|\mu_{\max}, b_{\max})} = \frac{P_{\mu,\hat{b}}(\boldsymbol{N})}{P_{\max}(\boldsymbol{N})} \qquad \text{with: } \boldsymbol{N} = (N_{\text{on}}, N_{\text{off}}) \tag{B.5}$$

$$\chi = -2\ln\lambda(\boldsymbol{N}) \qquad \Rightarrow \qquad \boldsymbol{N} \longmapsto P_{\chi^2}[-2\ln\lambda(\boldsymbol{N}); 1] \tag{B.6}$$

The only difference is that one tests the null hypothesis not only for zero but for all possible (positive) values of μ and the conditional maximum likelihood estimate $\hat{b}(\mu)$. The function $\mathcal{L}(\boldsymbol{N}|\mu, \hat{b})$ is called the *profile likelihood* of μ. The hypothesis for a specific μ is true if $\boldsymbol{N} \in A(\mu, \hat{b})$. The idea is basically to search for all μ, whose two dimensional acceptance region $\mathrm{A}(\mu, \hat{b})$ contains the observed values N_{on}

and N_{off}, which in turn is the same what has been done to construct a confidence interval in section B.1. With the following derivation one can understand how the likelihood ratio is used to estimate the acceptance region and the confidence interval:

$$\text{if:} \quad \int_0^{\chi_\alpha} P_{\chi^2}[-2\ln\lambda(\boldsymbol{N});1] = \alpha \qquad \text{with:} \quad \chi_\alpha = -2\ln\lambda_\alpha \tag{B.7}$$

$$\Rightarrow \quad P(\lambda(\boldsymbol{N}) \geqslant \lambda_\alpha) = \alpha \qquad \Rightarrow \quad P\left[P_{\mu,\hat{b}}(\boldsymbol{N}) \geqslant \lambda_\alpha P_{\max}(\boldsymbol{N})\right] = \alpha \tag{B.8}$$

$$\text{with:} \quad P_{\mu,\hat{b}}(\boldsymbol{N}_{\text{A}}) \geqslant \lambda_\alpha P_{\max}(\boldsymbol{N}_{\text{A}}); \quad \boldsymbol{N}_{\text{A}} = \text{events in acceptance region} \tag{B.9}$$

$$\Rightarrow \quad P(\boldsymbol{N} \in \boldsymbol{N}_{\text{A}}|\mu,\hat{\text{b}}) = P(N_{\text{on}}, N_{\text{off}} \in A(\mu,\hat{\text{b}})|\mu,\hat{\text{b}}) = \alpha \tag{B.10}$$

If one is looking for all μ that fulfill this criteria after a data point $\boldsymbol{N}_0 = (N_{\text{on}}, N_{\text{off}})$ was measured, one has to look for those μ with $P_{\mu,\hat{b}}(\boldsymbol{N}_0) \geqslant \lambda_\alpha P_{\max}(\boldsymbol{N}_0)$:

$$-2\ln P_{\mu,\hat{b}}(\boldsymbol{N}_0) \leqslant -2\ln\lambda_\alpha - 2\ln c; \quad c = P_{\max}(\boldsymbol{N}_0) = \text{const.} \tag{B.11}$$

$$\Rightarrow \quad -2\ln\mathcal{L}(\boldsymbol{N}_0|\mu,\hat{b}) \leqslant \chi_\alpha + c' \tag{B.12}$$

In the end one just has to check where the function $l(\mu) = -2\ln\mathcal{L}(\boldsymbol{N}_0|\mu,\hat{b})$, which can be approximated by a quadratic function of μ, intersects with the horizontal line at $\chi_\alpha + c'$. The two intersection points will then mark the upper and the lower limit of the confidence interval. χ_α is the α percentile of the χ^2 distribution and depends just on the confidence level one wants to achieve.
One can see that it is not necessary to know the exact value of b if one is just interested in estimating μ. It is enough to calculate $\hat{b}(\mu)$ under the condition that it maximizes $\mathcal{L}(\boldsymbol{N}_0|\mu,\hat{b})$ for a specific μ. It is also clear that c' is the minimum of $l(\mu)$. Hence one has to find the points where $l(\mu)$ deviates exactly χ_α from its minimum. In case of a small number of signal events the minimum of $l(\mu)$ is close to zero, hence there will be only one limit that has a physical valid value. It was decided (see [Rolke *et al.* (2005)]) to set the lower limit to zero and just report an upper limit instead. A more extreme case occurs when the signal events N_{on} are even smaller than the the background events N_{off}. This time the minimum is lower than zero and only a small part of $l(\mu)$ covers the area of $\mu \geqslant 0$ until it reaches χ_α. An option is now to search for a μ_{up} with $l(\mu_{\text{up}}) - l(0) = \chi_\alpha$ which leads to a higher upper limit.
As a last remark I want to point out that this method is also applicable for more than just one nuisance parameter. For example one wants to include the uncertainty of the signal efficiency ϵ. Therefore a third measured number N_ϵ, besides N_{on} and N_{off}, is necessary to estimate the efficiency. If the distribution of N_ϵ is known one can just construct a new profile likelihood function with both parameters b and ϵ being functions of μ [Rolke *et al.* (2001), Rolke *et al.* (2005)].

B.4 Median and confidence interval of a unknown distribution

Sometimes it can happen that the distribution of a parameter measurement does not follow any known distribution. In this case one can calculate the median instead of the mean value. Then, also the error of the median has to be determined in a different way. Since it should also represent the 68% confidence interval, the calculations of the median and its error are executed as follows:
First, it is necessary to sort all N measurements, that will be used to calculate the median, from its lowest to its highest value and store them in an array $A[N]$. Because we start with the assumption of an unknown distribution with a true unknown median, the N measurements are supposed to be a subset of this distribution. The probability for each of these measurements is $q = 0.5$ of having a value that is smaller than the true median. We are now able to use the rules for a binomial distribution and calculate the expected number of values below the true median that will be found in the subset: $m = N \cdot q$. Hence, the entry with the index m in our ordered array provides the expected median of the unknown distribution: $A[m]$ (=m_{th} event in the ordered array). As m is just an estimate also the indexes in the 68% confidence interval around m should be taken into account: $n \in [m - \sigma_{\text{Binom.}}, m + \sigma_{\text{Binom.}}]$. With $\sigma_{\text{Binom.}} = \sqrt{Nq(1-q)}$ and $q = 1/2$ we get the following equation for the two confidence limits of the array indexes:

$$n_{\text{up}} = \frac{N}{2} + \frac{\sqrt{N}}{2} \qquad \text{and} \qquad n_{\text{low}} = \frac{N}{2} - \frac{\sqrt{N}}{2} \tag{B.13}$$

Because an index can be only an integer we have to round-off both results: $i_{\text{up}} = \lfloor n_{\text{up}} \rfloor$ and $i_{\text{low}} = \lfloor n_{\text{low}} \rfloor$. Similar to the determination of the median, one hast to look into the array at the index positions i_{up} and i_{low} to find the entries whose values finally provide the confidence limits $CL'_{\text{up}} = A\left[i_{\text{up}}\right]$ and $CL'_{\text{low}} = A\left[i_{\text{low}}\right]$. To be more accurate one can even take into account the deviation of the original n_{up} and n_{low} due to rounding:

$$CL_{\text{up(low)}} = CL'_{\text{up(low)}} + \left(A\left[i_{\text{up(low)}} + 1\right] - CL'_{\text{up(low)}}\right)\left(n_{\text{up(low)}} - i_{\text{up(low)}}\right) \tag{B.14}$$

Bibliography

[Abdo *et al.* (2009)] A. Abdo et al., *Fermi Observations of GRB 090902B: A Distinct Spectral Component in the Prompt and Delayed Emission*, Astrophys.J. **706**, L138–L144 (2009), arXiv:0909.2470.

[Abdo *et al.* (2011)] A. A. Abdo, M. Ackermann, M. Ajello, L. Baldini, J. Ballet, G. Barbiellini, D. Bastieri, K. Bechtol, R. Bellazzini, B. Berenji and et al., *Fermi Large Area Telescope Observations of Markarian 421: The Missing Piece of its Spectral Energy Distribution*, Astrophysical Journal **736**, 131 (August 2011), 1106.1348.

[Ackermann *et al.* (2011)] M. Ackermann et al., *Detection of a spectral break in the extra hard component of GRB 090926A*, Astrophys.J. **729**, 114 (2011), arXiv:1101.2082.

[Actis *et al.* (2011)] M. Actis, G. Agnetta, F. Aharonian et al., *Design concepts for the Cherenkov Telescope Array CTA: an advanced facility for ground-based high-energy gamma-ray astronomy*, Experimental Astronomy **32**(3), 193–316 (2011).

[Aharonian *et al.* (1997)] F. Aharonian, W. Hofmann, A. Konopelko and H. Völk, *The potential of ground based arrays of imaging atmospheric Cherenkov telescopes. I. Determination of shower parameters*, Astroparticle Physics **6**(3–4), 343 – 368 (1997).

[Aharonian *et al.* (2004)] F. Aharonian, A. Akhperjanian and M. Beilicke, *Observations of 54 active galactic nuclei with the hegra system of Cherenkov telescopes*, Astron.Astrophys. **421**, 529–537 (2004), astro-ph/0401301.

[Aharonian (2007)] F. Aharonian, *An Exceptional Very High Energy Gamma-Ray Flare of PKS 2155-304*, Astrophys.J. **664**, L71–L78 (2007), arXiv:0706.0797.

[Albert *et al.* (2007)] J. Albert, E. Aliu, H. Anderhub, P. Antoranz, A. Armada et al., *Variable VHE gamma-ray emission from Markarian 501*, Astrophys.J. **669**, 862–883 (2007), astro-ph/0702008.

[Aleksic *et al.* (2011)] J. Aleksic et al., *MAGIC discovery of VHE Emission from the FSRQ PKS 1222+21*, Astrophys.J. **730**, L8 (2011), arXiv:1101.4645.

[Aleksić *et al.* (2013)] J. Aleksić et al., *Contemporaneous observations of the radio galaxy NGC 1275 from radio to very high energy gamma-rays*, (2013), arXiv:1310.8500.

[Aleksić *et al.* (2014)] J. Aleksić et al., *Measurement of the Crab Nebula spectrum over three decades in energy with the MAGIC telescopes*, (2014), arXiv:1406.6892.

[Arlen *et al.* (2013)] T. Arlen, T. Aune, M. Beilicke, W. Benbow, A. Bouvier et al., *Rapid TeV Gamma-Ray Flaring of BL Lacertae*, Astrophys.J. **762**, 92 (2013), arXiv:1211.3073.

[Atoyan *et al.* (2000)] A. M. Atoyan, F. A. Aharonian, R. J. Tuffs and H. J. Volk, *On the Gamma-ray fluxes expected from Cassiopeia A*, Astron. Astrophys. **355**, 211 (2000), astro-ph/0001186.

[Atwood *et al.* (2009)] W. Atwood et al., *The Large Area Telescope on the Fermi Gamma-ray Space Telescope Mission*, Astrophys.J. **697**, 1071–1102 (2009), arXiv:0902.1089.

[Aune (2012)] T. Aune, *Observations of gamma-ray bursts at extreme energies*, PhD thesis, University of California, Santa Cruz, 2012.

[Band *et al.* (1993)] D. Band, J. Matteson, L. Ford, B. Schaefer, D. Palmer et al., *BATSE observations of gamma-ray burst spectra. 1. Spectral diversity.*, Astrophys.J. **413**, 281–292 (1993).

[Barlow (1989)] R. Barlow, *Statistics: A Guide to the Use of Statistical Methods in the Physical Sciences*, Manchester Physics Series, Wiley, 1989.

[Barthelmy *et al.* (2005)] S. D. Barthelmy et al., *The Burst Alert Telescope (BAT) on the Swift MIDEX mission*, Space Sci. Rev. (2005), astro-ph/0507410, [Sov. Sci. Rev.120,143(2005)].

[Beckmann *et al.* (2013)a] V. Beckmann and C. Shrader, *Active Galactic Nuclei*, Physics textbook, Wiley, 2013.

[Beckmann *et al.* (2013)b] V. Beckmann and C. R. Shrader, *The AGN phenomenon: open issues*, (2013), 1302.1397.

[Bell (1978)] A. R. Bell, *The acceleration of cosmic rays in shock fronts. I*, Monthly Notices of the Royal Astronomical Society **182**, 147–156 (January 1978).

[Bender *et al.* (2007)] R. Bender and S. Lange, *Was ist der p-Wert?*, Dtsch med Wochenschr **132**(S 01), e15–e16 (2007).

[Beringer *et al.* (2012)] J. Beringer, J. F. Arguin et al., *Review of Particle Physics*, Phys. Rev. D **86**, 010001 (Jul 2012).

[Bernlöhr (2000)] K. Bernlöhr, *Cherenkov light simulation*, http://www.mpi-hd.mpg.de/hfm/CosmicRay/ /ChLight/ChLat.html, 2000.

[Biteau *et al.* (2011)] J. Biteau and B. Giebels, *Ultra fast variability monitoring with CTA*, PoS **AGN2011**, 018 (2011).

[Blandford *et al.* (1987)] R. Blandford and D. Eichler, *Particle acceleration at astrophysical shocks: A theory of cosmic ray origin*, Physics Reports **154**, 1–75 (October 1987).

[Bloom (2011)] J. Bloom, *What Are Gamma-Ray Bursts?*, Princeton Frontiers in Physics, Princeton University Press, 2011.

[Blumenthal *et al.* (1970)] G. R. Blumenthal and R. J. Gould, *Bremsstrahlung, Synchrotron Radiation, and Compton Scattering of High-Energy Electrons Traversing Dilute Gases*, Rev. Mod. Phys. **42**, 237–270 (Apr 1970).

[Boettcher (2007)] M. Boettcher, *Modeling the Emission Processes in Blazars*, Astrophys.Space Sci. **309**, 95–104 (2007), astro-ph/0608713.

[Boettcher (2012)] M. Boettcher, *Modeling the Spectral Energy Distributions and Variability of Blazars*, (2012), arXiv:1205.0539.

[Bosch-Ramon (2013)] V. Bosch-Ramon, *Clumpy stellar winds and high-energy emission in high-mass binaries hosting a young pulsar*, (2013), 1310.5641.

[Boutelier *et al.* (2008)] T. Boutelier, G. Henri and P.-O. Petrucci, *An inhomogeneous jet model for the rapid variability of TeV blazars*, Mon. Not. Roy. Astron. Soc. **390**, L73 (2008), 0807.4998.

[Briggs *et al.* (1999)] M. Briggs, D. Band, R. Kippen, R. Preece, C. Kouveliotou et al., *Observations of grb 990123 by the Compton gamma-ray observatory*, (1999), astro-ph/9903247.

[Bromberg *et al.* (2009)] O. Bromberg and A. Levinson, *Recollimation and Focusing of Relativistic, Radiative Jets: Applications to Blazars and M87*, Astrophys. J. **699**, 1274–1280 (2009), arXiv:0810.0562.

[Buckley *et al.* (2003)] J. H. Buckley, P. Dowkontt, K. Kosack and P. Rebillot, The VERITAS flash ADC electronics system, in *Proceedings, 28th International Cosmic Ray Conference (ICRC 2003): Tsukuba, Japan, July 31-August 7, 2003*, pages 2827–2830, 2003.

[Burrows *et al.* (2004)] D. N. Burrows et al., *The Swift X-Ray Telescope*, Proc. SPIE **5165**, 201–216 (2004).

[Cao *et al.* (2014)] G. Cao and J. Wang, *The hadronic origin of hard gamma-ray spectrum from blazar 1ES 1101-232*, (2014), 1401.3970.

[Cenko (2005)] S. B. Cenko, *GCN CIRCULAR 10752*, http://gcn.gsfc.nasa.gov/gcn3/10752.gcn3, 2005.

[Chaisson *et al.* (2013)] E. Chaisson and S. McMillan, *Astronomy Today*, Pearson Education, 2013.

[Chincarini *et al.* (2010)] G. Chincarini et al., *Unveiling the origin of X-ray flares in Gamma-Ray Bursts*, Mon. Not. Roy. Astron. Soc. **406**, 2113 (2010), arXiv:1004.0901.

[Cogan (2006)] P. Cogan, *Nanosecond Sampling of Atmospheric Cherenkov Radiation Applied to TeV Gamma-Ray Observations of Blazars with VERITAS*, PhD thesis, University College Dublin, 2006.

[Cucchiara *et al.* (2011)] A. Cucchiara, A. Levan, D. Fox, N. Tanvir, T. Ukwatta et al., *A Photometric Redshift of z 9.4 for GRB 090429B*, Astrophys.J. **736**, 7 (2011), arXiv:1105.4915.

[Davies *et al.* (1957)] J. M. Davies and E. S. Cotton, *Design of the quartermaster solar furnace*, Solar Energy **1**(2–3), 16 – 22 (1957), The Proceedings of the Solar Furnace Symposium.

[Drury (1983)] L. O. Drury, *An introduction to the theory of diffusive shock acceleration of energetic particles in*

tenuous plasmas, Reports on Progress in Physics **46**(8), 973 (1983).

[Dubus (2013)] G. Dubus, *Gamma-ray binaries and related systems*, Astron.Astrophys.Rev. **21**, 64 (2013), 1307.7083.

[Fan *et al.* (2013)] Y.-Z. Fan, P. Tam, F.-W. Zhang, Y.-F. Liang, H.-N. He et al., *High energy emission of GRB 130427A: Evidence for inverse Compton radiation*, Astrophys.J. **776**, 95 (2013), arXiv:1305.1261.

[Feldman *et al.* (1998)] G. J. Feldman and R. D. Cousins, *A Unified approach to the classical statistical analysis of small signals*, Phys.Rev. **D57**, 3873–3889 (1998), physics/9711021.

[Fermi (1949)] E. Fermi, *On the Origin of the Cosmic Radiation*, Phys. Rev. **75**, 1169–1174 (Apr 1949).

[Funk *et al.* (2013)] S. Funk and J. A. Hinton, *Comparison of Fermi-LAT and CTA in the region between 10-100 GeV*, Astropart. Phys. **43**, 348–355 (2013), arXiv:1205.0832.

[Gaisser (1990)] T. Gaisser, *Cosmic Rays and Particle Physics*, Cambridge University Press, 1990.

[Galante (2011)] N. Galante, *VERITAS observation of Mrk421 flaring activity*, **8**, 63–66 (2011), arXiv:1109.6059.

[Gehrels *et al.* (2004)] N. Gehrels et al., *The Swift Gamma-Ray Burst Mission*, The Astrophysical Journal **611**(2), 1005 (2004).

[Ghisellini (2010)] G. Ghisellini, *Gamma Ray Bursts: basic facts and ideas*, (2010), arXiv:1010.3015.

[Giannios *et al.* (2009)] D. Giannios, D. A. Uzdensky and M. C. Begelman, *Fast TeV variability in blazars: jet in a jet*, Mon. Not. Roy. Astron. Soc. **395**, 29 (2009), arXiv:0901.1877.

[Gomboc (2012)] A. Gomboc, *Unveiling the Secrets of Gamma Ray Bursts*, (2012), arXiv:1206.3127.

[Grieder (2010)] P. Grieder, *Extensive Air Showers: High Energy Phenomena and Astrophysical Aspects - A Tutorial, Reference Manual and Data Book*, Astrophysics and space science library, Springer, 2010.

[Hall *et al.* (2003)] J. Hall, V. V. Vassiliev, D. B. Kieda, J. Moses, T. Nagai and J. Smith, *Veritas CFDs*, International Cosmic Ray Conference **5**, 2851 (July 2003).

[Hanna *et al.* (2010)] D. Hanna, A. McCann, M. McCutcheon and L. Nikkinen, *An LED-based flasher system for VERITAS*, Nuclear Instruments and Methods in Physics Research A **612**, 278–287 (January 2010), arXiv:0911.2015.

[Hays (2007)] E. Hays, *VERITAS Data Acquisition*, (2007), arXiv:0710.2288.

[Hillas (1985)] A. M. Hillas, *Cerenkov light images of EAS produced by primary gamma*, International Cosmic Ray Conference **3**, 445–448 (August 1985).

[Hofmann *et al.* (1999)] W. Hofmann, I. Jung, A. Konopelko, H. Krawczynski, H. Lampeitl et al., *Comparison of techniques to reconstruct vhe gamma-ray showers from multiple stereoscopic Cherenkov images*, Astropart.Phys. **122**, 135–143 (1999), astro-ph/9904234.

[Holder *et al.* (2006)] J. Holder et al., *The first VERITAS telescope*, Astropart.Phys. **25**, 391–401 (2006), astro-ph/0604119.

[Holder *et al.* (2011)] J. Holder, E. Aliu, T. Arlen, T. Aune, M. Beilicke et al., *VERITAS: Status and Highlights*, International Cosmic Ray Conference **12**, 137 (2011), arXiv:1111.1225.

[Holder (2005)] J. Holder, *Exploiting VERITAS timing information*, **5**, 383 (2005), astro-ph/0507450.

[Hopkins *et al.* (2006)] P. F. Hopkins, L. Hernquist, T. J. Cox, T. Di Matteo, B. Robertson et al., *A Unified, merger-driven model for the origin of starbursts, quasars, the cosmic x-ray background, supermassive black holes and galaxy spheroids*, Astrophys.J.Suppl. **163**, 1–49 (2006), astro-ph/0506398.

[Inoue *et al.* (2013)] S. Inoue, J. Granot, P. T. O'Brien, K. Asano, A. Bouvier et al., *Gamma-Ray Burst Science in the Era of the Cherenkov Telescope Array*, Astropart.Phys. **43**, 252–275 (2013), arXiv:1301.3014.

[Ioka *et al.* (2005)] K. Ioka, S. Kobayashi and B. Zhang, *Variabilities of Gamma-Ray Burst Afterglows: Long-acting Engine, Anisotropic Jet, or Many Fluctuating Regions?*, The Astrophysical Journal **631**(1), 429 (2005).

[Israel *et al.* (2001)] G. L. Israel, S. Campana, S. Covino, D. D. Fiume, D. Lazzati, T. Oosterbroek, M. Orlandini, M. R. Panzera, A. N. Parmar, D. Ricci, G. Tagliaferri and L. Stella, *A systematic search for new X-ray pulsators in public ROSAT HRI and BeppoSAX SMC fields*, X-ray Astronomy: Stellar Endpoints, AGN, and the Diffuse X-ray Background **599**, 674–677 (December 2001).

[Jackson (1998)] J. Jackson, *Classical Electrodynamics*, Wiley, 1998.

[Jelley *et al.* (1963)] J. V. Jelley and N. A. Porter, *Cerenkov Radiation from the Night Sky, and its Application to gamma-Ray Astronomy*, QJRAS **4**, 275 (September 1963).

[Karniadakis *et al.* (2003)] G. Karniadakis and R. Kirby, *Parallel Scientific Computing in C++ and MPI: A Seamless Approach to Parallel Algorithms and Their Implementation*, Cambridge University Press, 2003.

[Kelner *et al.* (2008)] S. R. Kelner and F. A. Aharonian, *Energy spectra of gamma rays, electrons, and neutrinos produced at interactions of relativistic protons with low energy radiation*, Phys. Rev. D **78**, 034013 (Aug 2008).

[Kieda (2011)] D. Kieda, *Status of the VERITAS Upgrade*, (2011), arXiv:1110.4360.

[Kobayashi *et al.* (1997)] S. Kobayashi, T. Piran and R. Sari, *Can internal shocks produce the variability in GRBs?*, Astrophys. J. **490**, 92–98 (1997), astro-ph/9705013.

[Krawczynski *et al.* (2013)] H. Krawczynski and E. Treister, *Active Galactic Nuclei - the Physics of Individual Sources and the Cosmic History of Formation and Evolution*, Front.Phys.China. **8**, 609–629 (2013), 1301.4179.

[Levinson (2007)] A. Levinson, *On the Origin of Rapid Flares in TeV Blazars*, Astrophys. J. **671**, L29 (2007), arXiv:0709.1549.

[Li *et al.* (1983)] T.-P. Li and Y.-Q. Ma, *Analysis methods for results in gamma-ray astronomy*, Astrophys.J. **272**, 317–324 (1983).

[Longair (2011)] M. Longair, *High Energy Astrophysics*, Cambridge University Press, 2011.

[Maier *et al.* (2007)] G. Maier and J. Knapp, *Cosmic-Ray Events as Background in Imaging Atmospheric Cherenkov Telescopes*, Astropart.Phys. **28**, 72–81 (2007), arXiv:0704.3567.

[Maier (2007)] G. Maier, *Monte Carlo studies of the VERITAS array of Cherenkov telescopes*, (2007), arXiv:0709.4195.

[Matthews (2005)] J. Matthews, *A Heitler model of extensive air showers*, Astroparticle Physics **22**, 387–397 (January 2005).

[McCann *et al.* (2010)] A. McCann, D. Hanna, J. Kildea and M. McCutcheon, *A New Mirror Alignment System for the VERITAS Telescopes*, Astropart.Phys. **32**, 325–329 (2010), arXiv:0910.3277.

[Meegan *et al.* (2009)] C. Meegan et al., *The Fermi Gamma-Ray Burst Monitor*, Astrophys. J. **702**, 791–804 (2009), arXiv:0908.0450.

[Meszaros (2006)] P. Meszaros, *Gamma-Ray Bursts*, Rept.Prog.Phys. **69**, 2259–2322 (2006), astro-ph/0605208.

[Meszaros (2013)] P. Meszaros, *Gamma Ray Bursts*, Astropart.Phys. **43**, 134–141 (2013), arXiv:1204.1897.

[Mirabel *et al.* (1998)] I. F. Mirabel, V. Dhawan, S. Chaty, L. F. Rodriguez, J. Marti, C. R. Robinson, J. Swank and T. Geballe, *Accretion instabilities and jet formation in grs 1915+105*, Astron. Astrophys. **330**, L9 (1998), astro-ph/9711097.

[Mirabel (2010)] I. Mirabel, *Microquasars: summary and outlook*, Lect.Notes Phys. **794**, 1–15 (2010), 0805.2378.

[Mirabel (2012)] I. F. Mirabel, *Gamma-Ray Binaries Revealed*, Science **335**(6065), 175–176 (2012), http://www.sciencemag.org/content/335/6065/175.full.pdf.

[Müller (1967)] J. W. Müller, *On the interval-distribution for recurrent events with a non-extended dead time*, BIPM Reports **105**, 7 pp (1967).

[Müller (1973)] J. W. Müller, *Dead-time problems*, Nuclear Instruments and Methods **112**(1–2), 47 – 57 (1973).

[Nagai *et al.* (2007)] T. Nagai, R. McKay, G. Sleege and D. Petry, *Focal Plane Instrumentation of VERITAS*, (2007), arXiv:0709.4517.

[Neyman (1937)] J. Neyman, *Outline of a Theory of Statistical Estimation Based on the Classical Theory of Probability*, Philosophical Transactions of the Royal Society of London. Series A, Mathematical and Physical Sciences **236**(767), pp. 333–380 (1937).

[Nolan *et al.* (2012)] P. L. Nolan et al., *Fermi Large Area Telescope Second Source Catalog*, Astrophys.J.Suppl. **199**, 31 (2012), 1108.1435.

[Otte (2007)] A. Otte, *Observation of VHE Gamma-rays from the Vicinity of Magnetized Neutron Stars and Development of New Photon-detectors for Future Ground Based Gamma-ray Detectors*, PhD thesis, Technische Universität München, 2007.

[Paredes (2011)] J. M. Paredes, *Gamma-ray binaries: microquasars and binary systems with pulsar*, Nuovo Cim. **C034N3**, 167–172 (2011), 1101.4843.

[Perkins *et al.* (2009)] J. S. Perkins and G. Maier, *VERITAS Telescope 1 Relocation: Details and Improvements*, (2009), arXiv:0912.3841.

[Piran (1999)] T. Piran, *Gamma-ray bursts and the fireball model*, Phys.Rept. **314**, 575–667 (1999), astro-ph/9810256.

[Prahl (1999)] J. Prahl, *A fast unbinned test on event clustering in Poisson processes*, ArXiv Astrophysics e-prints (September 1999), arXiv:astro-ph/9909399.

[Preuss *et al.* (2002)] S. Preuss, G. Hermann, W. Hofmann and A. Kohnle, *Study of the photon flux from the night sky at La Palma and Namibia, in the wavelength region relevant for imaging atmospheric Cherenkov telescopes*, Nucl.Instrum.Meth. **A481**, 229–240 (2002), astro-ph/0107120.

[Prokoph (2013)] H. Prokoph, *Observations and modeling of the active galactic nucleus B2 1215+30 together with performance studies of the ground-based gamma-ray observatories VERITAS and CTA*, PhD thesis, Humboldt-Universität zu Berlin, 2013.

[Rees *et al.* (1994)] M. Rees and P. Meszaros, *Unsteady outflow models for cosmological gamma-ray bursts*, Astrophys.J. **430**, L93–L96 (1994), astro-ph/9404038.

[Rieke (2012)] G. Rieke, *Measuring the Universe: A Multiwavelength Perspective*, Cambridge University Press, 2012.

[Rolke *et al.* (2001)] W. A. Rolke and A. M. Lopez, *Confidence intervals and upper bounds for small signals in the presence of background noise*, Nucl.Instrum.Meth. **A458**, 745–758 (2001), hep-ph/0005187.

[Rolke *et al.* (2005)] W. A. Rolke, A. M. Lopez and J. Conrad, *Limits and confidence intervals in the presence of nuisance parameters*, Nucl.Instrum.Meth. **A551**, 493–503 (2005), physics/0403059.

[Romero *et al.* (2007)] G. E. Romero, V. Bosch-Ramon, J. M. Paredes and M. Orellana, Gamma-Ray Emission from Microquasars: Leptonic vs. Hadronic Models, in *Relativistic Astrophysics Legacy and Cosmology - Einstein's Legacy*, edited by B. Aschenbach, V. Burwitz, G. Hasinger and B. Leibundgut, page 480, 2007.

[Rosswog *et al.* (2007)] S. Rosswog and M. Brüggen, *Introduction to High-Energy Astrophysics*, Cambridge University Press, 2007.

[Sakamoto *et al.* (2011)] T. Sakamoto, S. Barthelmy, W. Baumgartner, J. Cummings, E. Fenimore et al., *The Second Swift BAT Gamma-Ray Burst Catalog*, Astrophys.J.Suppl. **195**, 2 (2011), arXiv:1104.4689.

[Scargle *et al.* (2013)] J. D. Scargle, J. P. Norris, B. Jackson and J. Chiang, *Studies in Astronomical Time Series Analysis. VI. Bayesian Block Representations*, Astrophys.J. **764**, 167 (2013), 1207.5578.

[Scargle (1998)] J. D. Scargle, *Studies in Astronomical Time Series Analysis. V. Bayesian Blocks, a New Method to Analyze Structure in Photon Counting Data*, Astrophys. J. **504**, 405 (September 1998), arXiv:astro-ph/9711233.

[Schlickeiser (2002)] R. Schlickeiser, *Cosmic Ray Astrophysics*, Astronomy and Astrophysics Library, Springer, 2002.

[Schmidt (2005)] F. Schmidt, *CORSIKA Shower Images*, http://www.ast.leeds.ac.uk/ fs/showerimages.html, 2005.

[Sol *et al.* (2013)] H. Sol et al., *Active Galactic Nuclei under the scrutiny of CTA*, Astroparticle Physics, **43**, , 215–240 (2013), 1304.3024.

[Tavecchio *et al.* (2011)] F. Tavecchio, J. Becerra-Gonzales, G. Ghisellini, A. Stamerra, G. Bonnoli et al., *On the origin of the gamma-ray emission from the flaring blazar PKS 1222+216*, (2011), arXiv:1104.0048.

[Toor *et al.* (1974)] A. Toor and F. Seward, *The Crab Nebula as a calibration source for X-ray astronomy*, Astronomical J. **79**, 995–999 (October 1974).

[Trümper *et al.* (2008)] J. Trümper and G. Hasinger, *The Universe in X-Rays*, Astronomy and Astrophysics Library, Springer, 2008.

[Urry *et al.* (1995)] C. M. Urry and P. Padovani, *Unified schemes for radio-loud active galactic nuclei*, Publ.Astron.Soc.Pac. **107**, 803 (1995), astro-ph/9506063.

[V. Bosch-Ramon *et al.* (2006)] V. Bosch-Ramon, G. E. Romero and J. M. Paredes, *A broadband leptonic model for gamma-ray emitting microquasars*, A & A **447**(1), 263–276 (2006).

[Varlotta (2013)] A. Varlotta, *Gamma-ray observations of X-ray binaries*, PhD thesis, Purdue University, 2013.

[Vedrenne *et al.* (2009)] G. Vedrenne and J. Atteia, *Gamma-Ray Bursts: The brightest explosions in the Universe*, Springer Praxis Books, Springer, 2009.

[Voges *et al.* (1999)] W. Voges, B. Aschenbach, T. Boller, H. Brauninger, U. Briel et al., *The ROSAT all - sky survey bright source catalogue*, Astron.Astrophys. **349**, 389 (1999), astro-ph/9909315.

[von Kienlin *et al.* (2014)] A. von Kienlin, C. A. Meegan, W. S. Paciesas, P. Bhat, E. Bissaldi et al., *The Second Fermi GBM Gamma-Ray Burst Catalog: The First Four Years*, Astrophys.J.Suppl. **211**, 13 (2014), arXiv:1401.5080.

[Wakely *et al.* (2016)] S. Wakely and D. Horan, *TeVCat*, http://tevcat.uchicago.edu/, 2016.

[Wang *et al.* (2006)] X.-Y. Wang et al., *GeV-TeV and X-Ray Flares from Gamma-Ray Bursts*, The Astrophysical Journal Letters **641**(2), L89 (2006).

[Weekes *et al.* (1989)] T. Weekes, M. Cawley, D. Fegan, K. Gibbs, A. Hillas et al., *Observation of TeV gamma rays from the Crab nebula using the atmospheric Cerenkov imaging technique*, Astrophys.J. **342**, 379–395 (1989).

[Weekes (2003)] T. Weekes, *Very High Energy Gamma-Ray Astronomy*, Series in Astronomy and Astrophysics, Taylor & Francis, 2003.

[Weinstein (2007)] A. Weinstein, *The VERITAS Trigger System*, (2007), arXiv:0709.4438.

[White (2005)] R. White, *Rise time of the simulated VERITAS 12-m Davies-Cotton reflector*, AIP Conf.Proc. **745**, 797–802 (2005).

[Wilks (1962)] S. Wilks, *Mathematical statistics*, Wiley series in probability and mathematical statistics. Probability and mathematical statistics, Wiley, 1962.

[Zhang (2007)] B. Zhang, *Gamma-ray burst afteglows*, Adv. Space Res. **40**, 1186 (2007), astro-ph/0611774.

[Zitzer (2013)] B. Zitzer, *The VERITAS Upgraded Telescope-Level Trigger Systems: Technical Details and Performance Characterization*, (2013), arXiv:1307.8360.

Acknowledgments

First and foremost I would like to thank my advisor, Dr. Gernot Maier, for his guidance and patience over the last years. I am deeply grateful to him for providing me the opportunity to do my Ph.D. in his group at DESY. His profound knowledge of gamma-ray astronomy, data analysis and code development lead to many prolific discussions which helped me to improve my own skills and to structure my work. Furthermore, I would like to thank the members of my Ph.D. committee for refereeing this thesis.
But of course there are many other people who helped me during my time at DESY and during the completion of my dissertation. Thanks to Stephane Vincent for his theoretical point of view and the many helpful suggestions to different drafts of the text. Together with Lucie Gérard and Gareth Hughes he helped me to shape a real thesis. In addition, I would like to thank Gareth for his support right from the start and all the non-work-related activities we did together outside of DESY. It was a great pleasure for me to have somebody in the same group that has a similar taste in music and was always able to come up with an anecdote that fits the situation. Also Heike Prokoph was a constant companion from the beginning. I'm very grateful that I could share a room with her because, besides her knowledge of physics and computing, no one else had more information about the processes and bureaucracies at DESY than her.
I would also like to express my gratitude to the rest of the VERITAS group at DESY and of course to all the VERITAS collaborators around the globe. My work would not have been possible without the effort of so many people involved with the construction and operation of the experiment.
Last but not least, I am deeply thankful to my family and all my friends. Only their love, support and constant encouragement made me able to finally reach this point of my life.

Selbstständigkeitserklärung

Ich erkläre, dass ich die Dissertation selbständig und nur unter Verwendung der von mir gemäß § 7 Abs. 3 der Promotionsordnung der Mathematisch-Naturwissenschaftlichen Fakultät, veröffentlicht im Amtlichen Mitteilungsblatt der Humboldt-Universität zu Berlin Nr. 126/2014 am 18.11.2014 angegebenen Hilfsmittel angefertigt habe.

Berlin, den 17.03.2016 Christian Skole